The Influence of Warm-Season Precipitation on Water Cycling and the Surface Energy Budget within and just-above a Colorado Subalpine Forest in Mountainous Terrain: Measurements and Modeling

by

Sean Peter Burns

B.S., University of Washington, 1990

M.S., University of California, Irvine, 1993

A thesis submitted to the

Faculty of the Graduate School of the

University of Colorado in partial fulfillment

of the requirements for the degree of

Doctor of Philosophy

Department of Geography

2018

This thesis entitled:
The Influence of Warm-Season Precipitation on Water Cycling and the Surface Energy Budget within and just-above a Colorado Subalpine Forest in Mountainous Terrain: Measurements and Modeling
written by Sean Peter Burns
has been approved for the Department of Geography

_____
Professor Peter Blanken

_____
Prof. Julie Lundquist

_____
Dr. Jielun Sun

_____
Dr. Edward Patton

Date _____

The final copy of this thesis has been examined by the signatories, and we find that both the content and the form meet acceptable presentation standards of scholarly work in the above mentioned discipline.

Burns, Sean Peter (Ph.D., Geography Department)

The Influence of Warm-Season Precipitation on Water Cycling and the Surface Energy Budget within and just-above a Colorado Subalpine Forest in Mountainous Terrain: Measurements and Modeling

Thesis directed by Professor Peter Blanken

Environmental towers are used at measure the pulse of the terrestrial biosphere at over 500 sites around the world and form a global network of measurements that is commonly known as FLUXNET (http://fluxnet.ornl.gov/). This thesis uses over a decade of data from the Niwot Ridge Forest AmeriFlux site in a high-elevation subalpine forest to examine how warm-season precipitation affected the above-canopy diel cycle of net radiation R_{net}, ecosystem eddy covariance fluxes (sensible heat H, latent heat λE, and CO_2 net ecosystem exchange NEE) and vertical profiles of scalars (air temperature T_{a}, specific humidity q, and CO_2 dry mole fraction χ_{c}). This analysis allowed us to examine how precipitation modified these variables from hourly (i.e., the diel cycle) to multi-day time-scales (i.e., typical of a weather-system frontal passage). Even though precipitation caused mean changes on the order of 50–70 % to mid-day R_{net}, H, and λE, the surface energy balance (SEB) was relatively insensitive to precipitation with mid-day closure values ranging between 90–110 %. With respect to measured λE during the warm-season we found that during the day following above-average precipitation, λE was enhanced at mid-day by $\approx 40\,\mathrm{W\,m^{-2}}$ (relative to dry conditions), and nocturnal λE increased from $\approx 10\,\mathrm{W\,m^{-2}}$ in dry conditions to over $20\,\mathrm{W\,m^{-2}}$ in wet conditions. The ecosystem fluxes were also modeled using the Community Land Model (CLM, version 4.5), and a comparison between the model and observations was presented. With default settings, CLM4.5 did not successfully model the changes in λE due to precipitation. However, by increasing the amount of time that rainwater was retained by the canopy/needles, CLM was able to better match the observed mid-day increase in λE on a dry day following a wet day. This thesis demonstrates techniques which can be used to compare observed and modeled ecosystem fluxes.

Dedication

First, to my parents, Stephen and Vicki Burns, for providing a lifetime of support and love. Second, to my wife Peisang Tsai for her support, the adventures and laughs we have had together, and tolerating my late night work schedule (and for taking such excellent care of our wonderful children, Jia and Bo). Love, always.

Acknowledgements

Many people helped make this work possible. First, I would like to thank my primary advisor, Peter Blanken, for his steady leadership and guidance throughout this process. I also thank Jielun Sun, Ned Patton, Julie Lundquist, Noah Molotch, and Mark Williams for taking time from their busy schedules to serve on my committee. Russ Monson and Andrew Turnipseed provided my initial opportunity to work at the Niwot Ridge AmeriFlux site. Jeff Beauregard assisted with site operations in 2007–2008. During my time in the Monson Lab, many post-docs, students, and field assistants helped at the site and also taught an old engineer a few things about biology and trees. In Appendix D, I photographically acknowledge many of the people I have had the pleasure to interact with throughout this journey. Thank you all very much.

The data collected for this thesis, would not have been possible without help and advice from many at NCAR EOL (Gordon Maclean, Steve Oncley, Kurt Knudsen, Tony Delany, Steve Semmer, Tom Horst, John Militzer, Britt Stephens, and Andy Watt), and the support of the Mountain Research Station and LTER staff (Bill Bowman, Jennifer Morse, Kurt Chowanski, Mark Losleben, John Knowles, and many others). For the IRGA comparison, I am grateful for discussions and data shared from Stefan Metzger, George Burba, Ed Swiatek, and Jiahong Li. Additional data used in this thesis came from Doug Weibel (UAV photos), Dave Bowling (CO_2 profiles), the Boulder Creek CZO (airborne Lidar data), the NOAA U.S. Climate Reference Network (USCRN, precipitation data from Hills Mill), MRS LTER C-1, Jia Hu (transpiration measurements), Andrew Richardson (PhenoCam photos), and Howland Forest data from Dave Hollinger and his group. Over the years, members of the AmeriFlux Tech Team (Hank Loescher, Christoph Thomas, Sébastien

Biraud, and Stephen Chan) have provided instruments and comparisons to ensure that the US-NR1 measurements are of high quality.

For my research into the maps and history of the forest near the US-NR1 site, I am grateful to the Boulder Carnegie Library for Local History, the CU Special Collections and Archives, the CU Earth Sciences & Map Library (Naomi Heiser, Ilene Raynes), and Sue Struthers from the US Forest Service. Several others provided valuable information and discussion on this topic, including, Bill Bowman (CU MRS), Duane Kitzis (NOAA), and Tom Veblen (CU Geography).

Running CLM was a new challenge which Sean Swenson, Will Wieder, Dave Lawrence, and Gordon Bonan helped make possible. Sean Swenson was especially quick to answer all my CLM-related questions. Conversations with Thomas Foken and Arnold Moene were also very insightful. Being an, older, "non-traditional" student, many people have contributed to my scientific training over the years: Stephen J. Burns, John LaRue, Carl Friehe, Djamal Khelif (and others at the UCI Atmospheric Turbulence Lab), Don Lenschow, Ned Patton, Jielun Sun (and others at the NCAR/MMM group formerly known as BLT), Larry Mahrt, Dave Bowling, Dean Anderson, Russ Monson, Chuixiang Yi, Peter Blanken, and Bill Massman, to name a few. I also appreciate the scientific (and non-scientific) discussions with my lunchtime compadres at NCAR (Peter Sullivan, Jeff Weil, Ned Patton, Tom Horst, and many visitors)—thanks for the years of stimulating lunches together! I also thank the staff in the CU Geography office (Karen Weingarten, Darla Shatto) for all their help.

None of this work would have been possible without funding from the DOE through the AmeriFlux Management Project at Lawrence Berkeley National Laboratory. Earlier support was from Russ Monson with grants from the DOE and NSF. For the CLM work, I also acknowledge and appreciate partial support from the NCAR MMM Director (Chris Davis and Rich Rotunno) and CGD (Gordon Bonan). Finally, thanks to my entire family. This work was only possible because of your support.

Contents

Tables

Table

Figures

Figure

Chapter 1

Introduction

Forests cover approximately 30% of the land surface on the Earth and have a large impact on the exchanges of energy, water, carbon dioxide, and chemical species between the ground and atmosphere [Baldocchi et al., 1988, Kaimal and Finnigan, 1994, Bonan, 2008a]. Vegetation shelters the ground surface from strong evaporation-enhancing winds, changes the dynamics of the near-surface winds [e.g., Raupach et al., 1996], increases the effective surface area for evaporation of intercepted precipitation, and draws soil-water from the roots to the leaf stomates where it is transpired. At the ecosystem scale, these exchanges are often measured using the micrometeorological eddy-covariance technique, which works best for near-neutral, stationary conditions over flat terrain [Baldocchi et al., 1988, Aubinet et al., 2012]. This thesis uses over a decade of nearly continuous 30-min eddy-covariance flux data collected at the Niwot Ridge Subalpine Forest AmeriFlux site (US-NR1) to deepen our understanding of the ecosystem-scale surface-atmosphere exchange of water, heat and carbon for a high-elevation subalpine forest within the Rocky Mountains of Colorado, USA.

A primary objective of this research is to improve our understanding of how warm-season precipitation affected the above-canopy diel cycle of wind and turbulence, net radiation R_{net}, ecosystem eddy covariance fluxes (sensible heat H, latent heat λE, and CO_2 net ecosystem exchange NEE) and vertical profiles of scalars (air temperature T_{a}, specific humidity q, and CO_2 dry mole fraction χ_{c}). The term "diel" is used to emphasize that we are looking at the full 24-hour cycle, not only daytime (diurnal) and nighttime (nocturnal) periods. The observational analysis, presented

in Chapter 5, allowed us to examine how precipitation modified these variables from hourly (i.e., the diel cycle) to multi-day time-scales (i.e., typical of a weather-system frontal passage).

Because land-surface models are often used to project changes in the hydrological cycle, modeling the effect of precipitation on the latent heat flux λE is an important aspect of land-surface models. In Chapter 6, we extend our observational analysis to determine how modeled turbulent fluxes reacted to warm-season precipitation; and how similar they were to the observed fluxes. To achieve this goal, we contrasted the conditionally-sampled diel composites of the eddy-covariance fluxes from the US-NR1 site with those from the Community Land Model (CLM, version 4.5). We found a mismatch between the CLM and observed fluxes, which resulted in an examination of the CLM parameterizations (primarily related to the capacity of the model forest to hold water, and the subcanopy turbulent parameterization). As part of this analysis, the sensitivity of the modeled fluxes to those parameterizations was also checked. This analysis also led us to take a closer look at the effect of sloping terrain on our observations. We achieved this by contrasting latent heat flux and friction velocity from the US-NR1 observations with those from an AmeriFlux site in Maine with terrain that is relatively flat (Howland Forest).

Within the rest of Chapter 1, the following information is provided: motivation for our study (Sect. 1.1), a summary of the surface energy budget (Sect. 1.2), a discussion of previous work related to ET in forests (Sect. 1.3) as well as how precipitation affects ecosystem fluxes (Sect. 1.4), and how we modeled the ecosystem fluxes (Sect. 1.5). In addition to the precipitation-related analysis in Chapters 5 and 6 (as described below), the other topics included in this thesis are as follows: the history of the US-NR1 site, as well as the history of the forest which surrounds US-NR1 (Chapter 2), the measurement techniques used (Chapter 3), and a general overview of the US-NR1 site characteristics (Chapter 4).

The focus of this thesis is on the the water vapor fluxes. For hydrologists and plant ecologists, water vapor exchange between the ground and atmosphere is typically called evapotranspiration (or, ET, for short). Since we are interested in the surface energy balance, we will usually express the water vapor evaporated and transpired to/from the surface as an energy flux, which is called

the latent heat flux λE [SI units: $\mathrm{W\,m^{-2}}$]. In our discussions, the terms evapotranspiration and latent heat flux are used interchangeably. Any mention of "partitioning of latent heat flux or ET" refers to the separation of ET into its component parts which, for our purposes, is transpiration and evaporation (this will be discussed in more detail below in Sects. 1.3 and 1.5). For the observations (Chapter 5), the effect of precipitation on NEE and vertical profiles of CO_2 are included in our analysis; however, in the CLM modeling part of the thesis (Chapter 6) only the sensible and latent heat fluxes will be examined.

Though the primary goal of our study is to quantify how precipitation modified the warm-season mean diel cycle of the measured scalars and fluxes, we also present the 14-year mean and interannual variability of the energy fluxes and NEE measured at the US-NR1 site in Chapter 5. These results are an update to the original set of papers [e.g., Monson et al., 2002, Turnipseed et al., 2002] that examined the ecosystem fluxes from the US-NR1 site over ten years ago and were based on two years of measurements.

1.1 Water resources in southwest North American

Water is a necessity for life. Worldwide, fresh water is a resource that is already becoming scarce, and will likely be a source of future conflicts around the world and between nations [McKie, 2015, Ripple et al., 2017]. In the western/southwestern United States, the Colorado River supplies water to over 30 million people and irrigates millions of acres of cropland [Zielinski, 2010, Jacobs, 2011]. Measurements show that, since the early 20th century, this critical resource has come under increasing stress and we are reaching a point where water supplied by the river no longer meets the demand (Fig. 1.1). In the early 1960s, the river stopped reaching the Gulf of California (except for the occasional controlled water releases from dams or El Niño years), turning the Colorado River delta into an arid wasteland with devastating impacts on fish and other wildlife populations around the Gulf of California [Postel, 2013, Pitt et al., 2017]. Between Mexico and the U.S. States that use Colorado River water, water allocation has been a long-standing contentious issue, that have been

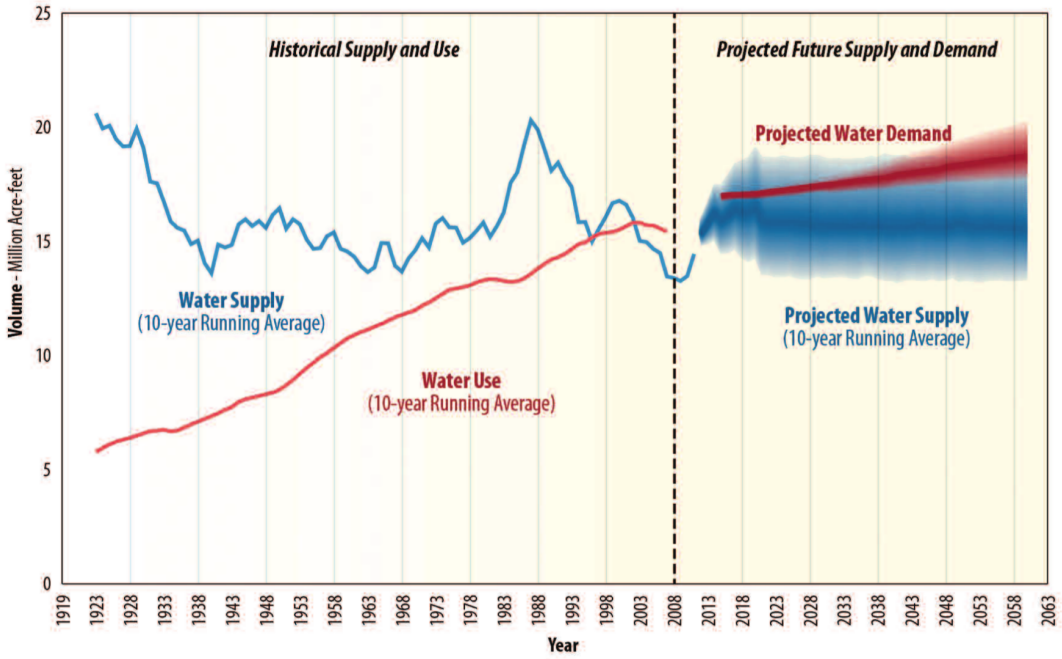

Figure 1.1: The Colorado River Basin water supply and usage shown as a volumetric flow rate from [Bureau of Reclamation, 2012]. The measured data are based on a 10-year running average and the projections of future flow and demand were created using different scenarios described in Bureau of Reclamation [2012].

grappled with since the 1920s. In 2009, the U.S. Government funded the Bureau of Reclamation to lead the "Colorado River Basin Water Supply and Demand Study". This large study, was to provide guidance for the allocation of Colorado River water over the next 50 years [Bureau of Reclamation, 2012]. This study concluded that the water storage within the Colorado river system (primarily, Lake Mead and Lake Powell) has been adequate to sustain water deliveries over the past decade or so. The study does not decide how future water shortfalls should be addressed; however, they present different scenarios to estimate what the magnitude of any future shortfalls might be (Fig. 1.1). An average of all scenarios suggests that the shortfall in the Colorado River flow will be about 3.2 million acre-feet by the year 2060 (at the time of this study there was an estimated 60 million acre-feet of water stored in the Colorado River system). Since the release of this 2012 report, the amount of water stored has further declined [Waterman, 2014].

Because the flow in the Colorado River is dependent on snowmelt from the Rocky Moun-

tains, and the demand for the river water is larger than the supply, the water resources have become sensitive to snowpack conditions. This causes concern for future, warmer climates and possible impacts on the Colorado River water supply [McCabe and Wolock, 2007, Christensen and Lettenmaier, 2007, Udall and Overpeck, 2017]. A southwestern drought combined with a low Colorado snowpack (winter of 2018) has generated much concern about the Colorado River flow and how downstream users might be impacted. This is witnessed by the many recent news stories on this topic [e.g., Brean, 2018, Lobeck, 2018, Runyon, 2018, among many others].

Though snowmelt is an important component, forests and how they use water is one of the largest contributors to a terrestrial ecosystem water balance [Bonan, 2008a]. Furthermore, if the climate warms as projected, the warm season will play a larger role within these ecosystems. More locally to the US-NR1 site, along the Front Range of the Rocky Mountains there has been a decline in glacier sizes and thickness since the early 1900s, and, if the trend continues, these glaciers could disappear within about 65 years [Hoffman et al., 2007, Haugen et al., 2010]. If these glaciers were to continue to decline, at some point it will impact our local ecosystem and water sources. As our need for better water-tracking within a watershed increases, any improvements in process-based understanding or modeling are useful. This thesis works to improve our knowledge on the effect of precipitation on the surface fluxes, as well presenting techniques to better assess land-surface models.

1.2 Surface energy balance

The surface energy balance describes how radiative fluxes affect the earth's surface, and, more specifically, how the radiative energy is partitioned between the latent heat flux (λE, evapotranspiration of water to/from the atmosphere) and sensible heat flux (H, heat exchange between the surface elements, ground, and atmosphere) [Stewart and Thom, 1973, Garratt, 1992, Oncley et al., 2007, Foken, 2008a]. Despite improvements in instrumentation accuracy, most flux-measuring sites find that the measured sensible and latent heat fluxes only account for $\approx 80\%$ of the available incoming energy [Wilson et al., 2002, Foken, 2008a]. The so-called "energy balance closure problem"

has been reviewed by Foken [2008a], Foken et al. [2011] with the conclusion that the imbalance can mostly be attributed to large-scale flux contributions from heterogeneous landscapes, which are not effectively measured by eddy-covariance techniques. Spatially homogeneous and moisture-limited environments such as deserts appear to be optimal for successfully closing the energy budget [Timouk et al., 2009, Foken, 2008a]. Energy balance closure typically improves under windy/turbulent daytime conditions when the ground and atmosphere are "well-coupled" [Franssen et al., 2010].

The terms in the surface energy balance (SEB) are,

$$R_\mathrm{a} \equiv R_\mathrm{net} - G - S_\mathrm{tot} = H + \lambda E + E_\mathrm{adv}, \tag{1.1}$$

where R_a is the available energy, R_net is net radiation, G is soil heat flux at the ground surface, and S_tot is the heat and water vapor storage terms in the biomass and airspace between the ground and flux measurement level as well as the energy consumed by photosynthesis. All terms in Eq. (1.1) have units of $\mathrm{W\,m^{-2}}$. Positive R_net indicates radiative warming of the surface, whereas a positive sign for the other terms in Eq. (1.1) indicate surface cooling or energy being stored. The S_tot terms are typically on the order of 10 % of R_net [Turnipseed et al., 2002, Oncley et al., 2007, Lindroth et al., 2010]. S_tot and G are discussed in detail in Sect. 5.4.9. The horizontal advection of heat and water vapor (E_adv) requires spatially distributed measurements, and is thought to be a primary reason that Eq. (1.1) does not balance at most flux sites [Leuning et al., 2012]. We will not discuss any details about water transport within the soil which can be found elsewhere [e.g., Ten Berge, 1990, Moene and Van Dam, 2014]. In our discussions, the SEB closure fraction refers to the ratio of the sum of the turbulent fluxes to the available energy, i.e., $(H + \lambda E)/R_\mathrm{a}$. An energy balance closure value of 50% means that the turbulent fluxes are only accounting for 50% of the available (mostly radiative) energy from the surface and the remaining 50% is unexplained or "missing".

When the winds are light (below about 3–4 $\mathrm{m\,s^{-1}}$), horizontal advection becomes important which results in a lack of SEB closure at the US-NR1 site [Turnipseed et al., 2002]. Turnipseed et al. [2002] also found that there was a lack of SEB closure in the presence of strong winds at night—several possible reasons for this nighttime discrepancy were discussed (e.g., instrument error,

footprint mis-match, horizontal advection), but none of these reasons could adequately explain the problem, and they concluded that insufficient resolution of the sonic anemometer temperature was the issue. Burns et al. [2012b] has since shown that this problem was actually due to a shortcoming in the sonic anemometer firmware and they suggested an empirical correction to partially fix the problem.

1.3 Evapotranspiration in forests

One of the drawbacks to the eddy covariance measurement of λE is that the physical process of evaporation is not easily separated from the biological process of transpiration. The partitioning of evapotranspiration for a forest depends on the vegetation density, and modeling by Lawrence et al. [2007] suggests that, for a canopy density similar to that of the US-NR1 forest (i.e., LAI ≈ 4), the ratio of transpiration to evapotranspiration (T/ET) should be around 80 % for an active forest. Near vegetated surfaces, it is known that the atmospheric fluxes of CO_2 and transpired water vapor are correlated to each other because the leaf stomates control both photosynthesis and transpiration [Monteith, 1965, Brutsaert, 1982, Jarvis and McNaughton, 1986, McNaughton and Jarvis, 1991, Katul et al., 2012, Wang and Dickinson, 2012, Beerling, 2015]. In 2013, a paper in the journal *Nature* used water isotopes to claim that transpiration accounted for 80–90% of ET in terrestrial ecosystems [Jasechko et al., 2013]. This high value of transpiration was debated within the literature [e.g., Coenders-Gerrits et al., 2014, Schlaepfer et al., 2014, Wang et al., 2014], and Schlesinger and Jasechko [2014] performed a followup survey of 81 different studies from around the world, concluding that the ratio of transpiration to evapotranspiration in temperate coniferous forests was usually in a range between 50-65%. This is a large-scale estimate from the perspective of an overall water budget that does not include details such as a dependence of evapotranspiration on LAI or surface wetness (they also note that uncertainties in their estimates are large).

The methods used to separate ET into its component parts typically require making some assumptions about stomatal behavior [e.g., Scanlon and Kustas, 2010], using isotopic methods [e.g., Yakir and Sternberg, 2000, Williams et al., 2004, Zhang et al., 2010, Werner et al., 2012,

Jasechko et al., 2013, Berkelhammer et al., 2016], or having additional measurements, such as sap flow [e.g., Hogg et al., 1997, Oishi et al., 2008, Staudt et al., 2011] or weighing lysimeters [e.g., Grimmond et al., 1992, Rana and Katerji, 2000, Blanken et al., 2001]. Another technique uses above-canopy eddy-covariance instruments for evapotranspiration coupled with sub-canopy instruments to estimate evaporation [e.g., Blanken et al., 1997, Law et al., 2000, Wilson et al., 2001, Molotch et al., 2007, Staudt et al., 2011]; this method, however, can have issues with varying flux footprint sizes [Misson et al., 2007]. There are also temporal changes (and feedbacks) to λE related to boundary layer growth and entrainment which are summarized by van Heerwaarden et al. [2009, 2010]. An accurate way to separate transpiration and evaporation has been a goal of the ecosystem-measurement community for many years, especially an understanding of how this ratio changes during the transition between a wet and dry canopy [e.g., Shuttleworth, 1976, 2007].

For the spruce forest studied by Staudt et al. [2011] with LAI ≈ 4.8, they found that transpiration accounted for about 90 % of total evapotranspiration (in generally dry conditions). Based on lysimeter measurements of evaporation, it was found that transpiration comprised about 95 % of total evapotranspiration during the growing season in a boreal aspen forest [Blanken et al., 2001]. The values of T/ET determined within this thesis were in the range of 75–90 %, of similar magnitude to those of previous studies.

1.4 The influence of warm-season precipitation on ecosystem fluxes

Warm-season precipitation is a common perturbation that changes the physical and biological properties of a forest ecosystem. The most obvious effect is the wetting of vegetation and ground surfaces which provides liquid water for evaporation and changes the surface energy partitioning between sensible heat flux H and latent heat flux λE. There is a long history of research into how canopy interception of precipitation modifies the water and energy budgets of an ecosystem [e.g., Rutter et al., 1975, Stewart, 1977, Klaassen, 2001, Shuttleworth, 2007, Kume et al., 2008, Moors, 2012, Kang et al., 2012, van Dijk et al., 2015]. Such changes are important in the modeling of ecosystem process on both local and global scales [e.g., Bosveld and Bouten, 2003, Bonan, 2008b,

Moene and Van Dam, 2014]. The soil and the atmosphere near the ground are closely coupled, and therefore soil moisture changes also affect near-ground atmospheric properties [Betts and Ball, 1995, Pattantyús-Ábrahám and Jánosi, 2004].

Evaporation from wet surfaces was initially modeled by Penman [1948] using available energy (primarily net radiation), the difference between saturation vapor pressure and atmospheric vapor pressure at a given temperature (i.e., $e_s - e_d$, also known as the vapor pressure deficit, VPD), and aerodynamic resistances to formulate an expression for surface λE. The concepts by Penman were extended to include transpiration by Monteith [1965] who introduced the concept of canopy resistance (a resistance to transpiration which is in series with the aerodynamic resistance, but controlled by the leaf stomates) leading to the Penman–Monteith equation for latent heat flux over dry vegetation. Based on these formulations, the fundamental variables which are believed to control evapotranspiration are net radiation, sensible heat flux, atmospheric stability (which affects the aerodynamic resistances), stomatal resistance, and VPD. In a fully wet canopy, transpiration becomes small and most available energy is used to evaporate liquid water intercepted by the canopy elements and within the soil [e.g., Geiger et al., 2003]. It has been questioned whether stomates respond to the rate of transpiration rather than VPD [e.g., Monteith, 1995, Pieruschka et al., 2010]. It has also been shown that stability/wind speed only has a small direct effect on transpiration [e.g., Kim et al., 2014]. In our study, we will not consider any effects on transpiration due to seasonal changes in leaf area [e.g., Lindroth, 1985] or variation in soil water potential [e.g., Tan and Black, 1976].

After entering the soil, rain can have either of two opposing mechanophysical effects on the soil-atmosphere CO_2 exchange. It can either displace high CO_2-laden air from the soil, or suppress the release of CO_2 because of inhibited diffusion/transport due to water-filled soil pore space [Hirano et al., 2003, Huxman et al., 2004, Ryan and Law, 2005]. Rain has also been shown to cause short-lived increases in soil respiration by microorganisms (by as much as a factor of ten) in diverse ecosystems ranging from: deciduous eastern US forests [Lee et al., 2004, Savage et al., 2009], ponderosa pine plantations [Irvine and Law, 2002, Tang et al., 2005, Misson et al., 2006], California

oak-savanna grasslands [Xu et al., 2004], Colorado shortgrass steppe [Munson et al., 2010, Parton et al., 2012], arid/semi-arid regions across the western US [Huxman et al., 2004, Austin et al., 2004, Ivans et al., 2006, Jenerette et al., 2008, Bowling et al., 2011], Mediterranean oak woodlands [Jarvis et al., 2007], and abandoned agricultural fields [Inglima et al., 2009]. The pulse of CO_2 emitted from soil that accompanies precipitation following a long drought period is one aspect of the so-called Birch effect (named after H. F. Birch (1912–1982), see Jarvis et al. [2007], Borken and Matzner [2009], Unger et al. [2010] for a summary). The timing, size, and duration of the precipitation event (as well as the number of previous wet–dry cycles) all affect the magnitude of the microbial and plant/tree responses to the water entering the system. The response of soil respiration to a rain pulse typically has an exponential decay with time [Xu et al., 2004, Jenerette et al., 2008]. The Birch effect is especially important for the carbon balance in arid or water-limited ecosystems where background soil respiration rates are generally low.

Net ecosystem exchange of CO_2 NEE is calculated from the above-canopy eddy covariance CO_2 vertical flux F_c plus the temporal changes in the CO_2 dry mole fraction integrated between the ground and the flux-measurement level z_{flux} (i.e., the CO_2 storage term),

$$\text{NEE} \quad = \quad F_c \quad + \quad \int_0^{z_{flux}} \frac{d(\overline{\rho_c})}{dt} dz \tag{1.2}$$

The studies listed in the previous paragraph have used a combination of eddy-covariance, soil chambers, and continuous in-situ CO_2 mixing ratio measurements to examine ecosystem responses to precipitation. Many of these studies have also shown that CO_2 pulses due to the Birch effect have an important influence on the seasonal and annual budget of NEE for that particular ecosystem [e.g., Lee et al., 2004, Jarvis et al., 2007, Parton et al., 2012]. In this thesis we will not be concerned with mechanistic or biological aspects of the Birch effect, but instead focus on how precipitation affects above-canopy NEE and any possible implications on the annual carbon budget.

Numerous studies have looked at the annual and interannual relationship between precipitation, water fluxes and NEE at the climate scale [Aubinet et al., 2000, Wilson et al., 2001, Law

et al., 2002, Malhi et al., 2002, Thomas et al., 2009, Hu et al., 2010a, Polley et al., 2010, and many others]. However, a comprehensive examination of the effect of precipitation on ecosystem-scale eddy covariance fluxes at the diel (i.e., hourly or "weather-front") time scale is lacking.

The observational part of the thesis (Chapter 5) uses fourteen years of data from the US-NR1 AmeriFlux site to explore how warm-season rain events (defined as a daily precipitation total greater than 3 mm during the snow-free part of the year) change the mean meteorological variables (horizontal wind speed U, air temperature T_a and specific humidity q), the surface energy fluxes (latent and sensible heat), and carbon dioxide (both CO_2 mole fraction and NEE) over the diel cycle. From this analysis we can evaluate both the magnitude and timing of how the energy balance terms and NEE are modified by the presence of rainwater in the soil and on the vegetation. Precipitation is also closely linked to changes in air temperature and humidity as weather fronts and storm systems pass by the site. Since NEE and the energy fluxes depend on meteorological variables such as net radiation, air temperature and VPD, it can be difficult to separate out the effect of precipitation vs. other environmental changes [Turnipseed et al., 2009, Riveros-Iregui et al., 2011].

1.5 Modeling forest ecosystem turbulent fluxes

Land-surface models typically view vegetation as either a single layer "big leaf" or resolve multiple vertical levels within the vegetation using a so-called multilayer modeling approach. Not surprisingly, there are trade-offs in complexity/simplicity and computational speed with each approach. For both approaches, the primary challenge is the determination of resistance parameters to the transfer of momentum and scalars between the surface and atmosphere [e.g., Raupach and Finnigan, 1988].

In the modeling portion of this thesis (Chapter 6), we extend the analysis of the observations to compare the measured above-canopy sensible and latent heat fluxes to those from a land-surface model, where the model is driven using meteorological and radiation data measured above the forest with the US-NR1 tower. From an analysis of the diel cycle, we evaluate both the magnitude and

timing of how the measured and modeled energy fluxes are modified by the presence of rainwater in the soil and on the vegetation. Two specific aspects of λE related to warm-season rainfall at US-NR1 are the focal point of our study: (i) for a dry day following a day with above-average precipitation, mid-day λE reached a peak value near $220\,\mathrm{W\,m^{-2}}$ (compared to $180\,\mathrm{W\,m^{-2}}$ for a dry day preceded by a dry day), and (ii) nocturnal λE increased from $\approx 10\,\mathrm{W\,m^{-2}}$ in dry conditions to over $20\,\mathrm{W\,m^{-2}}$ in wet conditions [Burns et al., 2015a].

To study the model physics it is advantageous to examine the full diel cycle [e.g., Matheny et al., 2014]. From the diel cycle, the timing of modeled phenomena, such as canopy evaporation, can be examined. The other advantage of analyzing the full diel cycle is that most land-surface exchange processes are very different at night compared to the daytime, primarily due to the effects of solar radiation on energy transformations. Radiative effects also change the atmospheric physics, such as the atmospheric stability. Historically, strongly stable conditions have been especially difficult to model due to the breakdown of the validity of Monin-Obukhov Similarity Theory (MOST) and issues such as surface-atmosphere decoupling and runaway cooling of the ground surface [e.g., Mahrt, 1999, Aubinet, 2008, Holtslag et al., 2013]. Runaway cooling occurs in models due to a positive feedback between the surface temperature and turbulence, where a cold surface temperature limits the turbulent exchange at the surface, which leads to an even colder surface temperature, and so on. Typically, MOST provides the theoretical underpinnings used by land-surface models. The key points about MOST relevant to this thesis are described in Sect. 6.3.7.1.

The model we use is the Community Land Model (CLM) version 4.5 [Oleson et al., 2013]. CLM uses a big leaf approach to model the effect of vegetation on the land-surface exchange; however, individual processes are uniquely calculated within the model. For example, latent heat flux has uniquely parameterized schemes for soil evaporation [Swenson and Lawrence, 2014], canopy evaporation [Lawrence et al., 2007, Oleson et al., 2008], and transpiration [Bonan et al., 2014]. The sum of these individual component terms (transpiration, ground evaporation, and canopy evaporation) produces the CLM latent heat flux. Several of the equations and constants within the CLM subcanopy turbulence parameterizations can be traced back to the Biosphere-Atmosphere

Transfer Scheme (BATS, Dickinson et al. [1993]) which was formulated over 25 years ago. Though certain components of CLM have been updated and investigated quite rigorously, there have only been a few studies related to the subcanopy turbulence [e.g., Zeng et al., 2005, Sakaguchi and Zeng, 2009] and a thorough sensitivity analysis is overdue.

Because these parameterizations affect the latent heat flux, they are relevant to our study and we perform a sensitivity analysis on several aspects of CLM, with an emphasis on the turbulence parameterization (details in Sects. 6.3.7 and 6.3.8). The aspects of CLM that we examine are: (1) sensitivity to leaf area index (LAI), which we expect to be an important factor controlling the CLM fluxes [e.g., Lawrence et al., 2007], (2) varying the CLM internal variable *maximum leaf wetted fraction* f_{wet}^{max} which controls how long precipitation resides on the vegetation surfaces, (3) replacing CLM-modeled friction velocity u_* with that measured on the tower, (4) using different forms of the so-called universal functions for modeling the vertical exchange of momentum, sensible, and latent heat [e.g., Foken, 2008b, 2006], and (5) varying two internal CLM variables: the subcanopy turbulent exchange coefficient, $C_{s,dense}$, and *zetamaxstable* ζ_{stable}^{max} which sets an upper-limit on the stable-side of the universal functions.

Another objective of this thesis is to provide a framework for evaluating models and observations at the diel-cycle scale. Systematic approaches to improving land-surface models have recently been suggested by the hydrology community [e.g., Clark et al., 2015]. Though flux measurements from towers have often been used to compare, constrain, and evaluate land-surface models [e.g., Pyles et al., 2000, Stöckli et al., 2008, Bonan et al., 2011, Lawrence et al., 2011, Bonan et al., 2012, Swenson and Lawrence, 2014, Raczka et al., 2016, among many others], in many of these studies the focus is on large-scale/global effects of model performance over different landscapes. This is a necessary first step because land-surface models such as CLM need to run at different locations and ecosystems worldwide (from forests, to crops, to polar regions, to urban areas). Here, CLM is run at a single forested site (US-NR1), using the diel cycle to examine the model performance. What is unique and different about this approach is that we conditionally sample the diel cycle to focus our analysis on the effect of warm-season precipitation on the CLM fluxes and temperature. Similar

techniques have been used for analysis of observations [e.g., Betts and Ball, 1995, Turnipseed et al., 2009, Burns et al., 2015a]; however, such techniques have rarely (as far as we have found) been applied to the diel cycle of model output.

Because US-NR1 is in complex, mountainous terrain there are potential issues related to drainage flows and horizontal advection that need to be considered [e.g., Finnigan, 2008]. As a step toward a better understanding of these issues, observations from the Howland Forest AmeriFlux site (US-Ho1) have been included in this thesis. US-Ho1 was chosen because it has a canopy density similar to US-NR1, but is in a location that is relatively flat compared to US-NR1. Though we do not perform a comprehensive analysis of the US-Ho1 data, we contrast the US-Ho1 and US-NR1 measurements to highlight potential effects of sloping terrain on the measurements and model performance, especially as-related to the nocturnal latent heat flux.

1.6 Conclusions

The motivation, goals and expectations of this thesis have been outlined within this chapter. If the goals of this thesis were to be summarized in only a few sentences, it would be as follows: the thesis is started by describing the history of the US-NR1 site and forest (Chapter 2), as well as the measurements made at the site (Chapter 3). These descriptions are meant to be fairly comprehensive and in-depth. This is followed by showing how the US-NR1 measurements can be used to evaluate the effect of warm-season precipitation on the diel cycle of the ecosystem fluxes, surface energy budget, and other variables (Chapter 5). Finally, modeled warm-season fluxes from the US-NR1 site are examined using the exact same techniques as in the observational analysis (Chapter 6).

Chapter 2

History of the Niwot Ridge Subalpine Forest US-NR1 AmeriFlux site

Abstract

In this chapter we introduce the location of the US-NR1 site, the history of the creation of the AmeriFlux site, and the much longer history of the forest that the site is within. The goal in this section is to better understand the nature of the logging that occurred in and near the forest in the early 1900s. In order to do this properly, we provide a short history of western Boulder County and the CU Mountain Research Station. Based on a combination of historical accounts, repeat photographs, and field observations, we found that the forest near the site was only selectively logged; this assessment agrees with recent tree-coring work, where many trees in the immediate vicinity of the tower date back to the 1700s.

2.1 Introduction

The Niwot Ridge Subalpine Forest AmeriFlux site (identified by AmeriFlux as site "US-NR1"; with the primary flux tower located at: 40°1′58″ N, 105°32′47″ W, 3050 m elevation) is the focal point of our study. The site is located within the Roosevelt National Forest below Niwot Ridge, Colorado, 10 km east of the Continental Divide near the Long-Term Ecological Research (LTER) "C-1" site (Fig. 2.1). Because many historical maps use the Public Land Survey System (PLSS), the white box in Fig. 2.1 shows the boundary of section 22 of Township 1 North, Range 73 West (for shorthand, we will identify any PLSS townships in the following way, T1N-73W). Each township is a 9.65 km × 9.65 km (i.e., 6 mile × 6 mile) square region composed of 36 sections.

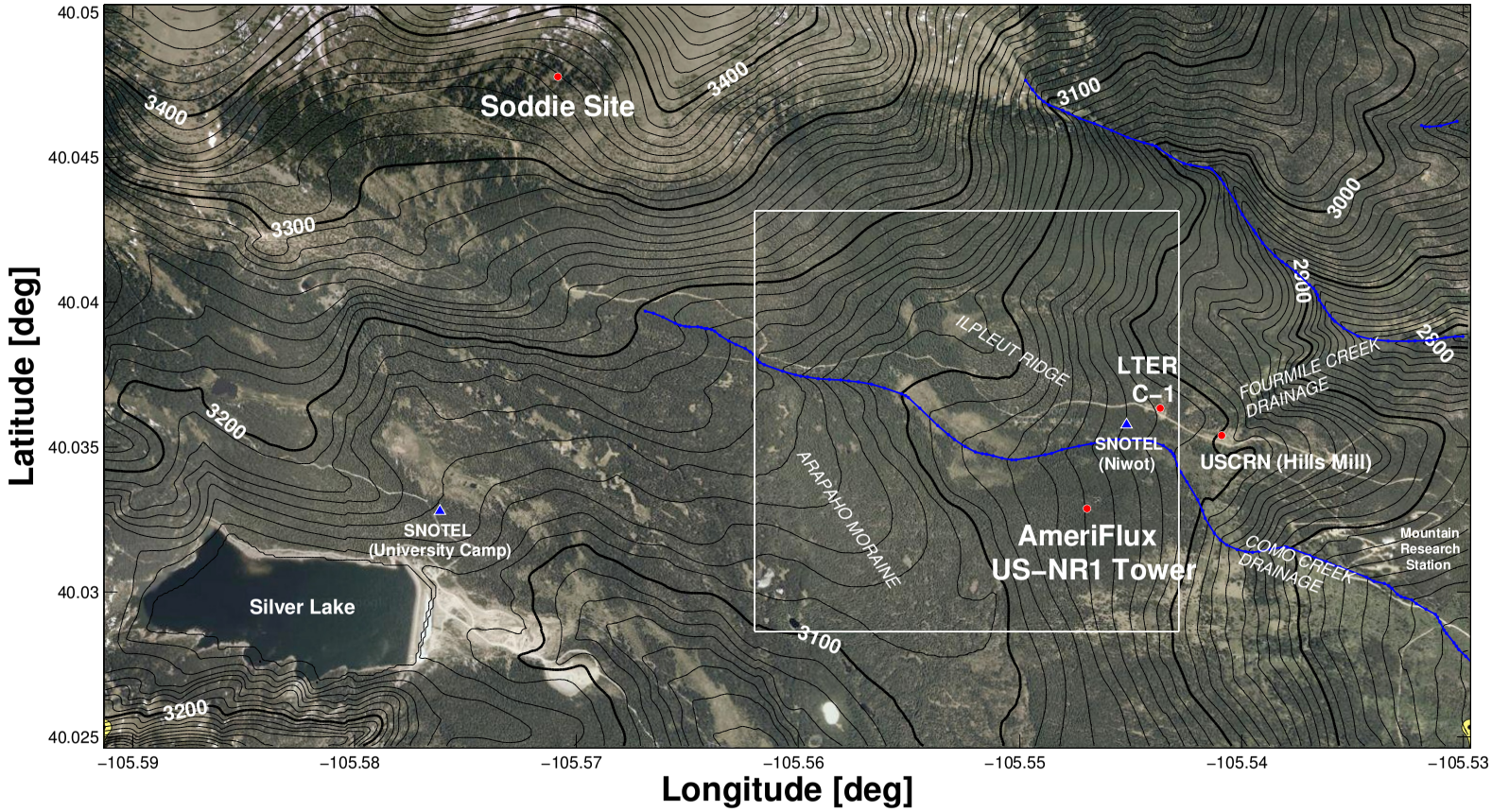

Figure 2.1: Overview map of the US-NR1 site. The red circles show the Soddie site, the US-NR1 AmeriFlux tower, the Long-Term Ecological Research (LTER) C-1 site, and the NOAA USCRN Hill's Mills climate station; the triangles show SNOTEL sites 663 (Niwot) and 838 (University Camp). The background image is from Google Maps (©2012 Google) and the elevation contours at 10-m intervals are from the U.S. Geologic Survey 7.5-min DEM. Four Mile Creek and Como Creek are highlighted in blue. The 4WD road going by LTER C-1 is known as the Niwot Ridge Road (USFS Road 506.1). The white box around the US-NR1 tower shows the border of section 22 of Township 1 North, Range 73 West (T1N-73W).

Within the township, each section covers an area of 1 square mile (2.59 km^2). As shown in Fig. 2.1, the US-NR1 site is also close to the University of Colorado (CU) Mountain Research Station (MRS) property, and 2.5 km east of the City of Boulder water source, Silver Lake. There are several long-term meteorological sites in the vicinity of C-1, run by LTER, SNOTEL, and NOAA (see Sect. 3.2 for details); as well as flux-measuring sites higher up on Niwot Ridge [Knowles et al., 2012]. These sites can be used to answer questions about spatial variations in ecosystem exchanges [e.g., Blanken et al., 2009, Knowles et al., 2015a]. Near/on Niwot Ridge, there is a climate record that dates back to the early 1900s for precipitation and the 1950s for other climate variables [e.g., Marr, 1961, Barry, 1973, Greenland, 1989, Kittel et al., 2015]. More about these historical measurements are provided below, when we discuss the history of MRS. Siting the US-NR1 AmeriFlux site near MRS builds on a long history of measurements in the area, which provides a plethora of climatic-scale data to work with (for an extensive list of past research near Niwot Ridge, see Halfpenny et al. [1986]). Additional details about the US-NR1 site characteristics will be described below, as well as in Chapter 4 (with more maps shown in Sect. 4.2).

The US-NR1 site was established in 1997–1998 by University of Colorado Professor Russell K. Monson to be part of the fledgling AmeriFlux network [Baldocchi et al., 2001, Boden et al., 2013]. The US-NR1 measurements started 1 November 1998 as described in several publications [e.g., Monson et al., 2002, Turnipseed et al., 2002, 2003, Burns et al., 2016b] and are still on-going today. Andrew Turnipseed led the initial infrastructure and instrumentation setup, and managed the site until 2003. In January 2003, the author of this thesis started working at the site, and became the site manager in September of 2003 (after Andrew Turnipseed left to start full-time work at NCAR). In January 2011, Professor R. K. Monson moved to the University of Arizona and Professor Peter Blanken (in the CU Geography Department) became the PI for the US-NR1 site. The US-NR1 site has been the focus of many PhD and Masters Theses. In 2012, based on the unique location and long, high-quality data record (almost 15 years of continuous measurements), US-NR1 became one of 10 "core sites" in the AmeriFlux network.

2.2 History of the US-NR1 forest

Thousands of years prior to the arrival of western civilization, there is evidence from remnant rock walls (used to drive animals), cairns, stone arrow points, and other slaughtering tools that the Paleo-Indians used the high-elevation Rocky Mountains for hunting [Benedict and Olson, 1978, Cassells, 2000]. More recently (hundreds of years ago), the Arapaho and Ute tribes used the high country for summertime hunting and to escape the heat of the lowlands. The Rocky Mountains also served as a physical barrier that separated the warring native tribes [Buchholtz, 1983]. It is likely that these nomadic people passed through the forest near the US-NR1 tower, but did not alter it in any significant way. Further discussion about these early peoples in the Rocky Mountains can be found in Buchholtz [1983], as well as Veblen and Lorenz [1991].

These early inhabitants touched the land lightly compared to the prospectors for gold and other minerals during the 1860s. It is impossible to consider the forests in Boulder County without a short history of the mining in the region. After the discovery of gold near Gold Hill in 1860, thousands of prospectors poured into Boulder County hoping to "strike it rich". Along with all the new arrivals came the suppliers of mining equipment, farmers, shopkeepers, etc. and many decided to stay and live in the area. The city of Boulder was incorporated in 1871. The earliest maps of Boulder County were from the 1880s and show that one of the early wagon/horse roads in the high country was to the small mining town of Albion (Fig. 2.2). Albion was occupied from the 1860s until around 1913 with a maximum of around 200 people living there in the early 1880s [Gleichman, 2005]. Using Como Creek as a reference, this early wagon road was very close to the road that currently passes by the LTER C-1 site today (which is visible in Fig. 2.1). In earlier times, this road was known as the "Albion Road" [Douglass, 1954], but it's now known as Niwot Ridge Road, or Forest Service Road 506.1 [United States Forest Service, 2016], which cuts through the MRS property and is closed to public vehicular traffic.

Within the Boulder County mountains and foothills, boomtowns appeared to support the mining industry. While gold was the initial metal of interest, silver, lead, copper, zinc, and tungsten

Figure 2.2: A portion of an 1888 map that includes T1N-73W in Boulder County, Colorado [Handy, 1888]. The road labeled, "County Road" goes to the mining town of Albion, and is just to the north of Como Creek, in the same approximate location as the current road that passes LTER C-1 (shown in Fig. 2.1). The body of water labeled "Lake" in the middle of the map is near the location of Silver Lake, where a dam was initially constructed in 1887 [Pettem and Ellinghouse, 2014].

were all important minerals mined within Boulder County. From 1905–1907, mining of these few elements produced nearly $2 million dollars of revenue [Drumm, 1908]. The most recognizable mining towns (i.e., Nederland and Ward) are still in existence today, whereas others have receded into the pages of history (i.e., Albion, Caribou, Eldora, and Sunset). Around 1898, there was renewed interest in mining after a narrow-gauge railroad between Boulder, Ward, and Eldora was completed. This railroad connected the mines, improved accessibility, and made the transport of heavy equipment and lumber much easier [Crossen, 1978]. The track ran from downtown Boulder up lower Boulder Canyon, and into Four Mile Canyon; after passing by Salina and Wall Street, the track split at Sunset, where a northern line ran to Ward and a southern line ran to Eldora. This track came to be known as the "Switzerland Trail of America" [Crossen, 1978]. A portion of the route is shown in Fig. 2.3, which comes from a series of Boulder County "pocket" maps drawn by Henry A. Drumm (1857–1937). Drumm was a local cartographer, and self-proclaimed "first graduate" of the University of Colorado, Boulder [Drumm, 1971]. This railway also helped

Figure 2.3: Portions of "Pocket" maps showing the area near the US-NR1 AmeriFlux site from year **(upper)** 1908 [Drumm, 1908], and **(lower)** 1932 [Drumm, 1932]. The US-NR1 site is in section 22 (T1N-73W) near the center of both maps. Dash-dot lines are defined as "Wagon Roads". In these maps, the upper portions of Como Creek appear to be called "Glacier Ditch", whereas further downstream it is labeled as Como Creek (section 36, T1N-73W). Each section comprises an area of 1 square mile.

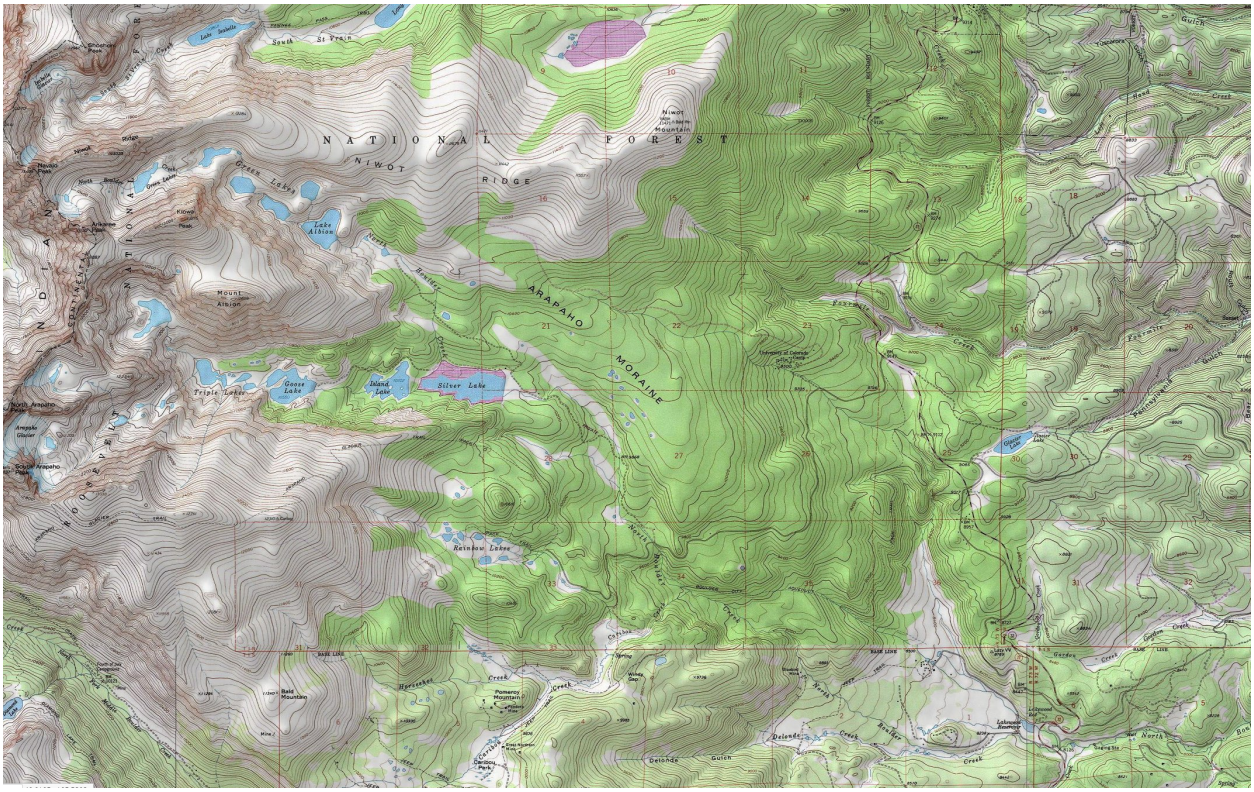

Figure 2.4: A modern USGS topographic map of the area near the US-NR1 AmeriFlux site. The area shown was chosen to be similar to that of Fig. 2.3. Section 22 (T1N-73W), which contains the US-NR1 AmeriFlux tower, is the same as that shown in other maps.

to open up the Rocky Mountains and Indian Peaks to tourism, and outings into the mountains became a popular event for Boulder residents and outside visitors. However, a combination of a general slow-down in the mining business [e.g., Worcester, 1920], the arduous task of keeping the trains running over the long winter, the development of inexpensive automobiles (and the creation of mountain roads for them to drive on), eventually led to the demise of the railroad, much to the dismay of many Boulder County residents. In 1919, the railway was dismantled [Worcester, 1920, Crossen, 1978], which is why it is shown as a dashed line in the 1932 Drumm map (Fig. 2.3, lower panel). Nearly all mining in Boulder County stopped in the early 1940s, though there is still modern interest in the subject [Pearson and Johnson, 1980]. To compare a modern USGS map with the Drumm pocket maps, USGS map sections near the US-NR1 site are shown in Fig. 2.4.

Figure 2.5: An 1897 glass plate negative photo by Joseph B. Sturtevant (1851–1910) of the Ruby Mine and Mill on Four Mile Creek, Sunnyside, Colorado. This image is available from the Boulder Carnegie Library for Local History (BHS S-1883 Photo).

Mining and the associated towns that sprung up with it, required construction materials, which, at that time, was timber. Between 1860 and the early 1900s, most of the montane forests in Boulder County were heavily logged to support the mining industry, as well as the building of houses and stores in towns [Veblen and Lorenz, 1991]. The subalpine forests were at a higher elevation than most mines, so access to logging was slightly more limited. The status of the Boulder County forests around 1919 is summarized by Worcester [1920] as follows:

> The vegetation over much of the region, as is indicated by the preceding paragraphs, is scanty. Where the slopes are sufficiently gentle to allow the accumulation of soil, grasses grow well, and such slopes are grazed by cattle or sheep.
>
> Good timber is scarce. There is considerable between Sunset and Sunnyside, and quite a good deal of pine is scattered over some of the higher slopes, but there is not enough to supply the demand in case of extensive mining operations. There is not enough to make large scale lumbering worth while, although there is sufficient timber to supply the present local demand. Some rather large areas should be re-forested, in order to prevent, or at least reduce, the dangers of soil removal in times of flood. Most of the timber on

the ground now is pine, although spruce and aspen are of common occurrence.

In Fig. 2.5 we provide an example of what logging near a mine looked like. This photo is from the Ruby mine which is in section 24 (T1N-73W), about 3 km due east of the current US-NR1 site (the Ruby mine can be found in the Drumm maps of Fig. 2.3). From the stumps in the photo, it is clear that the forest around the mine was clear-cut (based on the standing snags, there might have also been a fire). Veblen and Lorenz [1991] provide many excellent examples of photos from the late 1800s and early 1900s and compares them with photos taken at the same location during the mid-1980s (so-called "repeat photography"). From such photos, we can get a general sense of how these forests were logged to support the mining industry. With regard to the state of the forest, the results are often shocking, and the changes in the landscape over this nearly 100-year span were often dramatic. And it appears that clear-cutting near mines was a typical practice. Many of the older photos often show activity centered around logging (either logs piled up at a lumber mill, or wood being loaded for transport). Prior to around 1920 (when fire-suppression started in earnest), natural and human-caused forest fires were another factor that affected the lower-elevation forests of Boulder County [Veblen and Lorenz, 1991]; fire in the upper-subalpine, however, appears to have much less human impact. In general, subalpine forests in Colorado are naturally dense and subject to infrequent, stand-replacing fires which are correlated with periods of extremely dry weather [Sherriff et al., 2001]. More discussion about fire in the subalpine can be found in Sect. 4.4.

From the Drumm pocket maps in Fig. 2.3 we can see that section 22 of T1N-73W (i.e., where the US-NR1 tower is located) was relatively void of activity (other than the road to the mining town of Albion). A closer look at section 22 in a 1916 map of mining claims, clearly shows that most of the mining activity near the US-NR1 site occurred along Four Mile Creek, and Como Creek was void of mining activity (Fig. 2.6). This is likely, at least in-part, because the US-NR1 site is on the side of Arapaho moraine, and moraines are generally not ideal mining locations [Worcester, 1920]. It is interesting to note that the road to Silver Lake is shown in the 1916 map, but not the road

Figure 2.6: Portion of a 1916 map of the mining claims near the US-NR1 site [Clason Map Company, 1916]. The US-NR1 site is located in the lower southeast portion of section 22 (see Fig. 2.1 for details) which is labeled as "Agricultural Patented Land". The east side of Silver Lake is on the far right-side of the map. Como Creek is shown originating in the center of section 22. The Denver Boulder & Western Railroad (known as the Switzerland Trail) shown in sections 25, 29, 30, and 36 was removed in 1919. The map is overlain on a current map of the area, provided by the David Rumsey Map Collection (©2000, Cartography Associates, https://www.davidrumsey.com/).

to Albion (shown in the 1888 Handy map as well as the Drumm pocket maps). The Hill stop on the Switzerland Trail (shown on the west side of section 25 (T1N-73W) in Fig. 2.6), was named for Edgar Bratton Hill (1866–1939) who formed the E. B. Hill Coal & Lumber Company in 1908, and had a number of logging mills in the area [E. B. Hill also became a Boulder County Commissioner in the 1920s]. One of these logging camps (called Hill's Mill) was located in the upper part of the Four Mile Creek drainage, just down the road from the present-day LTER C-1 site. We will discuss Hill's Mill again, after a short history of the MRS.

The history of the MRS presented here is gleaned from much longer descriptions [e.g., Ives, 1980, Kindig, 2000], as well as vignettes described during the 50th anniversary of INSTAAR [INSTAAR, 2001]. Despite all the mining and logging activity in the early 1900s, there was also a

lot of promotion for tourism that emphasized the pristine beauty and clean air to be found in the mountains of Boulder County (which appears to be in conflict with some of the older photos of the mining and clear-cuts within the region). During this time, a group of CU biologists were interested in studying the plants and animals in the mountains west of Boulder. In the early 1900s, CU established the "University of Colorado Mountain Laboratory" research site along South Boulder Creek near the townsite of Tolland [Ramaley, 1909]. Research at this site was carried out until 1919. During this same period, another group of CU faculty (primarily, Frank E. Thompson (1871–1969) & Harry A. Curtis (1884–1963)) established a site named "University Camp" near Silver Lake, which forms the headwaters of North Boulder Creek (shown as "UNIV. CAMP (old)" in section 27 of the 1932 map in Fig. 2.3). This site was primarily used in the summer with recreational hikes and camping being a large part of the activities [Kindig, 2000]. In 1920, the city of Boulder purchased the Silver Lake watershed (for Boulder's drinking water), and worried about having too many people in proximity to the Boulder water source. Therefore, in 1920, the camp moved to its current location just to the north-northeast of Como Creek (shown as "UNIV. CAMP" in section 23 of the 1932 map in Fig. 2.3), and clearly visible in the modern maps (Fig. 2.1 and Fig. 2.4). In order to better protect this area for teaching and research, CU purchased 80 acres from the forest service in 1926. During the 1920s and 1930s there was much construction at the camp: many small student cabins, the "Megaron" building (still used today), a Dining Hall, and the "Science Lodge" were all built. Though recreational activities continued, there was also a shift toward more activities involving students and classes (mostly in Geology and Biology).

A key person in the history of the MRS was John W. Marr (1914–1989), who started teaching plant ecology classes at the MRS in 1946. He had the foresight to initiate two of the topics that have become the hallmark of MRS-related research: (1) the study of winter ecology and ecosystems (which eventually led to the formation of what is now called INSTAAR), and (2) the year-round study of the weather and climate in 4 different elevation bands from the Niwot Ridge alpine, down to the montane forests just west of Boulder. He labeled these sites using an alphanumeric ID, where the leading letter designated the elevation band ("D" being the highest, "C" the next highest, "B"

after that, and "A" the lowest), followed by a number, which designated a specific site within that elevation band. From October 1952 to October 1953, there were 16 stations operating with at least four sites in each elevation band; the subsampling was based primarily on aspect using a "1" to "4" designation for each subsampled site (i.e., C-1 (ridge top), C-2 (north-facing), C-3 (south-facing), and C-4 (valley floor)). Following the 1953 field season, the ridge top sites were deemed most valuable, and the other three subsampled locations were closed [Marr, 1967].

These IDs are still being used today; for example, the C-1 site shown in Fig. 2.1 is part of this legacy. In the 1950s and 1960s, collecting continuous data year-round in a high-mountain environment was an arduous task (especially in winter) that involved weekly trips to the stations, careful attention to safety, translating data from paper strip charts, as well as hand-recorded measurements [Marr, 1967]. Dr. Marr and his colleagues, however, saw the great utility of such measurements and secured funding to make them happen; he summarized the data collected in three papers [Marr, 1967, Marr et al., 1968b,a], which mostly consist of a long list of data tables after a brief introduction to the measurement concepts and methods.

Some of the results from these climate data have been published by others as journal articles [e.g., Barry, 1973, Greenland, 1989, Kittel et al., 2015] and the data have been used in a multitude of other studies to describe the local environmental conditions. Much of these historical data have been compiled and are available through the Niwot Ridge LTER program (http://niwot.colorado.edu/), which started in 1980 [Halfpenny, 1982, Williams et al., 2015]. As an ecologist, Dr. Marr supervised several theses that are relevant to the subalpine forest near the US-NR1 site [Douglass, 1954, Johnson, 1956, Mills, 1962, Amundsen, 1967]. The forests studied in theses from the 1950s were quite close to the US-NR1 site: the work by Douglass [1954] was on Ilpleut Ridge just west of LTER C-1, and the Johnson [1956] plots were located on the west side of Arapaho Moraine, closer to Silver Lake. The studies by Mills [1962] and Amundsen [1967] were both further north, in an apparent attempt to find a more pristine subalpine forest location than the ones below Niwot Ridge. The thesis by Douglass [1954] included a photo of Ilpleut Ridge which has been reproduced in Fig. 2.7 (upper panel). To get an idea of how much the forest has changed since the 1950s, we have included

Figure 2.7: Photos of **(upper)** Ilpleut Ridge likely taken around 1952 or 1953 near the Hill's Mill site looking west (this is Fig. 4 in Douglass [1954]), and **(lower)** photo taken on 30 May 2018 from the same approximate location. In the older photo, Ilpleut Ridge is the forested ridge on the left while the peak on the right side is Niwot Mountain, at the east end of Niwot Ridge. The remnant stumps from logging operations are apparent in the clearing. In the newer photo, the stumps are gone and the view of Ilpleut Ridge is obscured by trees.

a photo from the same approximate location taken in 2018 (Fig. 2.7, lower panel). The trees have grown to the point that Ilpleut Ridge (and Niwot mountain) are obscured from view. Also, any remnants of stumps from the logging are gone.

Since the 1960s, the MRS has become a world-renowned location for doing research in alpine and mountain areas with many international visitors and collaborators using the site. In 1979, U.S. Congress designated Niwot Ridge as a Biosphere reserve and it became a United Nations Educational Scientific and Cultural Organization (UNESCO) site which is part of an international network of Biosphere reserves. Today, modern instruments, computers, and reliable data loggers make yearly data collection much easier, and year-round data are being collected by the Niwot Ridge LTER program (as well as at the US-NR1 AmeriFlux site and other locations in the area), following the vision first put forward by John Marr in the 1950s.

Just downhill from the current LTER C-1 site is the remains of an old logging mill, called Hill's Mill (5BL13069). This was, we surmise, one of the logging camps created by the E. B. Hill Coal & Lumber company. Though the history is difficult to completely piece together, Douglass [1954] provides some valuable information about the Mill when discussing the "young" stand of lodgepole pines on the north side of Ilpleut Ridge, shown in Fig. 2.1. At the time of her thesis (1954), this was a uniform forest, with all trees younger than 50 years old, putting the establishment of this part of the forest at around 1904. For her thesis, Douglass [1954] interviewed Mr. E. C. Hill, and states the following:

> The history of the [young lodgepole] stand is somewhat strange. Considerable investigation has proved that the fire which burned both this patch of young lodgepole and the adjoining unreforested area occurred before 1895—probably in 1890 or 1891. Between 1896 and 1918 a good many of the standing dead trunks of burned trees were cut for firewood by the Hill Sawmill. Ordinarily lodgepole reproduction would be expected to start within a very few years after the burn....
> Mr. E. C. Hill, who came to live at Hill's Mill as a child in 1896, states that the young lodgepole area was bare of living trees then. Tree ring studies, giving a probable age maximum age of fifty years to the pioneers of the present stand, bear out his observations. Apparently the stand pioneers did not come in until ten or fifteen years after the fire. Figure 35, a copy of an old photograph of part of the area taken in 1929 by Mr. Hill, shows that 25 years ago the stand was still composed of a scattering of seedlings and saplings interspersed with the dead trunks of the burned forest.

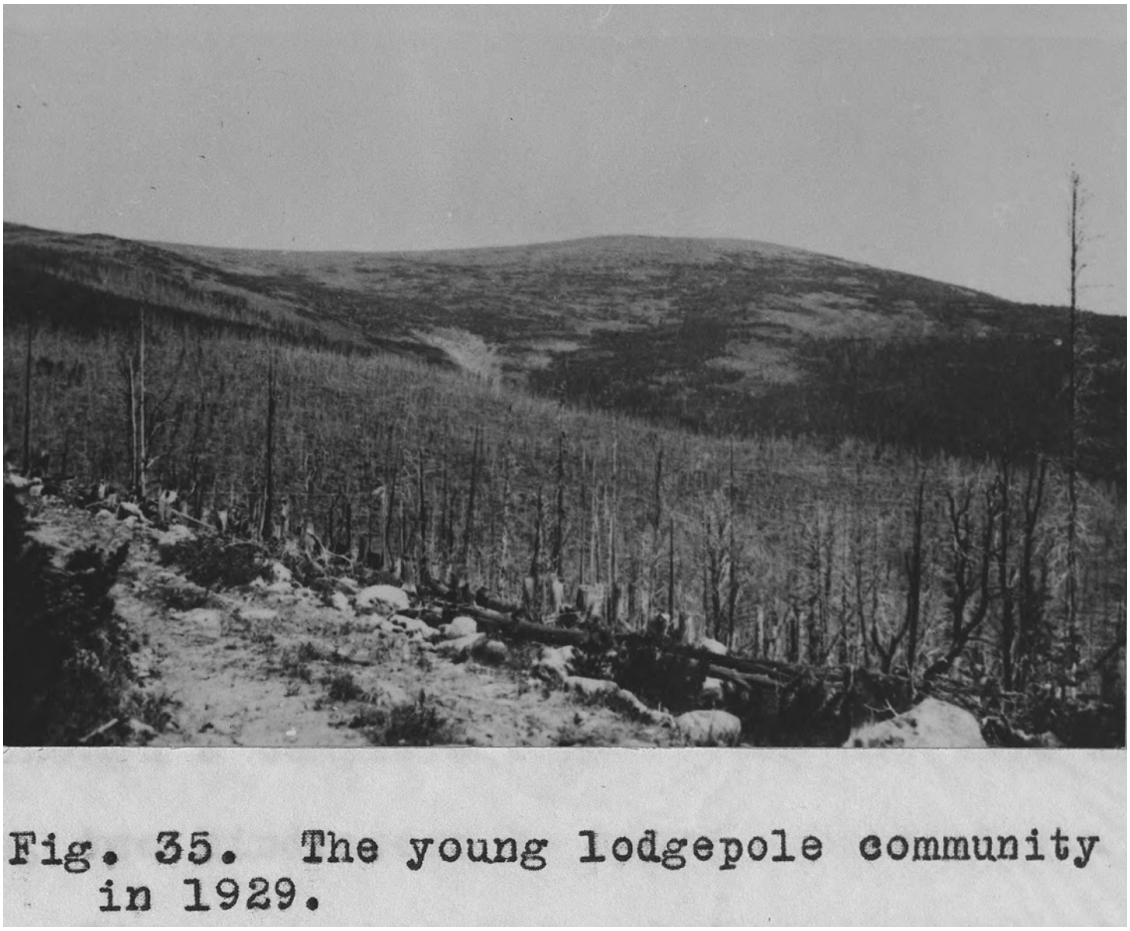

Figure 2.8: A 1929 photo of the forest below Niwot Ridge along the road to C-1. This is Fig. 35 in Douglass [1954]. At the time of the photo, the forest was recovering from a fire in the late 1890s. The peak in the center of the photo is Niwot Mountain at the east end of Niwot Ridge. Attempts to re-take a photo near this same location have proven to be difficult because the trees along the road have all grown considerably, blocking the view of the landscape behind them.

The relation of E. C. Hill to E. B. Hill is not known at this time, but E. C. does not appear to be one of E. B.'s children. Figure 35 mentioned in this quote is reproduced in Fig. 2.8. From Boulder County records, it appears that the E. B. Hill Coal & Lumber company was officially created in 1908, but it sounds like Hill's Mill was an active Mill well before that date. Timber processed at Hill's Mill were used to build some of the buildings at MRS at around 1920 [Kindig, 2000], and we would also guess that they were also used in the mines along Four Mile Creek (i.e., just downstream from Hill's Mill). The exact dates of Hill's Mill operation are a bit murky, because Marr [1961] reports that the Mill operation stopped around 1900 which is much earlier than the

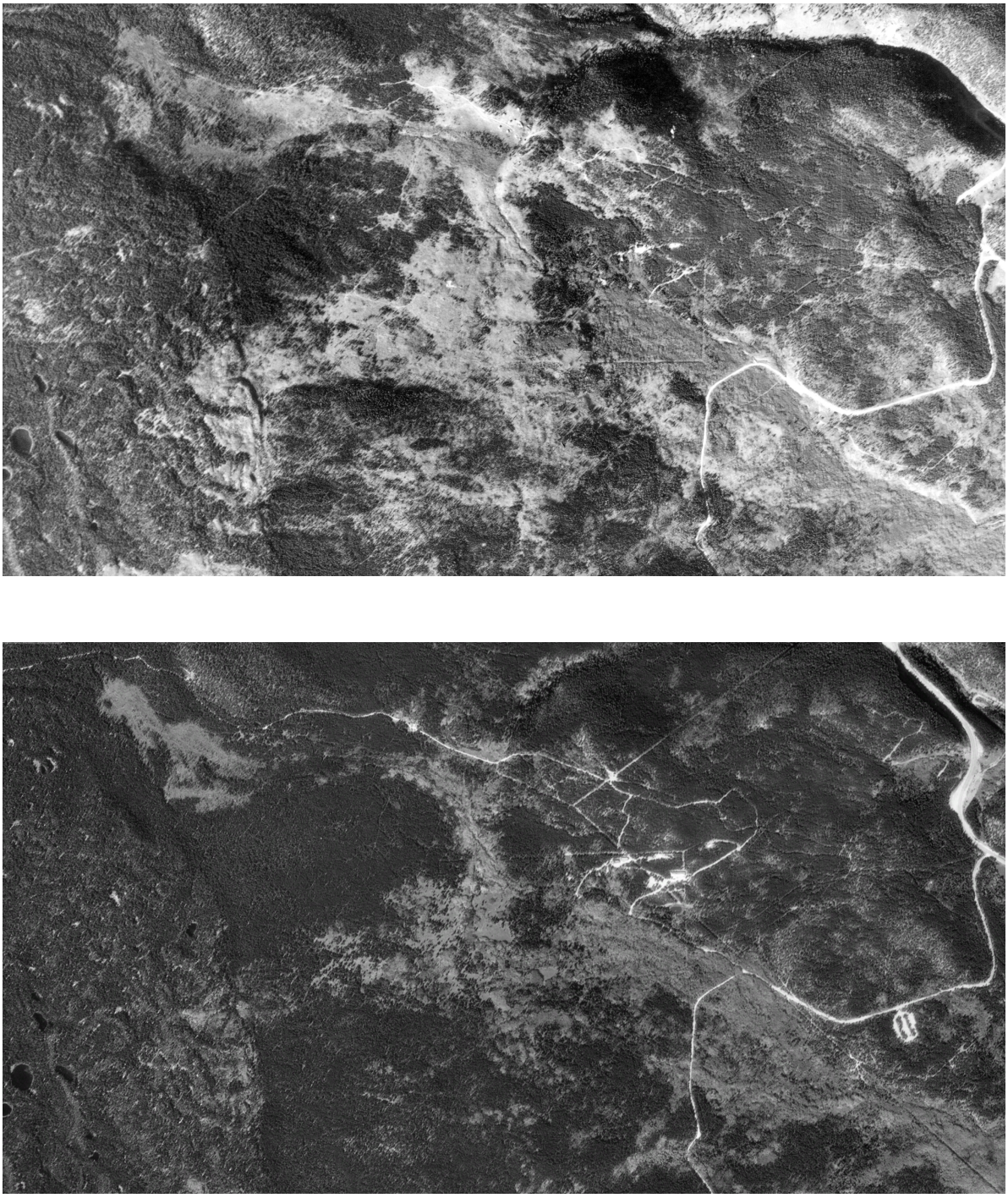

Figure 2.9: Aerial photos of the area near the US-NR1 AmeriFlux site from **(upper)** 26 October 1938 [United States Forest Service, 1938] and **(lower)** a 6 September 1999 image from Google Earth (©1999 Google). The spatial extent of each photo is approximately the same. In the 1938 photo, the buildings of Hill's Mill can be seen as well as areas that were logged.

1918 cessation year reported by Douglass [1954].

Further insight into Hill's Mill can be found by comparing an aerial photo from 1938 with a recent (1999) Google image over the same approximate area, as shown in the upper and lower panels of Fig. 2.9, respectively. The 1999 photo was chosen to be at nearly the same time of year as the 1938 photo. Observations by comparing these images are as follows: (1) in 1938, the extent of the forest was much smaller than it was in 1999, (2) it looks like there were about 4–5 structures that comprised Hill's Mill, and they were still standing in 1938 (they can be seen in middle of the 1938 photo about 1/5 below the top of the image), (3) the network of roads and powerlines from 1938 appear to be similar to those from 1999, but the locations have moved slightly, and (4) there was fairly extensive (clear-cut) logging in the forest near Hill's Mill, but the forest immediately around the US-NR1 tower/site appears to be mostly intact. At the US-NR1 site today, there are still tree stumps present (next to living trees) that suggest selective thinning of the forest was likely done at the US-NR1 site. This view is in contrast to the forest history previously reported by others [e.g., Thornton et al., 2002, Bradford et al., 2008], who suggested that up to 99% of the forest was logged around 1905.

Another piece of history related to the logging of the forest, is that E. B. Hill Coal & Lumber company is shown as the owner of the western part of section 23 (T1N-73W) in a 1932 mining map (Fig. 2.10). This area is where Hill's Mill near C-1 was located. This map corroborates our presumption that this forest was logged by E. B. Hill Coal & Lumber company; furthermore, between 1905 and 1908, there were deeds issued to E. B. Hill for sections 15, 20, and 21 in T1N-73W, according to the Boulder County recording office. It is known that E. B. Hill had several lumber mills in the area, and it is likely that his company logged the forest sometime starting in the 1890s and ending in the early 1920s. This range of years is in approximate agreement with the dates reported in Douglass [1954] (as well as tree age dates reported with tree-ring analysis by Kienast and Schweingruber [1986]). However, from what we can tell, the forest close to the US-NR1 main tower was only selectively logged. This description of the logging is consistent with recent tree-ring coring within US-NR1 site that found a significant presence of remnant trees which

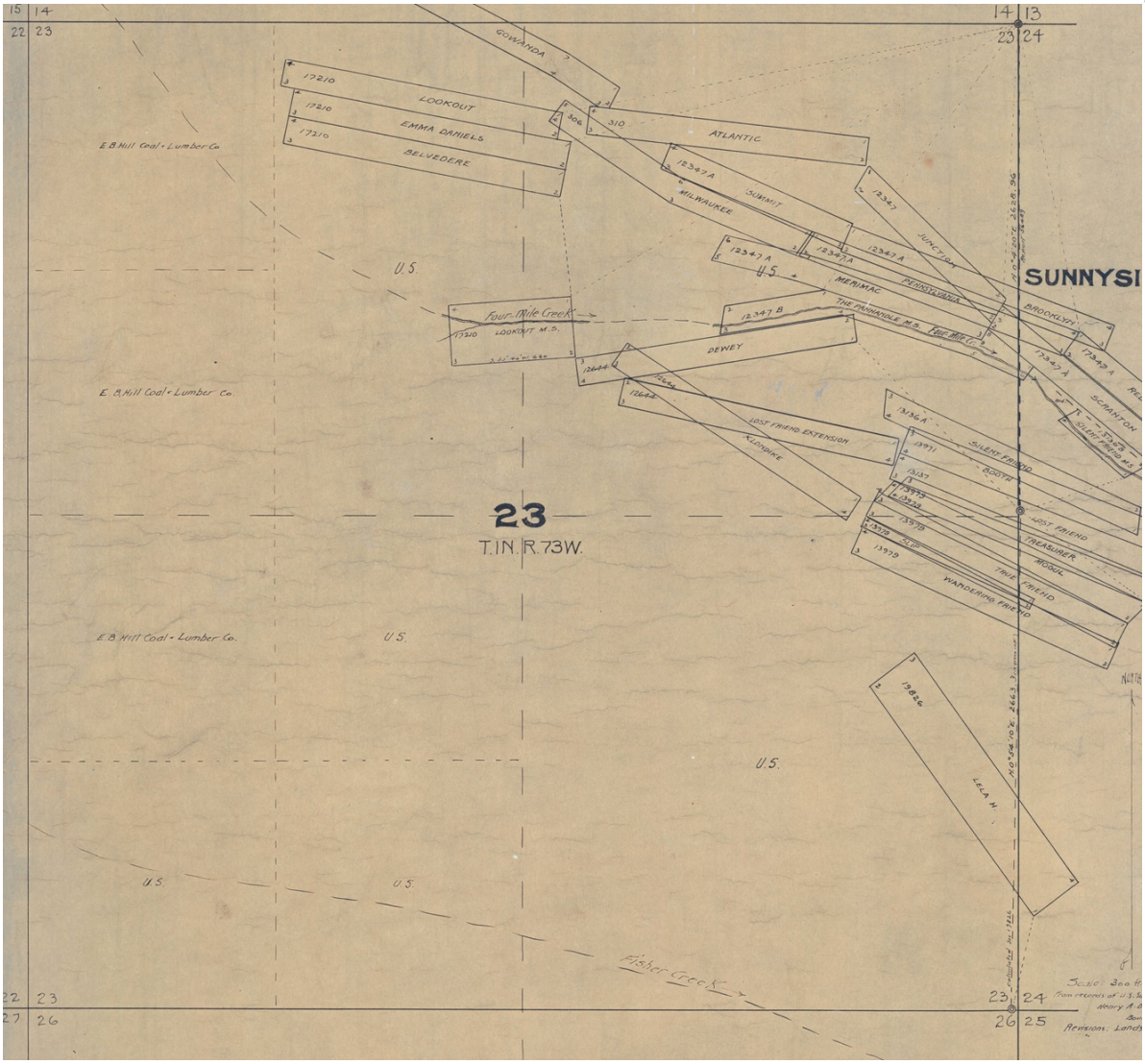

Figure 2.10: A 1932 blueprint map of section 23 (T1N-73W), drawn by Henry A. Drumm (1857–1937) which shows the Sunnyside mining camp, Fourmile Creek, Como Creek (labeled as Fisher Creek in this map), and land holdings of the E. B. Hill Coal & Lumber Company. This map is available from the Boulder Carnegie Library for Local History.

are over 200 years old, dating back to the late 1700s and well before any logging activity [Montané et al., 2017]. There are several long-term forest plots which are not far from the US-NR1 site and focus on the tree/forest health [e.g., Veblen, 1986, Villalba et al., 1994, Smith et al., 2015]. The tree-ring analysis from the Veblen stands near US-NR1 are discussed in Sect. 4.4.

Finally, after a fairly extensive search for a photo of Hill's Mill at ground-level, the closest one I was able to find is shown in Fig. 2.11. The back of the photo has a hand-written note suggesting

Figure 2.11: An undated photo by Ernest V. Hunt (1868–1941) of a sawmill with a horse and wagon, filled with lumber. For possible locations, the back of the photo has "E. B. Hill Mill?" and "Sawmill at Duck Lake?" written on it. This image is available from the Boulder Carnegie Library for Local History (BHS 163-1-17 Photo; Photo 7).

it might have been from a mill operated by E. B. Hill. Though we might not ever know if this is a photo of Hill's Mill near LTER C-1, the photo provides some insight into the character of the logging operation at that time, including the use of horses and carts to move the raw timber and processed lumber. The buildings at Hill's Mill are no longer standing, but an undated aerial photo from Marr [1967] (their Fig. 1) shows that Hill's Mill was still standing in the early 1960s. In the early 1970s some of the wood from these buildings was used for construction projects at the MRS (personal communication, William Bowman, 2018). In the early 1980s, the remnant structures were still obvious, though much of the wood was on the ground (personal communication, Thomas Veblen, 2018).

2.3 Conclusions

The history of the US-NR1 forest was explored. There was clearly a large fire to the east of C-1 in the 1890s, and the forest was still recovering from this fire in 1929 (Fig. 2.8). A comparison of aerial photos from 1938 and 1999 roughly show the extent of the logging and subsequent re-growth of the forest over that 60 year time span (Fig. 2.9). These photos (and evidence of stumps in the area) suggest that the forest in the immediate vicinity of the US-NR1 tower was only selectively logged. David J. P. Moore and collaborators at the University of Arizona corroborate this conclusion based on tree-ring analysis near the tower (finding many trees over 200 years old, with the oldest tree around 250 years old).

Chapter 3

Niwot Ridge Subalpine Forest US-NR1 AmeriFlux site measurements

Abstract

In this chapter the details about the measurements of the ecosystem turbulent fluxes (carbon, water, and heat), subalpine forest structure, and other variables at the US-NR1 AmeriFlux site are described. Some of the information within this chapter is part of a planned 3-part publication. Part I documents the data collection and documentation methods used at the AmeriFlux site and has already been published in the EGU journal Geoscientific Instrumentation, Methods and Data Systems [Burns et al., 2016b]. Part II is primarily related to the canopy structure around the tower and a manuscript has been started [Burns et al., 2019]. Part III will contain the details about the tower measurements, gap-filling, and data-processing. Here, we provide details of the US-NR1 tower measurements (as will be in Parts II and III of this series of papers). This chapter also describes the measurements which are the basis of the results presented in Chapters 4–6.

3.1 Introduction

Within this chapter we describe the instruments and data-processing techniques used to measure the environment at the AmeriFlux site. A majority of the sections within the chapter will discuss a specific variable and explain the instrumentation used to measure that variable; and, where appropriate, how that measurement has changed over time. As an overview, a photo of the US-NR1 main tower and the subalpine forest surrounding the tower is provided in Fig. 3.1.

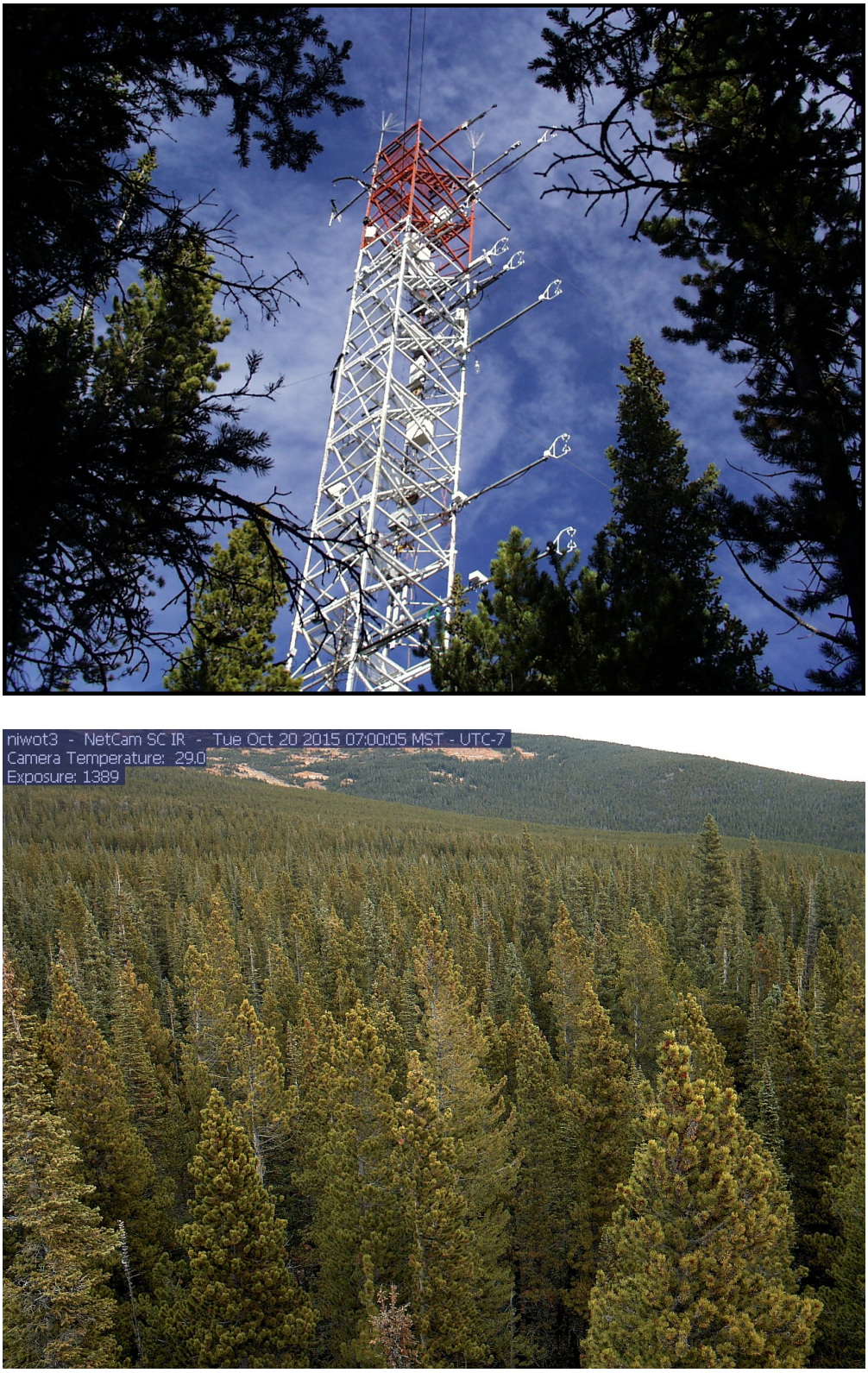

Figure 3.1: Photographs of: **(top)** the US-NR1 AmeriFlux tower taken on 7 October 2014, and **(bottom)** the subalpine forest looking to the north taken with the "niwot3" PhenoCam [Richardson et al., 2018] on 20 October 2015. In the upper photo, the main flux level is at 21.5 m (just below the orange sections); at the time of the photo there were 7 extra CSAT3 sonic anemometers deployed on the tower (see text for details).

This chapter will also include a comparison of infrared gas-analyzers (IRGAs) used to measure fluxes of CO_2 and H_2O that occurred on the US-NR1 main tower between the 2013 and 2014 [Burns et al., 2014, Metzger et al., 2016]. Though this increases the amount of information within this chapter, the IRGA comparison provides (i) a snapshot of the measurements on the tower at a particular time, (ii) an independent quality-control check of our flux measurements, (iii) highlights things to consider (or pitfalls to avoid) for any future comparisons or similar comparisons done by others. In the sections below, after we describe the long-term instruments and measurements at the US-NR1 site, we will also describe the setup for the IRGA comparison and a brief discussion of the IRGA comparison results (Sect. 3.22). Several other side-by-side instrument comparisons by the AmeriFlux QA/QC team [Schmidt et al., 2012] have found the US-NR1 measurements to be of high quality [e.g., Loescher, 2004, Thomas, 2007, Chan et al., 2014].

In general, the instruments used at the US-NR1 site have been remarkably stable (with a few updates and exceptions) over the nearly 20-year measurement period; as part of our internal QA/QC we have performed side-by-side instrument comparison to assess instrument quality. These comparisons have been useful in finding instrument problems, such as an issue with the sonic anemometer firmware in high winds [Burns et al., 2012b]. A summary of the primary measurements, instruments, and variable names used in our study is provided in Table 3.1. For additional details about the specific US-NR1 data files used in this thesis, see Appendix E. In addition to the US-NR1 site measurements, we describe the airborne lidar data collected by the Boulder Creek Critical Zone Observatory (CZO). These lidar data were used to evaluate the canopy structure of the US-NR1 forest, which will be shown in Chapter 4 (Sect. 4.4).

3.2 Ancillary Measurements

We start by briefly describing a past field project and few nearby long-term measurements sites within/near the US-NR1 forest that have sometimes been used for gap-filling the US-NR1 meteorological data, as well as exploring spatial variations within this subalpine ecosystem. Some of these sites will be discussed in subsequent sections so it seemed best to describe these locations

Table 3.1: A summary of the primary instrumentation and variables at the US-NR1 AmeriFlux site. For additional US-NR1 data details, see Appendix E.

Measured Variable[a]	Symbol	Sensor Type	Manufacturer Make/Model	Sensor Height(s) (cm)	Additional Comments
Air Temperature and Relative Humidity (°C, percent)	T_a, RH	Platinum resistance thermometer, Capacitive humidity sensor	Vaisala, HMP35D/45D	200, 800, 2150	Slow-response sensor within a mechanically-aspirated housing
Barometric Pressure (kPa)	P	Silicon capacitive sensor	Vaisala, PTB-101B	1200	Used along with T_a and RH to calculate specific humidity q and dewpoint temperature T_d
Net Radiation ($W\,m^{-2}$)	R_{net}	Thermopile	REBS[b], Q-7.1	2550	
Snow and Soil Temperature	T_{snow}, T_{soil}	Thermistor	MRC[c], TP 101 Probe	−10 to 190 (10 cm spacing)	After Oct 2005, deployed at one location near the North Canopy tower (see Fig. 4.1)
(°C)		Thermistor	Campbell Scientific 107 probe	−5	Installed horizontally near subcanopy tower in Fall, 2005
		Thermocouple (type T)	Campbell Scientific A3537	−20, 0, 20	
Soil Heat Flux ($W\,m^{-2}$)	R_{net}	Thermopile	REBS[b], HFT-1	−10	The average from multiple sensors was used
Soil Volumetric Water Content (V_{H_2O} $(V_{soil})^{-1}$, $m^3\ m^{-3}$)	VWC	Electromagnetic conductivity	Campbell Scientific, CS616	−5	Installed horizontally near subcanopy tower in Fall 2005; units are volume of water (V_{H_2O}) per volume soil (V_{soil})
Wind Speed and Direction ($m\ s^{-1}$, deg. from True North)	U, WD	Sonic anemometer	Campbell Scientific, CSAT3	256, 570 2150	
3-D Wind and Temperature Fluctuations[d] ($m\ s^{-1}$, °C)	u', v', w', T'_{son}	Sonic anemometer	Campbell Scientific, CSAT3	256, 2150	Includes the planar-fit; CSAT3 vertical wind fluctuations (w') were used to calculate turbulent fluxes
Sensible Heat Flux ($W\,m^{-2}$)	H	Sonic anemometer + Thermocouple (Type E)	Campbell Scientific, CSAT3 + Omega	2150 256	The thermocouple or sonic can be used to calculate 2150 cm H [Burns et al., 2012b]
Latent Heat Flux ($W\,m^{-2}$)	λE	Sonic anemometer + Krypton hygrometer (2150 cm) Open-path IRGA (256 cm)	Campbell Scientific, KH2O LI-COR, LI-7500	2150 256	A closed-path IRGA (LI-COR, LI-6262) was used at 2150 cm whenever the KH2O sensor was not available

[a] Variable units are shown in parentheses.

[b] REBS is Radiation and Energy Balance Systems.

[c] MRC is Measurement Research Corporation.

[d] u', v', w', are planar-fit wind fluctuations in the streamwise, crosswind, and vertical directions. T'_{son} are sonic temperature fluctuations.

and data sources upfront, before getting into the US-NR1 details. In some cases, these data sets were not directly used within the later chapters of this thesis, but they are described here to provide context and will be included in the gap-filling/data-processing (Part III) paper described in the abstract of this chapter.

There are several long-term measurement sites near the US-NR1 tower that have been an invaluable data resources, which is one of the advantages of the US-NR1 location. These sites

(whose locations are shown in Fig. 2.1) are: the University of Colorado Long-Term Ecological Research (LTER) C-1 site, the NOAA U.S. Climate Reference Network [USCRN; Diamond et al., 2013] climate stations (site name: "CO Boulder 14W, Mountain Research Station, Hills Mill"), and the Natural Resources Conservation Service (NRCS) Snowpack Telemetry (SNOTEL) sites 663 (Niwot) and 838 (University Camp). These four sites provide valuable local and historical data about precipitation, soil moisture, snow depth, snow density, air temperature, and winds. Data from these sites have been used for gap-filling meteorological data when the US-NR1 tower was not working or a sensor was broken. Furthermore, when examining these data, it often brings to light horizontal differences in variables that lead to deeper thinking about reasons or explanations (physical or sensor-related) for observed differences.

Additional tall towers deployed within the US-NR1 forest have provided useful data to assess horizontal gradients and spatial variations. A map in the next chapter (Fig. 4.1), shows their locations. The U.S. Geological Survey (USGS) 33-m tall tower was erected in the summer of 2000 and was located 200 m almost due west of the US-NR1 main tower (this tower was removed in August, 2017). In addition to the USGS tower, the USGS-North and USGS-South towers (just-reaching the top of the forest) were used to estimate the horizontal advection of CO_2 among the towers [Yi et al., 2008]. In summer of 2004, as part of the Carbon in the Mountains Experiment (CME04), the National Center for Atmospheric Research (NCAR) Earth Observing Laboratory (EOL) Integrated Surface Flux Facility (ISFF) group deployed three towers near the US-NR1 site to supplement the existing US-NR1 and USGS towers [Oncley, 2004, Sun et al., 2010, Burns et al., 2011]. The three EOL towers (called "Willow", "Pine", and "Aspen") followed Como Creek and were within 800 m of each other as shown in Fig. 4.1. Data from these towers were collected from mid-July until 30 September, 2004. The Willow Tower was in an open marshy area ($\approx$ 200 m $\times$ 100 m) dominated by low shrubs ($h < 0.5$ m), without any tall trees within 50 m of the tower. The Pine Tower was in a fairly dense section of the forest ($h \approx 13$ m). The Aspen Tower was near Como Creek in an area dominated by willows and shrubs that were around 3–4 m tall interspersed with several larger 10–15 m conifers, and within 30 m of a stand of aspen trees along Como Creek. The understory at

Aspen was more dense than the other sites. About 100 m northeast of Aspen a small clearing led down into the Fourmile Creek drainage. Burns et al. [2011] used CME04 data to examine how the wind fields varied spatially and with atmospheric stability near the US-NR1 site. Not surprisingly, the presence of the forest had a large impact on the direction of the above-canopy flow; in very stable conditions, the local topography and steep canyons controlled the subcanopy wind direction.

3.3 Infrared gas analyzer overview

Infrared gas analyzers (IRGAs) are a key component to the eddy covariance measurement of water vapor and carbon dioxide exchange between the surface and atmosphere [Aubinet et al., 2012]. Historically, closed-path IRGAs designed for laboratory use (such as the LI-COR, model LI-6262) were used to measure H_2O and CO_2 fluxes in the atmosphere [e.g., McDermitt, 1997]. These closed-path IRGAs worked best in climate-controlled conditions. In order to use them in the field these IRGAs were typically housed in temperature-controlled enclosures or buildings that were tens of meters away from the actual measurement location near the sonic anemometer. This necessitated the use of long tubing and high-power pumps to bring the air sample to the IRGA cell. Attenuation of H_2O and CO_2 fluctuations within the tubing was a persistent problem with such a setup, especially for H_2O [Massman, 1991, Lenschow and Raupach, 1991, Fratini et al., 2012]. As an alternative, open-path IRGAs have frequently been utilized, but the key trade-offs with the open-path design are: (i) precipitation and dew affecting the measurements and creating data gaps, and (ii) the need to account for effects of air density changes on measured H_2O and CO_2 along the air sampling path [Leuning and Judd, 1996]. Starting around 2010, a new type of closed-path IRGA emerged. This newly-designed IRGA is weather-proof, compact, and low-maintenance. Furthermore, because of its small size, short intake tubing can be used, which places the sampling cell close to the sonic anemometer and reduces high frequency signal loss [e.g., Clement et al., 2009, Burba et al., 2010, Nakai et al., 2011, Burba et al., 2012, Novick et al., 2013]. Two such IRGAs are the LI-COR LI-7200 and the Campbell Scientific EC155, which is part of the CPEC200 closed-path eddy covariance system (Fig. 3.2).

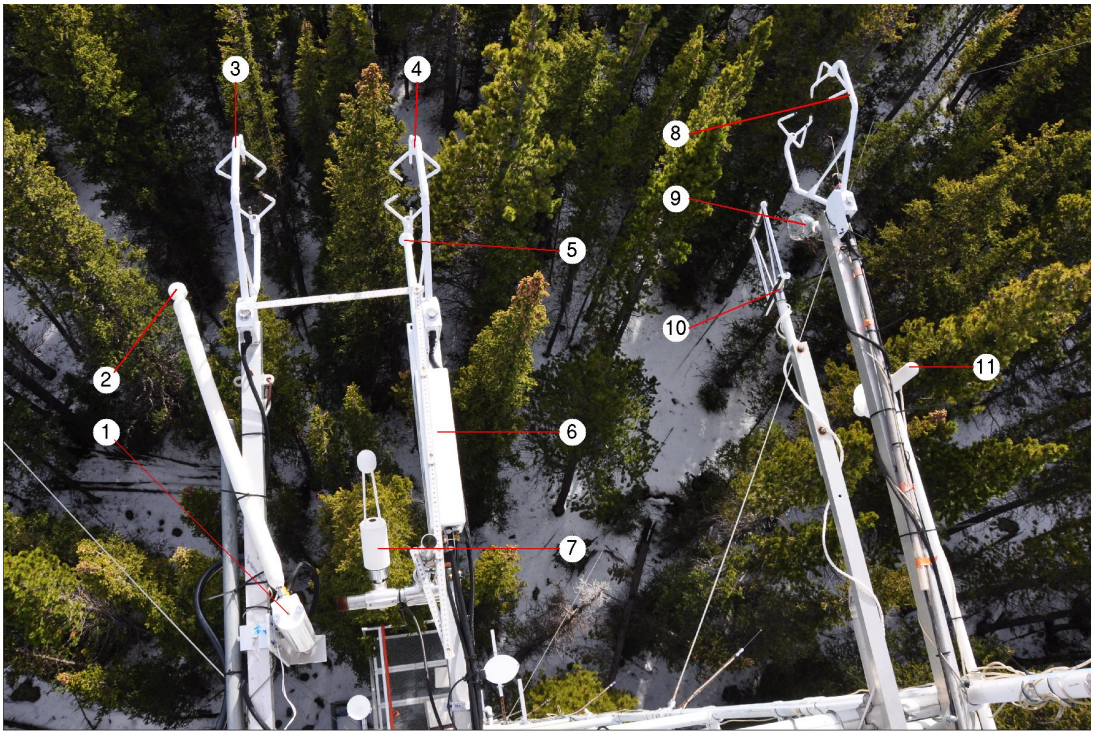

Figure 3.2: Photograph from 24 October 2013 looking down at the instrumentation deployed at 21.5 m on the University of Colorado AmeriFlux Tower. Various numbered instruments are described in Table 3.2. The booms for each CSAT3 are pointed in a nominal direction of 203 degrees from true north.

3.4 Motivation for the IRGA comparison at US-NR1

On the US-NR1 main tower, a LI-6262 IRGA has been deployed since 1998 to measure ecosystem fluxes with a 10 m long tube transporting the air sample from the 21.5 measurement level to the LI-6262 located about halfway up the tower [Monson et al., 2002]. The LI-6262 has been out of production for over 10 years and requires factory maintenance about every 3–4 years. To take advantage of the new design features mentioned above and reduce instrument maintenance costs, we wanted to upgrade the LI-6262 to a newer model IRGA. However, one difficulty with changing the analyzer in the middle of such a long-term measurement program is that the upgraded sensor can potentially bias conclusions about the environmental phenomena being measured. Therefore, we deemed it crucial to better understand any instrument-dependent measurement differences over

Table 3.2: Instrumentation and measurements on the Niwot Ridge US-NR1 AmeriFlux tower during the IRGA comparison in March, 2014. All sensors are at a nominal height of 21.5 m above the ground (see photo in Fig. 3.2).

Label from Fig. 3.2	Sensor type[a]	Manufacturer[b] make/model	Serial No. and CSAT3 firmware	Measured Variables[c]	Data Sample Rate samples/s	Deployment Dates[d]	Additional Comments
①, inlet ②, body	CP IRGA	LI-COR, LI-7200	72H-0479	χ_c, χ_h	20	2 Nov 2013–present	On 2 Nov 2013, sn 72H-0192 was replaced with sn 72H-0479
③	3D Sonic	CSI, CSAT3 ("EOL" CSAT3)	0254 (ver4)	u, v, w, $T_{\rm son}$	10	27 Jul 2012–present	
④	3D Sonic	CSI, CPEC200/ CSAT3A	2047 (ver4)	u, v, w, $T_{\rm son}$	10	8 Oct 2013–21 Jul 2015	On 21 Jul 2015, CPEC200 removed from US-NR1
⑤, inlet ⑥, body	CP IRGA	CSI, CPEC200/ EC155	1073	χ_c, χ_h	10	7 Jan 2014–present	On 7 Jan 2014, sn 1012 was replaced with sn 1073
⑦	OP IRGA	LI-COR, LI-7500	75H-0084	ρ_c, ρ_v	10	8 Oct 2013–16 May 2014	In May 2014, replaced with a LI-7500A
⑧	3D Sonic	CSI, CSAT3 ("CU" CSAT3)	0198 (ver4)	u, v, w, $T_{\rm son}$	10	28 Sep 2010–present	On 29 Oct 2016, CSAT3 sn 0198 (ver4) replaced with CSAT3 sn 0328 (ver5)
⑨, inlet	CP IRGA	LI-COR, LI-6262	IRG3-0638	χ_c, χ_h	10	7 May 2013–present	Factory service and recalibration in May, 2013
⑩	Krypton Hygrometer	CSI, KH2O	1249	ρ_v	10	23 Jul 2013–present	Factory service and recalibration in July, 2013
⑪	Platinum resistance, capacative humidity	Vaisala, HMP35-D	N.A.	$T_{\rm a}$, RH	1	N.A.	slow-response platinum resistance thermometer in a mechanically-aspirated housing

[a] CP and OP IRGA refers to closed-path and open-path infrared gas analyzers, respectively. 3D Sonic refers to a three dimensional sonic anemometer-thermometer.
[b] LI-COR: LI-COR Biosciences, Lincoln, NE 68504; CSI: Campbell Scientific, Inc., Logan, UT 84321.
[c] These are: CO_2 dry air mole fraction χ_c, H_2O dry air mole fraction χ_h, CO_2 density ρ_c, H_2O density ρ_v, air temperature $T_{\rm a}$, relative humidity RH, sonic temperature $T_{\rm son}$, and the planar-fit streamwise u, crossstream v, and vertical w wind components.
[d] Deployment dates refer to an instrument being located at this particular location.

the full range of environmental conditions experienced at this specific site. Consequently, starting in summer 2013, a LI-7200 (along with an open-path LI-7500) were deployed at 21.5 m on the US-NR1 tower. In Fall 2013, a EC155/CPEC200 was added so that a side-by-side comparison between all four IRGAs was possible (Fig. 3.2, Table 3.2). The IRGA comparison results presented herein use data collected during March, 2014 to compare: the CO_2 and H_2O mean, variance and vertical fluxes measured by each IRGA, the vertical wind statistics from three side-by-side sonic anemometers, as well as the corresponding spectra and cospectra from these sensors.

3.5 Nomenclature and units

The mole fraction of CO_2 relative to dry air (or mixing ratio) will be designated as χ_c (units: μmol CO_2 per mole of dry air; $\mu\mathrm{mol\,mol^{-1}}$) which we will refer to as "dry mole fraction" in our discussion [e.g., Kowalski and Serrano-Ortiz, 2007]. The ecosystem flux of CO_2 is designated F_c with units of $\mu\mathrm{mol\,m^{-2}\,s^{-1}}$. For CO_2, the World Meteorological Organization (WMO) maintains the WMO scale which is a set of calibration gases that are used world-wide as a standard against which all CO_2 measurements should be referenced [Zhao and Tans, 2006]. For water vapor, χ_h is the variable for the mixing ratio of H_2O (units: mmol H_2O per mole of dry air; $\mathrm{mmol\,mol^{-1}}$) and latent heat flux (λE, units: $\mathrm{W\,m^{-2}}$) for the ecosystem flux of water vapor. When we discuss water vapor in the atmosphere, the specific humidity q (units: grams of H_2O per gram moist air; typical units are $\mathrm{g\,kg^{-1}}$) or water vapor density ρ_v (units: grams of H_2O per volume moist air; $\mathrm{g\,m^{-3}}$) will also be used. Temperatures will be shown with units of °C and sensible heat flux with units of $\mathrm{W\,m^{-2}}$. Air temperature will be designated as T_a; however, when T is used without any subscript it could also mean air temperature or some other more general temperature (typically, additional explanation will be provided). Positive fluxes indicate transport of the scalar away from the surface and into the atmosphere. Unless noted otherwise, all statistics are made over a 30-min period. An overbar signifies the mean value and the prime are fluctuations over the 30-min period. Any symbols without an overbar are mean values unless noted otherwise.

3.6 Flux processing and calculations

In recent years there has been an active interest in ecosystem flux calculations using the eddy covariance technique which has led to several textbooks dedicated to the topic [e.g., Aubinet et al., 2012, Burba, 2013], as well as software development, such as LI-COR EddyPro© and Tovi© or Campbell Scientific EdiRe© software.

Prior to the flux calculations, the measured wind components were transformed using the planar-fit method [e.g., Wilczak et al., 2001] which projects the measured wind vector into stream-

wise u, crossstream v, and vertical w wind components relative to the plane formed by the long-term averaged u and v wind components. The wind components in the sonic-coordinate reference frame will be designated as u_1, v_1, and w_1. Turnipseed et al. [2003] compared the planar-fit rotation with the double and triple rotation methods [e.g., Finnigan, 2004] at the US-NR1 site and found that these alternative methods overestimated the fluxes at low wind speeds, but the flux differences were relatively small when the entire data set was considered.

For density-based measurements with an open-path IRGA, the vertical water vapor and CO_2 flux can be calculated by taking into account the WPL terms [Webb et al., 1980, Fuehrer and Friehe, 2002] as,

$$\underset{\substack{\mathbf{H_2O}\\ \mathbf{Flux}}}{E} = (1+\mu\sigma)\left\{\underbrace{\overline{w'\rho_v'}}_{\mathbf{Covariance}} + \underbrace{\frac{\overline{\rho_v}}{\overline{T}}\,\overline{w'T'}}_{\substack{\mathbf{Temperature}\\ \mathbf{Term}}}\right\}, \tag{3.1}$$

$$\underset{\substack{\mathbf{CO_2}\\ \mathbf{Flux}}}{F_c} = \underbrace{\overline{w'\rho_c'}}_{\mathbf{Covariance}} + \underbrace{\mu\,\frac{\overline{\rho_c}}{\overline{\rho_a}}\,\overline{w'\rho_v'}}_{\substack{\mathbf{Water\ Vapor}\\ \mathbf{Term}}} + \underbrace{(1+\mu\sigma)\,\frac{\overline{\rho_c}}{\overline{T}}\,\overline{w'T'}}_{\substack{\mathbf{Temperature}\\ \mathbf{Term}}}, \tag{3.2}$$

where ρ_c, ρ_v, and ρ_a are the density of CO_2, water vapor, and dry air [units: g m^{-3}], respectively. The vertical wind component is w, μ is the ratio of the molar mass of dry air to the molar mass of water, and σ is the ratio of mean water vapor density to the mean dry air density. In Eq. 3.1, E is expressed in units of g(H_2O) m^{-2} s^{-1} which gets converted into an energy flux (units: W m^{-2}), using the latent heat of vaporization of water vapor λ (units: J g^{-1}). In the above flux equations, we have not included any higher-order or pressure terms which are discussed elsewhere [e.g., Fuehrer and Friehe, 2002, Massman and Lee, 2002, Nakai et al., 2011, Burba et al., 2012]. On the US-NR1 tower, the flux measurements at 21.5 m were shown to be within the surface layer [Turnipseed et al., 2003]; though this depends on atmospheric conditions and is a topic which might need re-visiting.

In Eqs. 3.1 and 3.2, the temperature T would be T_a for an open-path IRGA, whereas for a closed-path IRGA it would be temperature fluctuations within the sample cell. For the purpose of this thesis, it is useful to realize that there are two WPL terms: one related to the water

vapor fluctuations (second term on right-hand side of Eq. 3.2) and one related to air temperature fluctuations (second term on right-hand side of Eq. 3.1 and third term on right-hand side of Eq. 3.2). In a closed-path system, the WPL temperature term is typically accounted for by either a fast-response temperature measurement of the air sample or through heat transfer within the air sample to remove any temperature fluctuations [e.g., Burba et al., 2012]. In this case, the CO_2 dry mole fraction can be calculated directly using the ideal gas law and measured cell temperature and pressure. The WPL water vapor term can be avoided by using coincident high-rate water vapor measurements within the sample cell to directly convert ρ_c to χ_c using the dilution properties of water vapor on the CO_2 measurement, though phase differences between the CO_2 and H_2O should be considered [e.g., Ibrom et al., 2007]. For the LI-6262 system at US-NR1, in addition to the long inlet tubing, a 1-m long coil of copper tubing inside the LI-6262 enclosure is designed to remove any residual temperature fluctuations within the air sample [Monson et al., 2002].

If fluctuations of air temperature are known, then the sensible heat flux H is calculated with,

$$H \;=\; \overline{\rho}\;\overline{c_p}\;\overline{w'T_a'}, \tag{3.3}$$

where ρ is the air density ($\mathrm{kg\,m^{-3}}$), w is the vertical wind, and c_p is the specific heat of moist air at constant pressure (note that $\overline{\rho} = \overline{\rho_a} + \overline{\rho_v}$ and $\overline{c_p} = \left(\overline{\rho_a} c_{pa} + \overline{\rho_v} c_{pv}\right) / \overline{\rho}$ where the subscripts a and v refer to dry air and water vapor, respectively). The air temperature T_a fluctuations could be measured, for example, by a fine-wire (fast-response) thermocouple.

A sonic anemometer, however, measures temperature based on the speed of sound c, which differs from true air temperature because sonic temperature is affected by atmospheric humidity and cross-path airflow. Therefore, the sonic anemometer-derived sensible heat flux is calculated with,

$$H \;=\; \overline{\rho}\;\overline{c_p}\left[\overline{w'(T_{\mathrm{son}}^{\mathrm{uc}})'} \;+\; 2\;\frac{\overline{T}\;\overline{u}}{\overline{c^2}}\;\overline{u'w'} \;-\; 0.51\;\overline{T}\;\overline{w'q'}\right], \tag{3.4}$$

where, u is the horizontal wind component in streamwise coordinates, and $T_{\mathrm{son}}^{\mathrm{uc}}$ is the sonic temperature T_{son} without the cross-wind correction; the $\overline{u'w'}$ term is the so-called cross-wind correction term but most modern sonic anemometers take this into account with internal processing software

that corrects each individual T_{son} sample for cross-wind effects [Hignett, 1992]. After correcting for the cross-wind effects, the equation for the sonic-derived sensible heat flux becomes,

$$H \;=\; \overline{\rho}\;\overline{c_p}\;\left[\overline{w'T'_{\mathrm{son}}} \;-\; 0.51\;\overline{T}\;\overline{w'q'}\right], \tag{3.5}$$

where the term involving $\overline{w'q'}$ takes into account the impact of the humidity fluctuations [Schotanus et al., 1983, Kaimal and Gaynor, 1991, Foken et al., 2012]. If fluctuations of humidity are measured/known, then this can be combined with the sonic temperature-vertical wind correlation term to give the sensible heat flux.

For the IRGA comparison, the calculation of the eddy covariance fluxes used a simple technique for all three IRGAs. Even though there is a long list of possible corrections to apply (see examples listed in Mauder et al. [2008]), one of the underlying assumptions of our comparison is that the vertical turbulent fluxes sampled by each IRGA were similar. Therefore, our goal with the IRGA comparison was not to measure the true ecosystem flux (which would require storage and horizontal transport estimations). Instead, out intention was to establish what differs in the vertical turbulent fluxes measured by each instrument. For this reason, we omit any spectral corrections for high-frequency signal loss. Rather, high-frequency signal loss is something we can evaluate by comparing the measurements from each instrument. For simplicity, only two transformations were applied to the high-rate data prior to calculating the fluxes: first, the planar-fit was applied to the wind components; second, each scalar was adjusted by a constant time-lag. The time-lag for the scalars were estimated from the time shift that resulted in the maximum correlation between the vertical wind fluctuations and the fluctuations of each scalar (either H_2O or CO_2). A rough estimate of the time lag can also be determined from the time it takes to flush the inlet tubing and sampling cell which are shown for each IRGA in Table 3.3. Future analysis will take into account more complicated corrections such as humidity-dependent lags which have been shown to be important, especially for water vapor fluxes [Fratini et al., 2012].

3.7 Data system

In order to properly collect high-frequency data, time-keeping and time-stamping of data samples is an important consideration. This becomes even more important when combining data from different data loggers or data systems. The data system at the AmeriFlux tower uses a set of Campbell Scientific CR23X data loggers coupled with the NCAR EOL In-Situ Data Acquisition Software (NIDAS; Maclean and Webster [2012]) to collect and archive the US-NR1 high-rate data [Burns et al., 2016b]. Over the years, the number of CR23Xs used has fluctuated between about 5–11. The primary CR23X data loggers we will refer to in our discussions below are called: CNR, UCB, SOIL, and TC; the complete list of CR23Xs is in Burns et al. [2016b], their Table 2. The future (Part III) publication about the US-NR1 measurements plans to document the changes to these data loggers over the lifetime of each logger (e.g., when they were moved, when sensors were added, etc.). Each CR23X streams serial data at a rate of either 1-Hz or 10-Hz to a computer at the tower. Even though the individual CR23X clocks may drift over time, the EOL data-acquisition software time-tags the incoming serial data samples as they are ingested by the computer. In the past the data system has used network time protocol (NTP) to ensure accurate time-stamps; however, starting in Fall of 2014, a GPS clock was installed for computer time-keeping. While the primary instruments have remained nearly the same, there has been an evolution of the data system hardware and software used at the US-NR1 site over the past 20 years. This history and evolution of the US-NR1 data system is described in Burns et al. [2016b], and we refer interested readers to this paper for the gory details.

The LI-7200 uses precision time protocol (PTP) to ensure accurate time-keeping and 20-Hz raw data were stored on the internal USB thumb drive. At the time of the IRGA comparison, a Linux-based PC located in a trailer about 500 m from the tower (connected to the tower by a fiber optic cable) acted as the NTP/PTP server for the tower. The CPEC200 system was equipped with an independent GPS for precise time-keeping and scan interval regulation. The CPEC200 10-Hz raw data were stored locally on a Campbell Scientific CR3000 data logger.

As a way to check for any potential differences among the clocks managing each of the three IRGAs, an analog CO_2 voltage from the LI-7200 and EC155 were ingested by the tower data system. This provided an easy way to check that the IRGAs were both working properly during the comparison as well as creating the potential for post-processing quality-control analysis of any time-stamp differences between the various data sets. By calculating the phase difference between the EC155 CO_2 stored locally and that from the analog signal, we were able to detect the small CR23X data logger time drift which was on the order of 0.2 to 0.4 $\mathrm{s\,day^{-1}}$ [Burns et al., 2016b].

3.8 Radiation

At US-NR1, net radiation R_{net} was measured at 25 m above ground level (AGL) with both a net (REBS, model Q-7.1) and four-component (Kipp and Zonen, model CNR1) radiometer. The CNR1 four-component radiometer has 2 pairs of upward/downward-looking pyranometers (model CM3) for shortwave radiation (over a spectral range of 0.3 to 3 μm) and pyrgeometers (model CG3) for longwave radiation (spectral range of 5 to 50 μm). The CNR1 at US-NR1 is unaspirated, but experiences some degree of natural ventilation from the wind at the top of the tower. Mechanical aspiration would be a possible way to improve the CNR1 performance [Michel et al., 2008]. The CNR1 only has average-to-moderate performance when compared to higher-quality radiation instruments [Brotzge and Duchon, 2000]. Net radiometers, such as the Q-7.1, have been known to produce data of suspect quality [Halldin and Lindroth, 1992]. As part of regular maintenance the domes on the Q-7.1 are replaced approximately every year. Despite the sometimes harsh conditions (e.g., hail, wind), these domes have never been cracked or broken. Over the years, several attempts to deploy higher-quality pyranometers or pyrgeometers side-by-side with the CNR1 on the US-NR1 tower have proven unsuccessful; partly because of a lack of available instruments, but also due to the significant effort required to do the installation. The last two AmeriFlux QA/QC visits have deployed additional CNR1 sensors; however this only compared one CNR1 sensor to another one. While useful for first-order errors, this does not allow us to characterize the accuracy of the CNR1 sensor itself.

The Q-7.1 R_{net} sensor was installed at the start of data collection (November 1998) while the CNR1 radiometer was initially installed on 12 July, 1999. This first CNR1 was removed on 5 December, 2003. Two years later, in December 2005, a newly-purchased CNR1 was deployed on the US-NR1 tower. Therefore, in the early summer of 1999 and years 2004–2005 there was no CNR1 on the US-NR1 tower. Because the Q-7.1 radiometer has operated nearly continuously since 1998, it is the primary R_{net} sensor used in this thesis. Furthermore, there were some obvious data differences in the two different CNR1 sensors—the initial CNR1 sensor used (i.e., prior to December 2003) had a much larger value of outgoing shortwave radiation than that from the CNR1 sensor installed in late 2005 (Fig. 3.3, upper panel). Based on a side-by-side comparison with a CNR1 sensor from AmeriFlux in 2006, the later CNR1 data were found to be accurate [Thomas, 2007]. Therefore, in the US-NR1 data released to AmeriFlux in Fall of 2015, there was an ad-hoc correction to the CNR1 outgoing shortwave radiation data collected prior to December 2003 (Fig. 3.3, lower panel). [The AmeriFlux comparison in summer of 2003 did not compare 4-component radiation measurements, so we were unable to directly evaluate the first CNR1 sensor [Loescher, 2004].] For the CLM modeling work (Chapter 6), incoming shortwave radiation was needed as an input to CLM, therefore only time periods when the CNR1 data were available were used.

Differences between the US-NR1 Q-7.1 and CNR1 have already been discussed within the literature (e.g., Turnipseed et al. [2002], see their p. 183 and pp. 189-190; and Burns et al. [2012a], see their Fig. 6). The main conclusion from these previous studies is that R_{net} from the aspirated Q-7.1 sensor was about 15 % closer to closing the SEB than with the CNR1 sensor, and that the CRN1/Q-7.1 differences were primarily in longwave radiation. During the daytime, the longwave radiation component of R_{net} is a small percentage of R_{net} so any effect on the SEB is small. At night, however, longwave radiation dominates R_{net}, and the sensor difference are more important.

To further explore and quantify any differences, a comparison of the diel cycle for R_{net} from the Q-7.1 and CNR1 sensors is shown in Fig. 3.4. The mean difference is between 5-20 W m^{-2} over the diel cycle (Q-7.1 > CNR1). This difference is slightly smaller in the afternoon and larger during the morning transition which suggests one sensor might be slightly tilted relative to the other.

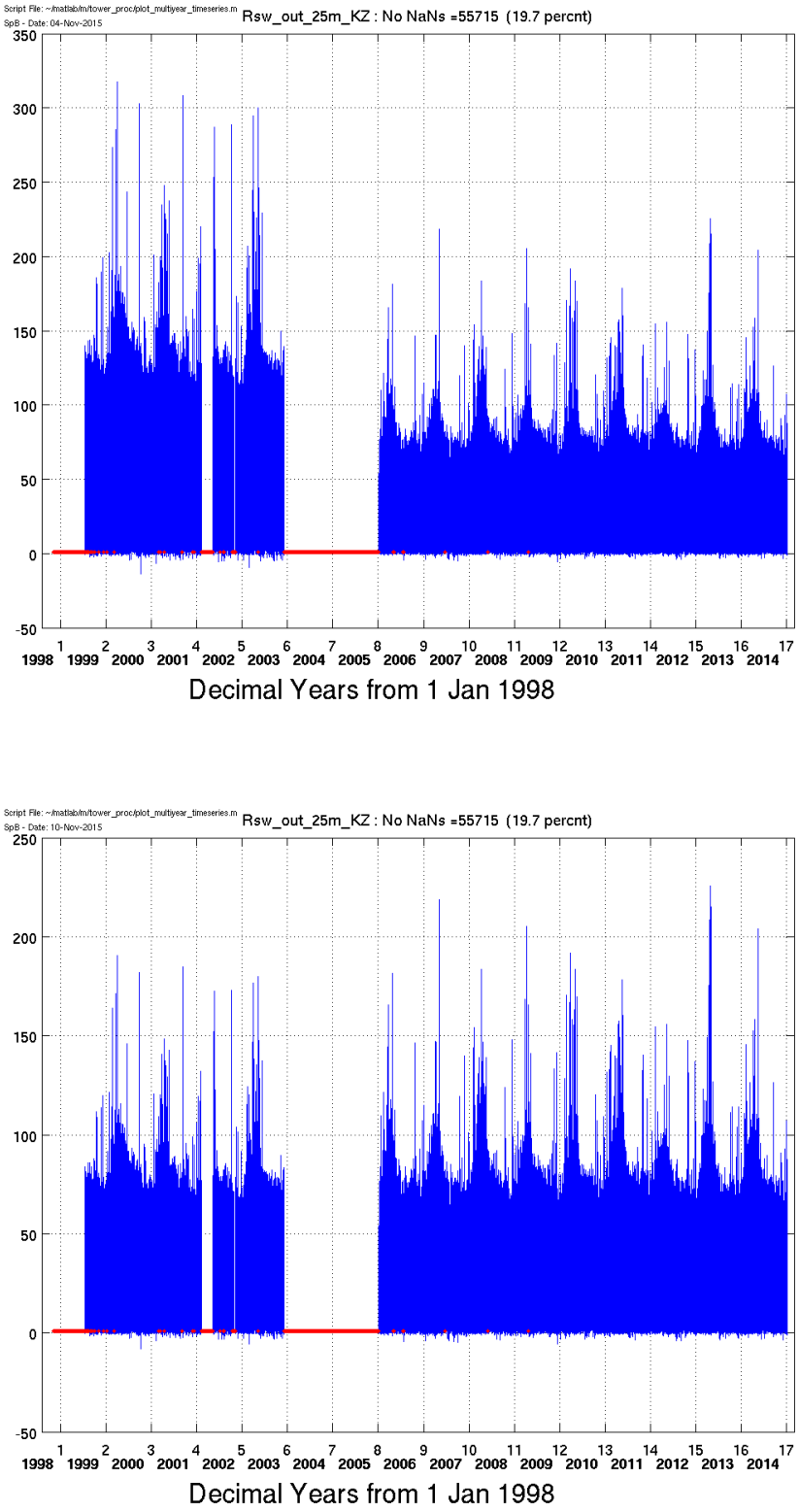

Figure 3.3: Time series of outgoing shortwave radiation from the Kipp and Zonen CNR1 sensor **(top)** before and **(bottom)** after an ad-hoc correction was applied to the data prior to 2005. Data with this ad-hoc correction were released in November of 2015. Starting on 1 January 2006, a new CNR1 sensor was deployed on the tower.

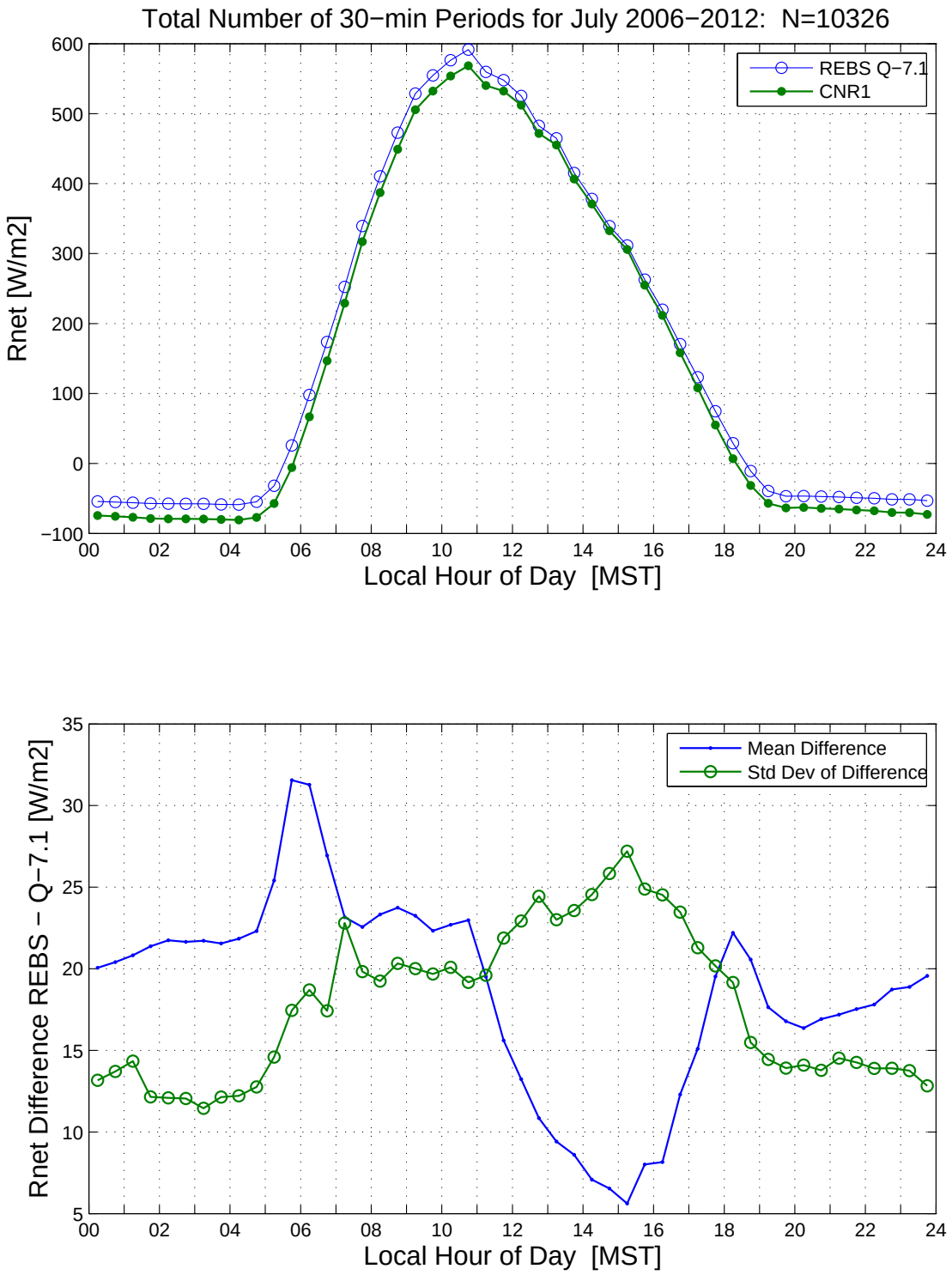

Figure 3.4: The six-year **(top)** mean and **(bottom)** difference statistics for net radiation R_{net} in July for the Q-7.1 and CNR1 sensors at the US-NR1 tower.

The standard deviation of the difference is fairly constant at night with a value of around 14 W m^{-2}. As mentioned above, the Q-7.1 sensor was found to be closer to closing the surface energy balance; however, this does not imply that the Q-7.1 is correct. Further study is probably needed to establish the reason for this difference.

In July, 2005 a second REBS Q-7.1 was installed at 2 m in the subcanopy. This Q-7.1 R_{net} sensor was connected to the UCB CR23X data logger. Prior to deploying it in the subcanopy it collected data next to the REBS Q-7.1 sensor at the top of the tower. Comparison between the two Q-7.1 sensors was reasonable. In contrast to the Q-7.1 at the top of the tower, the upper dome on the subcanopy Q-7.1 has cracked twice since 2005.

3.9 Photosynthetically active radiation (PAR)

Photosynthetic Photon Flux Density (PPFD) or PAR is the spectral range of incoming shortwave radiation (400–700 nm) which plants use for photosynthesis. In July 1999, silicon photodiodes (LI-COR, model LI-190SA "PAR" sensors) were added to the US-NR1 tower. A bandpass filter provides a spectral response range from 400 to 700 nm. Two LI-190SA quantum sensors were mounted together, one facing upwards, the other downwards. They were mounted such that leveling the upward facing quantum sensor automatically levels the other. Both were mounted at 25.5 m AGL on an eastward-pointed boom that extended the sensors to around 1.5 m away from the tower structure (to minimize any shadow-effects from tower structures). These sensors have been replaced once in the past 20 years and are checked annually with an independent, freshly calibrated PAR sensor (Kipp & Zonen, model PAR-LITE/PQS1 quantum sensor) provided by the AmeriFlux QA/QC team.

In July, 2005, a second pair of upward and downward-looking LI-190SA PAR sensors were added to the subcanopy tower and connected to the UCB CR23X data logger. Also, in summer of 2017, a new set of PAR sensors (Apogee, model SQ-500) were added both to the top of the tower and within the subcanopy by Dave Bowling's group from the University of Utah.

3.10 Wind measurements and sensible heat flux

Wind at the US-NR1 site has been measured with both a Campbell Scientific (model CSAT3) and Applied Technologies Inc. (ATI) "K" style 3-dimensional sonic anemometers. Turnipseed et al. [2002] found fairly good agreement (order of 5%) in sensible heat flux when the ATI-K and CSAT3 sonics were placed side-by-side at 21.5 m. In the early years of the site, the ATI-K sonic was moved to various levels on the tower, while the CSAT3 was left at the primary flux-measurement level of 21.5 m. [Turnipseed et al., 2003]. Between 2004 and 2012, the ATI-K probe was primarily located near the top of the canopy on the northeast corner of the tower. In late 2012, it was removed from the US-NR1 tower. In summer of 2000, additional CSAT3s were added to the subcanopy tower at 1.5 m and approximately 4 m AGL. In June 2003, the lower (1.5 m) CSAT3 was moved up to 5.7 m. Other than being swapped-out for re-calibration around 2008, these 2 CSAT3s have not moved again (and are still collecting data at this date). The data from these subcanopy sonic anemometers have been used in several publications [e.g., Turnipseed et al., 2003, Molotch et al., 2007, Burns et al., 2013].

As stated in the introduction (Sect. 1.2), the study by Turnipseed et al. [2002] found problems with sensible heat flux from the sonic anemometer at night under high winds. They concluded that the resolution of the CSAT3 temperature measurement was insufficient to capture the small temperature fluctuations that might be present in strong winds. Burns et al. [2012b] followed up on the Turnipseed study, and found that, in high winds, the CSAT3 sonic-path-transit times were overestimated using ver4 of the CSAT3 firmware. This led to an underestimation of T_{son} and resulted in an overestimation of the CSAT3 sensible heat flux. Though ver3 of the CSAT3 firmware was less susceptible to this problem, it could also occur on a ver3 CSAT3 that had experienced drift in the calibration. As far as we could tell, only the sonic temperature was affected, not the wind measurements. As a result of the Burns et al. [2012b] study, many different versions of CSAT3 sonic anemometers have been added to the US-NR1 tower and at least two have been deployed at the 21.5 m level since September 2009. For an example, of the tower equipped with three sonic

anemometers at the 21.5 m level, see Fig. 3.2. For historical reasons (described in Burns et al. [2012b]), the CSAT3 on the left side has always been labeled as the "EOL" CSAT3 while the one on the right corner is the "CU" CSAT3. In the summer of 2016, a CSAT3 with ver5 of the CSAT3 firmware was deployed on the US-NR1 tower to determine if the wind-dependent issue has been fixed (the analysis of these data has not been done yet).

The CU and EOL CSATs are both mounted on booms that are oriented at $\approx 203^\circ$ from True North (e.g., pointed toward the southwest). The winds at the site are typically either downslope ($WD \approx 270^\circ$) or upslope ($WD \approx 90^\circ$) such that winds coming from behind the CSAT3s and through the tower infrastructure are rare [e.g., Burns et al., 2015a].

From September 2014 to October 2015, seven CSAT3 sonic anemometers were added to the US-NR1 tower with a goal of enhancing the vertical resolution of the wind profile (Fig. 3.1, upper panel). For about half of this year-long period, the CSAT3s were sampled at a rate of 60 Hz. The goal of this work was to better understand the variability in the location and magnitude of the above-canopy drainage jet maximum, and how that jet structure might affect the fluxes measured at 21.5 m. Preliminary analysis of these data was presented at a meeting in 2016 [Burns et al., 2016a], but a comprehensive analysis is still forthcoming.

For the IRGA comparison, each IRGA in our study was paired with a CSAT3 sonic anemometer to measure the turbulent wind fluctuations. The vertical wind fluctuations from each CSAT3 are compared with each other to ensure that any differences in the calculated fluxes were not due to sonic anemometer differences. The EOL CSAT3 was paired with the LI-7200 inlet and the CU CSAT3 was paired with the LI-6262 inlet (Fig. 3.2). The EOL and CU CSAT3 have a 2 measurement sample pipeline delay which has been taken into account in the data analysis [Campbell Scientific, 2010]. These sonic data were collected using the Synchronous Device for Measurements (SDM) communication protocol developed by Campbell Scientific. The EOL CSAT3 also output an analog voltage into the LI-7550 Analyzer Interface Unit which serves as the electronic control and network interface for the LI-7200. This allowed for the CSAT3 wind data to become part of the LI-7200 high-rate data archive. However, the analog CSAT3 sonic data has a reduced reso-

lution compared to the SDM data. For example, the vertical wind analog output has a range of $\pm 8.192\,\mathrm{m\,s^{-1}}$ and resolution of $0.004\,\mathrm{m\,s^{-1}}$ whereas the SDM vertical wind has an autorange scale that goes up to $\pm 65.535\,\mathrm{m\,s^{-1}}$ and resolution between 0.00025 and $0.002\,\mathrm{m\,s^{-1}}$ [Campbell Scientific, 2010]. Because we have simultaneously collected the SDM and analog CSAT3 wind data we can evaluate the effect of the reduced measurement range and resolution on the ecosystem fluxes.

The CPEC200 system included a CSAT3A sonic anemometer which used the same support frame and transducers as the CSAT3, but included the EC100 electronics module to integrate the CSAT3A with the EC155 [Campbell Scientific, 2013a]. For our comparison project, the CPEC200 bandwidth setting was at 5-Hz and therefore the delays introduced in winds from the CSAT3A and CO_2/H_2O from the EC155 were 0.8 sec (8 samples). Unless stated otherwise, any comments provided about the CSAT3 equally apply to the CSAT3A. During the comparison, all of the sonic anemometers were using ver4 of the CSAT3 firmware.

3.11 Carbon dioxide measurements

As mentioned in Sect. 3.4, a closed-path IRGA (LI-COR, model LI-6262, sn IRG3-0638) has been deployed at US-NR1 since 1998 to measure ecosystem fluxes with 10 m long Synflex 0.625 cm composite tubing transporting the air sample from the 21.5 measurement level to the LI-6262 located halfway up the tower [Monson et al., 2002]. For usual operation, every four hours, the LI-6262 sampled a CO_2-free gas (Ultra High Purity (UHP) N_2) and a so-called span gas, which is air with a fixed CO_2 dry mole fraction close to that of the atmosphere (typically around $400\,\mu\mathrm{mol\,mol^{-1}}$). The UHP N_2 was used to determine the instrument offset while the span gas was used to determine any additional adjustment to the gain from the factory-determined calibration of the LI-6262. Prior to 2011, the dry mole fraction of the calibration span gas was determined using a second IRGA (LI-COR, model LI-6251) and a WMO-referenced calibration gas in a trailer near LTER C-1 [Monson et al., 2002]. Between 2011–2016, CO_2 measured by a tunable diode laser (described below) was used for an in-situ determination of the calibration span gas dry mole fraction. By using a CO_2-free gas and a single span gas, the LI-6262 can be considered a very precise

instrument, but not necessarily highly accurate relative to the WMO CO_2-scale which requires taking into account the non-linearity of the IRGA response [Trivett and Köhler, 1999, Welles and McDermitt, 2005, Burns et al., 2009a, Fratini et al., 2014]. Typical factory recalibration periods for the LI-6262 have been every 3–4 years, and LI-COR usually sends a "loaner" LI-6262 to use when these have occurred. The factory service for the LI-6262 will stop at the end of 2018.

Carbon dioxide dry mole fraction has also been measured on the US-NR1 tower with a tunable diode laser (TDL) absorption spectrometer (Campbell Scientific, model TGA100A), as described by Bowling et al. [2005], Schaeffer et al. [2008b]. Measurements were initially made in summer of 2003 and then (nearly) continuously from Fall 2005 until September 2016. The TDL CO_2 dry mole fraction measurement was calibrated with four WMO-scale-related calibration gases with a reproducibility estimated to be about 0.2 μmol mol^{-1} relative to the WMO scale [Schaeffer et al., 2008b]. Within this thesis, nine TDL inlets between 0.1 m and 21.5 m AGL were used to evaluate how precipitation affected the CO_2 vertical profile (Chapter 5). For the IRGA comparison, the TDL inlet at 21.5 m AGL was used to evaluate the mean CO_2 measured by the three IRGAs (i.e., Table 3.3) as well as an in-situ determination of the LI-6262 calibration span gas dry mole fraction (as described above). The TDL CO_2 and isotope data are available from the US-NR1 AmeriFlux website or from the Bowling Lab website at the University of Utah (http://biologylabs.utah.edu/bowling/).

The TGA vertical CO_2 profile has also been used to calculate the US-NR1 NEE storage term (Eq. 1.2). For this purpose, the TGA has often been a secondary/redundant CO_2-measurement system on the US-NR1 main tower. The US-NR1 tower had an independent CO_2-profile system with a closed-path IRGA (LI-COR, model LI-6251) that is described in Monson et al. [2002]. This system sampled a vertical profile of CO_2 mixing ratio at 0.5, 1, 2, 5, 10, and 21.5 m AGL, with each inlet sampled for 1 minute so that a complete vertical profile was measured every 6 minutes (for a total of 5 vertical profiles every 30 minutes). The same UHP N_2 and span gas that were used with the LI-6262, were also sampled by the LI-6251 every 4 hours. The LI-6251 vertical CO_2 profiles were used for calculating the NEE storage term until around 2014, when the system stopped

working properly due to leaking solenoid valves. During periods when both the TGA and LI-6251 systems were working, a comparison of the NEE storage term calculated from both systems showed similar results.

In addition to the LI-6262 and LI-6251 IRGAs, two open-path IRGAs (LI-COR, model LI-7500) have been operating at the tower from summer of 2000 to Fall of 2014. One of the LI-7500s was mostly in the subcanopy, co-located with the 2.5 m CSAT3, while the other was typically co-located with the ATI K-probe (mostly located at the top of the canopy, starting around 2003). In Fall 2014, with support from AmeriFlux, the two LI-7500s were replaced with LI-7500As (this is mostly an upgrade of the LI-7500 to a more modern interface and control box). Since that time, one LI-7500A has been co-located with the EOL CSAT3 and the other co-located with the 2.5 m CSAT3 on the subcanopy tower.

For the IRGA comparison, the characteristics of each CO_2-measurement system are described in Table 3.3. The LI-7200 and CPEC200 were generally operated according to the manufacturers recommendations. Both systems used the factory-calibration and were operated without any span or zero calibration gases. More details on the internal digital signal filtering and instrument frequency response for the CPEC200 can be found in Sargent [2012]. One goal of the IRGA comparison, was to use the LI-7200 to test a non-standard heated inlet assembly (designed in cooperation between LI-COR and the National Ecological Observatory Network (NEON)) which raised the temperature of the incoming air sample by about 5–7 °C. During the IRGA comparison, power to the heated inlet was controlled with an adjustable DC power supply that was set to ≈ 3.8 W. One of the findings confirmed from the US-NR1 field work, was that the inlet assembly design and rain-cup volume are important limiting factors in the IRGA frequency response [Metzger et al., 2016]. The heated inlet for the EC155 is a part of the CPEC200 system and can provide anywhere from 0–0.7 W of power (for the IRGA comparison it was set to 0.7 W).

Table 3.3: Details of the CO_2-measuring instruments used in the IRGA comparison study.

	LI-6262[a]	**LI-7200**	**EC155**	**TGA100A**[a]
Manufacturer Manual	LI-COR [1996]	LI-COR [2013]	Campbell Scientific [2013b]	Campbell Scientific [2004]
Alternate Reference	Monson et al. [2002]	Burba et al. [2010]	Novick et al. [2013]	Schaeffer et al. [2008b]
Calibration Gases [μmol mol^{-1}]	0 and 395.4	None	None	Four WMO-based Calibration Gases
Calibration Frequency	every 4 hrs	N.A.	N.A.	Hourly
Pump/Blower Characteristics	Rotary Vane (GAST, (model 1531-107B-G557X)	Blower (LI-7200-101 Flow Module)	Diaphragm (CPEC200 Pump Module)	Unknown
Inlet Distance from Sonic Path	≈15 cm	22.2[b] cm	15.6 cm	N.A.
Intake Tubing Characteristics	Bare Tubing, (Synflex, Type 1300)	Heated/Insulated Stainless Steel	Heated/Insulated Stainless Steel	Bare Tubing (Synflex, Type 1300)
Heated Inlet Assembly	No	Yes (≈3.8 W)	Yes (0.7 W)	No
Inlet Filter	Two 2-μm (NuPro)	2-μm (Swagelok)	20-μm (steel disk)	1-μm (Nuclepore)
Tubing Length	≈1000 cm	80 cm	58.4 cm	≈2000 cm
Tubing Inner DIA	0.4318 cm ID	0.533 cm ID	0.267 cm ID	0.4318 cm ID
Cell Volume	11.9 cm^3	16 cm^3	5.9 cm^3	N.A.
Tubing Volume	146.44 cm^3	17.85 cm^3	3.27 cm^3	N.A.
Nominal Flow Rate	8.5 lpm	16 lpm	7 lpm	N.A.
Sample Travel Time[c]	1.12 s	0.127 s	0.079 s	N.A.
Sample Rate of Archived Data	10 Hz	20 Hz	10 Hz	1 Hz (multiple levels)
Bandwidth Setting	None	10 Hz	5 Hz	None
Time Keeping[d]	NTP (russter2)	PTP (russter2)	GPS	Unknown
Data System	CR23X + NIDAS[e]	LI-7550 + USB	EC100 + CR3000	CR3000
Variables Ingested by NIDAS data system[f]	All	CO_2	CO_2	None

[a] Both the LI-6262 and TGA100A are no longer in production

[b] On 12 Nov 2013, the LI-7200 inlet was moved from approximately 29.7 cm to 22.2 cm from the EOL CSAT3 sonic path

[c] The time for the air sample to travel from the inlet through the sample cell is calculated based on the volumetric flow rate U_{flow} and total displacement volume of the travel path V_{tot}, following, $t_{\text{flush}} = V_{\text{tot}} \ / \ U_{\text{flow}}$

[d] Time keeping refers to how the data system clock is synced to the true time; "russter2" is the on-site linux-based PC that runs NIDAS, archives the AmeriFlux tower data, and is an NTP/PTP server

[e] The NCAR In-Situ Data Acquisition Software (NIDAS) is open-source software developed at NCAR EOL [Maclean and Webster, 2012]. The implementation of NIDAS at US-NR1 is described in Burns et al. [2016b].

[f] To ensure time stamps are correct between the various instruments, an analog CO_2 voltage output from both the LI-7200 and EC155 were collected at 10-Hz by the NIDAS data system

3.12 Water vapor measurements

On the AmeriFlux tower, the LI-6262 measures the water vapor fluctuations needed to calculate latent heat flux; however, the primary sensor used to measure the water vapor fluctuations at US-NR1 has usually been the krypton hygrometer (Campbell Scientific, model KH2O) which is located within about 30 cm of the CU CSAT3 [Turnipseed et al., 2002, Foken and Falke, 2012]. The krypton hygrometer is preferred to avoid the long (10 m) tubing used by the LI-6262 which attenuates the high-frequency water vapor fluctuations. Turnipseed et al. [2002] generally found good agreement between λE from the LI-6262 and Krypton hygrometer, except after snowfall events, when the Krypton λE was about 50% larger than λE from the LI-6262 (they suspected this was due to condensation of water vapor within the long LI-6262 tubing). There are several time periods when the krypton hygrometer was not available and the LI-6262 has been used for gap-filling during these times (with an empirical correction applied to try and compensate for the high-frequency signal loss). There are also periods when a LI-7500 (or, more recently LI-7500A) have been available for gap-filling. As with CO_2, the UHP N_2 was used to determine the offset in the LI-6226 water vapor calibration. However, because the span gas is dry, there is no easy way to calibrate the gain for the LI6262 H_2O; therefore, a slow-response Vaisala HMP temperature/humidity sensor located near the LI-6262 inlet has been used to "span" the water vapor measurement.

Because the latent heat flux used in our analysis (in Chapters 5 and 6) comes from both the krypton hygrometer and the LI-6262, it would be reassuring to confirm that these two independent λE measurements were similar during the warm season. In Fig. 3.5 we compare the data from each sensor which shows that, to first order, they are in reasonable agreement with each other (consistent with the findings by Turnipseed et al. [2002]). Sometime in the future, a more comprehensive comparison of the US-NR1 water vapor measurements (and λE) is needed (which can also include several recent years worth of λE collected with the LI-7200 and LI-7500A IRGAs).

For the IRGA comparison, each IRGA in our study measured water vapor along with CO_2. The measurement of both H_2O and CO_2 in the same closed-path sample cell allows for the dilution

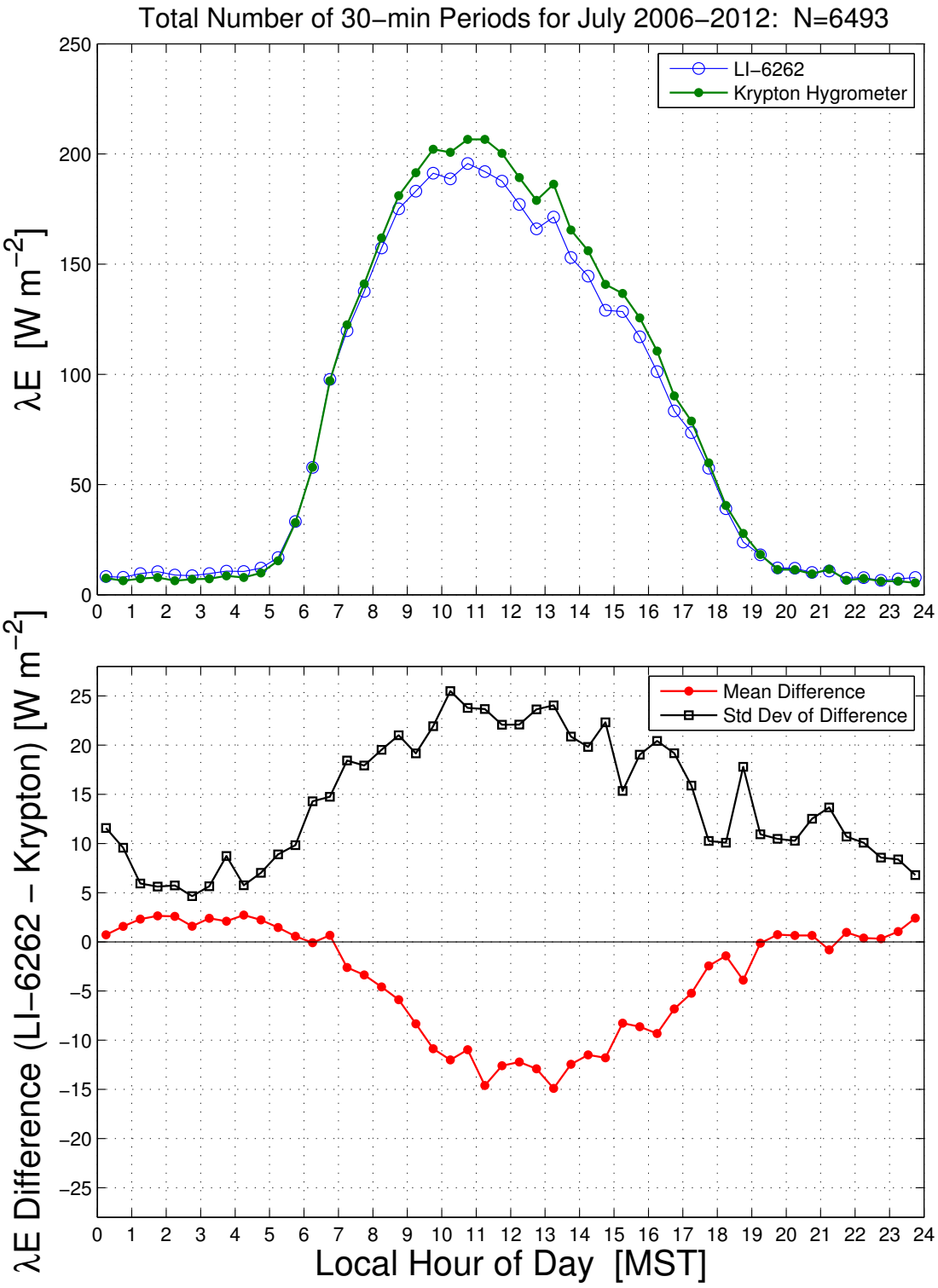

Figure 3.5: The six-year **(top)** mean and **(bottom)** difference statistics for latent heat flux λE in July for the LI-6262 and Krypton Hygrometer sensors at the US-NR1 tower. The Krypton Hygrometer and LI-6262 tubing inlet are both near the same sonic anemometer, which provides vertical wind fluctuations for the flux calculations. The number of 30-min samples that make up the statistics (N), are listed above the upper panel.

correction to be applied directly to the high-rate data samples which precludes use of the WPL water vapor term as discussed in Sect. 3.6.

An important environmental variable used in transpiration and evaporation studies is the vapor pressure deficit (VPD), which is the difference between the measured and saturated vapor pressure (in kPa). For our study, VPD was calculated using RH and air temperature from the slow-response temperature-humidity T/RH sensors (discussed in the next subsection) where the saturated vapor pressure was calculated using the Goff-Gratch formulation [Goff and Gratch, 1946], as described in the 1951 Smithsonian Meteorological Tables.

3.13 Air temperature

Mean air temperature and humidity profiles were measured with three mechanically aspirated, slow-response temperature-humidity T/RH sensors (Vaisala, model HMP35-D) installed at 2 m, 8 m, and 21.5 m AGL. In June and September of 2007 two additional slow-response T/RH sensors (Vaisala, model HMP35C) were added at 10.4 m and 4.6 m AGL, respectively. These sensors were housed in homemade mechanical aspiration units. In early July 2012, the 2-m T/RH HMP35 sensor failed; this was replaced with a REBS (model THP1) T/RH sensor in December, 2014. Between the years of 2008 to 2011, a "roving" temperature sensor was deployed on the US-NR1 tower. This sensor was periodically moved up and down the tower to co-locate with the fixed T/RH sensors on the tower. Evaluating the performance of this roving sensor will be included in the proposed manuscript related to data QA/QC and gap-filling.

In August 2002, the vertical resolution of the temperature measurements was enhanced by adding a set of twelve 0.254 mm diameter type-E chromel-constantan thermocouples distributed between the ground and 21.98 m AGL [Burns and Sun, 2000, Burns et al., 2015a]. This gauge of thermocouple wire is strong enough to withstand the environment on the tower and has a fast-enough time response to calculate a reasonable sensible heat flux [Burns et al., 2012b]. The thermocouples are unshielded so subject to radiation errors [e.g., Campbell, 1969, Foken, 2008b] which are on the order of 0.5 °C, as discussed by Burns et al. [2012b].

3.14 Forest biomass temperature

In July of 1999, a set of 0.511 mm diameter type-T copper-constantan thermocouples (Campbell Scientific, model A3537) were installed to measure tree bole temperature at the site. Though conduction down the copper wire can be problematic, these wires are encased in a thick plastic jacket to minimize conduction issues. Holes of specific depth were drilled in boles of designated trees. The thermocouples were coated with a thermal contact adhesive prior to insertion into the holes. Typically, each tree contained one thermocouple within the sapwood (depth of 2–4 cm) and one within the heartwood (depth of 6–8 cm). Two Spruce trees, around 4 Fir trees, and 6 Pine trees were instrumented in this fashion. The thermocouples were typically placed in two locations—at about 1.5 m AGL and/or near the base of the tree. The instrumented trees are located about 40 m northwest of the main US-NR1 tower next to what is known as the North Canopy tower (see Fig. 4.1). The same trees are still instrumented today (2018), though several of the sensors have stopped working (and one of the trees has died). The tree bole temperature data (as well as other temperature data, mentioned later) were collected with a multiplexer specifically designed to measure thermocouple temperatures (Campbell Scientific, model AM25T) which was connected to the TC CR23X, as described in Burns et al. [2016b]. Example photos of the Spruce #1 tree are in Fig. 3.6 and time series which shows the temperature time lag as a function of depth into the Spruce #1 bole are in Fig. 3.7. For the 6 cm and 2 cm depth, the lags are fairly constant at 300 min and 100 min, respectively. On certain afternoons (e.g., day 222), the sun appears to hit the tree causing the 2 cm bole temperature to become as much as 5 °C larger than the air temperature. These time lags are the source of phase shifts in the biomass storage term of the surface energy balance as discussed in Sect. 5.4.9.

In August 2015, a thermal infrared camera (FLIR Systems, Inc., model A655sc) along with several infrared temperature sensors (Apogee, model SI-121) were added to the US-NR1 tower for spatial monitoring of the canopy temperature [Aubrecht et al., 2016]; and to compliment the PhenoCams already on the main tower [Richardson et al., 2018, Burns et al., 2016b]. Data from

Figure 3.6: Photos from 2 November 2015 of **(left)** Spruce #1 tree, and **(right)** a closeup of the Spruce #1 bole where the thermocouple can be seen on the left side of the bole. The Spruce #1 tree had a DBH of 76 cm (as measured in summer of 1999) and was/is located next to the North Canopy tower.

the FLIR camera are just starting to be used [Aubrecht et al., 2016, Bowling et al., 2018], and further analysis is planned. The importance of the canopy temperature will be discussed again in the chapter on CLM modeling (i.e., Sect. 6.3.6).

3.15 Soil heat flux

In July, 1999 ten soil heat flux plates (REBS, model HFT-1) were placed in pairs within a 15 m diameter circle (for a total of 5 pairs). Locations of groups were chosen to maximize coverage of soil environments (e.g., open, dry clearing, vs. a damp, shadowed base of tree.) The probes were buried to a depth of around 8–10 cm below the surface of the ground by digging a small trench and then inserting a flat screwdriver into the soil at one end of the trench at a depth of 8-10 cm. The heat flux plate was inserted into the slot made by the screwdriver, making sure that it was in good

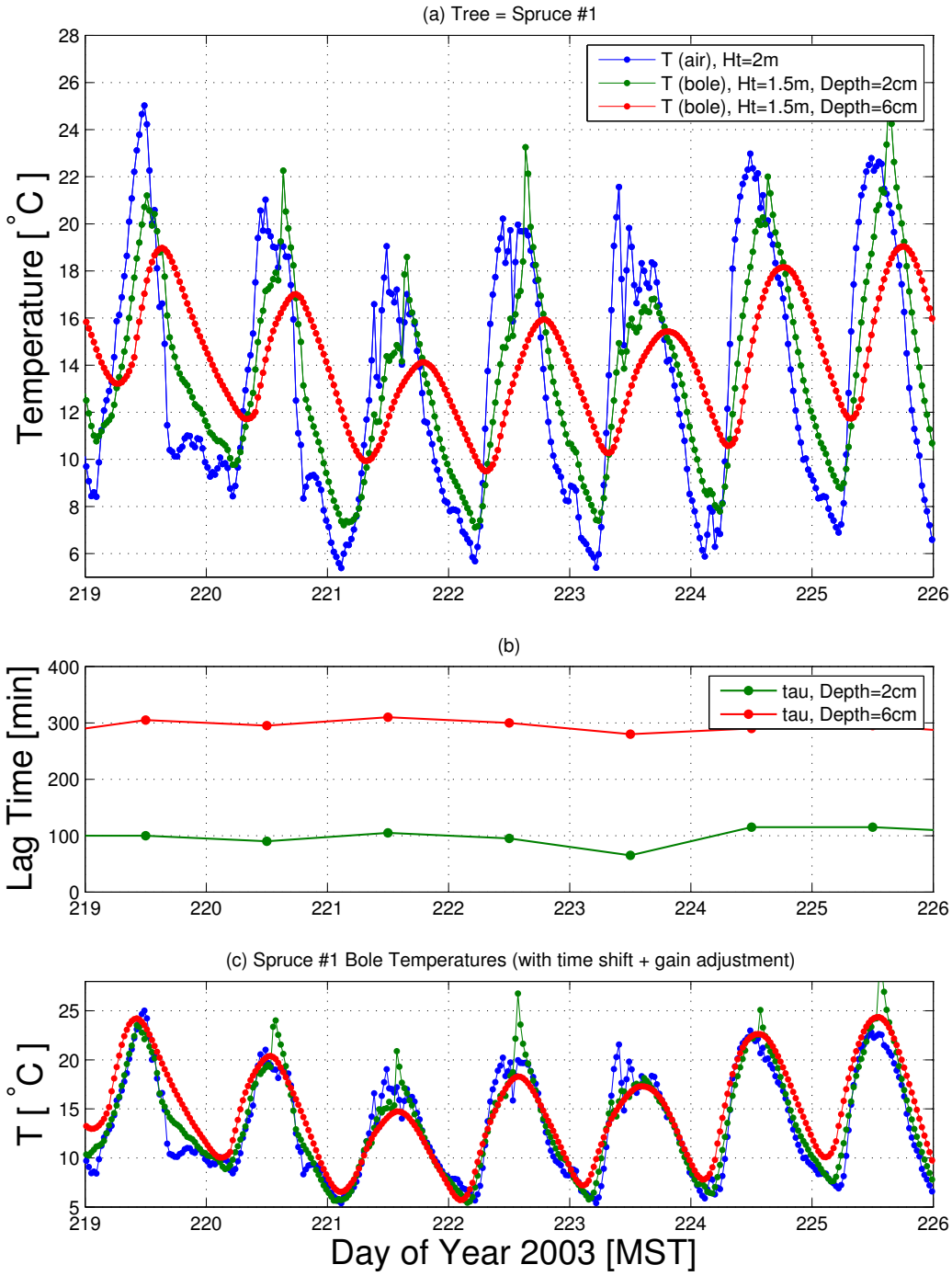

Figure 3.7: Time series of **(a)** 2-m aspirated air temperature and bole temperatures at two depths from the Spruce #1 tree, **(b)** estimated time lag of the bole temperatures relative to air temperature at depths of 2 cm and 6 cm into the tree bole, and **(c)** time series where the bole temperatures have been adjusted using the estimated lag time and a gain factor. The temperature time series are 5-min averages.

thermal contact with the soil. The sensor cable was run through the trench (about 30 cm long) at a depth of 10 cm to avoid water channeling towards the sensor. Soil was then replaced carefully over the trench. These sensors were all connected to the SOIL CR23X [Burns et al., 2016b].

In Fall of 2003, the SOIL CR23X was moved from the North Canopy tower to a location part-way along the path between the main tower and North Canopy tower. This move of the sensors was done in preparation for a series of experiments where CO_2 was measured underneath the snowpack [Monson et al., 2006a,b, Burns et al., 2009a]. The soil heat flux sensors have been in the same location since Fall, 2003. After nearly 20 years, about half of the soil heat flux plates are still working (as of 2018).

3.16 Soil temperature

In July, 1999, 5 soil temperature sensors (REBS, model STP-1) were co-located with the 5 pairs of heat flux plates. The sensor was inserted at a slight angle such that it just covered the sensor head. The STP-1 is a platinum resistance thermometer which is read by a 4-wire half-bridge relative to a known resistance. The sensor design is such that it gives an average temperature over the length of the sensor head (around 10 cm). The sensors provide an average temperature value over the upper 10 cm of the soil.

The REBS STP-1 soil temperature sensors were connected to the SOIL CR23X; therefore, as with the soil heat flux plates, they were moved in Fall of 2003. Sensor placement was either near a tree or in an open area. All the STP-1 sensors were deployed vertically such that the temperature represented an average over the upper 10 cm of the soil (as described in the previous paragraph).

In Fall 2005 two important changes were made: (1) a soil temperature (and moisture) profile was created where the probes were inserted parallel to the ground surface at three depths (5, 10, and 35 cm), and (2) a new soil temperature sensor (Campbell Scientific, model 107 temperature probe/thermistor) was installed at a depth of 5 cm near the 6-m subcanopy tower (Fig. 4.1), and connected to the UCB CR23X data logger. Prior to deployment, the 107 thermistor was calibrated against a NIST-standard temperature sensor at the NCAR ISFF calibration facility. Before con-

necting the 107 sensor to the UCB data logger it was briefly connected to the SOIL CR23X, for testing and to co-locate it with one of the REBS STP-1 sensors. However, being connected to the UCB CR23X had the advantage of being linked to the main data system (thus these data get saved at a rate of 1 sample/sec), and it provided another measure of soil temperature which was not connected to the SOIL CR23X.

For the US-NR1 data uploaded to AmeriFlux, the soil temperature data in the "climate" data files prior to 1 January 2006 comes from an average of the STP-1 sensors, whereas subsequent data are from the single (well-calibrated) 107 probe near the subcanopy tower. For the years between 2005-2011, we have also released special "soil" data files that include data from all the sensors discussed above. These are currently available from the urquell website (http://urquell.colorado.edu/data_ameriflux/data_30min/). Future data releases to AmeriFlux will include the soil temperature data from all the individual sensors.

3.17 Soil moisture

In December of 2001, 8 water content reflectometer soil moisture sensors (Campbell Scientific, model CS615) were installed within a 15 m $\times$ 15 m study area near the North Canopy tower. Locations were chosen to give a variety of soil conditions (near trees, within gaps, etc.). The CS615 sensor sends a square wave sent down two stainless rods (30 cm long) provides a measure of the soil volumetric water content (VWC). For deployment, the steel rods were inserted into the soil at a 45° angle, providing an average VWC over the upper 15 cm of the soil.

The CS615 sensors were connected to the SOIL CR23X data logger; therefore, just like the soil temperature and heat flux sensors, in Fall of 2003, the CS615 sensors were moved to various locations between the North Canopy tower and the main tower.

In Fall 2005, 3 new soil moisture sensors (Campbell Scientific, model CS616) were deployed at the tower. These sensors were co-located with the soil sensors so the description above is very similar for the CS616 sensors. One CS616 sensor was installed horizontally at a depth of 5 cm next to the 107 soil temperature sensor at the subcanopy tower (and connected to the UCB data logger).

The two of the other CS616 probes along with one CS615 sensor were buried (with an orientation parallel to the surface) in the same soil pit as the temperature sensors at depths of 5, 15, and 35 cm to create a soil moisture profile. Examination of the CS616 volumetric water content (VWC) data showed that it was much less sensitive to temperature variations than the older CS615 probes.

In addition to the 107 and CS616 probes added to the subcanopy tower a soil water potential probe (Campbell Scientific, model 257-L Soil Matric Potential Block) was installed vertically in the upper 15 cm of the soil. These three probes near the subcanopy tower have not moved since their installation in Fall of 2005.

3.18 Snow depth and snow temperature

Snow covers the ground at US-NR1 for over half the year. Though this thesis centers on the warm season, it seems appropriate to mention a few of the winter measurements. Vertical profiles of snowpack temperatures have been continually measured at the US-NR site for the past 15 years [Burns et al., 2013]. Since Fall 2005 there have been continuous measurements of snow depth near the North Canopy tower (both in clearings and near trees) by the Mountain Hydrology Group at INSTAAR [Molotch et al., 2009, Broxton et al., 2015]. As discussed in Sect. 3.2, snow depth has also been continuously measured at the C-1 site by LTER using an ultrasonic distance sensor (Campbell Scientific, model SR50-L). Since around 2011, LTER has also excavated snow pits near the US-NR1 tower, to provide manual profiles of snow density. Snow density and historical snow water equivalent (SWE) information are also available from the two nearby SNOTEL sites.

3.19 Precipitation

Starting in late summer 1999, precipitation was measured on the US-NR1 tower at 11.5 m (canopy top) with a tipping bucket rain gauge (Campbell Scientific, Met One Model 385). The USCRN and LTER measurement sites mentioned in Sect. 3.2 were used to check the Met One data for quality and gap-filling. Precipitation measurements at the USCRN Hills Mills site started in late 2003 using a Geonor T-200B precipitation gauge with a Small Double Fence Intercomparison

Reference (SDFIR) type of wind shield around the gauge. This setup is typically considered the "gold standard" for winter precipitation measurements by the World Meteorological Organization (WMO) [Goodison et al., 1998]. Precipitation measured near C-1 by the Niwot Ridge LTER used both a Geonor T-200B gauge (unshielded) and, for the longer-term record dating back to 1953, a Belfort precipitation gauge strip-chart recorder for daily precipitation amounts [e.g., Greenland, 1989, Williams et al., 1996]. The LTER sensors were located about 600 m northeast of the US-NR1 tower near C-1 and the USCRN site was about 700 m away. Though in winter the unshielded Met One gauge grossly underestimated total precipitation due to snow blowing by the tipping bucket gauge [e.g., Rasmussen et al., 2012, Kochendorfer et al., 2017], the warm-season cumulative precipitation between the USCRN and Met One gauges were typically within about 20 cm of each other (with a typical mean value of 250 cm).

The undercatch by the US-NR1 Met One gauge is shown more explicitly in Fig. 3.8a where the US-NR1 cumulative precipitation was smaller than USCRN for the annual totals. Based on a plot of the precipitation difference (Fig. 3.8b), it becomes more clear that most of the undercatch occurred in winter, whereas the warm-season difference was relatively flat (this is consistently true for the summers of 2005, 2006, 2007, and 2008). There appears to be a change to the calibration of one of the sensors in the winter of 2009 (we suspect the tipping bucket). And, starting in summer of 2011, the Met One gauge started showing much greater precipitation amounts which we suspect was due to the "points" which hold the tipping bucket becoming worn and loose (in winter of 2013, the sensor failed completely). Therefore, the precipitation data used in this thesis for the summers of 2011 and later were exclusively from the USCRN site. The US-NR1 precipitation data that have been uploaded to AmeriFlux website, use the USCRN data from 2011 onward.

Because the US-NR1 Met One sensor was not installed until late summer of 1999, the LTER Geonor data were used for the 1999 warm season. However, prior to year 2000, only daily precipitation was measured by LTER so hourly precipitation data were not available for 1999 which allows for the determination of a wet day, but not the diel cycle of precipitation.

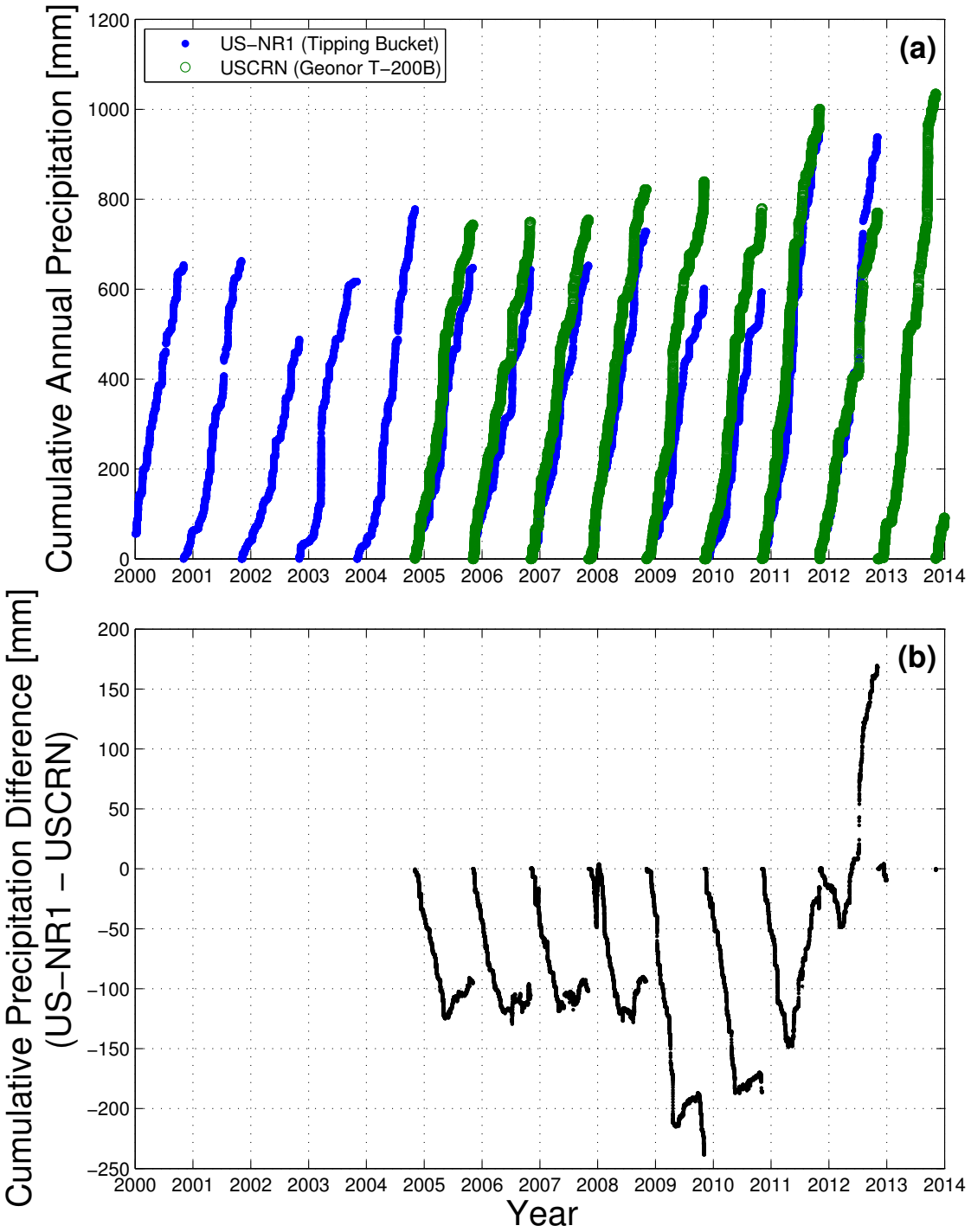

Figure 3.8: Time series of **(a)** cumulative precipitation over each water year (1 November to 31 October) from the US-NR1 tipping bucket (Met One, model 385) and the USCRN Geonor T-200B precipitation gauge with a Small Double Fence Intercomparison Reference (SDFIR) type of wind shield (see legend). In **(b)**, the difference in cumulative precipitation (US-NR1−USCRN) is shown. The USCRN precipitation station was installed in late summer of 2003.

3.20 Leaf wetness

Leaf wetness was measured just below canopy-top with a horizontally-oriented resistive-grid type wetness sensor (Campbell Scientific, model 237) between 1 July of 1999 to the present day. The output from the sensor has been normalized so that a value of zero corresponds to dry conditions while a value of one corresponds to completely wet conditions. Values between 0 and 1 correspond to "slightly wet" conditions.

3.21 Forest structure

Historically, collecting forest allometric data was an arduous task that involved tape measures and manual measurements of individual trees [e.g., Cain and de Oliveira Castro, 1959, Avery and Burkhart, 2002, West, 2009]. Recent advances in lidar (Laser Imaging Detection and Ranging) technology has led to revolutionary changes in our ability to characterize large forested regions [e.g., Dubayah and Drake, 2000, Lefsky et al., 2002, Popescu and Wynne, 2004, Reitberger et al., 2008, Tao et al., 2014, Harpold et al., 2015, and many others]. Pulsed lidar can be deployed as either airborne or ground-based (Terrestrial Laser Scanning, TLS) systems, where each platform has advantages and drawbacks [Lovell et al., 2003, van Leeuwen et al., 2011]. Another recent technological advance that is changing the way remote sensing of an ecosystem is accomplished, is the increased usage of Unmanned Aerial Vehicles (UAVs) equipped with lidar or cameras to study the surface [e.g., Grenzdörffer et al., 2008, Everaerts, 2008, Wallace et al., 2012].

The forest canopy structure has been measured by a variety of methods. The initial leaf area index (LAI) measurements were made by harvesting 15 trees of various species and sizes and examining the forest composition in a $1\,km^2$ around the main US-NR1 tower [Turnipseed et al., 2002]. In summer 2003, the canopy structure was measured in sixteen 10 x 10 m plots, eight east and eight west of the US-NR1 main tower. The first plot was established at 50 m east and west of the tower, with subsequent plots established at 20 m intervals out to 200 m. Each tree greater than 1 m in height was measured in all plots (total of 839 trees) for diameter at breast height, height to

crown and maximum diameter of crown (typically at the base of the crown) in the N-S and E-W perpendicular coordinates, and total tree height. A separate survey was done of 90 representative trees (30 lodgepole pines, 30 subalpine firs, and 30 Englemann spruces) in the plots, evaluating diameter at breast height against number of branches in the upper, middle and lower third of the trees, using binoculars to count branches. This method allows for the leaf area density versus height to be calculated [Yi et al., 2005], as well as quantifying the east-to-west distribution of tree species [Golub, 2010]. In summer 2006, further evaluation of the canopy structure was made by harvesting trees as described by Monson et al. [2010]. In our presentation of the results (Sect. 4.4), these methods will be labeled as the traditional ground-based forest measurements.

As part of the Boulder Creek Critical Zone Observatory (CZO), airborne scanning lidar measurements were made in 2010 over the entire Boulder Creek watershed [Anderson et al., 2012]. The point cloud data used in our study were collected with an Optech Gemini Airborne Laser Terrain Mapper (ALTM) deployed on a Piper Chieftan flying at 600 m above the surface. Flight with (snow-on) and without (snow-off) snow have been used to show how snow is distributed within the forest near US-NR1 [Broxton et al., 2015]. In our study, we use the snow-off flights. The tree locations determined with the airborne lidar use the method of Li et al. [2012], and one of our goals is to confirm the tree locations using a UAV equipped with a multi-spectral camera.

3.22 Results from the IRGA comparison

The results shown herein will focus on March 2014; the environmental conditions during that month are shown in Fig. 3.9. The IRGA comparison often involve measurement differences between two or three instruments. As part of our analysis, we will display these differences using box plots (e.g., box-and-whisker plots) which displays the data in quartiles [Hoaglin et al., 1983]. The inner box is the inner quartile range (IQR) which is where 50% of the data exist while the “whiskers” and outliers (shown as individual points) are where the other 50% exist. The outliers are defined as points that are beyond 1.5 times the IQR from the inner quartiles. The IQR is a robust estimate of the variability in the difference because data in the highest and lowest quartiles do not affect it.

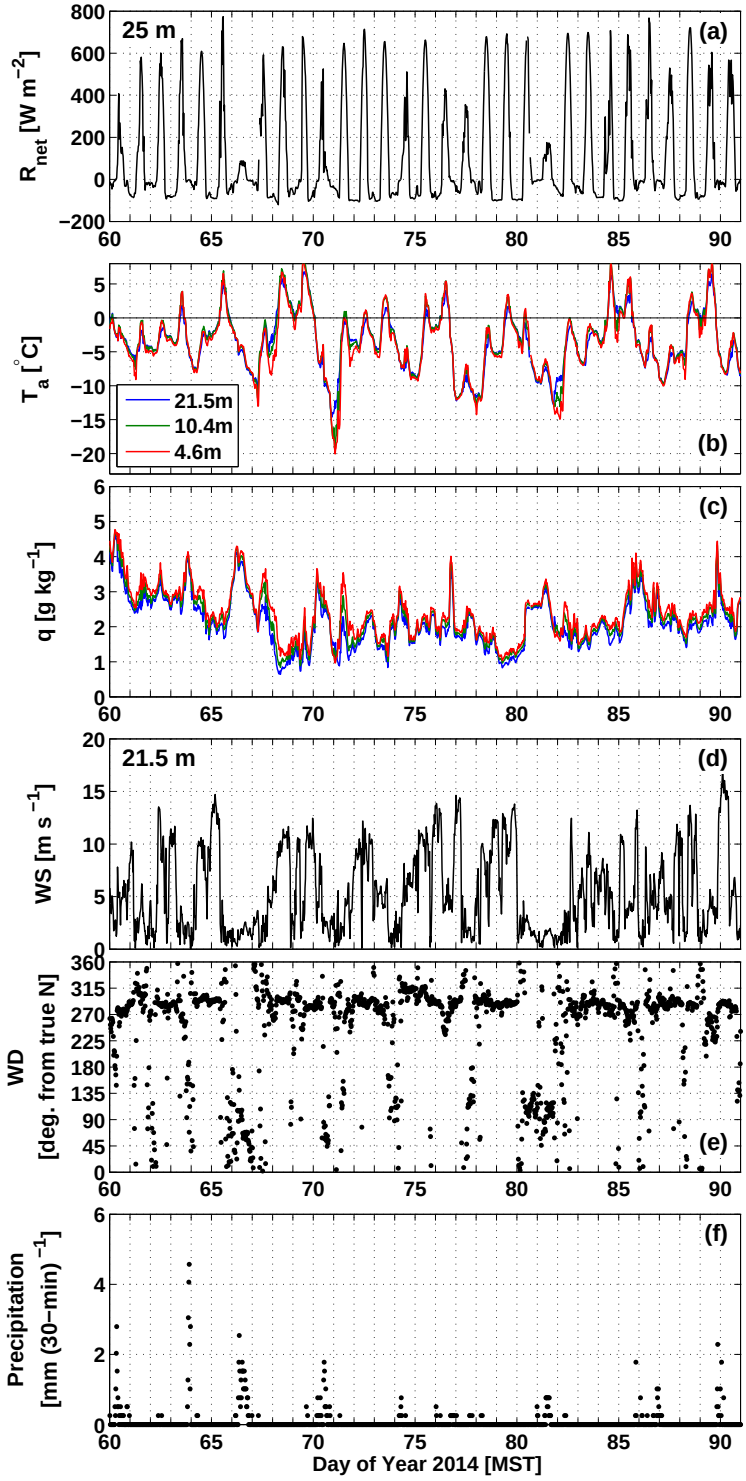

Figure 3.9: Time series of (a) 25-m net radiation $R_{\rm net}$, (b) air temperature $\mathrm{T_a}$, (c) specific humidity q, (d) 21.5-m wind speed WS, (e) 21.5-m wind direction WD, and (f) precipitation at the AmeriFlux tower during March, 2014. $\mathrm{T_a}$ and q are calculated from the slow-response Vaisala HMP35-D sensor while WS and WD are from the CU CSAT3 (Table 3.2).

We use the IQR extensively in these comparisons.

3.22.1 Comparison of CSAT3 vertical wind statistics

Because the sonic anemometers were nominally leveled according to gravity and the tower is situated on a ≈4–6% slope, a strong horizontal wind (i.e., wind speed $WS > 10$ m s^{-1}) produced a vertical wind component in sonic coordinates with mean values around 2 m s^{-1} (Fig. 3.10a). The mean differences in w_1 among the three CSAT3s were on the order of 0.2–0.4 m s^{-1} with an IQR of the difference that was around 0.3–0.5 m s^{-1} as shown by the difference box plots in Fig. 3.10a. These slight differences in the raw sonic wind statistics are likely related to differences in the droop from the booms.

After applying the planar-fit, the mean vertical wind in the rotated coordinate system for all three CSAT3s becomes smaller than ±0.2 m s^{-1} and the IQR of the differences among the CSATs is reduced by an order of magnitude (Fig 3.11a). In addition, the planar-fit reduced the difference of the standard deviation of the vertical wind between CSAT3s from an IQR of around 0.1 m s^{-1} (Fig. 3.10b) to less than 0.05 m s^{-1} (Fig 3.11b).

3.22.2 IRGA characteristics

The cell temperatures of each IRGA were affected by changes in air temperature. Because the LI-6262 cell is deep within the electronics and it was housed in an enclosure halfway up the tower, the LI-6262 cell temperature was typically about 12-17 °C higher than the air temperature (Fig. 3.12a). The LI-7200 inlet was heated such that the air entering the cell was about 5–7 °C above T_a. While inside the LI-7200 cell, the air sample was cooled by 2–5 °C suggesting that the overall cell temperature was anywhere from 1–5 °C above T_a. The CPEC200 sample intake was also heated and the cell temperature was around 1-2 °C above T_a.

One of the differences in instrument design between the LI-7200 and EC155 is how the cell temperature is measured. The LI-7200 uses two fast-response thermocouples to measure the temperature of the airstream as it enters and exits the sampling cell [e.g., Burba et al., 2010],

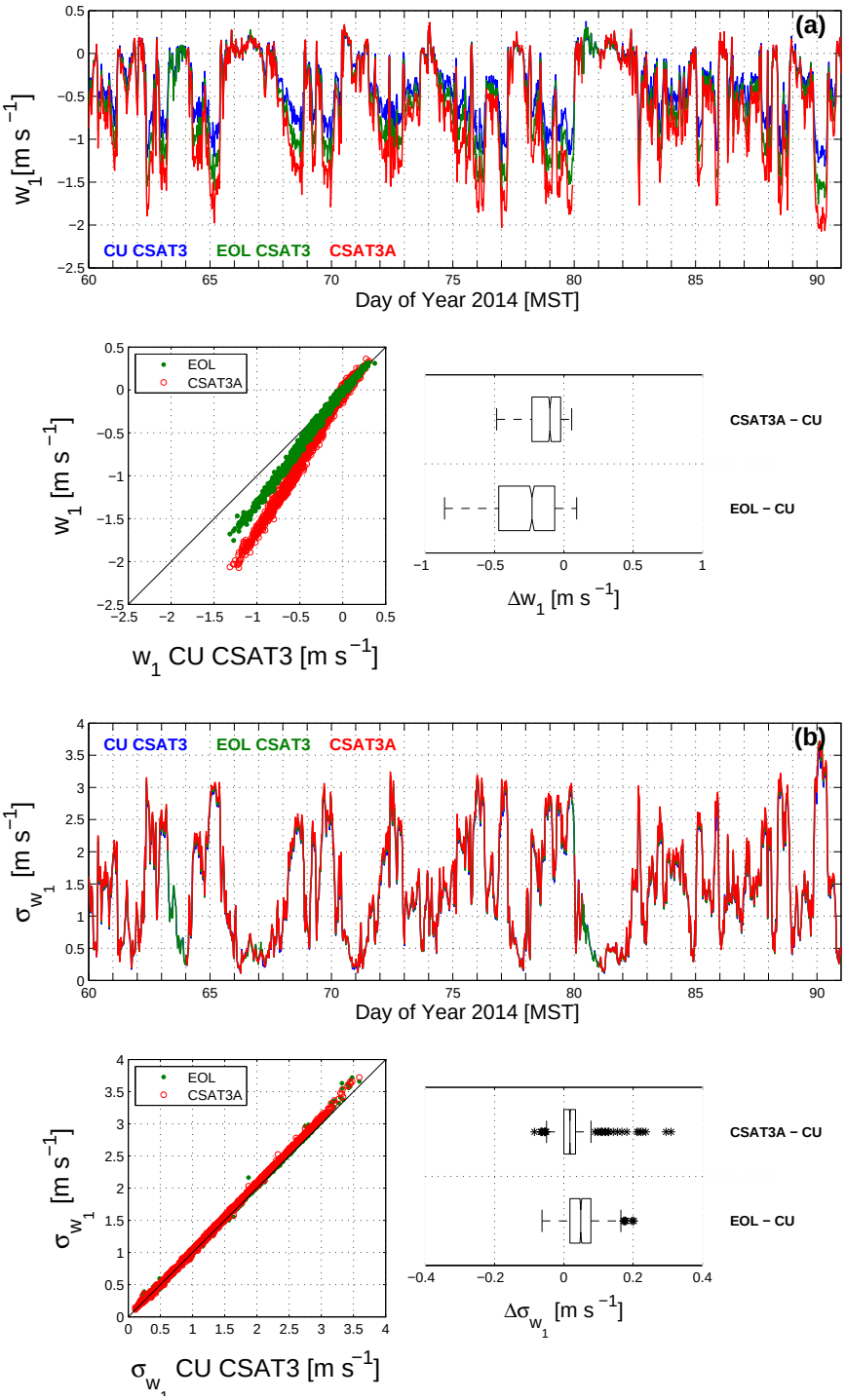

Figure 3.10: Time series, scatter plots, and box plots of (a) 30-min mean vertical wind in sonic coordinates w_1, and (b) standard deviation of vertical in sonic coordinates σ_{w_1} from March, 2014. In the scatter plots, the CU CSAT3 is on the abscissa. In the box plots, the differences relative to the CU CSAT3 are shown. The box plot shows the differences in quartiles where the inner box is the middle 50% of the data called the inner quartile range (IQR). In the box plot, outliers are shown as single points.

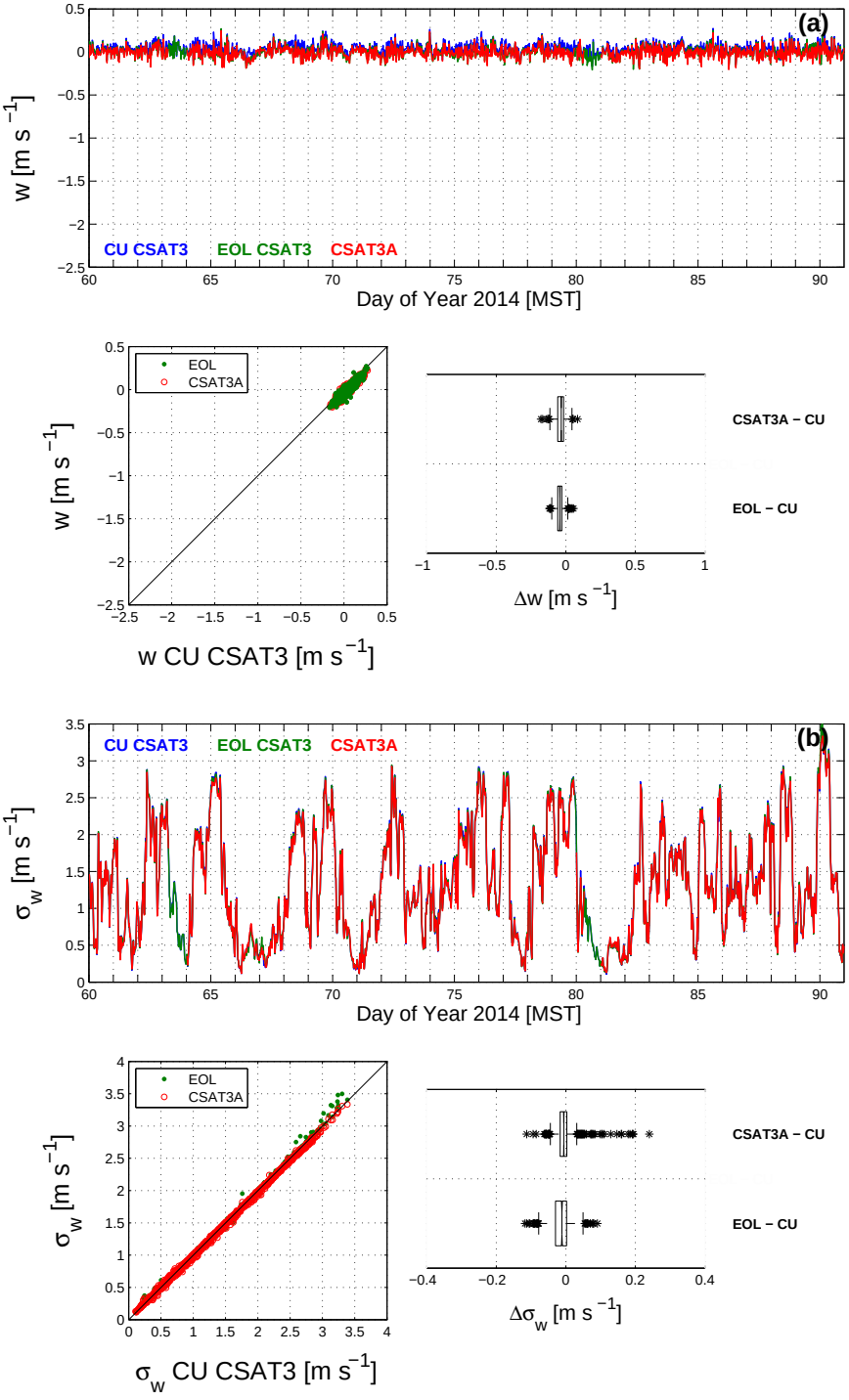

Figure 3.11: As in Fig. 3.10, except the vertical wind is shown in planar coordinates (i.e., w and σ_w).

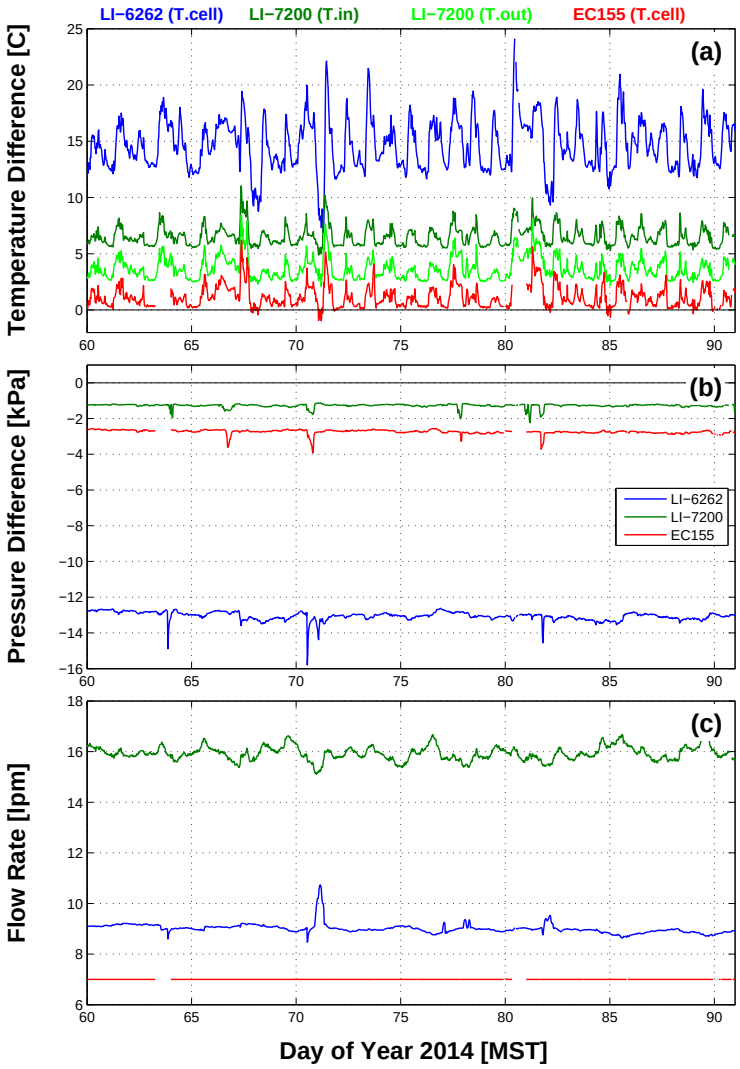

Figure 3.12: Time series of (a) temperature within the instruments relative to air temperature, (b) cell pressure relative to atmospheric pressure, and (c) the flow rate within each IRGA. The legend above (a) shows which temperature sensor is used and the legend in (b) also applies to (c).

whereas the CPEC200 uses a thermocouple embedded in the cell wall and is designed to remove any temperature fluctuations in the air sample so that the WPL temperature term in Eq.3.1 does not affect the flux measurements [Campbell Scientific, 2013b]. Removal of air temperature fluctuations within a sampling tube is a well-known process [e.g., Leuning and Judd, 1996, Rannik et al., 1997, Sahlee and Drennan, 2009]. It has been shown that a tubing length of 1000 times the tubing inner diameter will fully remove effects of temperature fluctuations on F_c though a significant percentage

of the fluctuations are removed by shorter tubes [Rannik et al., 1997, Burba et al., 2010]. Further evaluation of the temperature damping may be possible using the data collected during the IRGA comparison.

To overcome the viscous and turbulent drag resistance in the long tubing and pressure drops due to the two Nupro filters (one at the inlet and one just before entering the LI-6262 sample cell), the LI-6262 required a strong pump which created a pressure drop on the order of 13 kPa to maintain the flow rate at around 9 lpm (Fig. 3.12b, c). The cell pressure deficit and flow rates for the LI-7200 and EC155 were around 1 kPa and 16 lpm, and 3 kPa and 7 lpm, respectively.

3.22.3 Comparison of mean and variance of CO_2 and H_2O from IRGAs

If we examine the time series for CO_2 dry mole fraction, it is obvious that the EC155 χ_c had variations on the order of 15 μmol mol^{-1} that were not observed by any of the other three CO_2 instruments (Fig. 3.13a). Because the LI-6262 span gas dry mole fraction was based on the TGA measurements, these two systems were within 1 μmol mol^{-1} of each other and the IQR of the difference was less than 0.5 μmol mol^{-1} (box plot in Fig. 3.13a). Relative to the LI-6262, the LI-7200 had a bias of about 8.5 μmol mol^{-1}, but the IQR was less than 1 μmol mol^{-1} which suggests this difference was due to a calibration offset, not an error in the instrument gain (Table 3.4).

For the standard deviation of χ_c, the LI-7200 and EC155 both measured slightly smaller values than the LI-6262, however, similar to mean χ_c, there were larger variations in the EC155 – LI-6262 difference (IQR = 0.107 μmol mol^{-1}, Table 3.4) than the LI-7200 – LI-6262 difference which had an IQR of 0.022 μmol mol^{-1} (Fig. 3.13b).

For water vapor, the three IRGAs agreed much better with each other. The LI-7200 mean χ_h was around 0.7 mmol mol^{-1} smaller than the LI-6262, while the EC155 χ_h was about 0.3 mmol mol^{-1} smaller than the LI-6262 (Fig. 3.13c). The IQR of the differences for the instrument pairs were both around 0.16 mmol mol^{-1}. For the standard deviation of χ_h, the LI-7200 and EC155 were also both slightly larger than the LI-6262 and the box plots of the differences were similar (Fig. 3.13d).

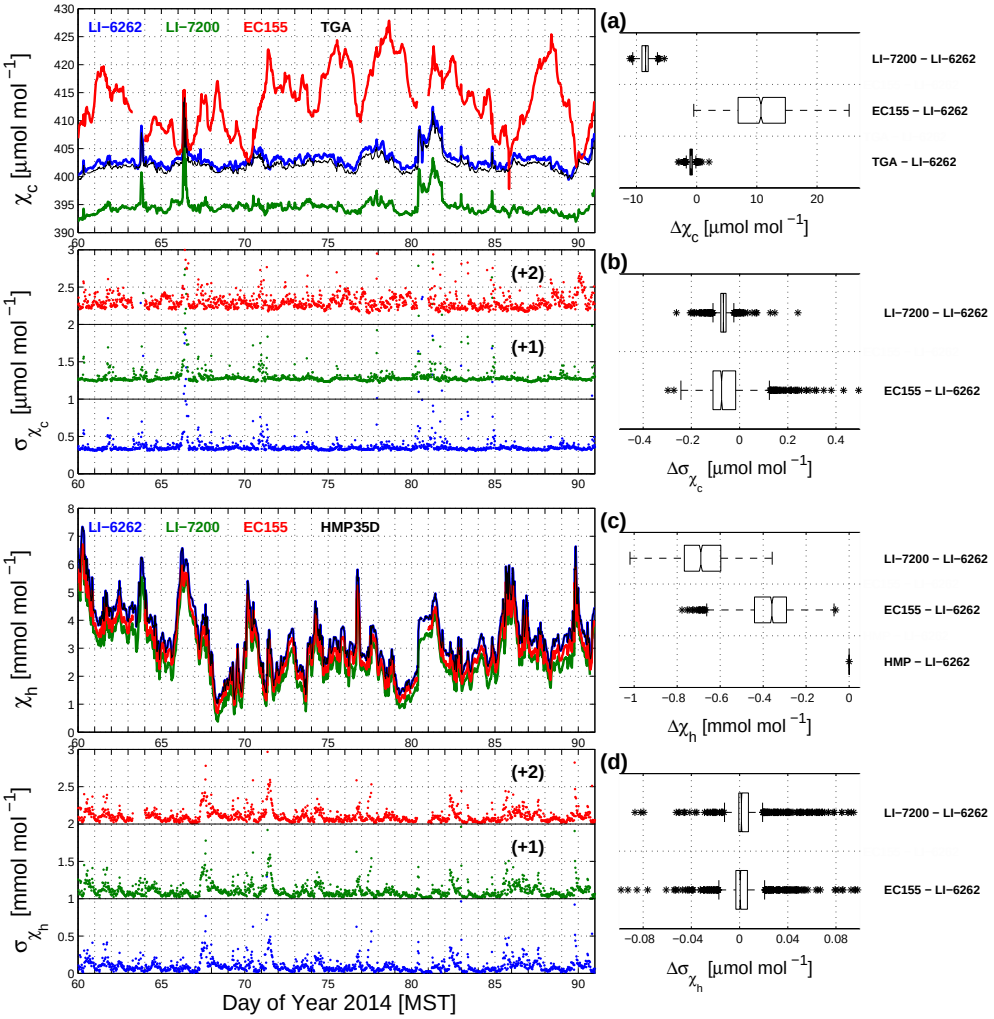

Figure 3.13: Comparison of the 30-min mean and standard deviation (σ) of (upper panels) CO_2 dry mole fraction χ_c and (lower panels) H_2O dry mole fraction χ_h from the LI-6262, LI-7200, and EC155 from March, 2014. Left panels are time series while the right columns are box plots of the differences. For mean χ_c, the University of Utah TGA100A 21.5m χ_c is the black line. For χ_h, the slow-response HMP T/RH χ_h is the black line. The TGA100A and HMP data are used for calibration of the LI-6262 χ_c and χ_h (see text for details).

3.22.4 Calculated time lags

As mentioned in Sect. 3.6, time lags were estimated based on the maximum correlation between the vertical wind and the scalar. Typically the vertical wind precedes the scalar because of the time it takes the air sample to travel from the inlet location to the measurement cell. The lag results for CO_2 and H_2O for each of the three IRGAs are shown in Fig. 3.14 where a negative

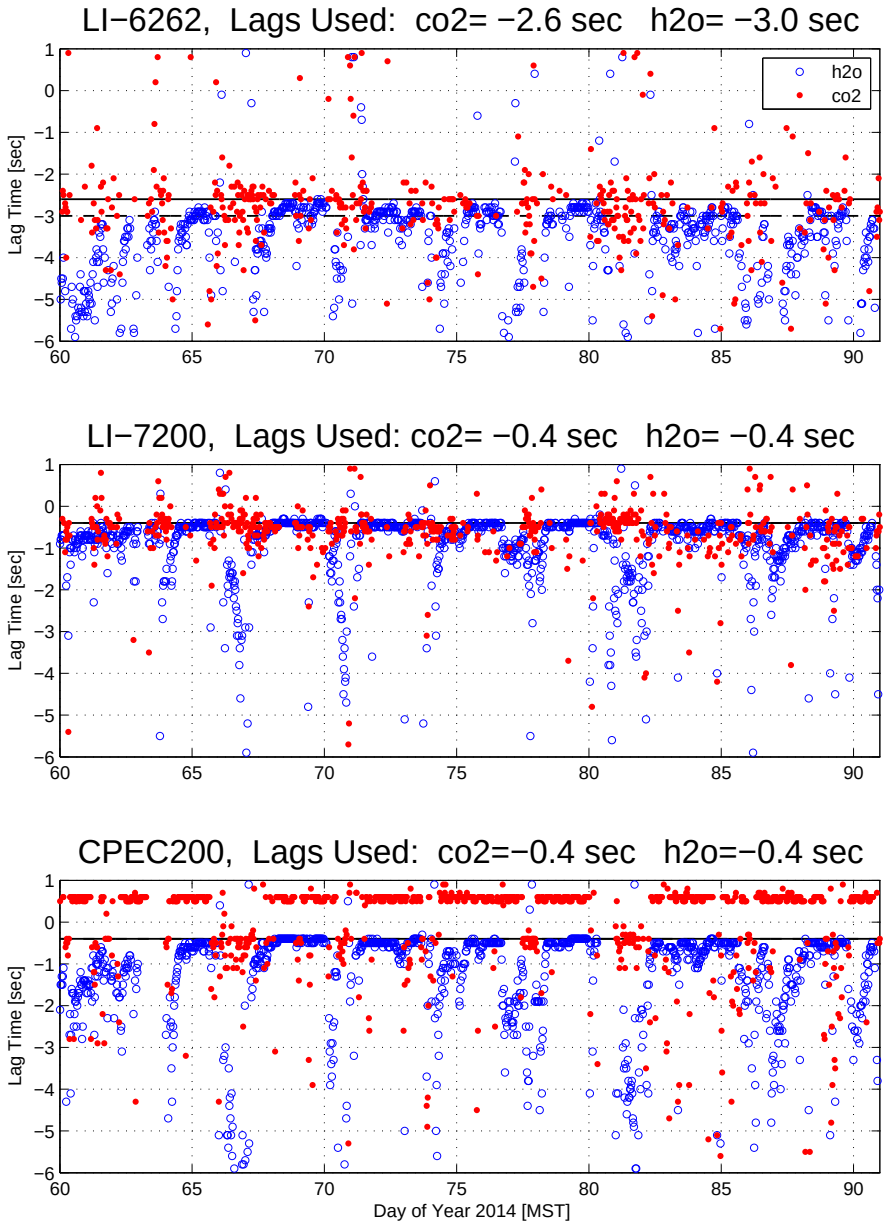

Figure 3.14: Estimated lag times between vertical wind and scalars from the LI-6262/CU CSAT3, LI-7200/EOL CSAT3, and EC155/CSAT3A. Only time periods with a p-value [e.g., Devore, 1987] smaller than 10^{-15} are shown. The text above each panel and horizontal black lines show the lag times used in the flux calculations.

value indicates how many seconds the scalar was behind the vertical wind. Because of the long tubing, the LI-6262 had the largest lags, with an average lag time of 2.6 s for CO_2 and 3.0 s for H_2O. When the humidity was high and/or precipitation occurred there were large changes to the lag for H_2O. For example, precipitation occurred on days 67, 70, and 86 (Fig. 3.9f) and all three IRGAs show that the lag for H_2O increased dramatically on those dates (Fig. 3.14).

We also roughly estimated the flushing time based on the volumetric flow rate and total air volume of the sample cell and tubing (Table 3.3). In general these travel times were about 50–75% shorter than those estimated from the correlation technique. This rough estimate does not take into account that the air travel time depends on several additional items such as: the state of the airflow (turbulent versus laminar), filters, bends and turns in the airstream path, as well as the separation distance between the air inlet and the CSAT3 measurement volume.

One unusual result from the lag calculation was that CO_2 for the EC155 was found to lead the vertical wind (except during periods of precipitation) as shown in the bottom panel of Fig. 3.14. Though the scalar might lead the vertical wind for certain conditions, it is unlikely that this would be a typical state. One would also not expect the lag for CO_2 to be opposite in sign to the H_2O lag. Therefore, for the data processing, the EC155 lag for H_2O was used for CO_2 as shown in Fig. 3.14. Future analysis should take into account the effect of humidity on the scalar lag times.

3.22.5 Comparison of calculated fluxes

The CO_2 flux measured by the LI-6262 in March was around 0.5 μmol m^{-2} s^{-1} with very little diurnal changes which is indicative of the ecosystem respiring CO_2. This is the expected winter state for this subalpine forest since the trees are dormant, but the microbes in the soil (under the snow) are continuing to live and generate CO_2, which gets released into the atmosphere. The LI-7200 produced very similar results for F_c and the mean difference relative to the LI-6262 was only -0.04 ± 0.32 μmol m^{-2} s^{-1} with an IQR of 0.62 μmol m^{-2} s^{-1} (Table 3.4). Though the IQR was on the order of the mean F_c it should be noted that the box plot of the LI-7200 – LI-6262 difference is centered on zero indicating little bias between these instruments (Fig. 3.15a). In contrast, the

Table 3.4: Summary of the IRGA comparison from March, 2014. The 30-min mean and standard deviation (σ) are both compared. The second and third columns are the mean and standard deviation of the LI-6262 measurements. The comparison results are presented as a mean ± the standard deviations of the difference relative to the LI-6262. Where appropriate, the inner quartile range (IQR) of the difference is shown in parentheses below the other statistics (see text for discussion of the IQR).

Variable (units)	LI-6262 Value		LI-7200−LI-6262		EC155−LI-6262	
	Mean	σ	Mean	σ	Mean	σ
χ_c [μmol mol^{-1}]	403.13 ±1.76	0.41 ± 1.46	−8.54 ± 0.81 (1.04)	−0.07 ± 0.06 (0.022)	10.87 ± 5.54 (7.87)	−0.04 ± 0.31 (0.107)
χ_h [mmol mol^{-1}]	3.40 ± 1.15	0.10 ± 0.10	−0.69 ± 0.12 (0.17)	0.005 ± 0.038 (0.014)	−0.37 ± 0.12 (0.16)	0.003 ± 0.035 (0.021)
F_c [μmol m^{-2} s^{-1}]	0.53 ± 0.39	N.A.	−0.04 ± 0.32 (0.62)	N.A.	−0.93 ± 1.06 (1.36)	N.A.
λE [W m^{-2}]	24.08 ± 31.68	N.A.	6.11 ± 16.59 (28.12)	N.A.	4.17 ± 13.56 (20.47)	N.A.

EC155 F_c had periods of negative F_c that were as large as -5 μmol m^{-2} s^{-1}, and the IRQ of the F_c difference relative to the LI-6262 was 1.36 μmol m^{-2} s^{-1}. The negative CO_2 flux values suggest that the forest ecosystem is absorbing CO_2 which is typically achieved by photosynthesis and is not ecologically likely for a subalpine forest in mid-winter.

Latent heat flux was more episodic and all three IRGAs showed a similar trend (Fig. 3.15b). The mean λE from the LI-7200 and EC155 were both slightly larger than the LI-6262 (by 6 W m^{-2} for the LI-7200 and 4 W m^{-2} for the EC155) and there was fairly large variability in the differences (IQR for the LI-7200 – LI-6262 difference was 28.1 W m^{-2} while the EC155 – LI-6262 difference was 20.4 W m^{-2}, Table 3.4).

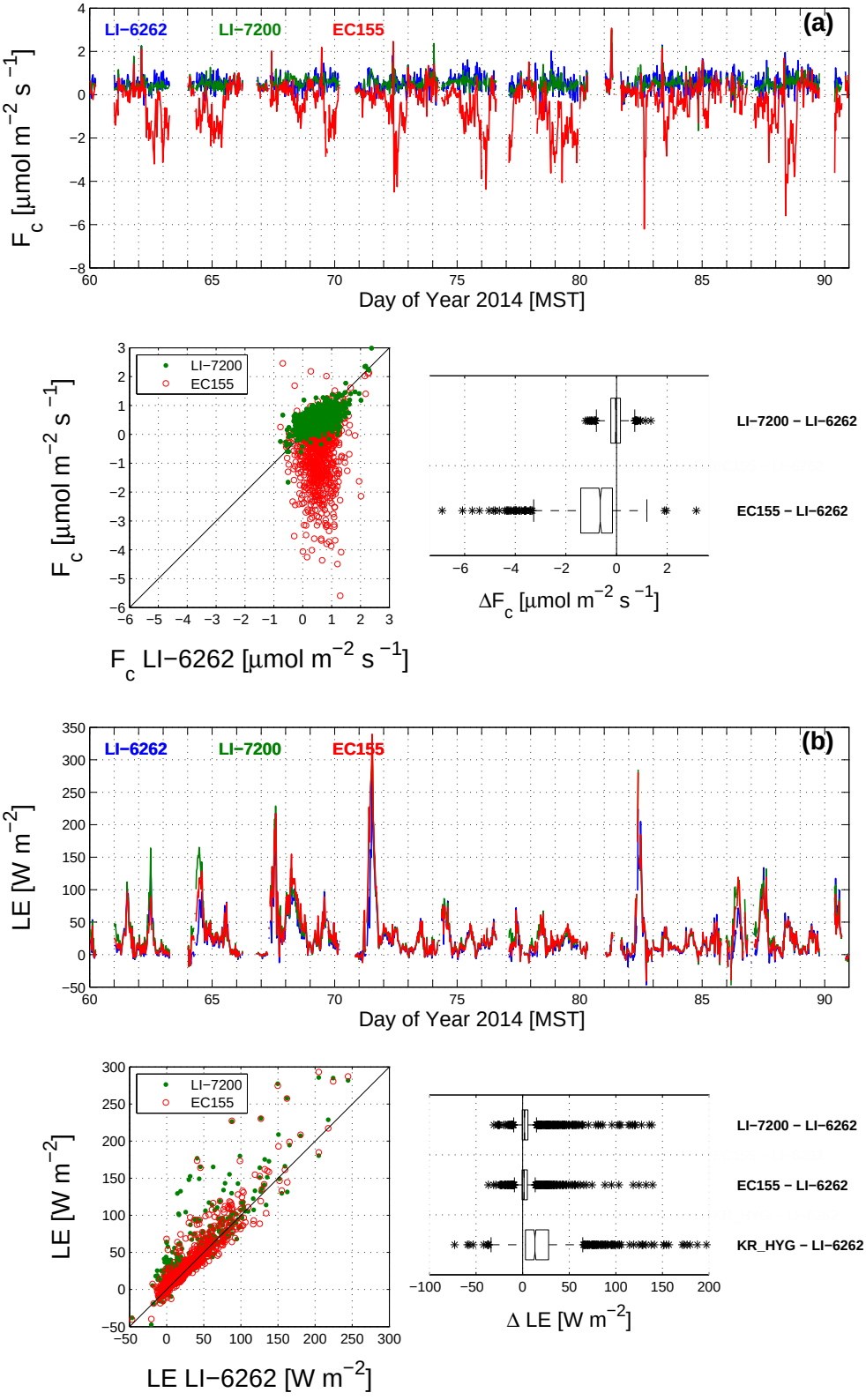

Figure 3.15: Time series, scatter plots, and box plots of the fluxes of (a) CO_2 F_c and (b) latent heat flux (λE) for the month of March, 2014. In the scatter plots, the fluxes from the LI-6262 is on the abscissa. In the box plots the differences relative to the LI-6262 fluxes are shown. In (b), the box plot includes the λE difference between the krypton hygrometer and LI-6262.

3.22.6 Comparison of spectra and ogives

Another way to examine the scalars and fluxes is to look at how the variance and flux change in the frequency domain. To achieve this, we created composite spectra and ogives [e.g., Friehe et al., 1991, Sievers et al., 2015] where the data were selected based on daytime (Fig. 3.16) and nighttime (Fig. 3.17) periods. Because there are not large diurnal changes in F_c or λE during March, the results from the daytime and nighttime are similar, though stable, nocturnal conditions are typically more challenging for eddy-covariance instrumentation due to the smaller flux and variance magnitudes and the non-stationary, intermittent nature of turbulence in stable conditions.

The vertical wind and sonic temperature spectra were similar for the three CSAT3's; however, there was less noise at high frequency in the CSAT3A data, presumably because the EC100 used a bandwidth filter set at 5 Hz. The CO_2 spectra from all three IRGAs shows mostly white noise (i.e., following a f^{+1} rise with increasing frequency) at frequencies larger than about 0.2 Hz [Kaimal and Gaynor, 1991]. The LI-6262 CO_2 spectra also appear to contain extra variance in the frequency range of 0.002 to 0.1 Hz. Presumably, this was due to a combination of a weak CO_2 signal, long tubing, and (possibly) resonance from the rotary-vane pump increasing the variance in the measured CO_2. This extra variance does not appear to significantly affect the fluxes because the LI-6262 and LI-7200 F_c ogives are in good agreement which suggests that the extra LI-6262 CO_2 variance was not coupled with the vertical wind. The EC155 CO_2 spectra exhibit a strange peaked shape between about 0.1 and 1 Hz which appears to have a large effect on the resulting F_c ogives (suggesting that there was some correlation between this odd shape and the vertical wind). The reason for this odd spectral shape for EC155 CO_2 was not known at the time of the comparison, but the CPEC200 system has since been changed and this particular aspect of the EC155 has been fixed.

The specific humidity spectra from the three IRGAs agree well with each other up to a frequency of around 0.1 Hz (Figs. 3.16 and 3.17). At higher frequencies the LI-7200 stands out as having the largest variance/energy and does not start showing an effect of white noise until

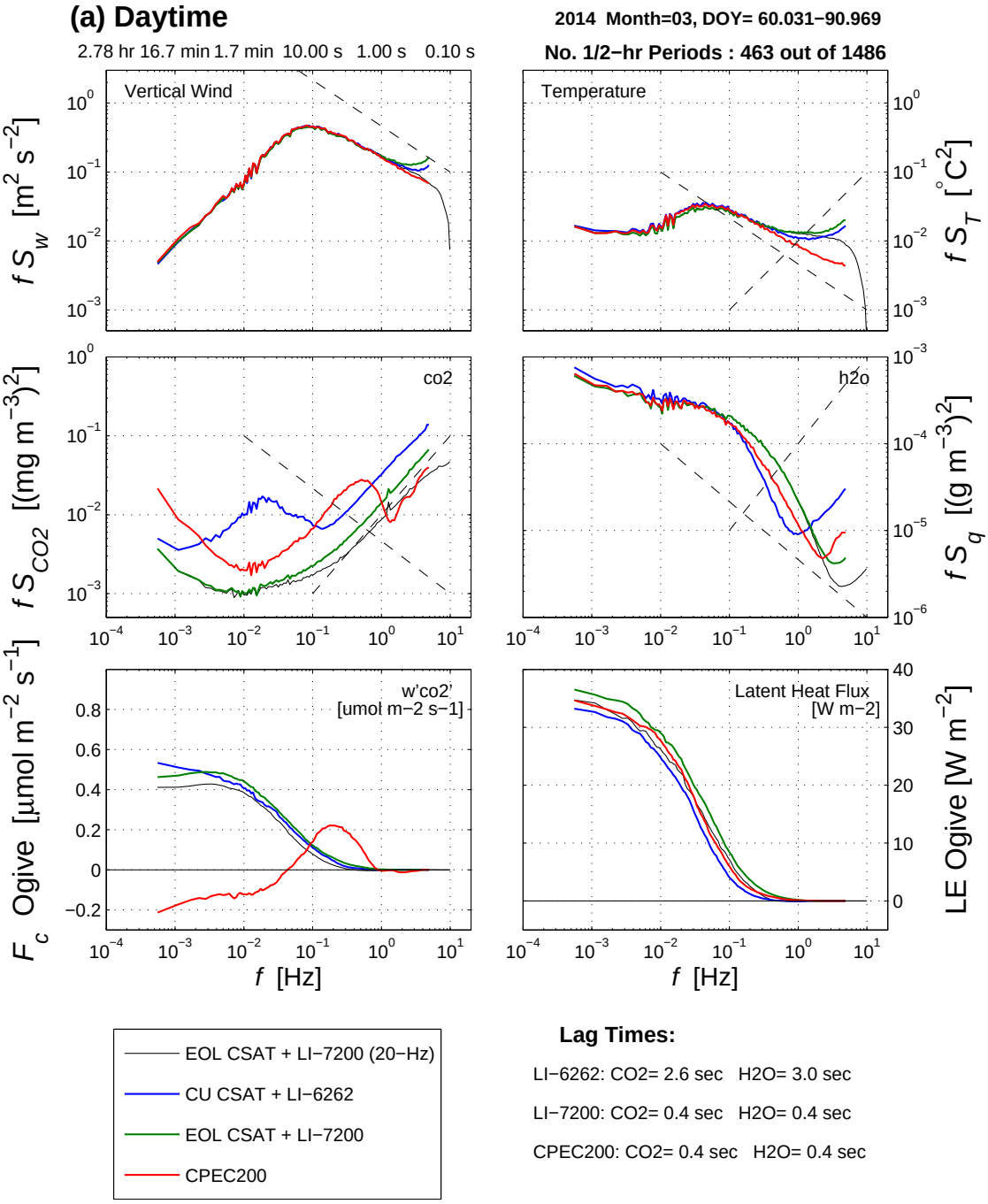

Figure 3.16: Median ensemble values of: vertical wind spectra S_w, sonic temperature spectra S_T, CO_2 spectra S_{CO_2}, specific humidity spectra S_q, and ogives of CO_2 flux F_c, and latent heat flux λE versus frequency f for daytime periods. These are 30-min periods from March, 2014 with the number of periods in the ensemble listed above the S_T panel. The legend and lag times shown apply to all panels. For S_{CO_2}, the CO_2 density ρ_c is used rather than χ_c (the conversion from μmol mol^{-1} to mg m^{-3} uses the molecular weight of CO_2 and the mean molar volume for each 30-min period). The dashed lines show a $f^{-2/3}$ and f^{+1} slope.

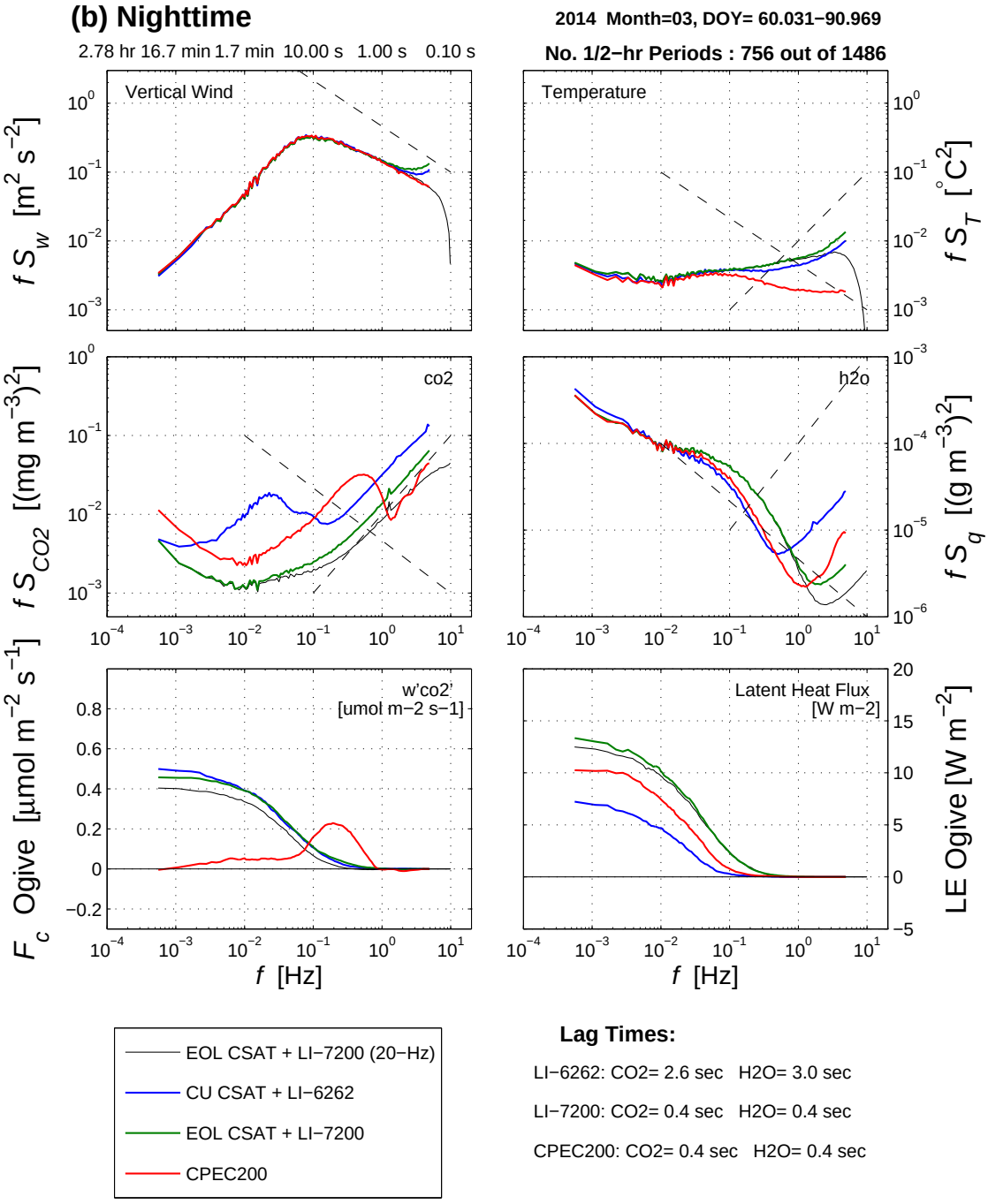

Figure 3.17: As in Fig. 3.16, except for nighttime periods.

$f \approx 2$–3 Hz. In general, the white noise occurs at a slightly lower frequency during the nighttime periods than during the daytime (presumably due to the effects of stability on the atmospheric turbulence). The improved high-frequency response of the LI-7200 is likely due to a combination of: (1) the higher flow rate in the LI-7200, and (2) the heated intake tube which can extend the high-frequency range of an IRGA by several Hz [Metzger et al., 2016]. In contrast, the LI-6262 shows the effects of white noise at $f \approx 0.8$–1 Hz and the EC155 at $f \approx 1$–2 Hz. Consistent with these responses to water vapor, the LI-7200 λE ogives have the largest flux, followed by the EC155 and the LI-6262. If we revisit the overall comparison of λE (i.e., Sect. 3.22.5, Table 3.4), the LI-7200 – LI-6262 mean λE difference was around 6 W m^{-2} whereas the EC155 – LI-6262 λE difference was around 4 W m^{-2}. Note that in March the average λE is on the order of 25 W m^{-2} so these mean differences are a significant percentage of the typical λE. Furthermore, the composite ogives shown in Figs. 3.16 and 3.17 suggest that these high-frequency differences in response led to the significant differences in the resulting λE flux.

3.23 Conclusions from the IRGA comparison

One of the surprising results from our comparison is that F_c from the EC155 measured large negative fluxes during the month of March (Fig. 3.15a). In order to examine the reason for this behavior, we have plotted F_c for each IRGA versus the environmental variables of wind speed, air temperature, and relative humidity in Fig. 3.18. This plot reveals that the negative EC155 F_c were related to periods with high wind speeds. If we also examine the mean CO_2 in a similar way, and find that χ_c was not affected by wind speed in the same way (Fig. 3.19). In fact, none of these environmental variables could explain why χ_c displayed variations on the order of 15 μmol mol^{-1}. This comparison helped to reveal some issues with the EC155/CPEC200 hardware and software that Campbell Scientific has since corrected. Therefore, this result from our comparison is somewhat obsolete; however, the methodology and strategy for making the comparison are still valid and worthy of future consideration for others planning similar types of comparisons.

Considering the data problems with the EC155 CO_2, we were unable to fully examine the

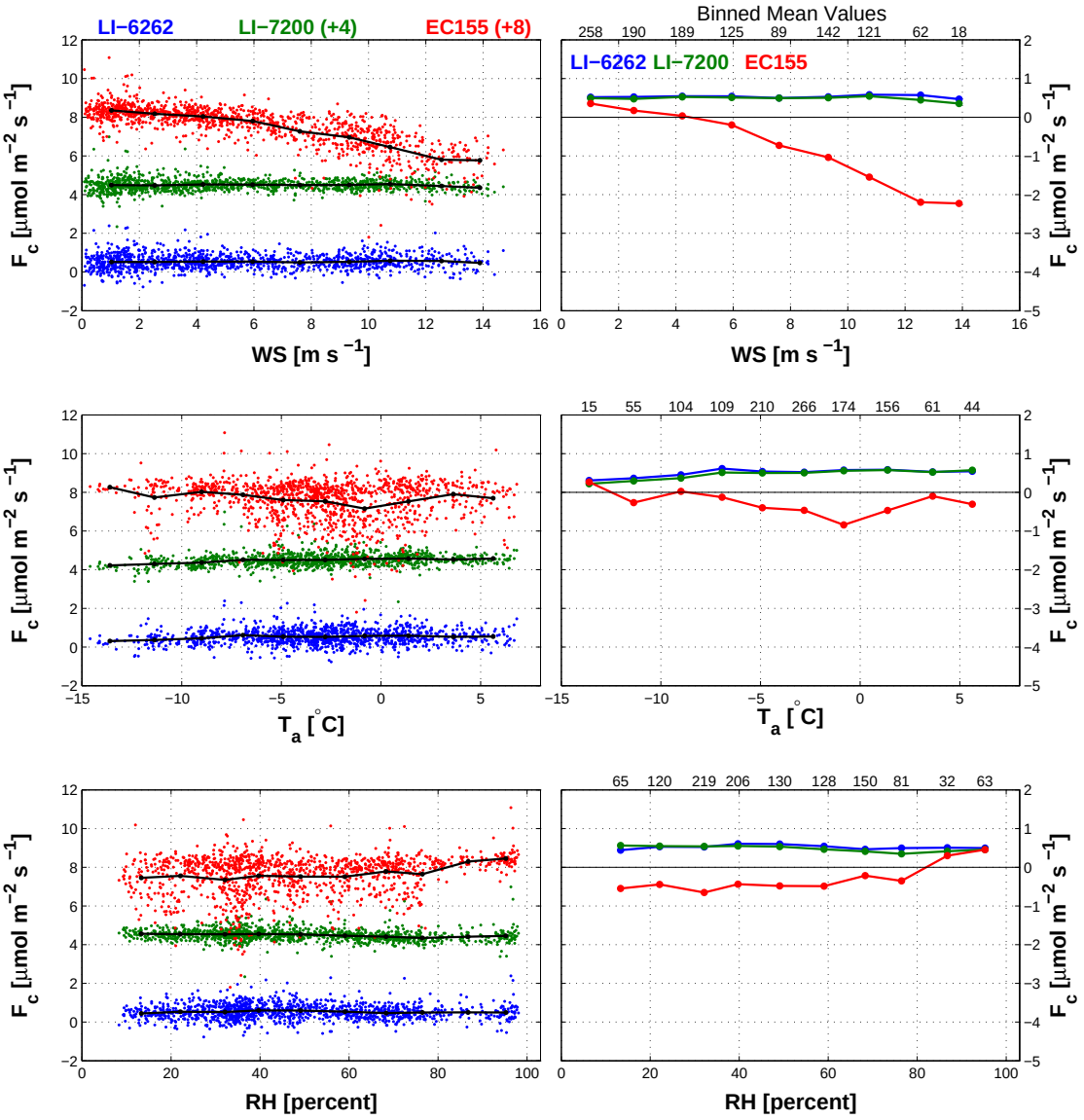

Figure 3.18: Turbulent vertical CO_2 fluxes F_c measured by the LI-6262, LI-7200, and EC155 versus the environmental variables of (top) wind speed WS, (middle) air temperature T_a, and (bottom) relative humidity RH. The left-hand panels show the 30-min values and the black line is the mean binned values. The data from the LI-7200 and EC155 are offset according to the text above the upper panel. The right-hand panel shows the mean binned values for each IRGA without any offset.

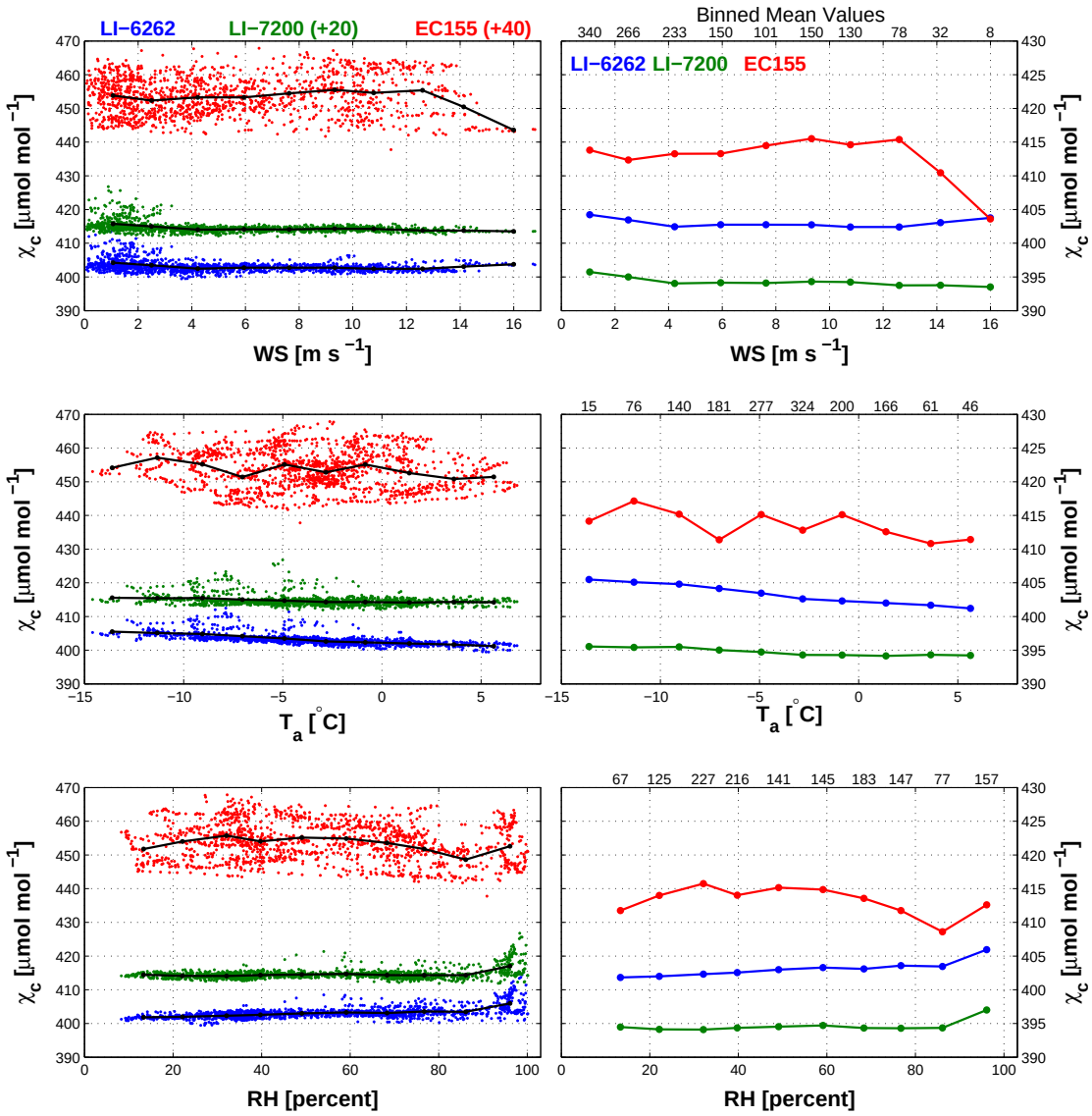

Figure 3.19: As in Fig. 3.18, except for CO_2 dry mole fraction χ_c.

differences in F_c between these two systems. Furthermore, the scale of the above-canopy turbulent transport of the scalars at nearly twice canopy height might make it difficult to detect any high-frequency differences in the IRGAs. Such testing may be better suited in a region of higher turbulence such as a forest canopy or closer to the ground. Our main findings from the IRGA comparison are as follows:

- After applying the planar-fit, the statistics and vertical wind spectra from three side-by-side CSAT3's were fairly similar.

- Compared to the LI-6262, the LI-7200 had a 8.5 μmol mol^{-1} (2%) offset in mean CO_2, but F_c was similar. Spectral analysis revealed extra variance in the LI-6262 CO_2 in the frequency range of 0.002 to 0.1 Hz; however, ogive analysis of F_c showed little to no impact on the CO_2 flux.
- The EC155 measured large, unexplainable, variations in χ_c on the order of 15 μmol mol^{-1} (4%) that were not observed by any of the other CO_2 instruments. F_c and σ_{χ_c} from the EC155 exhibited an apparent wind speed dependence that resulted in unrealistic ecosystem fluxes of CO_2 in high winds.
- The estimated lag between the EC155 CO_2 and vertical wind resulted in the EC155 CO_2 fluctuations preceding those of the vertical wind. This is physically unlikely to occur on a regular basis. In contrast, the EC155 H_2O estimated time lags appeared reasonable.
- Based on water vapor spectra, the noise floor for H_2O during daytime was 3 Hz for the LI-7200, 2 Hz for the EC155, and 0.9 Hz for the LI-6262. The noise floor for the LI-7200 water vapor was improved by heating the incoming air [e.g., Metzger et al., 2016] which also appears to result in a higher latent heat flux. The noise floor for CO_2 spectra were less distinct.
- Consistent with the water vapor frequency response from each IRGA, the latent heat fluxes from the LI-6262 were smaller than the LI-7200 by around 6 W m^{-2} and smaller than the EC155 by around 4 W m^{-2}. The ogives of λE suggest that these differences were due to differences in frequency response of each system, especially the long tubing used by the LI-6262.

In order to complete the comparison, the humidity-dependence in the lag-time calculations as well as the decoupling of CO_2 and H_2O within the inlet tubing needs to be considered. Also, a more careful comparison to the open-path LI-7500 and KH2O sensor might provide additional insights not included here. Future possible analyses include: spectral coherence/phase differences between the sensors, closer examination of possible temperature fluctuations within the sample cell, and assessing the importance of using the lower-resolution analog CSAT3 winds ingested by

the LI-7550 on the calculated fluxes. Finally, contrasting the cold-season IRGA comparison results presented here with those from the growing season will provide a more complete evaluation of the three IRGA sensors.

3.24 Conclusions

Within this chapter, the measurements on the tower have been documented. Each measured variable was given a subsection with the hope that relevant information can be quickly and easily found within the chapter. The information provided attempts to include how instrumentation has changed over time (which requires good record-keeping and close attention to documentation details). In this regard, this chapter is only a first step in that direction, and more work is needed before a manuscript on instrumentation record, QA/QC, and gap-filling procedures is ready for submission. It should also be noted that there are many additional measurements that have occurred near the site (over the years), which were not included here (some of these are listed at the end of Chapter 4). Our focus here has been on the primary/base measurements at US-NR1 site which are used in the site description (Chapter 4) and precipitation-based analysis of the fluxes and scalars (Chapters 5 and 6).

Chapter 4

Niwot Ridge Subalpine Forest US-NR1 AmeriFlux site characteristics

Abstract

In this chapter we provide a description of the US-NR1 AmeriFlux site characteristics (location, topography, geology, forest characteristics, and climate). Within this chapter, we emphasize the forest structure based on two different measurement techniques (ground-based and airborne lidar, as described in the previous chapter).

4.1 Introduction

In order to properly model the exchange of carbon, heat, and water vapor between the underlying surface and the atmosphere, an intimate knowledge of the surface and soil characteristics is needed [e.g., Oleson et al., 2008, Koster et al., 2009]. In forested regions, canopy density, canopy gaps or clearings, and variations in topography all play an important role in controlling the air flow and near-ground turbulence which, in turn, affects the exchange of air and scalars between the atmosphere and land-surface [e.g., Katul et al., 2006, Sun et al., 2007, Belcher et al., 2008, Finnigan, 2008, Harman and Finnigan, 2008, Burns et al., 2011, Dupont et al., 2012, Grant et al., 2015]. This means that knowledge of the fine-scale surface properties are important, and in this chapter, we use lidar data to show how the forest properties change near the US-NR1 tower as well as a comparison between the lidar-based measurements and traditional ground-based approaches.

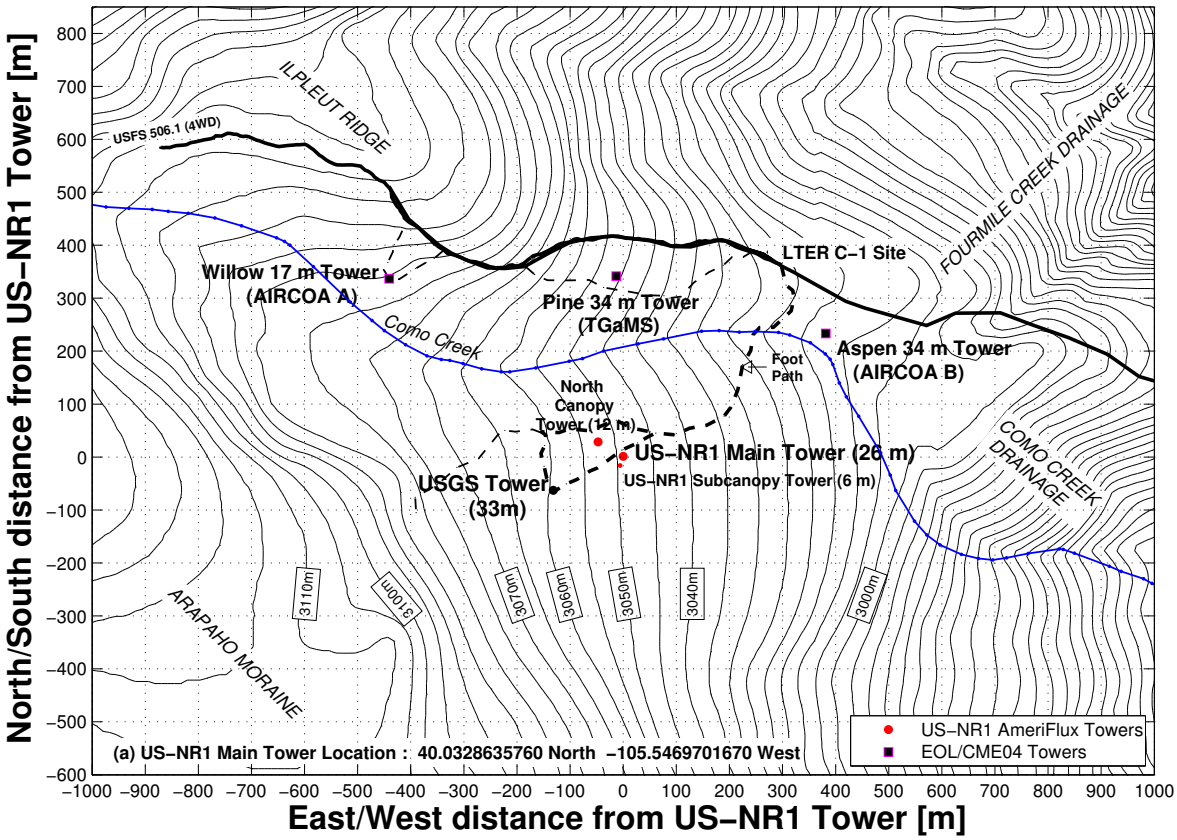

Figure 4.1: A map of the US-NR1 site showing the local topography and the US-NR1 towers that surround the 26-m US-NR1 AmeriFlux main tower. Elevation contours at 5 m intervals are from the U.S. Geologic Survey 7.5-min DEM. The 6-m subcanopy tower is just to the southwest of the main tower, while the north canopy tower is northwest of the main tower. Three towers (Willow, Pine, and Aspen) deployed by NCAR EOL during the 2004 Carbon in the Mountains Experiment (CME04) are just north of Como Creek are shown; as well as the USGS tower and the LTER C-1 site. The thick black line that passes by LTER C-1 is Niwot Ridge Road (USFS Road 506.1).

4.2 Site setting and topography

The US-NR1 site is located on the gently sloping eastern side of Arapaho moraine, within the drainage basin of Como Creek (Figs. 2.1, 4.1, and 4.2). In earlier times, Arapaho moraine was known as Albion moraine [Ives, 1953]. Following snowmelt in early to mid-June, the flow in Como Creek can increase to as much as $500\,\mathrm{L\,s^{-1}}$, and the snowmelt-enhanced flows typically last until mid-July, after which time the flow drops to below $50\,\mathrm{L\,s^{-1}}$ [e.g., Knowles et al., 2015b]. In late summer, Como Creek ranges anywhere from 1 to 3 m wide. It feeds into North Boulder Creek

Figure 4.2: Photograph taken on 14 September 2004 of (from left-to-right) the US-NR1 AmeriFlux tower, Aspen tower, and Pine tower during the Carbon in the Mountains Experiment (CME04). The photo was taken about 2 km east and slightly north of the US-NR1 site. The forested ridgeline that goes from left-to-right across the photo is the crest of Arapaho moraine. The Fourmile Creek drainage/canyon runs from the middle of the photo to the lower-right corner, and the peaks in the background are Caribou Peak and Old Baldy which form the southern boundary of Silver Lake Valley and are east of North and South Arapaho peaks.

which eventually runs down Boulder Canyon and out onto the plains. The geographic features that form the headwaters of Como Creek drainage are Arapaho Moraine to the south and west, and Ilpleut Ridge to the north, which separates the hydrologic drainage of Como Creek from Fourmile Creek. Como Creek drains a small area (3–4 km^2) northwest of the US-NR1 site [Knowles et al., 2015b]. The section of Como Creek just south of Ilpleut Ridge contains a large wet meadow, which are common in the subalpine [Douglass, 1954, Johnson, 1987] and shows up in aerial photos as a light-colored patch surrounded by a green forest (e.g., Fig. 2.1). This wet, treeless meadow was the location of the Willow tower during CME04 (Fig. 4.1). The main US-NR1 tower is in a

fairly gently-sloped location, with a topographic slope angle of around 4.3° within 100 m of the US-NR1 tower (Fig. 4.1). Terrain within 5 km of the site (in all directions), however, can be quite steep as shown in Fig. 4.2 (also see Fig. 2.4 which shows the topography between US-NR1 and the Continental Divide, which is about 10 km west and 700 m higher than US-NR1).

4.3 Geology and soil characteristics

During the Upper Pleistocene, glacial advances from headwall cirques located near North and South Arapaho Peaks formed what is now known as the Silver Lake Valley [Ives, 1951, 1953]. Two distinct glacial periods helped form Arapaho moraine (where the US-NR1 site is located). The oldest was the Bull Lake glaciation period which began about 200,000 years ago and lasted for 70,000 years. This was followed by the Pinedale glaciation period, which was the last glacial period to occur in this area and ended about 10,000 years ago. These are the local names of glacial periods, specific to the Rocky Mountain region. These glaciers originated at the upper end of the Silver Lake valley near the Continental Divide and came down to an elevation of around 2450 m (Arapaho and Henderson glaciers just below the Arapaho peaks are the remnants of these ancient glaciers). As shown in Fig. 4.3a, the east side of Arapaho moraine is composed of glacial till from the Bull Lake glaciation, while the west side of the moraine is from the (younger) Pinedale glaciation. The west side of Arapaho moraine contains several permanent kettle ponds, whose ecology has been studied over a full year [Ellsworth, 1983]. The glacial drift and moraines formed by the Bull Lake glaciation are more weathered, and have more well-developed, deeper soils (typically 1-2 m) than moraines of the Pinedale age [Madole, 1969]. The glacial drift material of these moraines are composed of granites, gneisses, schists, felsite, and diorites [Douglass, 1954]. Igneous and metamorphic rock form bedrock [Marr, 1961]. In 2011, a groundwater well drilled near Como Creek and C-1 found that the bedrock (underneath the morainal material) was at a depth of around 28 m [Dailey, 2016]. From measurements of soil moisture at C-1 down to 2 m depth (Fig. 4.4), it was found that, most years, the water table rose to the level of the bottom of the soil moisture probe during snowmelt (e.g., 2005), but some years it did not (e.g., 2006).

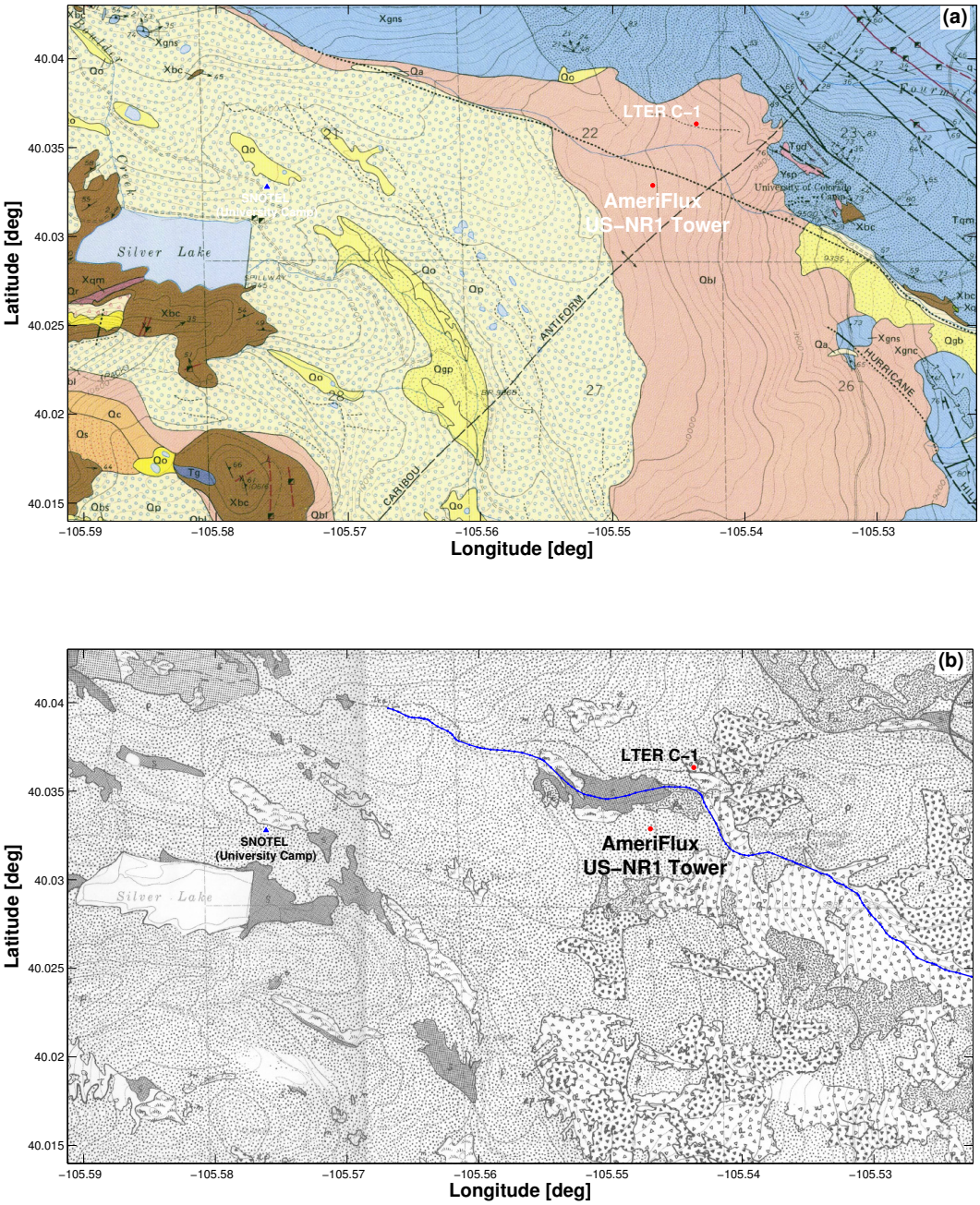

Figure 4.3: Maps of the area near the US-NR1 AmeriFlux site showing the **(a)** geological features (from Gable and Madole [1976]) and **(b)** vegetation (from Gable [1978]). In **(a)**, the east side of Arapaho moraine (where the US-NR1 main tower is located) is in region "Qbl" which is described by Gable and Madole [1976] as: "Till of Bull Lake Age (Upper Pleistocene)—Subangular to subrounded boulders, cobbles, and pebbles set in a silty sand matrix." The west side of Arapaho moraine is in region "Qp" which is till of the Pinedale Age. In **(b)**, the dotted region that contains the US-NR1 tower is simply labeled as "Forest". Along Como Creek, the darker regions (just North of the US-NR1 tower) are "Scrub" and "Meadow" while further downstream the white regions with triangles are labeled "Aspen".

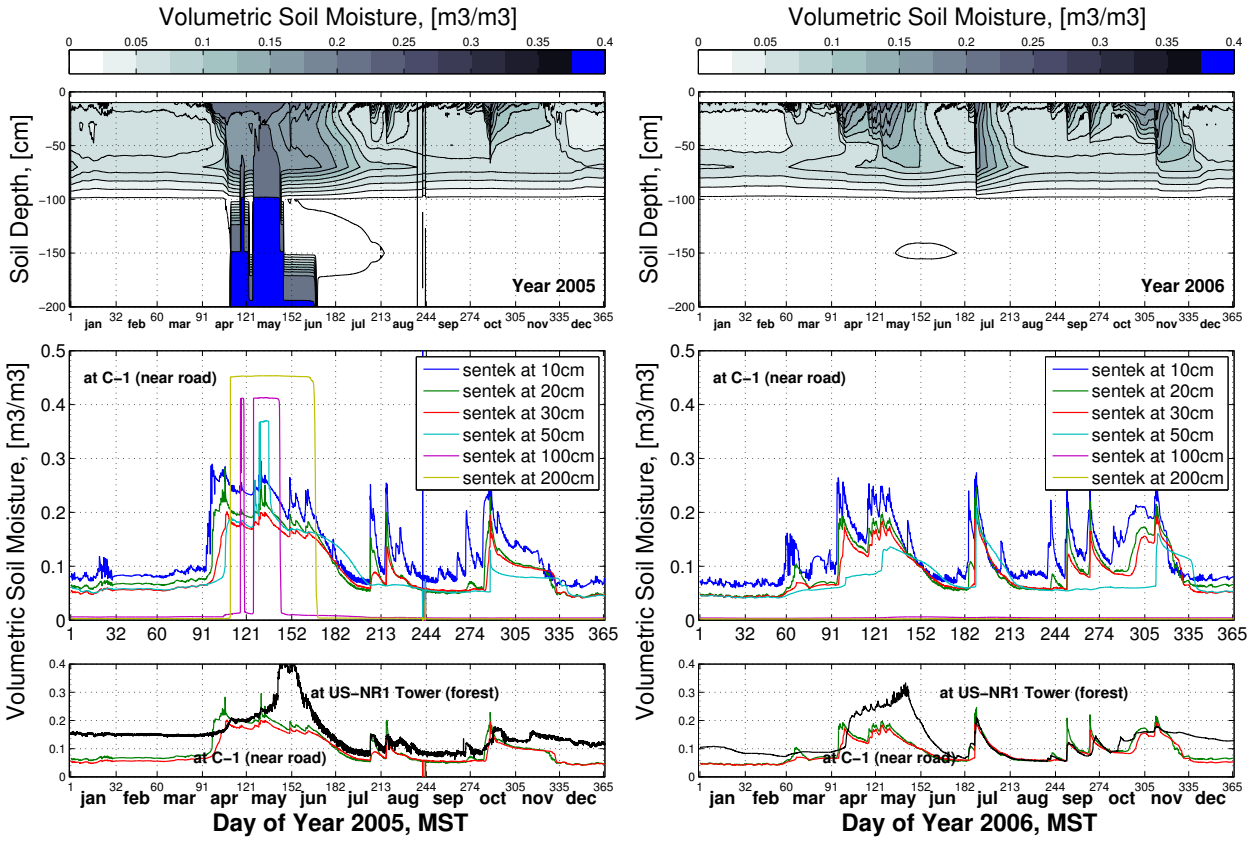

Figure 4.4: Soil moisture at LTER C-1 to a depth of 2 m from a Campbell Scientific Sentek EnviroSMART soil water content probe from years **(left)** 2005 and **(right)** 2006. The upper panels show a depth/time contours of the volumetric soil water content for each year, the middle panels show the water content time series from each level (as described in the legend), and the lowest panels compare the soil moisture at C-1 with the US-NR1 forest.

Soils in the subalpine forest region are highly variable, mostly due to the presence of wetland areas (discussed above). However, in dry locations, there are typically podzolic soils (i.e., formed under coniferous forests) which are composed of 60–70% sand (classified as either a sandy loam or loamy sand). On top of the mineral soil, is a shallow layer ($\approx$10 cm) of organic material [Douglass, 1954, Marr, 1961, Madole, 1969, Gable and Madole, 1976, Scott-Denton et al., 2003]. Around 2011, Nicole Trahan and Ben Braydon from CU collected soil samples somewhere between the US-NR1 tower and Como Creek and had them analyzed by the Colorado State University Soil, Water and Plant Testing Laboratory in Fort Collins. The report from this soil analysis is included in Appendix C. In the distant past (mid-Holocene), wind-transported particles might have added

trace elements (Ca, Mg, K, N) to subalpine soils near Niwot Ridge [Muhs and Benedict, 2006].

In order to estimate the soil heat (or storage) term for the surface energy budget, several assumptions about the US-NR1 site soil properties were made. These assumptions and calculations are described in Sect. 5.4.9, and interested readers can find more details there.

4.4 Forest characteristics

In Boulder County, subalpine forests typically lie between 2750 and 3500 m elevation [Young, 1907, Marr, 1961, Peet, 1981]. Subalpine forests in Colorado have been affected by disturbances from fire, insects, and logging [Alexander, 1987, Veblen et al., 1991, 1994]. These forests are subject to infrequent, intense, stand-replacing fires that occur under natural conditions (often lightning-related) which are correlated with periods of extended low atmospheric humidity [Schoennagel et al., 2004]. While fires can be widespread, they also might affect one portion of the forest, leaving other areas intact [Buechling and Baker, 2004, Sibold and Veblen, 2006].

As described in Sect. 2.2, the forest near the US-NR1 tower experienced light/selective logging in the early 1900s, with some clear-cutting done within 1–2 km of the main tower (mostly to the east and south of the tower). The US-NR1 forest is composed mostly of: subalpine fir (*Abies lasiocarpa* var. *bifolia*), lodgepole pine (*Pinus contorta*), Englemann spruce (*Picea engelmannii*), quaking aspen (*Populus tremuloides*), and limber pine (*Pinus flexilis*). Strong winter winds often snap trees or blow them over. The tree density near the US-NR1 main tower is around 4000 trees ha^{-1} (0.4 trees m^{-2}) with a leaf area index (LAI) of 3.8–4.2 $\mathrm{m}^2\mathrm{m}^{-2}$ and canopy height ranging between 12–13 m [Turnipseed et al., 2002, Monson et al., 2010]. Near the US-NR1 main tower, the maximum leaf density occurs at $z \approx 9$ m [Yi et al., 2005, Moore et al., 2008, Monson et al., 2010] (more about this in Sect. 4.4.1, below). The site sits at an ecotone with a higher concentration of spruce/fir trees west of the tower and more lodgepole pine trees east of the tower. Fir and spruce are generally slow-growing trees which take about 100 years to increase by ≈ 4 m in height [Shea, 1985], though this growth rate depends on the age of the trees [Ryan and Yoder, 1997] as well as the local micro-environment (slope aspect, soil moisture). Throughout the summer, the US-NR1 trees continue to

access snowmelt water which helps sustain them during dry periods [Hu et al., 2010a]. However, there are also indications that moisture stress caused by warmer and drier summers since 2008 has lead to more tree die-off in subalpine forests [Smith et al., 2015]. And, long periods of warm, dry weather are when subalpine forests have experienced increased forest fire activity in the past [Sherriff et al., 2001, Buechling and Baker, 2004].

There are several long-term plots started in the 1980s which monitor tree growth and health within a few km of the US-NR1 site [Veblen, 1986, Villalba et al., 1994, Smith et al., 2015]. The closest of these sites are about 700–1000 m north/northwest of the US-NR1 tower (Fig. 4.1). Kienast and Schweingruber [1986] describe the dendrochronological techniques used for dating subalpine trees, and performed tree-ring analysis on limber and lodgepole pine trees near Hill's Mill. Based on these tree-ring analyses, the range of ages from these nearby stands date from 1895 (for the 120 year-old lodgepole pine stands located on the east side of Ilpleut ridge) to a spruce-fir stand which dates back to 1374 (over 640 years old) [Veblen, 1986, Villalba et al., 1994, Smith et al., 2015]. There was a growth release in the limber pine near Hill's Mill around 1894, indicating that the forest was thinned at that time [Kienast and Schweingruber, 1986]. Douglass [1954] found that the fir and older lodgepole stands on Ilpleut ridge started after a fire that occurred at that location around 1650, while younger lodgepole stands formed after a fire in the late 1890s (this forest is in the same area as the younger forest studied by Smith et al. [2015], and a portion of the forest recovering from that fire is shown in a 1929 photo in Fig. 2.8). Analysis of tree rings just-below Silver Lake suggest that a large fire occurred in that area sometime between 1650–1750, but the forest just-above Silver Lake (in the "3-C" spruce-fir stand) dates back to around 1450 [Johnson, 1956]. Fire typically has a fairly sharp boundary between burned and unburned areas. These previous studies provide a rough idea of the ages of the trees which are near US-NR1 and when major forest fires might have occurred in the area. These tree ages roughly corroborate with recent tree-ring studies by D. J. P. Moore and his colleagues at the University of Arizona (as discussed in Sect. 2.2).

The subalpine forest research directed by J. W. Marr [e.g., Douglass, 1954, Johnson, 1956,

Marr, 1961, Amundsen, 1967] was usually focused on understanding "climax" forest stands within this region. The general conclusion for forests at an elevation of around 3000 m is that lodgepole pine and aspen are successional species that thrive after disturbances (fire, beetles, or logging). The pine trees are eventually replaced by fir and spruce who are better adapted to survive in windy, high-elevation conditions. Spruce tend to live longer, but subalpine fir have a greater abundance of young trees [Veblen, 1986]. The establishment of spruce and fir seedlings have been found to be more successful during cooler, wetter summers with ample soil moisture availability [Andrus et al., 2018]. In dry locations, fir and spruce tend have similar responses to climate—growing better during years when the fall season is cool and wet. However, in wet/mesic locations, fir was found to be more sensitive to variations in temperature and precipitation than spruce, possibly due to physiological differences in fir such as a lower transpiration rate and lower water use efficiency [Villalba et al., 1994, Hu et al., 2010b]. Limber pine are typically found in small numbers and seem adapted to windy locations with coarse, rocky soil. Limber pines reproduce poorly in lodgepole stands because the seedlings do not compete very well with other species, due to their relatively inefficient photosynthetic capacity; in contrast, lodgepole pines grow poorly at dry, windy sites [Douglass, 1954].

4.4.1 Lidar measurements

Airborne lidar is a powerful tool for determining the characteristics of a forest. For the 10 August 2010 lidar flight over the US-NR1 area, in each 0.5 m x 0.5 m-sized area, the number of returns was typically between 5 and 20 (Fig. 4.5). The pattern in the number of returns shown in Fig. 4.5 was related to the land cover type, and we would also expect the attitude and motion of the aircraft to play a role as the laser beam scans from side-to-side.

By taking the difference between the ground elevation surface and the lidar cloud data, the trees and gaps in the forest near the US-NR1 main tower can be observed (Fig. 4.6b). This image is centered on the US-NR1 tower which rises above the trees and was fairly well resolved by the lidar, and the lidar-estimated tower height was approximately correct (25 m). Here, the method

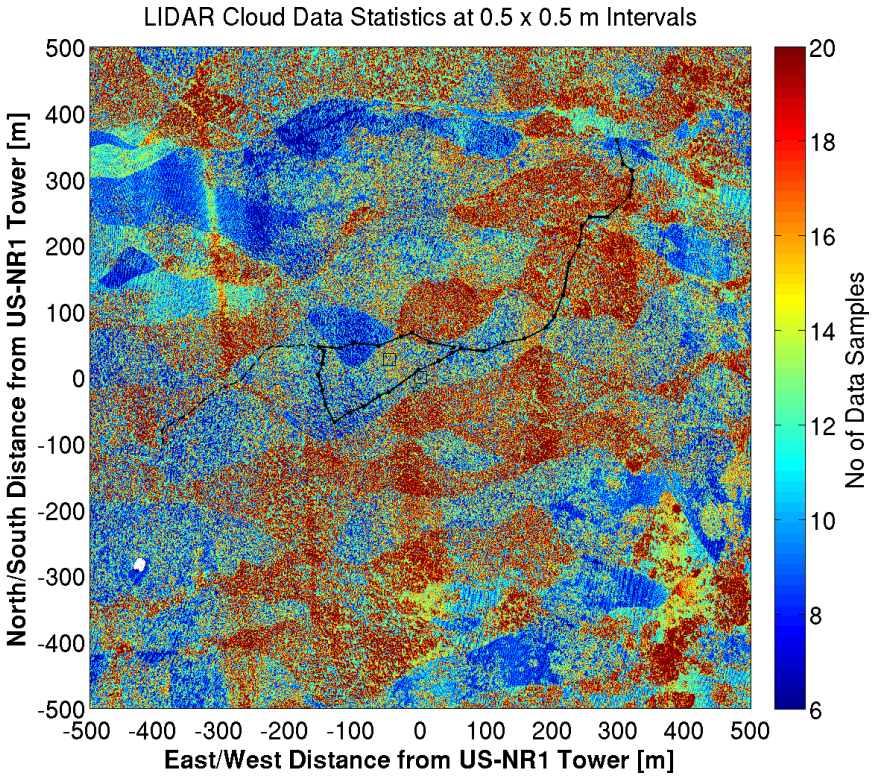

Figure 4.5: The number of airborne lidar returns within each 0.5 x 0.5 m area in a 1 km box around the US-NR1 tower. The black line is the trail from LTER C-1 to the US-NR1 main tower.

of Li et al. [2012] has been used to identify trees and we can observe a dense cluster of trees with heights taller than 12 m just to the southeast of the main tower. Near the tower, the number of lidar returns was clearly higher than just to the south of the tower (Fig. 4.6a), but there does not appear to be any obvious artifact of this on the tree heights (i.e., compare the region of the taller trees to the location of the higher number of lidar returns in Fig. 4.6).

To gain confidence in the lidar-derived canopy heights, we start by comparing the canopy structure in different parts of the forest. Ground-based measurements at US-NR1 (as described in Sect. 3.21), have found a difference in forest composition (both tree density and species composition) east and west of the main tower [e.g., Moore et al., 2008, Monson et al., 2010, Golub, 2010]. In general, the forest east of the tower has been found to have more pine trees which were shorter and

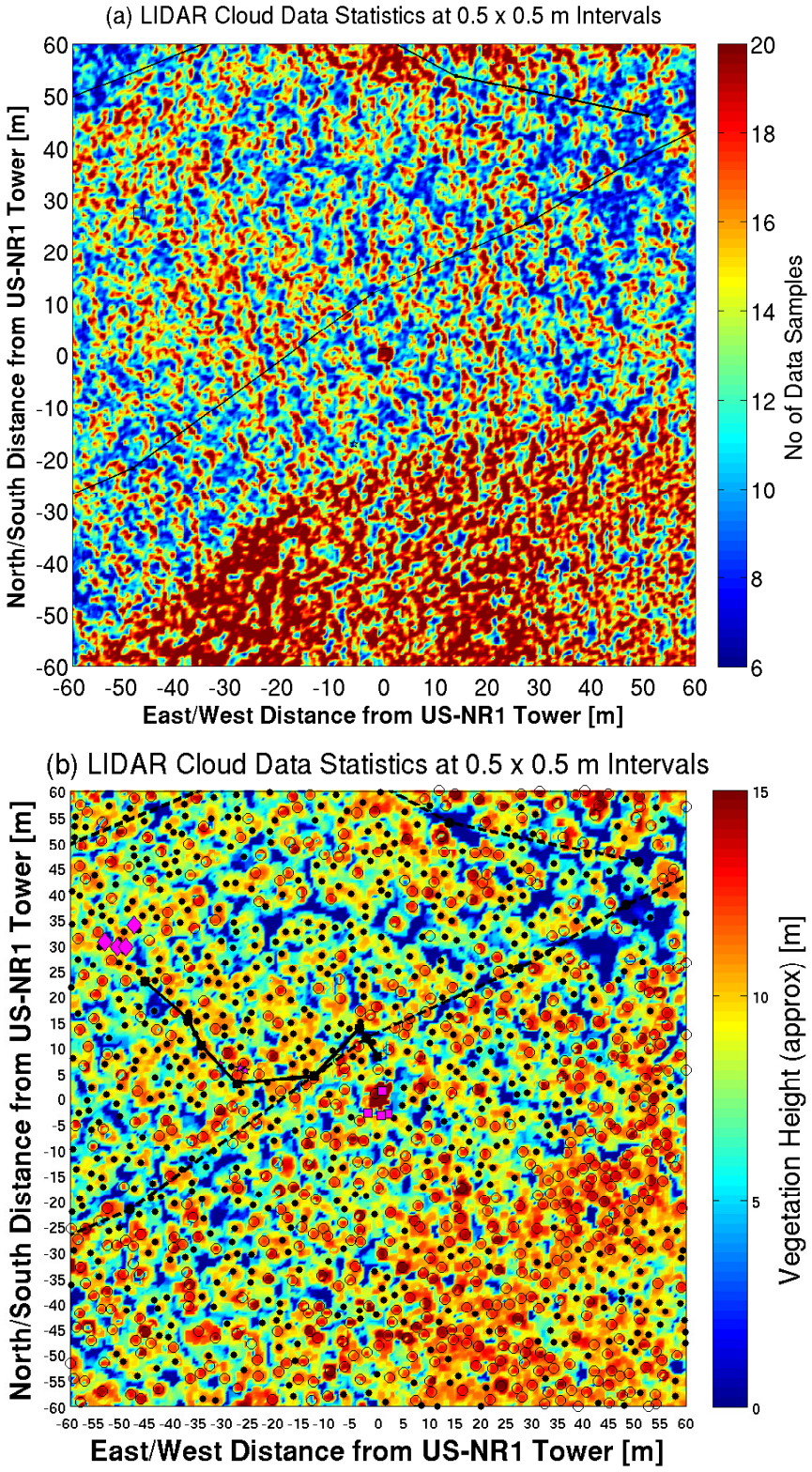

Figure 4.6: Airborne lidar data showing **(a)** the number of returns in each 0.5 x 0.5 m area and **(b)** the vegetation heights derived from the lidar data near the US-NR1 tower. In **(b)**, the symbols indicate tree locations where filled circles indicate trees shorter than 12 m and open circles indicate trees taller than 12 m. The black line is the trail near the tower.

Table 4.1: Statistics from 200 m × 200 m regions due east and west of the US-NR1 AmeriFlux tower. The statistics shown are the number of lidar returns between 15 and 18 m, between 12 and 13 m, and returns that are at height less than 1 m (considered open ground).

	West Section			East Section		
Variable	15–18 m	12–13 m	Open Ground	15–18 m	12–13 m	Open Ground
N	7524	14573	12074	1896	20810	7759
Fraction of Pts	0.05	0.09	0.08	0.01	0.13	0.05
Max (m)	18.0	13.0	1.0	17.9	13.0	1.0
Min (m)	15.0	12.0	0.0	15.0	12.0	0.1
Mean (m)	16.0	12.5	0.6	15.8	12.5	0.6
Std Dev (m)	0.8	0.3	0.2	0.7	0.3	0.2

closer together than the more open spruce/fir-dominated forest to the west of the tower [Monson et al., 2010]. The lidar data can be used to confirm/check these east-west differences. To do this, we used the lidar cloud data in 200 m × 200 m regions due east and west of the tower and sum the number of lidar returns in 0.5 m vertical bins above the ground (Fig. 4.7a). Statistics from the lidar data are shown in Table 4.1, where it can be observed that west of the tower, the taller trees cover more of the landscape (i.e., in the west, 5% of total returns are between 15 and 18 m compared to only 1% in that size range east of the tower), and the forest is more open (i.e., a higher percentage open ground to the west than east of the tower).

For something to compare the lidar data with, we use the mean leaf area density profile from the ground-based measurements in 2003 (described in Sect. 3.21 as well as in Yi et al. [2005]), which is an average profile from trees both east and west of the tower (Fig. 4.7b). Considering how different these two methods are, there are some remarkable qualitative similarities between them: (1) the level of maximum vegetation density is at about 9 m AGL from both the lidar and ground-based methods (there is also a similar maximum for lidar data east and west of the tower), and (2) the general shape of the vegetation profile with height are similar. From the lidar east

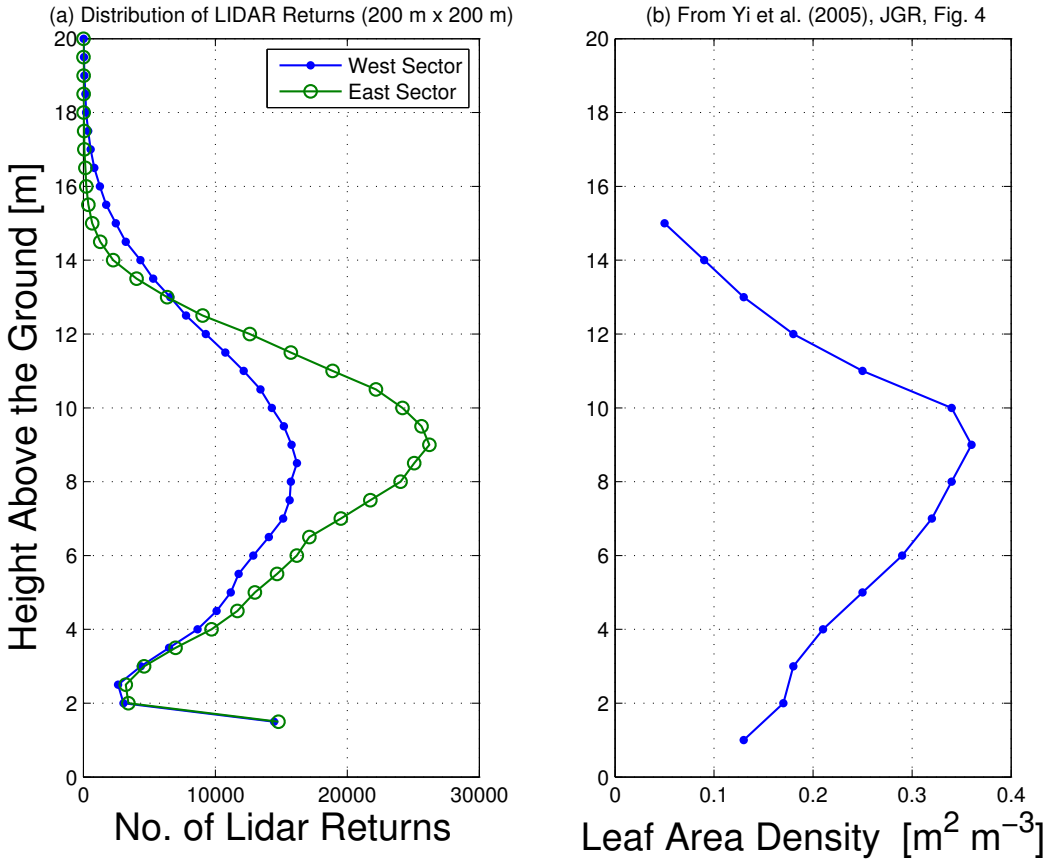

Figure 4.7: Vertical profiles of **(a)** the number of lidar returns, and **(b)** traditional ground-based measurement of leaf area density as presented in Yi et al. [2005]. In **(a)**, the vertical profile is shown for 200 m $\times$ 200 m square regions due east and west of the US-NR1 tower (as described in the legend).

and west profiles it can be observed that the west region had taller trees than the east, but there were fewer returns between 6 m and 12 m suggesting the trees were spaced farther apart. This is consistent with the east-to-west forest characteristics reported by Monson et al. [2010]. However, it appears the lidar data has an issue when sampling below around 2 m where there was a sharp increase in the number of returns (unless this was due to low vegetation, rocks, stumps, etc). These initial results are promising, but more work is needed to do a complete comparison.

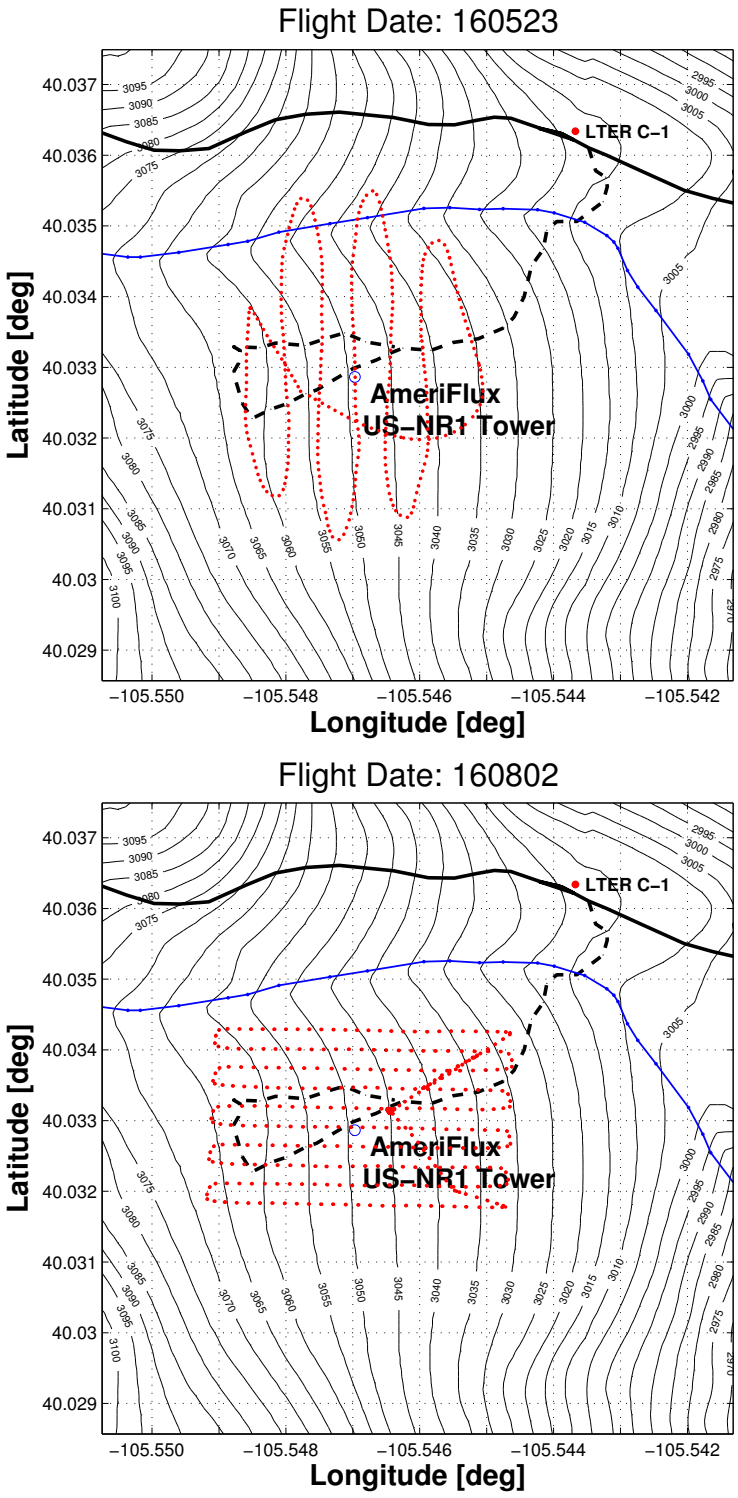

Figure 4.8: Flight tracks from two UAV flights near the US-NR1 tower on **(top)** 23 May and **(bottom)** 2 August, 2016. The small, red-filled circles indicate image/photo locations by the UAV.

Figure 4.9: A raw near-infrared image taken from a UAV directly over the US-NR1 tower on 23 May 2016. The subcanopy (6 m) tower is visible in the lower portion of the photo. For the flight elevation and camera settings used here, the area captured by the image is roughly 60 m × 40 m.

4.4.2 Unmanned Aerial Vehicle (UAV) images

UAVs are a method growing in popularity for examining forests (as well as a wide range of other tasks). In spring and summer of 2016, Douglas E. Weibel from the Integrated Remote and In Situ Sensing (IRISS) group at CU led an effort to fly a UAV on Niwot Ridge. Doug and his team agreed to do several flights near the US-NR1 tower, and typical flight paths are shown in Fig. 4.8. This provided a new opportunity to view the forest from above and we thought the images for these flights could be used to verify the tree locations based on the airborne lidar data (as shown in Fig. 4.6b).

An example of a raw near-infrared image taken almost directly over the US-NR1 tower is shown in Fig. 4.9. For reference, the booms on the lower-left side of the tower are pointed at

an angle of $\approx 203^\circ$ from true north. So, this image happens to be oriented such that north is approximately toward the top of the image. If one looks carefully it is also possible to see the subcanopy tower which is about 6 m southwest of the main tower (along a similar axes as the booms at the top of the tower). Even though these images provide a spectacular, unique view of the forest, there are also several challenges that need to be dealt with. First, there is a lot of distortion at the edges of the photo. Second, the photos need to be geo-referenced to be useful to compare the tree locations. Geo-referencing was done by using known points that show up in the images to rotate and transform the original image to match these locations. In Fig. 4.10 we show an image that has been geo-referenced and the tree locations from the lidar data have been overlain on top of the image. If the edges of the photo are ignored, on average, the method of Li et al. [2012] determines the locations of the trees remarkably well. However, there are a few locations (such as that highlighted by the red circle in Fig. 4.10) where the trees are under-counted. The method of Li was reported to find about 85–90% of the trees in a forest [Li et al., 2012]. Identifying individual trees in a complex forest is a known challenge within the lidar community [Tao et al., 2014, Hu et al., 2014]. A lesson learned from examining the UAV images from these few flights is that the UAV photos needed more overlap to effectively stitch together the photos (the spacing between photos was about 15 m for the flights we looked at). This could be achieved by either flying slower or taking photos more frequently. More comprehensive and quantitative work needs to be done to understand and improve the utility of the UAV and lidar data at the US-NR1 forest, but these initial steps show how powerful and useful this technology can be.

4.5 Ecological, climatological, and meteorological characteristics

At the US-NR1 subalpine forest, ecosystem processes are closely linked to the presence of snow [Knowles et al., 2015a], which typically arrives in October or November, reaches a maximum depth in early April (snow water equivalent (SWE) ≈ 30 cm), and melts by early June. Sometime in March or April, the snowpack becomes isothermal [Burns et al., 2013] and liquid water becomes available in the soil, which initiates the photosynthetic uptake of CO_2 by the forest [Monson et al.,

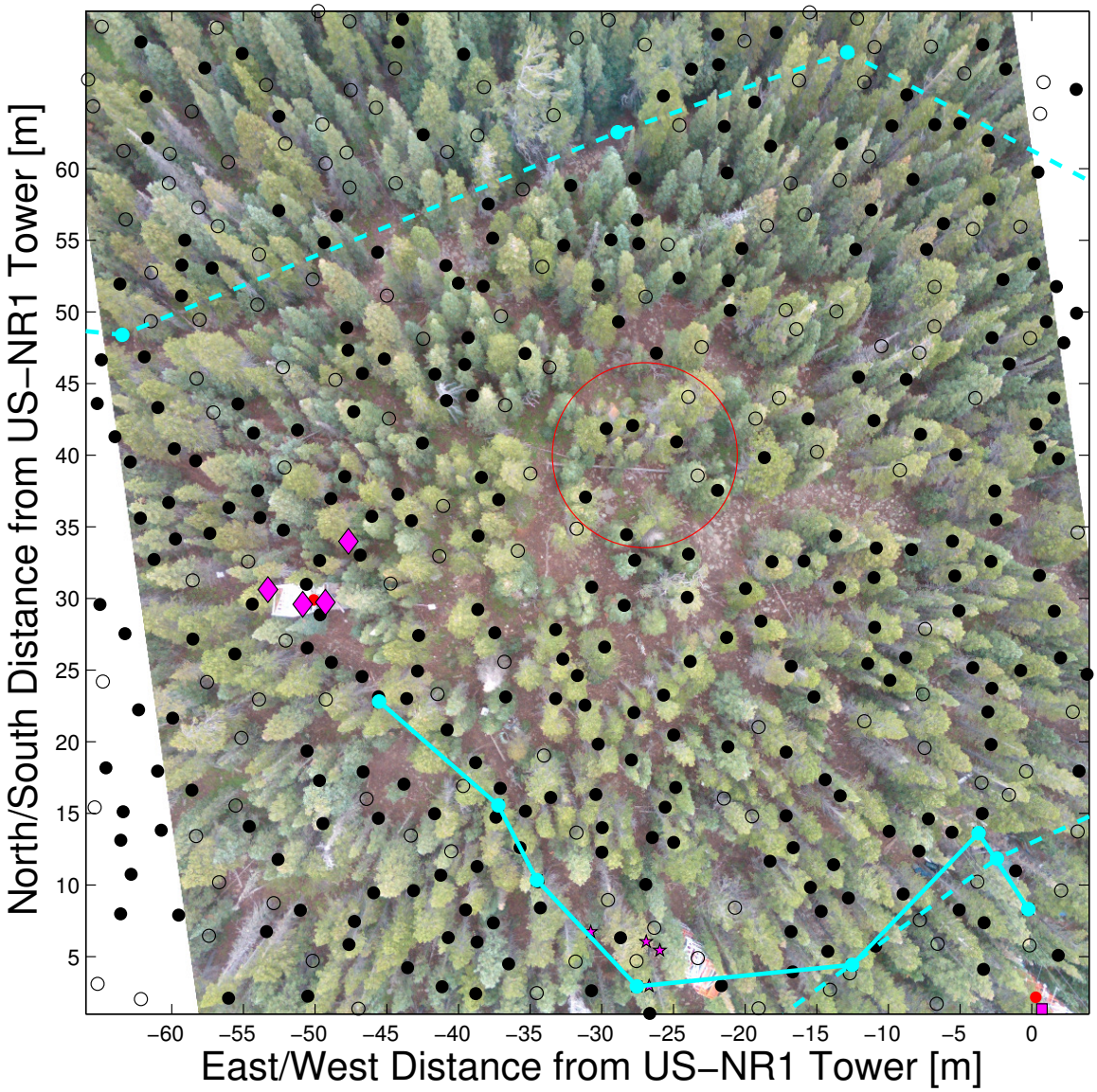

Figure 4.10: A geo-referenced visible photo from the UAV taken on 2 August 2016 with tree locations from Fig. 4.6 included. As in Fig. 4.6, filled circles indicate trees shorter than 12 m and open circles indicate trees taller than 12 m. The red circle indicates a region where some trees were not identified. The solid and dashed lines indicate trails at the site, and the North Canopy tower is located about 50 m west and 30 m north of the US-NR1 tower.

2005]. The warmest month is July with an average above-canopy air temperature of around 15 °C and average soil temperature (at −5 cm depth) of 10 °C [Burns et al., 2009b]. In late July and August, the North American Monsoon period [e.g., Adams and Comrie, 1997] is characterized by relatively higher atmospheric humidity ($q \approx 7$ g kg^{-1}; whereas in the winter q is on the order of

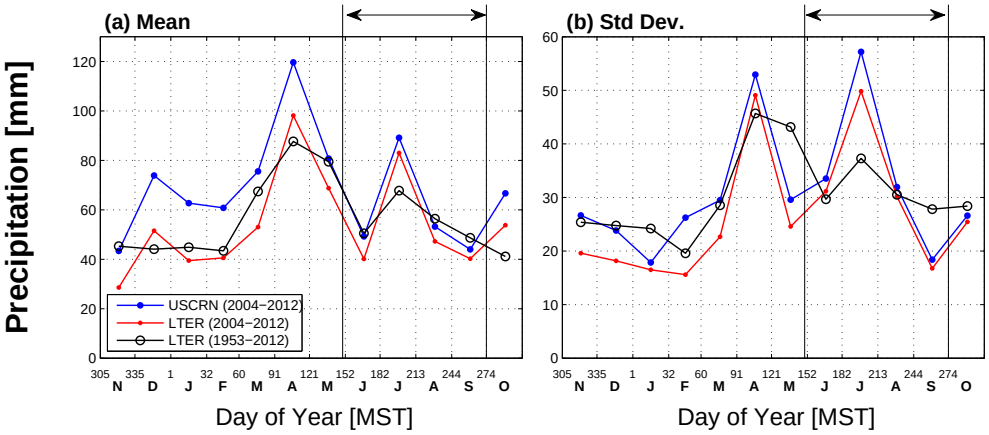

Figure 4.11: Monthly precipitation statistics from the LTER C-1 climate station between years 1953–2012 (Belfort gauge) and the USCRN Hills Mill station between years 2004–2012 of **(a)** the mean monthly cumulative precipitation and **(b)** the standard deviation of monthly totals among years. Additional details about the precipitation measurements are in Sect. 3.19. For comparison, the LTER Belfort gauge data between years 2004–2012 are also shown. Vertical lines with the arrows indicate the average warm-season period used for our study.

2 g kg^{-1}). A detailed description of seasonal aspects of the ecosystem turbulent fluxes is in Sect. 5.3.

The period from November to February is often, cold, windy and relatively dry (average air temperature during this period is around −5 °C with the coldest periods approaching −30 °C). Upslope, springtime storms have the potential to provide large amounts of wet, heavy snow. For many years the single-storm record snowfall within the continental US was from April, 1921 when 221 cm of snow fell over a 28-hr period at Silver Lake [e.g., Paulhus, 1953], which is only a few kilometers west of the US-NR1 site (Fig. 2.1). The long-term mean annual precipitation at the site is around 800 mm (Fig. 3.8a), with about 40% of the total from warm-season rain, which typically occurs every 2–4 days and has an average daily total of around 4 mm [Hu et al., 2010a]. Based on eight years of precipitation data from the nearby USCRN Hill's Mills site (Sect. 3.2), April had the most precipitation (with a mean of around 120 mm, almost all falling as snow) followed by July with 90 mm of precipitation (Fig. 4.11a). April and July were also the months with the largest variability between years and the variations between years were about 50 % of the mean value (Fig. 4.11b). In Fig. 4.11, there is a suggestion that the years 2004–2012 had higher July rainfall (with more variability) compared to the LTER average for July for years 1953–2012. Otherwise, the LTER C-1

statistics between years 2004–2012 and years 1953–2012 generally agree with each other. The effect of undercatch by the LTER Belfort gauge was noticeable during the winter months (by comparison with the USCRN winter precipitation). The issue of undercatch during winter was discussed in detail in Sect. 3.19.

The summer precipitation timing is primarily controlled by the diel cycle of the mountain-plain wind system [e.g., Whiteman, 2000, Zardi and Whiteman, 2013] which generates downslope flows at night and upslope flows during the daytime. Such a pattern in winds is well-documented at the US-NR1 site [Brazel and Brazel, 1983, Parrish et al., 1990, Turnipseed et al., 2004, Burns et al., 2011]. The upslope daytime flows leads to convergence over the mountain crest, which triggers the formation of afternoon thunderstorms (at night, the downslope winds tend to reduce cloudiness and precipitation) [Zardi and Whiteman, 2013]. Depending on the prevailing wind conditions, these convective thunderstorms can be enhanced by waves generated off the crest of the mountains, or when the flow over the mountain meets the upslope winds, which generates convergence and further intensifies the lee-side convection [Banta, 1984, Houze, 2012, Kirshbaum et al., 2018].

According to the Köppen–Geiger climate classification system [Kottek et al., 2006] the site is type Dfc which corresponds to a cold, snowy/moist continental climate with precipitation spread fairly evenly throughout the year. The forest could also be classified as climate type H which is sometimes used for mountain locations [Greenland, 2005].

Though this thesis has focused on water vapor and carbon dioxide, there has been a lot of work on the role of other chemical species within the US-NR1 forest, including: ozone [Turnipseed et al., 2009], nitrogen [Tomaszewski et al., 2003, Sievering et al., 2007, Tomaszewski and Sievering, 2007], methane [Bowling et al., 2009], and biogenic volatile organic compounds [Karl et al., 2002, Gray et al., 2010, 2014, 2015]. There is also an $\approx$10-year time series record of CO_2 carbon isotope measured at multiple heights on the US-NR1 main tower [e.g., Bowling et al., 2005, Zobitz et al., 2006, 2008, Schaeffer et al., 2008b, Riveros-Iregui et al., 2011, Bowling et al., 2014], and about a 2-year time series of the water oxygen isotope [Berkelhammer et al., 2016]. Soil respiration studies have been another popular topic of study at the site [e.g., Scott-Denton et al., 2003, 2006,

Weintraub et al., 2007, Moore et al., 2013, Bowling et al., 2015]. At C-1 there is a NOAA/ERSL gas chromatograph system which provides a long time series of atmospheric chlorofluorocarbons (CFCs), hydrochlorofluorocarbons (HCFCs), and hydrofluorocarbons (HFCs) [e.g., Hall et al., 2014, Vollmer et al., 2016].

4.6 Conclusions

This chapter provided a general overview of the US-NR1 site characteristics. A review of previous studies of tree ages near the US-NR1 tower found that unburned portions of the forest were established around the year 1400. Stand-replacing fires occurred about 1–2 km east of the US-NR1 main tower in the 1890s. These burned areas are currently (primarily) occupied by lodgepole pine stands. The use of lidar and UAVs appears to be a promising tool for examining the forest structure and how it varies spatially. Some initial examples of how these tools might be used are shown, as well as a comparison of lidar-derived and ground-measured vertical profiles of forest vegetation density, which were qualitatively similar.

Chapter 5

The influence of warm-season precipitation on the diel cycle of the surface energy balance and carbon dioxide at a Colorado subalpine forest site

Abstract

This work was published in the EGU journal Biogeosciences [Burns et al., 2015a]. Within this chapter we describe the analysis techniques used, followed by the results. Using a precipitation-based conditional sampling technique and 14 years of data from the US-NR1 micrometeorological tower, we examined how warm-season precipitation affected the above-canopy diel cycle of wind and turbulence, net radiation R_{net}, ecosystem eddy covariance fluxes (sensible heat H, latent heat λE, and CO_2 net ecosystem exchange NEE) and vertical profiles of scalars (air temperature T_a, specific humidity q, and CO_2 dry mole fraction χ_c). This analysis allowed us to examine how precipitation modified these variables from hourly (i.e., the diel cycle) to multi-day time-scales (i.e., typical of a weather-system frontal passage). For context, we first examine how the warm season fluxes compare to the full annual cycle.

During mid-day in the warm season we found: (i) even though precipitation caused mean changes on the order of 50–70 % to R_{net}, H, and λE, the surface energy balance (SEB) was relatively insensitive to precipitation with mid-day closure values ranging between 90–110 %, and (ii) compared to a typical dry day, a day following a rainy day was characterized by increased ecosystem uptake of CO_2 (NEE increased by ≈ 10 %), enhanced evaporative cooling

(mid-day λE increased by $\approx 30\,W\,m^{-2}$), and a smaller amount of sensible heat transfer (mid-day H decreased by $\approx 70\,W\,m^{-2}$). Based on the mean diel cycle, the evaporative contribution to total evapotranspiration was, on average, around 6 % in dry conditions and between 15-25 % in partially-wet conditions. Furthermore, increased λE lasted at least 18 hours following a rain event. At night, even though precipitation (and accompanying clouds) reduced the magnitude of R_{net}, λE increased from $\approx 10\,W\,m^{-2}$ to over $20\,W\,m^{-2}$ due to increased evaporation. Any effect of precipitation on the nocturnal SEB closure and NEE was overshadowed by atmospheric phenomena such as horizontal advection and decoupling that create measurement difficulties. Above-canopy mean χ_c during wet conditions was found to be about 2–3 $\mu mol\,mol^{-1}$ larger than χ_c on dry days. This difference was fairly constant over the full diel cycle suggesting that it was due to synoptic weather patterns (different air masses and/or effects of barometric pressure). Finally, the effect of clouds on the timing and magnitude of daytime ecosystem fluxes is described.

5.1 Introduction

During the warm season, rain is a common event at the US-NR1 forest. Despite being common, it has a large impact on the health of the forest and the surface energy budget. Within this chapter, we examine how precipitation changed the fluxes and other measured variables (such as atmospheric scalars and soil properties such as soil temperature and moisture). The chapter starts by explaining the analysis methods, then the warm-season fluxes are put in the context of the full annual cycle. This is followed by the results from the analysis of the influence of precipitation on the fluxes and other variables over the diel cycle.

5.2 Analysis Methods

5.2.1 Conditional sampling of the diel cycle based on precipitation

Precipitation is notoriously difficult to study because of its intermittent, binary nature (e.g., it will often start, stop, re-start, and falls with varying intensity) which leads to non-normal statistical properties [e.g., Zawadzki, 1973]. To study the impact of rain, we followed a methodology similar to that of Turnipseed et al. [2009] and tagged days when the daily rainfall exceeded 3 mm as "wet" days. Table 5.1 shows the number of wet days for each year and warm-season month within our study. The choice to use 3 mm as the wet-day criteria was a balance between effectively capturing the effect of precipitation and providing enough wet periods to improve the wet-day statistics. If we designate the precipitation state of the preceding day with a lower-case letter, then diel patterns for "dry days following a dry day" (dDry days), "wet days following a dry day" (dWet days), "wet days following a wet day" (wWet days), and "dry days following a wet day" (wDry days) were analyzed to determine the effect of precipitation on the weather and climate as well as the fluxes. The term "wet days" includes both dWet and wWet days whereas the term "dry days" includes both dDry and wDry days. These techniques are similar to the clustering analysis used by Berkelhammer et al. [2013]. In addition to these categories, we further separated the dDry days into sunny (dDry-Clear) and cloudy (dDry-Cloudy) days. Clear skies were identified when the morning and afternoon incoming shortwave radiation measured at the US-NR1 tower was within 2% of a scaled value of the top of the atmosphere radiation.

In addition to analyzing the mean diel cycle, we also examined the day-to-day variability in the diel cycle by calculating the standard deviation of the 30 min data within each composited time-of-day bin. This statistic will be designated the SD-Bin or variability. For brevity, the focus herein is on the mean results; more details on variability can be found within the discussion paper [i.e., Burns et al., 2015b]. To further quantify and summarize the main results of our analysis, the diel cycle was broken up into three distinct periods: mid-day (10:00–14:00 MST), late evening (19:00–23:00 MST), and nighttime (00:00–04:00 MST). Motivation for breaking up the night

Table 5.1: Precipitation statistics for the US-NR1 AmeriFlux site. The number of days with a daily precipitation greater than 3 mm day^{-1} for each year and month is shown. These are defined as "wet" days in the analysis (see text for details). If the warm-season started in June, then the May column is filled with "NA". The total cumulative precipitation from the wet days is given immediately below the number of days. In the two right-hand columns the cumulative precipitation from the wet days only and from all days within the warm season are provided. Precipitation units are mm.

	Day of Year						Cumulative Precipitation	
Year	Start[a]	May	June	July	August	September	(Wet Days)	(Warm Season)
2012[b]	135	3	2	12	2	5	24	140
		25.0	10.5	214.0	13.5	58.8	321.8	353.2
2011[b]	168	NA	3	7	3	6	19	106
			49.9	72.5	27.8	56.6	206.8	230.6
2010	156	NA	4	7	6	1	18	118
			64.8	53.8	63.5	4.1	186.2	211.6
2009	153	NA	8	5	1	6	20	121
			54.6	38.1	3.6	37.6	133.9	175.9
2008	160	NA	0	6	10	4	20	115
				31.7	134.9	49.9	216.5	241.9
2007	160	NA	1	8	8	6	23	114
			10.7	74.9	57.9	32.8	176.3	211.5
2006	142	1	1	6	2	5	15	132
		10.9	3.6	120.9	13.0	54.9	203.2	245.6
2005	152	NA	9	3	7	4	23	122
			48.5	36.1	45.6	30.7	160.9	191.2
2004	138	1	11	6	7	6	31	137
		4.6	111.3	89.6	61.7	56.2	323.4	365.3
2003	153	NA	4	6	6	4	20	121
			24.2	32.1	52.7	17.9	126.9	161.5
2002	137	2	3	5	6	6	22	137
		32.3	37.6	43.7	50.0	63.5	227.1	249.6
2001	142	2	4	7	7	4	24	132
		7.6	21.3	98.0	81.5	44.9	253.4	301.8
2000	142	2	6	4	6	6	24	133
		15.5	65.8	42.1	53.3	65.3	242.0	268.1
1999[c]	158	NA	4	5	8	6	23	116
			18.0	106.0	73.7	43.0	240.7	290.0
Total		11	60	87	79	69	306	1744
Mean	149.7	6.8	37.2	75.3	52.3	44.0	215.6	249.8

[a] This column indicates the day of year the warm season started based on diel changes in the soil temperature as shown in Fig. 5.1.

[b] For 2011 and 2012, precipitation from the NOAA U.S. Climate Reference Network [USCRN; Diamond et al., 2013] MRS "Hills Mills" station was used due to instrument problems with the tipping bucket at the AmeriFlux tower (see text for details).

[c] For 1999, precipitation from the LTER C-1 site was used.

into two distinct periods is provided by Burns et al. [2011] who showed that the variability of the turbulence activity (expressed by the SD-Bin of the standard deviation of the vertical wind) increased by about a factor of two at around 23:00 MST (see their Fig. 4d). Other flux sites with sloped terrain have also shown distinct differences in the CO_2 storage before and after midnight [e.g., Aubinet et al., 2005]. Choosing these particular periods avoids the evening and morning transition periods which are complicated by the fluxes and scalar gradients becoming small and/or changing sign [e.g., Lothon et al., 2014].

Since not every variable was continuously measured for all 14 years, some variables were necessarily analyzed over shorter periods than others. A summary of the variables studied, the number of days each variable falls into each precipitation category, and gap-filling statistics of selected variables is provided in Table 5.2. Unless noted otherwise, the data analysis used in our study are based on 30-min statistics.

5.2.2 Categorizing atmospheric stability

When examining atmospheric stability near the ground a useful variable is the bulk Richardson number $\mathrm{Ri_b}$. Large negative $\mathrm{Ri_b}$ indicates unstable "free convection" conditions and large positive $\mathrm{Ri_b}$ indicates strong stability. In more stable conditions, less mixing is expected and larger vertical scalar gradients should exist. We calculated $\mathrm{Ri_b}$ between the highest ($z_2 = 21.5$ m, around twice canopy height) and lowest ($z_1 = 2$ m) measurement level using:

$$\mathrm{Ri_b} = \frac{g}{\overline{T}_\mathrm{a}} \frac{(\theta_2 - \theta_1)(z_2 - z_1)}{U^2}, \tag{5.1}$$

where g is acceleration due to gravity, $\overline{T}_\mathrm{a}$ is the average air temperature of the layer, θ is potential temperature, and U is the above-canopy horizontal vectorial mean wind speed (i.e., $U = (u^2 + v^2)^{1/2}$ where u and v are the streamwise and crosswise planar-fit horizontal wind components). As shown by Burns et al. [2011], in strongly stable conditions $\mathrm{Ri_b}$ provides an extra 2 decades of resolution where the dimensionless stability parameter ζ is nearly constant. For this reason, we will use $\mathrm{Ri_b}$ to examine the variables and parameters in strongly stable conditions.

Table 5.2: Variables, symbols, units, and height above ground of measurements along with the number of days each variable falls within each precipitation category. Where appropriate, the percentage gap-filled 30 min data for each particular variable is shown. If any variable is missing for a 30 min period, then all variables within that particular group are excluded.

Variable	Symbol	Units	Sensor height (cm)	Total number of days and percentage of gap-filled values dDry	dWet	wWet	wDry	Notes
Measurements between 1999 and 2012				**1209**	**194**	**99**	**199**	
Net radiation	R_{net}	$W\,m^{-2}$	2550	0.5 %	2.1 %	2.8 %	1.6 %	
Photosynthetically active radiation	PAR	$\mu mol\,m^{-2}\,s^{-1}$	2550	1.3 %	3.0 %	3.6 %	2.2 %	
Barometric Pressure	P	kPa	1050	1.1 %	3.4 %	3.6 %	2.2 %	
Air temperature, Relative humidity Specific humidity	T_a, RH q	°C, percent $g\,kg^{-1}$	2150	0.6 %	2.3 %	2.9 %	1.5 %	
Soil temperature	T_{soil}	°C	−5	3.5 %	3.5 %	4.3 %	4.7 %	A
Wind speed, Wind direction	U, WD	$m\,s^{-1}$, deg from true N	2150	1.7 %	5.8 %	11.0 %	3.2 %	B
Friction velocity	u_*	$m\,s^{-1}$	2150	2.3 %	5.5 %	7.9 %	3.0 %	
Sensible heat flux	H	$W\,m^{-2}$	2150	6.0 %	15.8 %	29.1 %	10.9 %	C
Latent heat flux	λE	$W\,m^{-2}$	2150	7.2 %	15.4 %	25.8 %	11.6 %	C
Net ecosystem exchange of CO_2	NEE	$\mu mol\,m^{-2}\,s^{-1}$	2150	12.0 %	24.9 %	37.5 %	20.8 %	C
Measurements between 2000 and 2012				**1144**	**186**	**97**	**188**	
Precipitation	Precip	$mm\,(30\,min)^{-1}$	1050	3.8 %	2.8 %	3.0 %	1.5 %	D
Measurements between 2002 and 2012				**924**	**148**	**76**	**148**	
Volumetric water content	VWC	$m^3\,m^{-3}$	−5	0.01 %	0.01 %	0.01 %	0 %	A
Soil heat flux	G_{plate}	$W\,m^{-2}$	−10	0.02 %	0.3 %	0.1 %	0.04 %	
Measurements between 2006 and 2012				**530**	**83**	**46**	**82**	
CO_2 Dry mole fraction	χ_c	$\mu mol\,mol^{-1}$	2150	37.3 % 10.7 %	34.8 % 6.5 %	35.8 % 6.2 %	37.3 % 8.0 %	E
Thermocouple temperature	T_{tc}	°C	2198	6.6 %	2.3 %	1.0 %	2.2 %	

A: In October 2005, a soil moisture sensor (Campbell Scientific, model CS616) and soil temperature sensor (Campbell Scientific, model 107) were installed horizontally at a depth of 5 cm within 50 m of the AmeriFlux tower. The 107 thermistor was calibrated against a NIST-standard temperature sensor at the National Center for Atmospheric Research (NCAR) Integrated Surface Flux System (ISFS) calibration facility. These sensors were incorporated in the US-NR1 dataset starting in January, 2006. Prior to this, an average of 5 soil temperature sensors (REBS, model STP-1) and 8 soil moisture sensors (Campbell Scientific, model CS615) were used to determine the soil properties. The CS615 sensors were inserted into the soil at a 45 degree angle providing an average moisture content over the upper 15 cm of the soil.

B: Whenver possible, U and WD were gap-filled with a prop-vane sensor at 25 m on US-NR1 tower. Otherwise, gap-filling was performed using U and WD from the LTER C-1 climate station which have been adjusted to US-NR1 winds using a linear relationship.

C: NEE includes both the u_* filter and storage term gap-filling. The flux data have been screened such that around 2% of the extreme values have been removed.

D: Gap-filling for the Met One tipping bucket on the US-NR1 tower is shown. The gap-filling flags for precipitation were incorrect prior to year 2003. Therefore, the gap-filling values listed here are for years 2003–2010. After year 2010, USCRN data were used (see Sect. 3.19 for details).

E: Between years 2008 to 2010, the CO_2 was sampled hourly rather than half-hourly. During periods with hourly measurements a linear interpolation was used to create data with half-hourly time stamps. The upper values shows the number of 30-min values missing prior to interpolation, while the lower numbers shows the number of missing values after interpolation.

5.2.3 Ecosystem respiration

The ecosystem respiration R_{eco} was estimated for each 30 min time period based on measured nocturnal NEE (both with and without the friction velocity (u_*) filter applied), as well as two flux-partitioning algorithms that separate NEE into R_{eco} and gross primary productivity GPP [Stoy et al., 2006]. One algorithm takes into account the seasonal temperature-dependence of R_{eco} [Reichstein et al., 2005], and the other uses light-response curves [Lasslop et al., 2010]. Reichstein and Lasslop R_{eco} were calculated with on-line flux-partitioning software [Max Planck Institute for Biogeochemistry, 2013]. With regard to our analysis, R_{eco} from the flux-partitioning methods and measured nocturnal NEE produced very similar results which are shown in Burns et al. [2015b]. Therefore, we only use the measured nocturnal NEE herein, and will not include the Reichstein or Lasslop R_{eco} results. Unless noted otherwise, we will use the u_*-filtered NEE (with a cut-off value of $u_* = 0.2\,\text{m}\,\text{s}^{-1}$) in our analysis. Further discussion of partitioning NEE at the US-NR1 site is provided elsewhere [Zobitz et al., 2008, Bowling et al., 2014].

5.2.4 Defining the warm season

We chose to define the start of the warm-season as the date when diurnal changes in the soil temperature, at a depth of $-5\,\text{cm}$, first occurred (i.e., the date of near-complete snowpack ablation). For the 14 years of our study, the warm-season start dates ranged from mid-May to mid-June with an average start date of around 1 June (as shown in Fig. 5.1a and listed in Table 5.1). Though snow can occur during the warm season, it is a rare event and usually melts quickly. The start of the growing-season (based on NEE, as described in Hu et al., 2010a) typically preceded the start of the warm-season by 2–4 weeks (Fig. 5.1a). The warm-season start date was also around the time that the volumetric soil moisture content (VWC) reached a maximum (Fig. 5.1b), and the month following the disappearance of the snowpack was usually when the soil dried out (though there were exceptions, such as 2004). In the warm-season, large precipitation events led to a sharp increase in VWC followed by a gradual return (over several days or weeks) to drier soil conditions. We chose

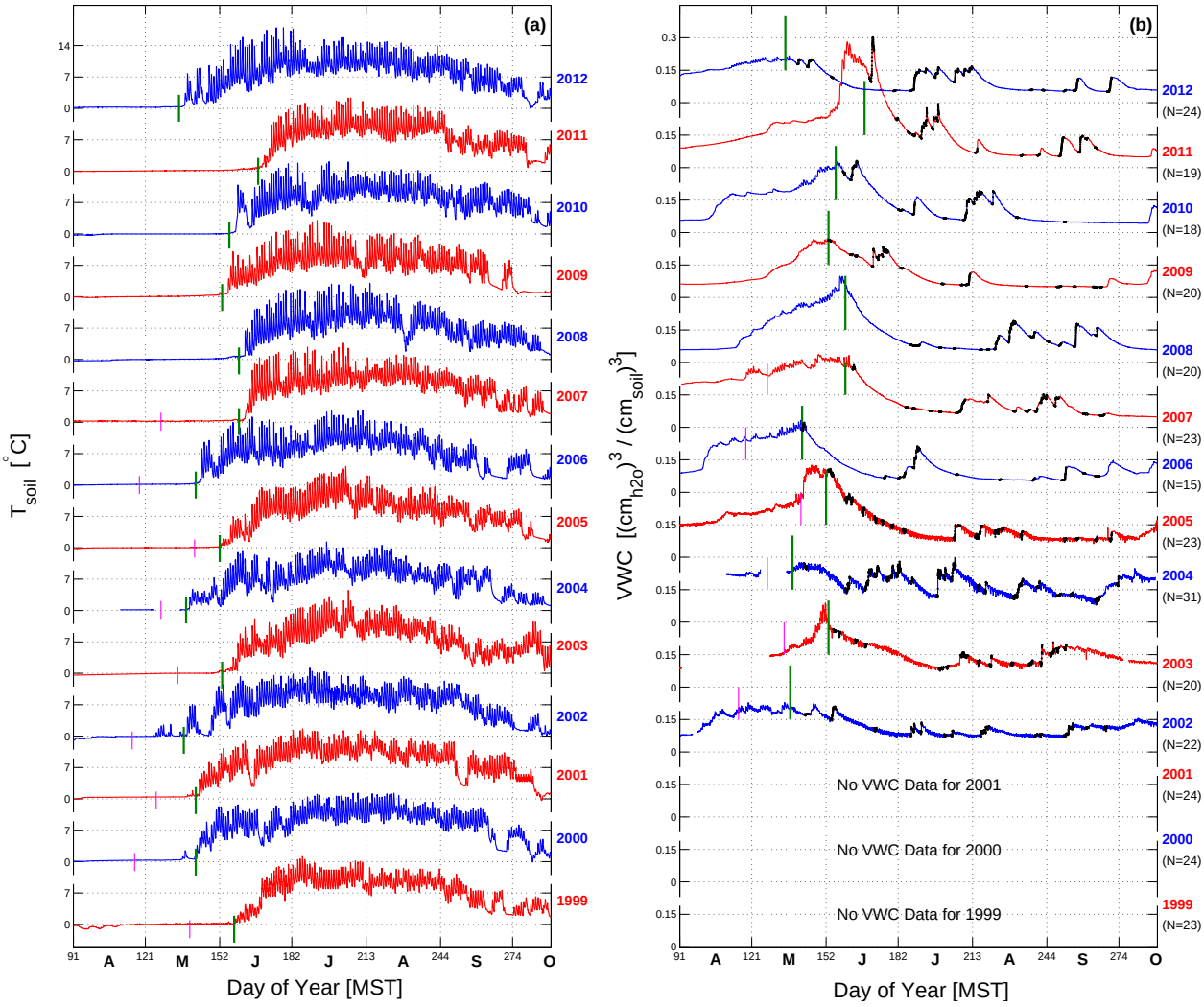

Figure 5.1: **(a)** Soil temperature and **(b)** soil moisture for years 1999 to 2012. In **(b)**, the black dots indicate wet days and the number of wet days for each year is shown to the right of the panel underneath the year. The warm-season start date was chosen based on the date that the soil temperature diurnal changes started to occur as indicated by the vertical green lines. The vertical mauve lines for years 1999–2007 are the start date of the growing season as determined by Hu et al. [2010a]. Starting with year 2006, a single set of soil sensors at a depth of 5 cm were used (see Sect. 3.17 for details).

30 September as the end of the warm-season for reasons described below.

5.3 Seasonal cycle of precipitation, scalars, and turbulent fluxes

To examine the warm-season relative to the annual cycle, NEE and the turbulent energy fluxes were smoothed using a 20 day mean sliding window applied to the 30 min data. Smoothing diminishes the effect of large-scale weather patterns (and precipitation) which typically have a period of 4–7 days. Interannual variability was calculated by taking the standard deviation among the 14 yearly smoothed time series. Since our interest is in the diel cycle, these statistics were determined for mid-day (10:00–14:00 MST), nighttime (00:00–04:00 MST), and the full (24 hour) time series.

The typical smoothed seasonal cycles of above-canopy NEE, λE and H are shown in Fig. 5.2a. The dormant period (i.e., when the forest was photosynthetically inactive) was exemplified by almost no difference between the daytime and nighttime NEE, which lasted from roughly early November to mid-April. When daytime NEE switches from positive to negative, it indicates the start of the growing season. The snowmelt period exhibited strong CO_2 uptake because soil respiration was suppressed due to low soil temperature (Fig. 5.2a). In February–March, daytime H reached a maximum because net radiation increased and transpiration was small. Nighttime H stayed at around $-50\,\mathrm{W\,m^{-2}}$ throughout the entire year. One might expect nocturnal H in winter to be different than summer, but in winter most of the above-canopy H was due to heat transfer between the forest canopy and atmosphere, not the atmosphere and snow-covered ground [Burns et al., 2013]. Related to λE, there are two interesting observations in Fig. 5.2a. First, outside the growing season, daytime λE was larger than nighttime λE. This is presumably because air temperature is higher during the daytime which increases the saturation vapor pressure and results in a larger sublimation/evaporation rate [e.g., Dalton, 1802]. Second, nighttime λE in winter was around $25\,\mathrm{W\,m^{-2}}$ which decreased to $10\,\mathrm{W\,m^{-2}}$ in summer. Despite warmer summer temperatures, we suspect the larger nocturnal λE in winter was due to the ubiquitous presence of a snowpack that serves as a source of sublimation/evaporation for 24 hours every day (compared to summer

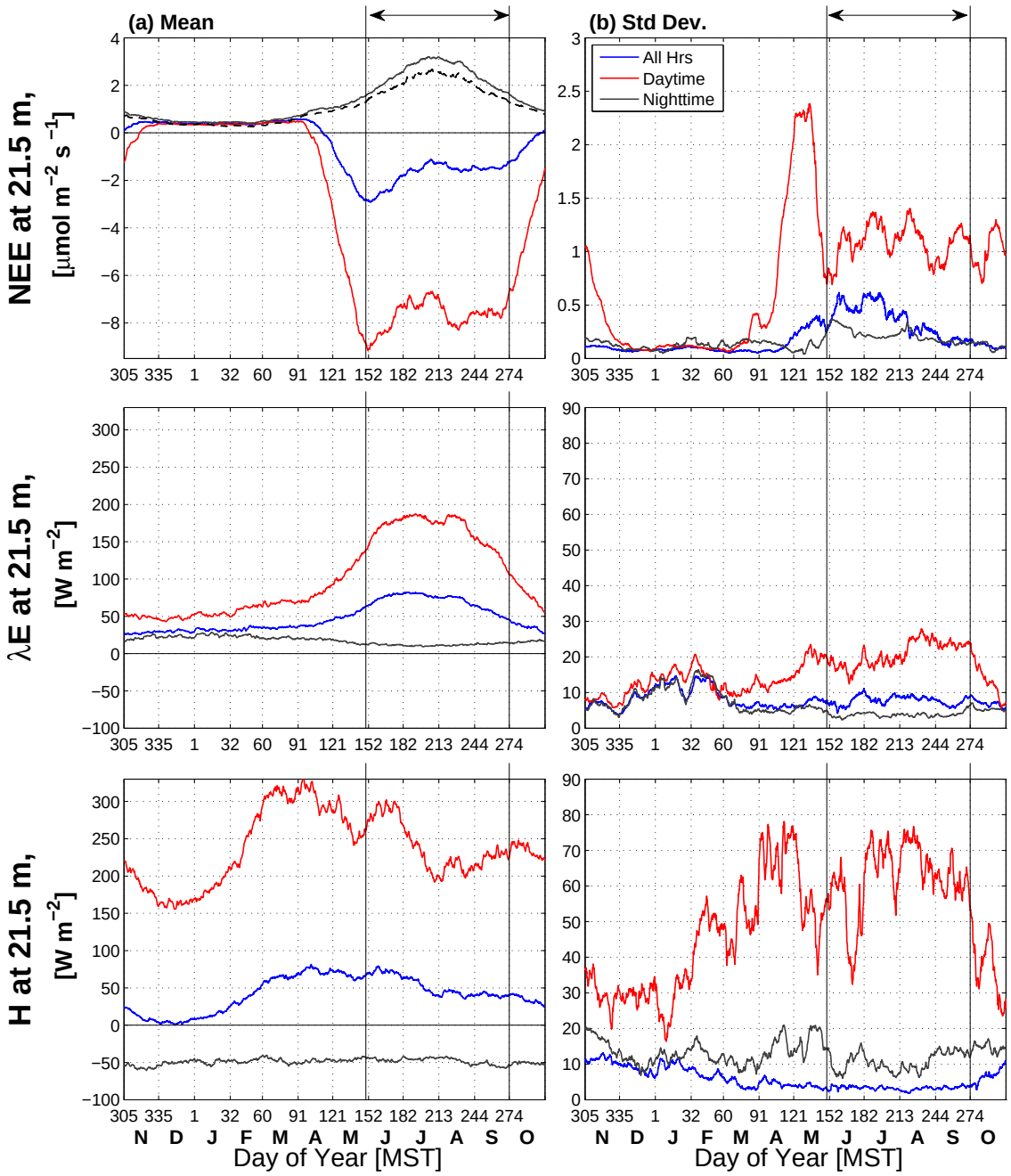

Figure 5.2: Fourteen-year **(a)** mean and **(b)** interannual standard deviation ($n = 14$ years) of (top) CO_2 net ecosystem exchange NEE, (middle) latent heat flux λE, and (bottom) sensible heat flux H. To remove the effects of short-term changes due to weather each 30 min yearly time series is averaged with a 20 day mean sliding window. In all panels, the statistics are calculated for all hours, daytime (10:00–14:00 MST), and nighttime (00:00–04:00 MST) periods following the legend in **(b)**. In **(a)**, nocturnal NEE calculated without the u_* filter is shown as a dashed line. These data were collected between 1 November 1998 and 31 October 2012. Vertical lines with the arrows indicate the average warm-season period used for our study.

when the ground periodically dries out). Also, winds are much stronger between November and February which promotes higher sublimation/evaporation. In the spring and summer λE increased during the day from around 50 to 150 $\mathrm{W\,m^{-2}}$ primarily due to increased forest transpiration as well as increased VPD. In July–August, as the soil dried out and warmed up, soil microbial activity increased [e.g., Scott-Denton et al., 2006], and NEE moved closer to having photosynthetic uptake of CO_2 balanced by respiration.

When winds are light and mechanical turbulence is small, decoupling between the air near the ground and above-canopy air can occur [e.g., Baldocchi et al., 2000, Baldocchi, 2003]. This means that the measured (above-canopy) fluxes are no longer representative of the true fluxes at or near the ground surface. The nocturnal NEE data shown in Fig. 5.2a have been calculated both with (solid line) and without (dashed line) the u_* filtering technique [Goulden et al., 1996] which replaces NEE during periods of weak ground-atmosphere coupling ($u_* < 0.2\,\mathrm{m\,s^{-1}}$) with an empirical relationship between NEE and soil temperature. Though the u_* filter enhanced the value of nocturnal NEE by around 0.5 $\mu\mathrm{mol\,m^{-2}\,s^{-1}}$ compared to unfiltered NEE, the mid-summer increase was present in both. Recent research in the ecosystem-flux community has suggested that the standard deviation of the vertical wind σ_w [e.g., Acevedo et al., 2009, Oliveira et al., 2013, Alekseychik et al., 2013, Thomas et al., 2013] or the Monin–Obukhov stability parameter [e.g., Novick et al., 2004] are better measures of decoupling than u_*; however, the results we show are not going to be strongly affected by which variable is used to determine the coupling state.

The daytime interannual variability of NEE, λE and H was larger than the nighttime interannual variability (Fig. 5.2b) due to the wide range of daytime surface solar conditions (e.g., clear or cloudy days). The peak in the interannual variability of daytime NEE during April and May was due to year-to-year differences in the timing of snowmelt and initiation of photosynthetic forest uptake of CO_2 at the site [Monson et al., 2005, Hu et al., 2010a]. Though NEE interannual variability peaked at this time, there was no corresponding peak in λE or H variability.

The average start of the warm season occurred when daytime NEE uptake was strong (greater than 8 $\mu\mathrm{mol\,m^{-2}\,s^{-1}}$) and immediately followed the peak in NEE interannual variability (Fig. 5.2b).

There was not a similar increase in NEE variability to mark the end of the warm season; however, the date when daytime NEE decreased sharply was the end of September. For this reason, we chose the end of September as the end of the warm-season. By choosing the end of September we also avoid periods in October when snowfall occurred.

5.4 The influence of precipitation on environmental conditions, turbulence, scalars, and fluxes in the warm-season

After each day was organized into the precipitation categories described in Sect. 5.2.1, we observed a peak in precipitation during the early afternoon on wet days as would be expected for a mountain-plain type wind system (Fig. 5.3b). Over the 14 years of our study, the average length of time for a dry period was around 2.5 days with a standard deviation of 3 days. Two days in a row with above-average rain (i.e., wWet days) was recorded around 90 times out of 1740 total warm-season days between 1999 and 2012 (Table 5.2). These rare events were typically the result of large-scale synoptic weather systems which explains why significant morning precipitation occurred on wWet days (i.e., Fig. 5.3b). The leaf wetness data reveals that, on average, dDry days had mean value less than 0.2 while wet periods were closer to 0.8 (Fig. 5.3c). On wDry days there was a steady decrease in leaf wetness from midnight until the early morning hours. All precipitation states had a minimum in leaf wetness between around 0800–1000 MST which is likely related to a large-scale phenomena, such as the entrainment of dry air at the top of the boundary layer.

One obvious complication with the precipitation-related analysis is that the open-path instrumentation (e.g., sonic anemometers) are affected by water droplets, and do not work properly during heavy precipitation events which is why the percent of gap-filling periods for the fluxes increases on the wet days (Table 5.2). Though we do not have a way around this issue, we can only point out that the scalar measurements were not affected by precipitation which provides some degree of insight. When we restricted the analysis to time periods without any gap-filled flux data, the results are similar to what we are showing here (see the supplemental material of Burns et al. [2015a] for an example).

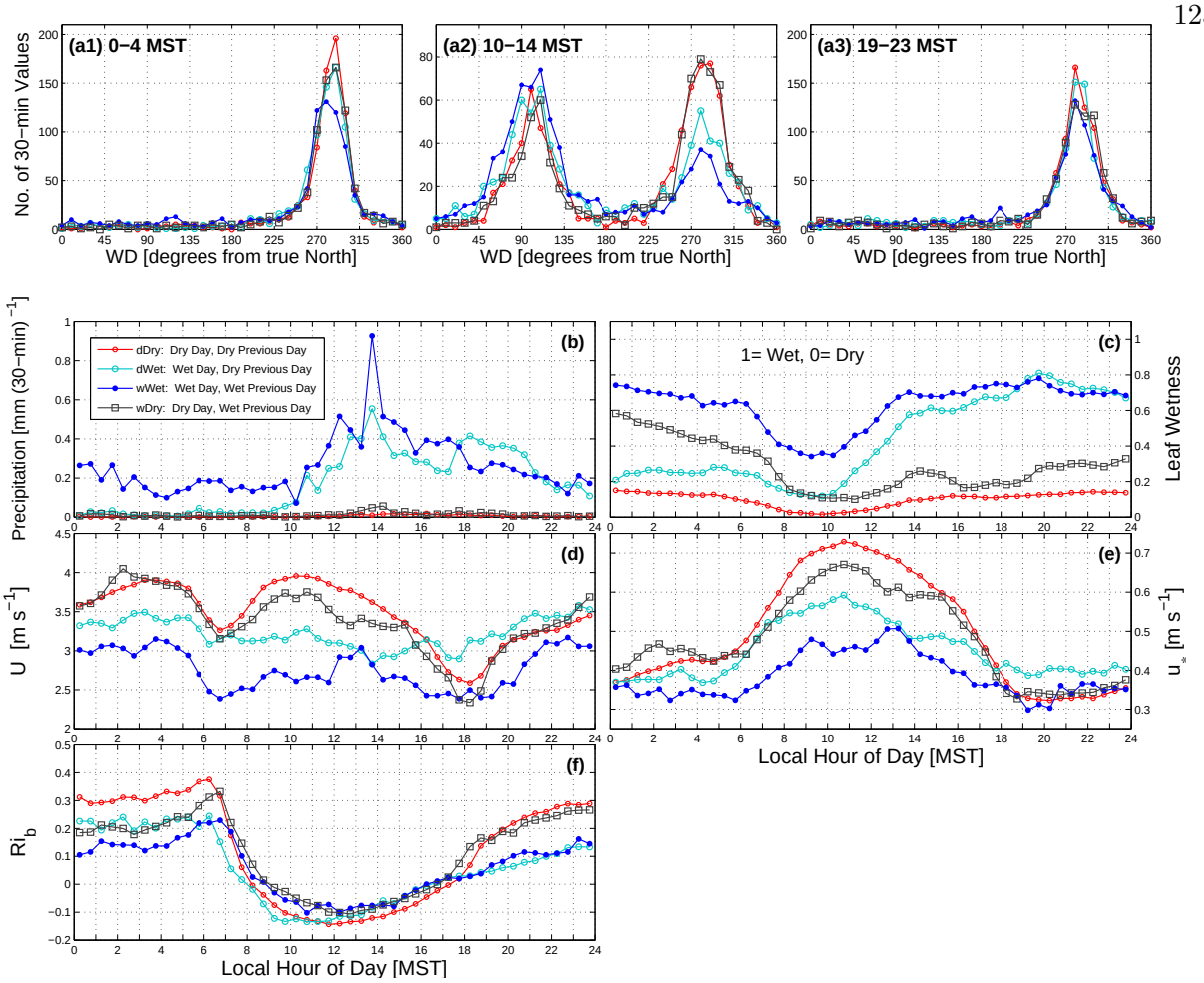

Figure 5.3: Frequency distributions of wind direction WD for different precipitation states for **(a1)** nighttime (00:00–04:00 MST) **(a2)** mid-day (10:00–14:00 MST), and **(a3)** late evening (19:00–23:00 MST) periods. Because there are a different number of 30 min periods within each precipitation state, the frequency distributions were created by randomly selecting 800 values for each precipitation state. Below **(a1–a3)**, the mean warm-season diel cycle of **(b)** precipitation, **(c)** leaf wetness, **(d)** 21.5-m horizontal wind speed U, **(e)** 21.5-m friction velocity u_*, and **(f)** bulk Richardson number $\mathrm{Ri_b}$ are shown. These composites are from 30 min data during the warm-season between years 1999–2012. For all panels, each line represents a different precipitation state as shown in the legend of panel **(b)**.

Over the next several sections we will examine how the diel cycle of the measurements (winds, soil properties, radiation, scalars, and fluxes) were affected by these different precipitation states. Because dDry conditions were the most common, we will typically describe the changes or differences relative to the dDry state.

5.4.1 Wind, turbulence, vertical temperature profiles, and near-ground stability

As mentioned in Sect. 4.5, the above-canopy wind direction at the site is primarily controlled by the large-scale mountain-plain dynamics resulting in directions that were typically either upslope (from the east) or downslope (from the west). At night, the above-canopy winds were almost exclusively downslope with very little effect from precipitation except for a small occurrence of upslope flow during wWet conditions (i.e., Fig. 5.3a1). There was a more consistent flow direction in the early morning hours as demonstrated by the higher peak in the frequency distribution of Fig. 5.3a1 compared to Fig. 5.3a3. This suggests that the drainage flow became more persistent and consistent as the night progresses. During mid-day, wet conditions had a more frequent occurrence of upslope winds than downslope winds, whereas during dry days there was nearly an equal number of upslope and downslope winds (Fig. 5.3a2). This is to be expected because the upslope winds can trigger convection which (potentially) leads to precipitation.

The diel cycle of horizontal wind speed during dry conditions was characterized by a dip of about $1\,\mathrm{m\,s^{-1}}$ during the morning and evening transitions, with the evening transition having the lowest wind speed values (Fig. 5.3d). On dDry and wDry days the wind speed overnight (on average) increased from a minimum of around $2.5\,\mathrm{m\,s^{-1}}$ at 19:00 MST to a maximum of $4\,\mathrm{m\,s^{-1}}$ at 04:00 MST. During wet conditions the dip in wind speed during the transition periods did not exist and the mean wind speed on wWet days was typically smaller than other conditions throughout the diel cycle. Mechanical turbulence (characterized by the friction velocity u_*) generally follows the pattern of wind speed at night, however, during the daytime, the buoyancy generated by surface heating enhanced u_* relative to nocturnal values (Fig. 5.3e). In dDry conditions the maximum variability in U and u_* was in the early morning (at around 06:00 MST) with less variability in the late afternoon and evening (e.g., Fig. 3 in Burns et al. [2015b]).

Near-ground vertical air temperature differences (Fig. 5.4d–f) are considered because these help control the near-ground stability. In wWet conditions, the vertical air temperature difference was at a minimum during all times of the day. This is expected during the daytime because solar

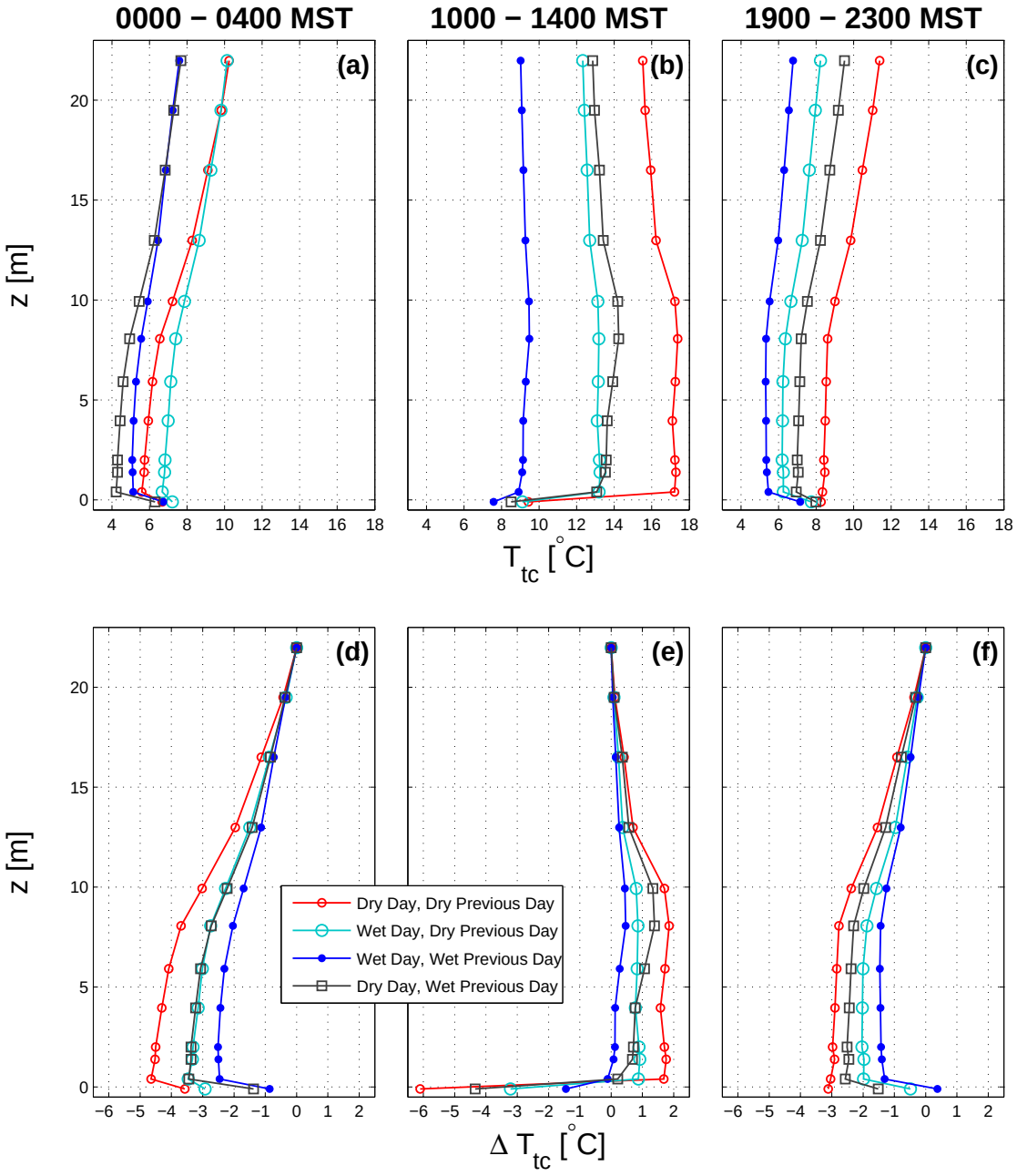

Figure 5.4: Vertical profiles of mean warm-season thermocouple air temperature T_{tc} and soil temperature T_{soil} (at a depth of 5 cm) for (left) nighttime (00:00–04:00 MST), (middle) mid-day (10:00–14:00 MST), and (right) late evening (19:00–23:00 MST). The upper row is the absolute temperature while the bottom row is the temperature difference relative to the highest level (21.98 m). Each line represents a different precipitation state as shown in the legend. These measurements are from the warm-season in years 2006–2012.

radiation, which warms the canopy and ground to create the air-surface temperature differences, was reduced on wWet days (radiation will be discussed in Sect. 5.4.4). In wDry conditions during daytime, the mid-canopy was about 1 °C warmer than the air near the ground (Fig. 5.4e). This stable layer in the lower canopy did not exist in any other conditions and we presume this state was due to a combination of strong net radiation (which warmed the canopy) combined with evaporation near the ground (which cooled the ground surface). The soil during a wDry day would have recently experienced rain, providing a source of liquid water for evaporation within the soil. We also note that the magnitude of the temperature difference during dDry days were the largest of all precipitation states for the three periods shown in Fig. 5.4d–f.

To combine the effects of wind speed and temperature differences on atmospheric stability, the bulk Richardson number $\mathrm{Ri_b}$ is also considered (Fig. 5.3f). Following the evening transition, dry conditions tended to result in a more stable atmosphere ($\mathrm{Ri_b} > 0.2$) than that of wet conditions ($\mathrm{Ri_b} < 0.1$). This suggests that there should be larger vertical scalar differences (i.e., less vertical mixing) during the late evening period of dry days.

5.4.2 Atmospheric scalars, soil temperature, soil moisture, and soil heat flux

We now consider how air temperature and humidity change over the diel cycle. dDry conditions were associated with slightly higher barometric pressure (Fig. 5.5a), relatively warmer air temperatures (Fig. 5.5c), a drier atmosphere (Fig. 5.5e), warmer and drier soils (Fig. 5.5b and d), and larger 10-cm soil heat fluxes (Fig. 5.5f). Barometric pressure had a mid-morning and evening peak that existed for all precipitation states which are created by thermal tides within the atmosphere [e.g., Lindzen and Chapman, 1969]. The variables for dDry days generally had smaller variability compared to any of the other conditions with the one exception being a high variability in VPD during the dDry afternoon and evening period [Burns et al., 2015b]. In contrast to dDry days, mean conditions during wWet days were associated with (relatively) lower barometric pressure and cooler, wetter conditions in the atmosphere and soil.

For wWet days, the soil moisture content (VWC) increased by over 50 % and T_{soil} dropped by

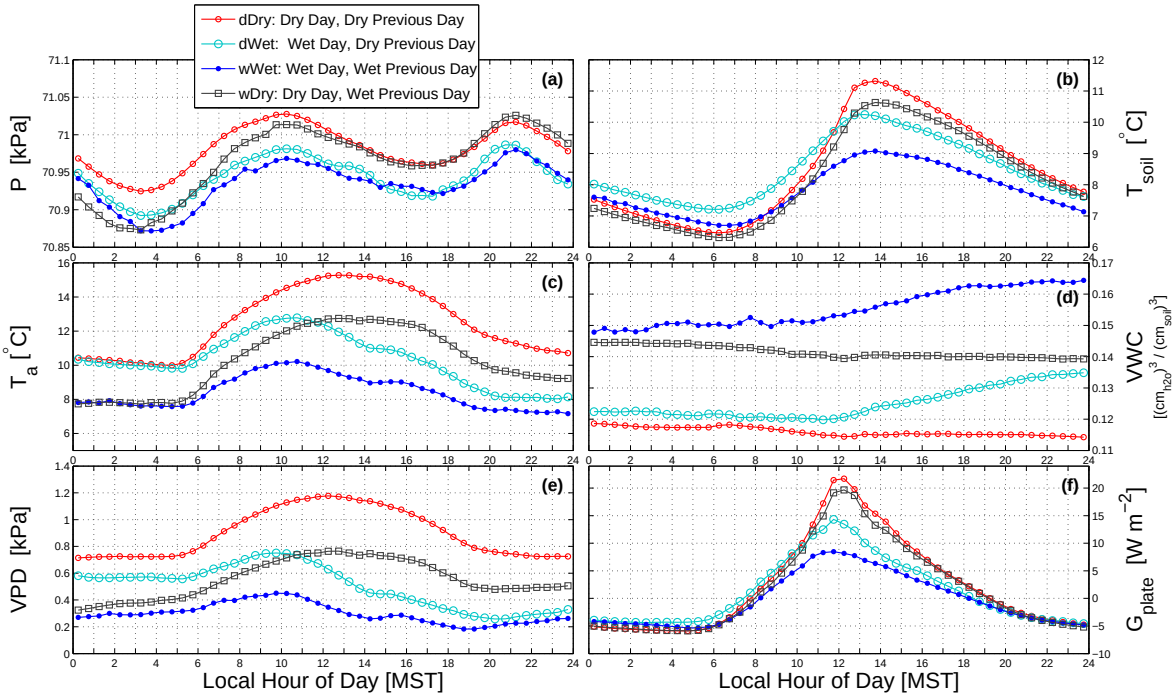

Figure 5.5: The mean warm-season diel cycle of **(a)** barometric pressure P, **(b)** 5-cm soil temperature T_{soil}, **(c)** 21.5-m air temperature T_{a}, **(d)** 5-cm soil moisture VWC, **(e)** vapor pressure deficit VPD, and **(f)** 10-cm soil heat flux G_{plate}. Each line represents a different precipitation state as shown in the legend.

around 2 °C relative to dDry conditions (Table 5.3 and Fig. 5.5b and d). The timing of precipitation within the diel cycle is important. For example, on the morning of dWet days, T_{soil} was about 1 °C larger than in other conditions because on dWet days the rain occurred primarily in the afternoon, not the morning (i.e., Fig. 5.3b). In fact, 21.5 m air temperature on the morning of dWet days was nearly the same as that of dDry days (Fig. 5.5c). The main effect of precipitation on the deep-soil heat flux was between the hours of 11:00 and 18:00 MST, where G_{plate} in dDry conditions had a peak of 20 W m^{-2} while in wWet conditions the peak was less than 10 W m^{-2} (Fig. 5.5f). At night, G_{plate} was similar for all precipitation states suggesting that either the deeper (10 cm) soil was protected from the effect of changes in nocturnal net radiation by the overlying canopy and soil or else the changes in R_{net} were small enough that the deep soil temperature was not dramatically affected. Though the soil heat flux peaked at around mid-day, the 5-cm soil temperature peaked two hours later at around 14:00 MST.

Table 5.3: Daytime and nighttime statistics of selected variables for different precipitation conditions.

Variable	Symbol	Sensor height (cm)	Night (00:00–04:00 MST) dDry	dWet	wWet	wDry	Daytime (10:00–14:00 MST) dDry	dWet	wWet	wDry	Evening (19:00–23:00 MST) dDry	dWet	wWet	wDry
Primary measurements														
Precipitation	Precip	1050	0.002	0.017	0.201	0.010	0.007	0.288	0.401	0.018	0.006	0.264	0.213	0.008
Net radiation	R_{net}	2550	−71.7	−53.0	−33.3	−52.2	582.2	349.3	286.8	528.2	−64.7	−29.7	−30.3	−55.5
Photosynthetically active radiation	PAR	2550	0	0	0	0	1408.4	865.6	715.8	1273.4	0	0	0	0
Barometric pressure	P	1050	70.91	70.86	70.85	70.84	70.97	70.91	70.92	70.93	70.97	70.91	70.94	70.95
Air temperature	T_{a}	2150	10.0	9.7	7.0	7.3	14.8	11.7	8.9	11.9	11.1	7.8	6.8	9.3
		200	5.7	6.6	4.8	4.1	17.1	13.0	9.4	13.2	8.4	6.1	5.3	6.8
Thermocouple	T_{tc}	2198	10.2	10.1	7.6	7.7	15.5	12.3	9.0	12.9	11.4	8.2	6.8	9.5
temperature,		40	5.6	6.7	5.1	4.2	17.2	13.2	8.9	13.1	8.3	6.2	5.5	6.9
Vertical difference	ΔT_{tc}	(2198 − 40)	4.65	3.46	2.46	3.45	−1.69	−0.87	0.11	−0.21	3.04	1.98	1.31	2.57
Soil temperature	T_{soil}	−5	6.8	7.4	6.9	6.4	9.6	9.2	8.1	8.7	8.4	7.8	7.4	8.0
Soil heat flux	G_{plate}	−10	−5.6	−4.2	−4.6	−5.5	17.0	11.5	7.4	15.3	−2.6	−3.1	−3.2	−2.9
Volumetric water content	VWC	−5	0.118	0.122	0.149	0.144	0.115	0.121	0.153	0.140	0.115	0.133	0.163	0.140
Wind speed	U	2150	3.8	3.4	3.0	3.7	3.8	3.1	2.8	3.5	3.2	3.2	2.7	3.1
CO_2 dry mole	χ_{c}	2150	389.9	390.8	392.7	390.6	385.3	386.8	387.1	386.0	390.5	391.2	392.4	391.5
fraction,		100	424.1	425.8	426.8	421.9	388.8	391.9	395.2	391.6	421.9	415.0	417.7	423.5
		10	434.0	437.4	438.7	432.0	394.2	400.1	405.0	400.0	433.8	426.0	429.5	437.6
Vertical difference	$\Delta\chi_{\mathrm{c}}$	(2150 − 10)	−44.12	−46.58	−45.96	−41.42	−8.84	−13.32	−17.96	−13.94	−43.31	−34.81	−37.05	−46.11
Calculated variables														
Specific humidity	q	2150	4.9	6.2	7.0	6.4	5.2	7.4	7.9	6.6	5.5	7.4	7.3	6.5
		200	5.4	6.5	7.4	6.8	5.7	8.0	8.7	7.6	6.0	7.9	7.6	7.0
Vapor pressure deficit	VPD	2150	0.7	0.54	0.25	0.34	1.1	0.61	0.31	0.71	0.74	0.28	0.20	0.47
Friction velocity	u_*	2150	0.40	0.38	0.34	0.41	0.70	0.55	0.47	0.63	0.33	0.37	0.31	0.33
Bulk Richardson number	$\mathrm{Ri_b}$		0.31	0.22	0.14	0.21	−0.13	−0.12	−0.08	−0.09	0.24	0.09	0.11	0.22
Sensible heat flux	H	2150	−48.9	−39.2	−38.6	−54.0	278.6	146.4	84.8	200.8	−35.5	−43.0	−33.0	−33.6
Latent heat flux	λE	2150	9.1	8.6	17.4	22.7	169.7	123.1	118.2	192.4	9.2	24.7	18.4	12.5
Net ecosystem exchange of CO_2	NEE	2150	2.5	2.6	2.6	2.5	−7.9	−6.6	−5.6	−8.5	3.0	2.9	2.8	2.9

If plots for each precipitation condition are arranged in the order of dDry, dWet, wWet, and wDry days the characteristics of a composite summertime cold-front passing the tower can be approximated (Fig. 5.6). Classical cold-front systems over flat terrain are associated with pre-frontal wind shifts and pressure troughs [e.g., Schultz, 2005]. Mountains, however, have a large impact on the movement of air masses and can considerably alter the classical description of frontal passages [e.g., Egger and Hoinka, 1992, Whiteman, 2000, Houze, 2012]. Our classification of the composite plots as a "frontal passage" is simply because there was colder air present at the site during the

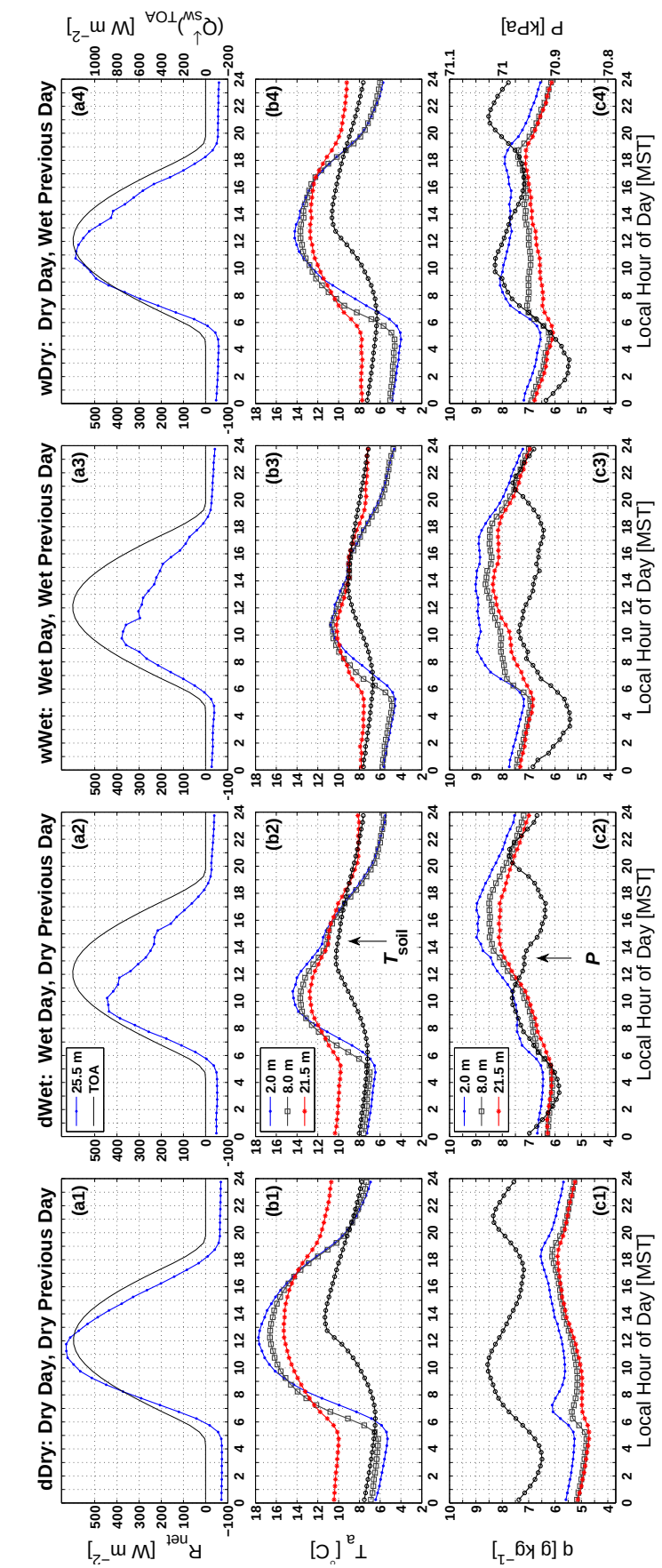

Figure 5.6: The warm-season mean diel cycle of: **(a1–a4)** net radiation R_{net} (left-hand axis) and top-of-the-atmosphere incoming shortwave radiation $(Q^{\downarrow}_{\mathrm{SW}})_{\mathrm{TOA}}$ (right-hand axis), **(b1–b4)** air and soil temperature T_{a}, T_{soil}, and **(c1–c4)** specific humidity q and barometric pressure P. Within each column the data are separated into diel periods based on whether significant rain occurred on that day. A "wet" day has a total daily precipitation of at least 3 mm (see text for further details). The legend in the 2nd column applies to all panels within each row.

dWet and wWet periods. For example, during dDry days the 21.5 m air temperature was around 5 °C greater than T_{soil} (Fig. 5.6b1). As the composite "front" passed by the tower (i.e., dWet and wWet days) 21.5 m T_a dropped to near T_{soil} (Fig. 5.6b2 and b3) and specific humidity increased by $\approx 50\,\%$ (Fig. 5.6c2 and c3). After the frontal passage (i.e., wDry days), the 21.5 m air temperature returned to being higher than the soil temperature (Fig. 5.6b4). Specific numerical values and a summary of the atmospheric conditions for each precipitation state are provided in Table 5.3.

5.4.3 Atmospheric CO_2 dry mole fraction

For CO_2 dry mole fraction χ_c, we found that above-canopy χ_c was largest during wWet conditions and lowest in dDry conditions with a fairly consistent difference of around 2–3 μmol mol^{-1} across the entire diel cycle (Fig. 5.7a). We initially considered this to be an artifact of dilution due to boundary layer height differences [e.g., Culf et al., 1997], however we ruled this out because the difference was fairly consistent throughout the day and night when boundary layer heights change dramatically. We confirmed that similar χ_c differences between precipitation states existed using CO_2 measured above tree-line on Niwot Ridge about 3.5 km northwest of the US-NR1 tower [Stephens et al., 2011] (results not shown). Since our analysis uses a composite which approximates a cold-front passage, there is an influence of large-scale weather systems on the overall atmospheric CO_2 magnitude [e.g., Miles et al., 2012, Lee et al., 2012]. This suggests that the dependence of above-canopy χ_c on the precipitation state was due to either the composition of large-scale air masses or subsidence/convergence caused by high/low barometric pressure.

Within the canopy, this same precipitation-dependent pattern existed in the morning and during the daytime, however, in the evening, χ_c in dry conditions was about 5–8 μmol mol^{-1} larger than χ_c in wet conditions (Fig. 5.7b–c). These differences clearly show up in a vertical χ_c profile (Fig. 5.8c). To avoid the confounding factor of synoptic weather systems, the lower panels in Fig. 5.8 show the vertical χ_c differences ($\Delta\chi_c$) relative to the top tower level (21.5 m a.g.l.). The mid-day $\Delta\chi_c$ profile (Fig. 5.8e) shows a photosynthetic deficit of around 1 μmol mol^{-1} in the mid-canopy due to vegetative uptake of CO_2 which is consistent with previous studies at the site [Bowling et al.,

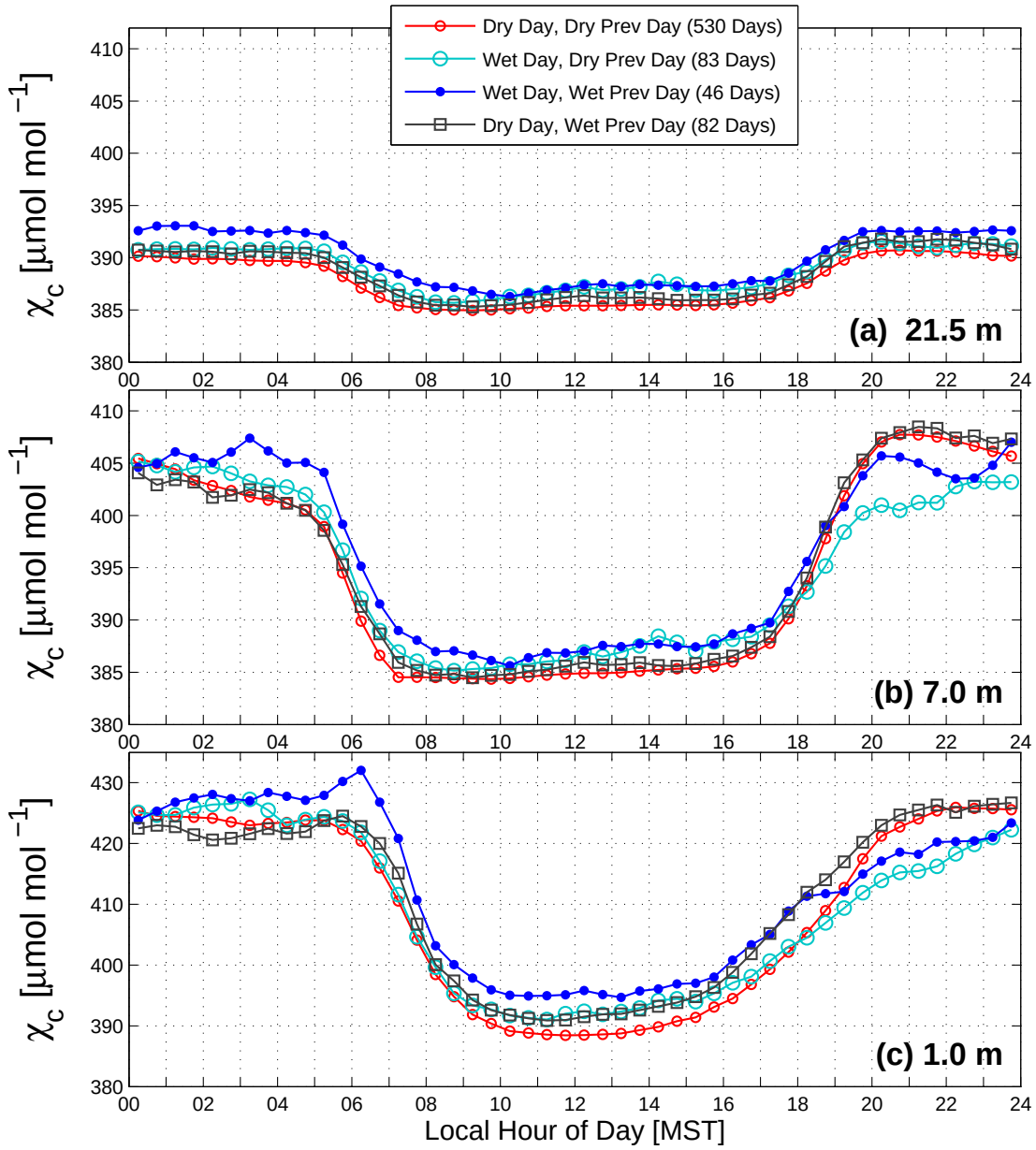

Figure 5.7: The warm-season mean diel cycle of CO_2 mole fraction χ_c at three different heights above the ground. Each line represents a different precipitation state as shown in the legend. These measurements are from the warm-season in years 2006–2012.

2009, Burns et al., 2011]. In the nighttime hours (00:00–04:00 MST) the different precipitation states did not affect the $\Delta\chi_c$ profile (Fig. 5.8d) which contrasts with the late evening $\Delta\chi_c$ profile that shows a difference of around 5–9 μmol mol^{-1} between wet and dry conditions within the lower canopy (Fig. 5.8f).

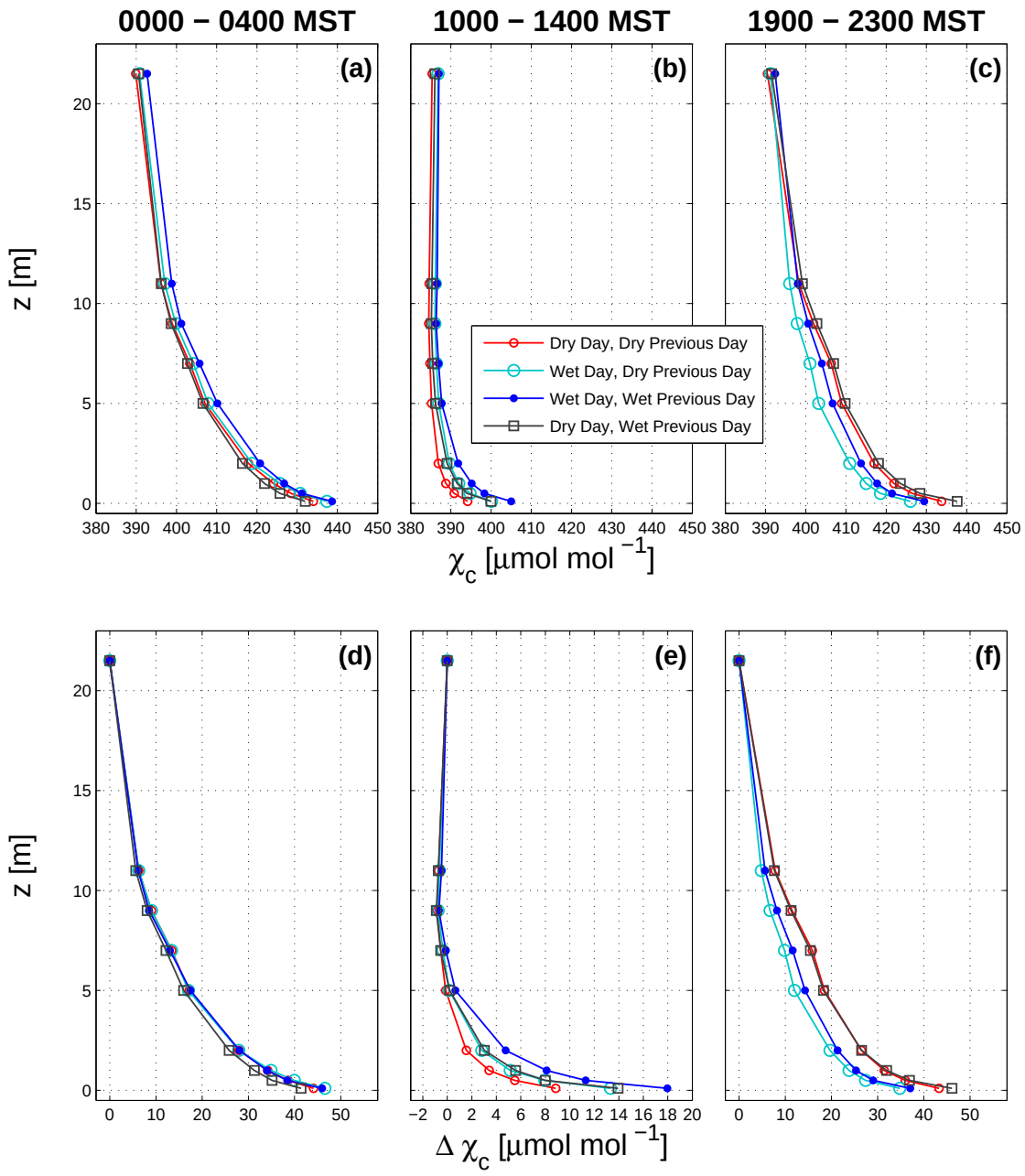

Figure 5.8: Mean vertical profiles of CO_2 mole fraction χ_c for (left) nighttime (00:00–04:00 MST), (middle) mid-day (10:00–14:00 MST), and (right) late evening (19:00–23:00 MST). The upper row is absolute χ_c while the bottom row is the χ_c difference relative to the highest level (21.5 m). Each line represents a different precipitation state as shown in the legend. These measurements are from the warm-season in years 2006–2012.

Though synoptic barometric pressure changes have recently been suggested as a mechanism for enhancing the exchange of deep-soil CO_2 with the atmosphere [e.g., Sánchez-Cañete et al.,

2013], the larger $\Delta\chi_c$ differences in dry conditions are consistent with the near-ground atmospheric stability being larger during dry conditions (discussed in Sect. 5.4.1). Between 00:00–04:00 MST Ri_b was generally near or above 0.2 for both wet and dry conditions whereas in the evening period on wet days Ri_b was ≈ 0.1. As shown in previous work at the US-NR1 site [e.g., Schaeffer et al., 2008a, Burns et al., 2011], $\Delta\chi_c$ differences have a transition region between weakly stable and strongly stable conditions that occurs at $Ri_b \approx 0.25$ which is nominally related to the change from a fully turbulent to non-turbulent flow. It appears that the stability in the early evening on wet days is such that the atmosphere was slightly unstable which enhanced the vertical mixing and reduced the vertical $\Delta\chi_c$ differences. Furthermore, the controls on the stability between dWet and wWet days were slightly different. On dWet evenings, wind speed was slightly elevated (Fig. 5.3d) which resulted in less stable conditions. In contrast, on wWet evenings it was the reduced vertical temperature differences (Fig. 5.4f) that was the primary controlling factor in reducing the stability.

5.4.4 Net radiation and turbulent energy fluxes

The full diel cycle of net radiation, the turbulent energy fluxes, NEE, and transpiration are shown in Fig. 5.9 where the diel cycles are arranged by dDry, dWet, wWet, and wDry conditions. The dDry conditions are repeated in each column to make comparison between conditions easier. In order to better quantify the impact of precipitation state on the fluxes, we also show a summary that only includes mean mid-day (Fig. 5.10, left-column) and late evening and nighttime values (Fig. 5.10, right-column). To make interpretation of the quantitative changes more accessible, each panel in Fig. 5.10 shows the fractional change from the maximum (or minimum) value within that panel. The mean values for each precipitation state are also listed in Table 5.3.

When precipitation occurred, cloudiness increased and net radiation at mid-day was reduced (Fig. 5.9a). dDry days had a mean mid-day value of nearly $600\,W\,m^{-2}$ which decreased by around 50 % to $300\,W\,m^{-2}$ during wWet days, then recovered on wDry days to nearly $550\,W\,m^{-2}$ (i.e., about 10 % smaller than R_{net} during dDry conditions) (Fig. 5.10a1).

At night, though the absolute value of the mean net radiation was an order of magnitude

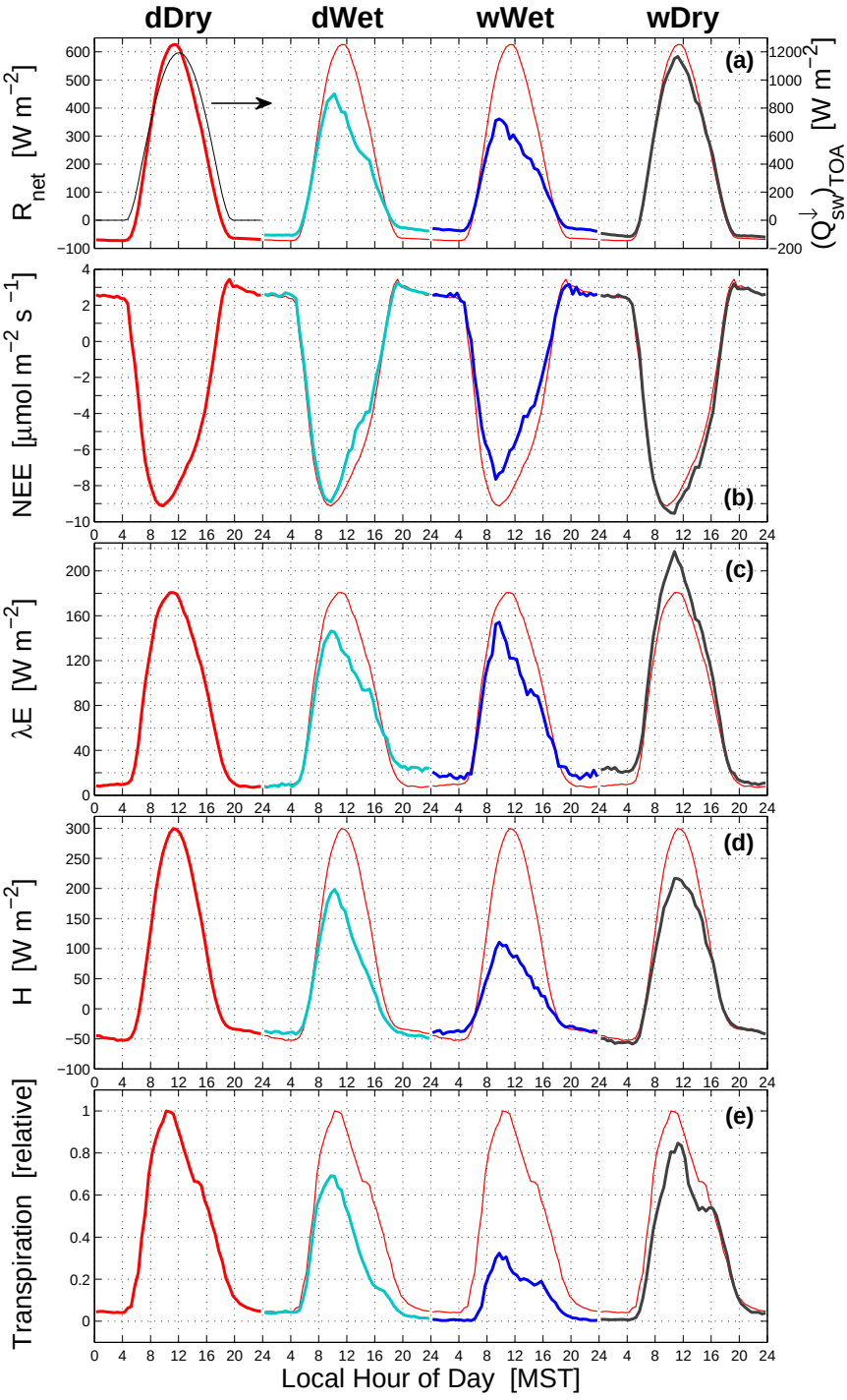

Figure 5.9: The mean warm-season diel cycle of **(a)** net radiation R_{net}, **(b)** net ecosystem exchange of CO_2 NEE, **(c)** latent heat flux λE, **(d)** sensible heat flux H, and **(e)** transpiration (in relative units). The diel cycle for each precipitation states are shifted to the right following the description above panel **(a)**. For reference, the dDry diel cycle is repeated in all columns as a red line. In **(a)**, incoming shortwave radiation at the top of the atmosphere $(Q^{\downarrow}_{\text{SW}})_{\text{TOA}}$ is shown as a black line in the dDry column (using the right-hand axis). Transpiration is estimated from several pine trees near the US-NR1 tower during the summers of 2004, 2006, and 2007. For all other variables, the diel cycle is calculated from 30 min measurements between years 1999–2012.

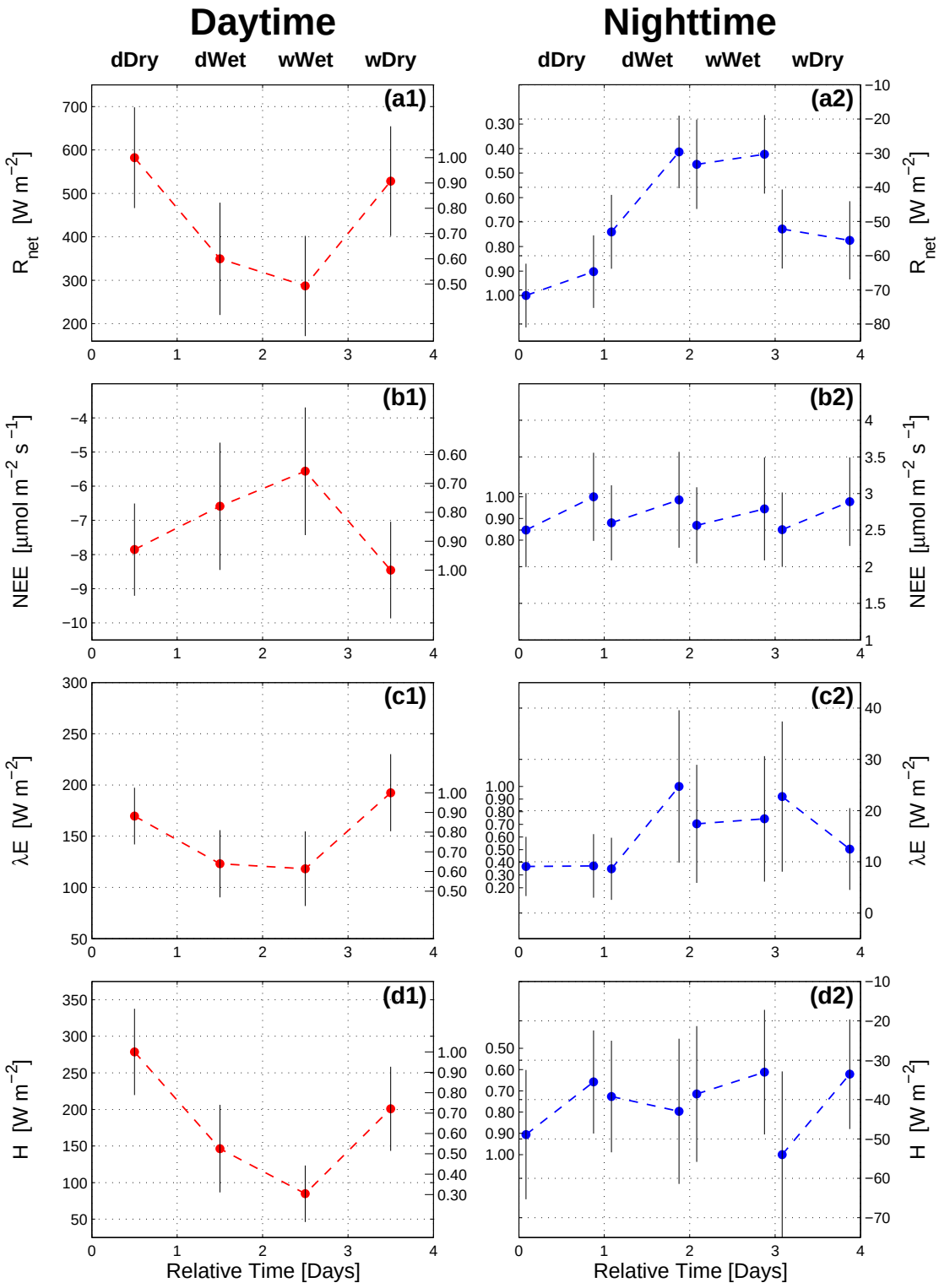

Figure 5.10: Mean values for (left column) daytime (10:00–14:00 MST) and (right column) night (00:00–04:00 MST) and evening (19:00–23:00 MST) periods of: **(a1, a2)** net radiation R_{net}; **(b1, b2)** net ecosystem exchange of CO_2 NEE; **(c1, c2)** latent heat flux λE; and **(d1, d2)** sensible heat flux H. The values are arranged from left-to-right in the order of dDry, dWet, wWet, and wDry conditions. The vertical black lines represent the mean absolute deviation (MAD) of the 30 min data within that particular category and time period. The numerical values shown between the daytime and nighttime panels represent the fractional change relative to the largest (or smallest) data value within the panel.

smaller than the daytime values, the fractional changes and pattern of nocturnal R_{net} due to different precipitation states (Fig. 5.10a2) were similar to those of mid-day R_{net} (Fig. 5.10a1). If we assume that wet nights were cloudier than dry nights, the radiative surface cooling on clear nights was around $-70\,\text{W}\,\text{m}^{-2}$ while cloudy nights was closer to $-30\,\text{W}\,\text{m}^{-2}$. The reduction of the magnitude of R_{net} on wet nights was primarily due to changes in cloud cover as well as changes to the turbulent fluxes.

Sensible heat flux during mid-day had a similar pattern to net radiation, with a large decrease in H (by $\approx 70\,\%$) between dDry and wWet conditions, followed by a return toward dDry H on wDry days (Fig. 5.10d1). In contrast, latent heat flux followed a different pattern—the largest mean mid-day λE occurred on a wDry day with a value of around $200\,\text{W}\,\text{m}^{-2}$, which was around $15\,\%$ larger than mid-day λE on dDry days (Fig. 5.9c, Fig. 5.10c1). The extra energy used by λE (coupled with slightly lower R_{net} values on wDry days) explains why mid-day H only recovered to within $80\,\text{W}\,\text{m}^{-2}$ (or $30\,\%$) of dDry H as dictated by the SEB (Eq. (1.1)) and shown in Fig. 5.9d.

At night, latent heat flux cooled the surface and was strongly affected by changes in the precipitation state (Fig. 5.10c2) following a pattern similar to that of nocturnal R_{net} (Fig. 5.10a2). Nocturnal sensible heat flux changed by around 30–40 % during the different precipitation states but the pattern did not clearly follow that of either R_{net} or λE (Fig. 5.10d2). At night, H generally warms the surface (including the forest vegetation and other biomass) following the air-surface temperature gradient (i.e., similar to the vertical temperature differences shown in Fig. 5.4d and f). In this way, H acts to compensate for air-surface temperature differences that might be generated by the surface cooling effects of R_{net} and λE. Even though the vertical air temperature differences were largest during dDry conditions (Fig. 5.4d and f) the largest sensible heat flux occurred during wDry periods between 00:00–04:00 MST (Fig. 5.10d2). This is exactly when λE was at a maximum (so evaporative cooling would be expected) and a close look at Fig. 5.4f reveals that the temperature difference between the air just above the ground and soil was larger in wDry conditions than dDry conditions. We should also note that what is shown in Fig. 5.4d and f are vertical air temperature differences which serve as a surrogate for the actual difference between air temperature and the

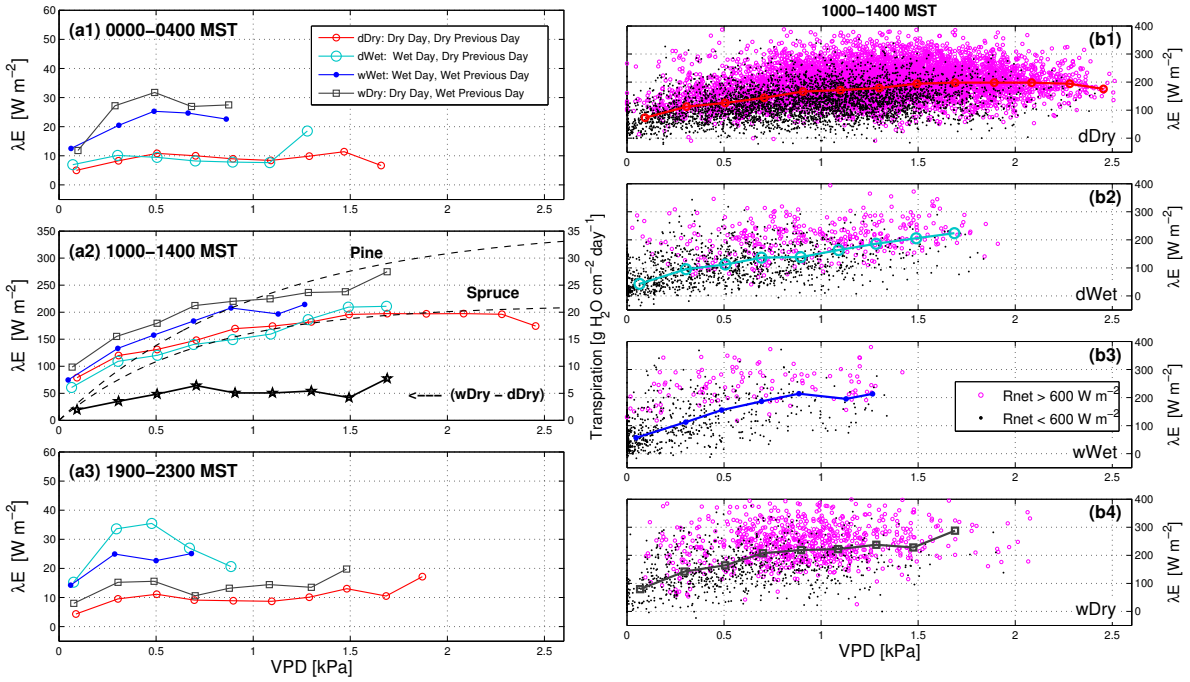

Figure 5.11: The (left column) binned 21.5 m latent heat flux λE vs. 8 m vapor pressure deficit VPD for **(a1)** night (00:00–04:00 MST), **(a2)** daytime (10:00–14:00 MST), and **(a3)** evening (19:00–23:00 MST) periods. Each line represents a different precipitation state as shown in the legend. In **(a2)**, the dashed black lines are the empirical exponential fits of transpiration per unit sapwood area vs. VPD for 2006 as determined by Hu et al. [2010b] for pine and spruce trees (using the right-hand axis). Also, the difference in λE between wDry and dDry conditions is shown as a solid black line. As an example of the variability in the binned data, the right-column panels show the 30 min daytime data used to create the binned daytime lines (i.e., corresponding to what is shown in panel **a2**). The right-column panels are for **(b1)** dDry, **(b2)** dWet, **(b3)** wWet, and **(b4)** wDry periods. In the scatter plots, the individual points are distinguished by R_{net} as shown by the legend in **(b3)**,

surface elements (i.e., tree branches, needles, boles, and the soil surface) [e.g., Froelich et al., 2011].

5.4.5 The evaporative contribution to λE

The increased λE values on wDry days was presumably due to evaporation of the intercepted liquid water present on vegetation and in the soil. Because of the effect of temperature on saturation vapor pressure (and thus VPD) one cannot assume outright that nocturnal λE is representative of daytime evaporation [e.g., Brutsaert, 1982]. To further explore this issue, we have plotted λE vs. VPD in Fig. 5.11 where we observe that nocturnal λE in dry conditions was $\approx 10\,\text{W}\,\text{m}^{-2}$ with

a weak dependence on VPD. The trend toward less evaporation in dDry conditions is due to a large soil resistance to evaporation when the soil/litter surface under a canopy is dry [Baldocchi and Meyers, 1991]. This is consistent with there being a small, persistent baseline level of evaporation in dry conditions and we make an assumption that this level of evaporation is similar during the daytime. Therefore, in dDry conditions we can estimate that evaporation was $\approx 10\,\mathrm{W\,m^{-2}}$ and evapotranspiration was $\approx 170\,\mathrm{W\,m^{-2}}$ (based on mid-day λE, Fig. 5.10c1). This suggests that, on average, evaporation comprised about 6 % of evapotranspiration in dry conditions.

Can we make a similar estimate of the evaporative contribution to λE as the canopy and soil are drying out? By comparing dDry and wDry conditions we make the following observations: (1) mid-day λE in wDry conditions was larger than dDry conditions (Fig. 5.9c), (2) mid-day transpiration was relatively smaller in wDry conditions than dDry conditions (Fig. 5.9e), (3) net radiation in dDry and wDry conditions was similar (Fig. 5.9a), (4) soil moisture content was relatively high on wDry days (Fig. 5.5d), suggesting the presence of an available source of liquid water for evaporation, and (5) previous research of transpiration at the US-NR1 site [Turnipseed et al., 2009, Hu et al., 2010b] has shown that ecosystem-scale transpiration increases as VPD increases. We also observe that daytime λE follows a trend with VPD that is very similar to that of transpiration measured within the forest (as shown by the dashed black lines in Fig. 5.11a2). From (1) and (2) above, we can conclude that the daytime increase in wDry λE was primarily caused by an increase in evaporation, not transpiration. If we also consider how λE varied with VPD a rough estimate of daytime evaporation comes from the λE difference during dDry and wDry conditions (shown as the solid black line in Fig. 5.11a2). As the atmosphere becomes drier the λE difference increased from near $15\,\mathrm{W\,m^{-2}}$ to around $50\,\mathrm{W\,m^{-2}}$ where it flattens out in drier conditions (for VPD > 0.5). Therefore, following a rain event, daytime evaporation was somewhere between 15–$50\,\mathrm{W\,m^{-2}}$, while mid-day evapotranspiration increased from 100–$225\,\mathrm{W\,m^{-2}}$ (wDry line in Fig. 5.11a2). If we take the overall average of this ratio, it suggests that evaporation comprised between 15-25 % of evapotranspiration as the forest transitioned from wet to dry conditions.

Our results are mean estimates and the variability around these mean values can be large

[e.g., Burns et al., 2015b]. Some of this variability is due to the random nature of turbulence in the atmosphere, whereas some can be explained by differences in net radiation, atmospheric stability, air temperature, and stomatal control. For example, in the scatter plots of Fig. 5.11b1-b4, the λE data with larger R_{net} values generally fall above the bin-averaged line that is drawn through the cloud of data points.

We also observed that increased λE lasted throughout a wDry day until around 18:00 MST when λE came within around 10 % of λE in dDry conditions (Figs. 5.9c and 5.11a3). This suggests that the evaporative effect lasted at least 18 hours following a significant precipitation event. Central to our calculations is the assumption that λE at night was primarily evaporation. Some evidence exists that the needle stomates opening at night combined with cuticular water loss could lead to small amounts of nocturnal transpiration [e.g., Novick et al., 2009]. If this occurred at US-NR1, it is likely a small effect which is further discussed by Turnipseed et al. [2009].

5.4.6 Net ecosystem exchange of CO_2 (NEE)

As one would expect, the magnitude of daytime NEE was reduced during wet conditions due to decreased photosynthetically active radiation (PAR) which is shown as a decrease in R_{net} in Fig. 5.9a [Yi et al., 2004]. The ratio between mid-day PAR and R_{net} was similar for all precipitation states (Table 5.3) and we will use R_{net} as a surrogate for PAR in our discussion. The wDry days were when the forest was most effective at assimilating CO_2 and NEE increased by over $3\,\mu\text{mol}\,\text{m}^{-2}\,\text{s}^{-1}$ ($\approx 30\,\%$) between wWet and wDry days (Fig. 5.10b1).

Nocturnal NEE was not affected very much (less than 10 %) by changes in the precipitation state and any effect was overshadowed by the difference between NEE in the late evening compared to the early morning (Figs. 5.9b and 5.10b2). Though the seasonal nocturnal ecosystem respiration signal was, at least for the seasonal-scale, apparently captured at the 21.5 m measurement level (i.e., Fig. 5.2a), it appears that the effect of advection on the diel cycle is larger than any effect of precipitation.

The lack of any strong effect of precipitation on the flux of CO_2 (NEE) compared to water

vapor (λE) is perplexing because one would expect the turbulence to transport water vapor and CO_2 in a similar manner. A few possible reasons for this difference are: (1) soil respiration at the US-NR1 site was not strongly affected by precipitation, (2) long dry periods are rare enough that the Birch effect (i.e., CO_2 pulse following precipitation) did not have a large impact on the overall warm-season NEE statistics, (3) the measurement of NEE at 21.5 m was not accurately describing the soil respiration at the soil surface due to surface decoupling and/or other problems related to stable conditions [e.g., Holtslag and De Bruin, 1988, Mahrt, 1999, Staebler and Fitzjarrald, 2004, Finnigan, 2008, Aubinet, 2008, Thomas et al., 2013], (4) the difference in vertical location of these two scalar sources (e.g., liquid water evaporates from the vegetation surfaces as well as at the ground whereas respiration of CO_2 occurs almost exclusively at the ground) caused differences in the sensitivity to precipitation [Edburg et al., 2012], or (5) an effect of the shorter atmospheric residence-time and larger background variability of water vapor compared to CO_2 which affects the surface fluxes. Previous measurements (mostly during the daytime) of soil respiration R_{soil} at US-NR1 with a manual chamber system by Scott-Denton et al. [2003, 2006] found that the dependence of soil respiration on soil moisture over a given summer was small. It has also been suggested by Huxman et al. [2004, 2003] that ecosystem respiration at the US-NR1 site is subject to controls from temperature and radiation as much as from precipitation (in contrast to an arid or semi-arid ecosystem such as a desert grassland where R_{eco} is strongly dependent on precipitation). The CO_2 pulse related to the Birch effect has been detected by eddy-covariance at a wide variety of ecosystems that are listed in the introduction. For the current study, the relevant results are: (i) the 21.5 m nocturnal NEE measurements were able to detect the increase in nocturnal ecosystem respiration over the warm-season (Fig. 5.2a), and (ii) the nocturnal NEE was not strongly affected by precipitation (Fig. 5.10b2). This suggests that, at the seasonal/annual time-scale, precipitation plays a minor role in modifying the contribution of ecosystem respiration to the above-canopy NEE for this subalpine ecosystem.

5.4.7 Asymmetry in the diel cycle of net radiation and turbulent fluxes

One other interesting aspect of the diel cycle is related to the timing of fluxes relative to solar noon. As one would expect, the top of the atmosphere radiation reached a maximum near 12:00 MST (Fig. 5.9a). In contrast, the maximums for composited R_{net}, λE, and H occurred at about 11:00 MST on dry days and 10:00 MST on wet days (Fig. 5.9a, c–d). For NEE, the peak uptake of CO_2 was between 09:00–10:00 MST on both wet and dry days (Fig. 5.9b). The fact that the peak in the energy fluxes was different for wet and dry conditions suggests that clouds were affecting the composited diel cycle.

In Fig. 5.12 we further examine the role of clouds on the diel cycle by sub-dividing the dDry days into clear sky (dDry-Clear) and cloudy (dDry-Cloudy) days. Clear skies occurred on about 18 % of the dDry days and this is reflected by the fact that the dDry statistics closely follow those of dDry-Cloudy statistics. The peak in R_{net} and H during dDry-Clear days were all near 12:00 MST which was consistent with the timing of the maximum top of the atmosphere radiation. The peak in λE moved closer to noon, but was still slightly before noon.

On dDry-Clear days, R_{net} was enhanced by an additional 30 % compared to cloudy days (Fig. 5.12a). This enhanced incoming radiation was reflected by larger turbulent energy (λE and H) fluxes on dDry-Clear days (Fig. 5.12c–d). Consistent with the findings by Monson et al. [2002], the magnitude of NEE was slightly smaller on clear-sky days suggesting that the forest was taking up more CO_2 when clouds were present (Fig. 5.12b). This result is primarily due to CO_2 uptake by vegetation being most efficient under diffuse radiative conditions [e.g., Gu et al., 1999, 2002, Law et al., 2002, Wang et al., 2008]. However, as noted by Monson et al. [2002], there can be a confounding effect between air temperature and PAR on NEE (where the warmest temperatures were on clear-sky days with high PAR/R_{net}), and Yi et al. [2004] showed that air temperature has a significant effect on NEE at US-NR1. Since the publication of Burns et al. [2015a], we have realized this might be an issue, and have plotted the air temperature in Fig. 5.13 where it can be observed that clear days had cooler morning air temperature and warmer afternoon temperatures.

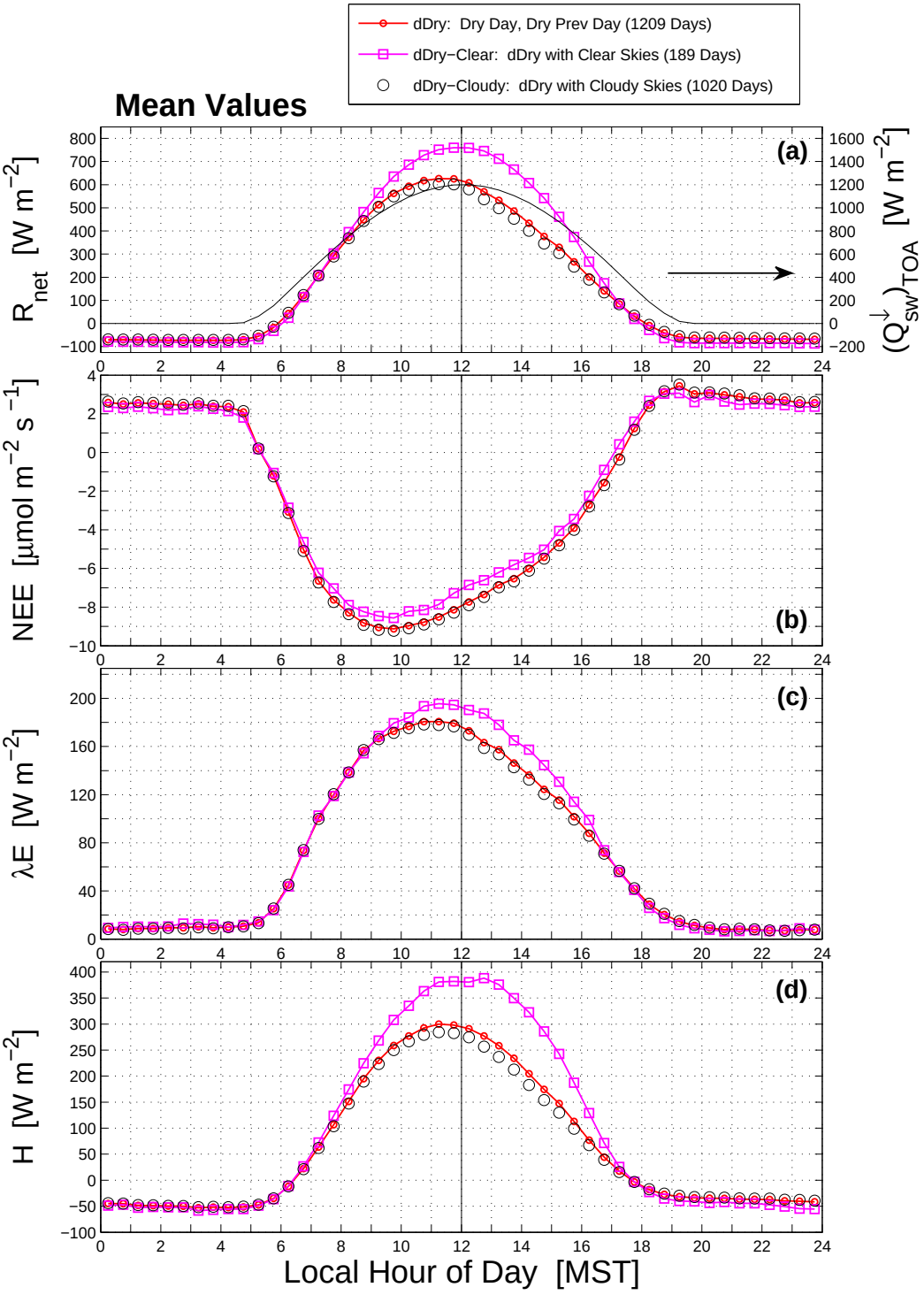

Figure 5.12: The mean warm-season diel cycle of **(a)** net radiation $R_{\rm net}$ (left-hand axis) and top-of-the-atmosphere incoming shortwave radiation $(Q^{\downarrow}_{\rm SW})_{\rm TOA}$ (right-hand axis, thin black line), **(b)** net ecosystem exchange of CO_2 NEE, **(c)** latent heat flux λE, and **(d)** sensible heat flux H, for dDry conditions. This is the same as the dDry column in Fig. 5.9, except the data have been further separated into dDry-Clear and dDry-Cloudy conditions as specified by the legend. For further details see the caption of Fig. 5.9.

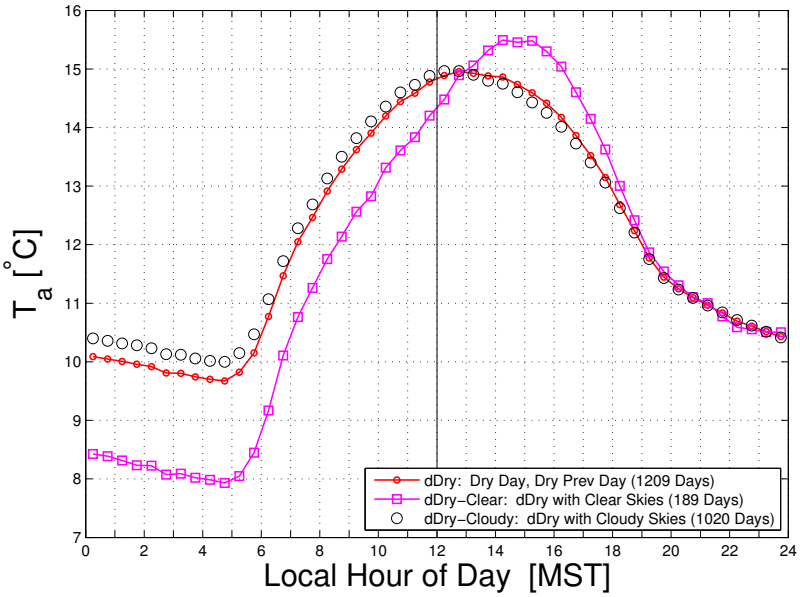

Figure 5.13: As in Fig. 5.12, but the 21.5 m air temperature is shown.

Because the trend in NEE does not change before/after noon, air temperature doesn't completely explain the trend, but the effect of air temperature on NEE (as well as seasonal changes) should be taken into consideration in the future. If λE was completely controlled by stomates, one would expect λE to mimic NEE and be larger on dDry-Cloudy days. However, the effect of higher R_{net} on clear days also affects λE (through the SEB equation) and drives it to slightly higher levels on dDry-Clear days.

5.4.8 The surface energy balance (SEB) closure

Though the individual components in the SEB balance equation (i.e., Eq. 1.1) were dramatically affected by precipitation (i.e., Fig. 5.10), the overall mean SEB closure fraction during mid-day was fairly consistent at around 0.9–1.1 (Fig. 5.14a1). This degree of energy closure is similar to that observed by previous research at the site [e.g., Turnipseed et al., 2002]. It appears that wet conditions lead to values which are slightly above 1 and dry conditions are slightly below 1. This suggests that there could be some small effect of precipitation on the SEB closure.

The nighttime SEB closure during the evening hours (19:00–23:00 MST) was at around 0.3-

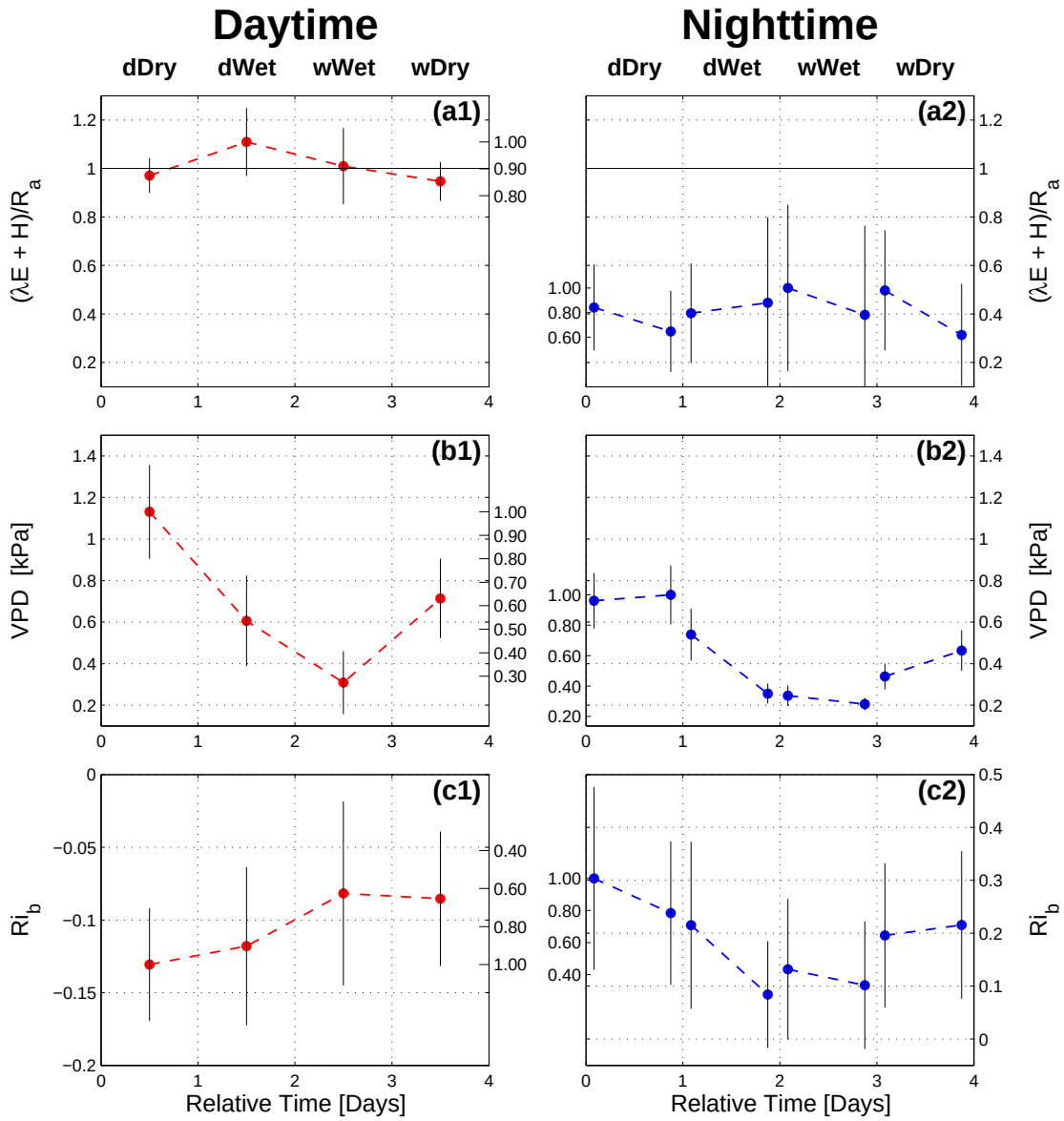

Figure 5.14: As in Fig. 5.10, showing **(a1, a2)** the surface energy balance closure fraction $(\lambda E + H)/R_a$; **(b1, b2)** vapor pressure deficit VPD; and **(c1, c2)** bulk Richardson number $\mathrm{Ri_b}$.

0.4 while closure during the early morning hours (00:00–04:00 MST) was closer to 0.4-0.5. Previous research has shown that these low nocturnal closure values are during periods of low winds that lead to large horizontal advection [Turnipseed et al., 2002, Burns et al., 2012b]. Any effect of precipitation on the SEB at night was overshadowed by differences related to the time of day. The effect of drainage flows on horizontal CO_2 advection at US-NR1 have been summarized in previous

studies [e.g., Sun et al., 2007, Yi et al., 2008] and our objective is to point out that the SEB closure improved after midnight, presumably because the wind speed and variability of mechanical turbulence increased. This result is consistent with the findings of Burns et al. [2011] that there is increased turbulence variability in the nocturnal boundary layer after around 23:00 MST. However, we have also reported (in Sect. 5.4.1) that stability tends to get stronger as the night progresses, especially in dDry conditions. Though outside the scope of the current study, our suspicion is that as the stability and wind speed increase during the night it leads to the formation of intermittent turbulent events caused by increased wind shear. In terms of precipitation, it is clear that the pattern of stability was disrupted by the rain event (affecting both the wind speed and vertical temperature gradients) and the nocturnal dry periods tended to be more stable ($\mathrm{Ri_b} > 0.2$) than the wet periods ($\mathrm{Ri_b} < 0.2$) as shown in Fig. 5.14c2. The decreased stability in wet conditions is especially prevalent in the early evenings as discussed previously in relation to the vertical CO_2 profiles (Sect. 5.4.3). Changes in VPD were closely related to changes in air temperature as reflected in how mean VPD changed with the precipitation state (Fig. 5.14b1 and b2). It is interesting that the pattern for nocturnal VPD (Fig. 5.14b2) was similar to that of stability (Fig. 5.14c2).

5.4.9 Canopy storage and soil heat flux in the surface energy balance

As mentioned in the introduction, the magnitude of the storage terms in the SEB balance equation (Eq. 1.1) are typically considered to be about 10% the magnitude of net radiation. Even though these are considered more minor terms, they often lag the primary SEB terms which can introduce important phase shifts [e.g., Lindroth et al., 2010, Leuning et al., 2012]. The storage terms related to the above-ground biomass and canopy airspace in the surface energy balance are,

$$S_{\mathrm{tot}} \;=\; S_H \;+\; S_{\mathrm{LE}} \;+\; S_{\mathrm{b}} \;+\; S_{\mathrm{n}} \;+\; J_A, \tag{5.2}$$

where S_H and S_{LE} are the sensible and latent heat energy stored in the air space between the ground and flux-measurement level, S_{b} is heat stored in the tree boles, and S_{n} is heat stored in the tree needles. J_A is the energy consumed by photosynthesis which was estimated by Turnipseed

et al. [2002] to be small, so we have neglected it. The tree bole temperatures were measured with thermocouples in each tree species (7 pine trees, 3 fir trees, and 2 spruce trees) at a nominal depth of 3 cm into the bole and at three vertical heights (near the ground, 0.5 m, and 1.5 m). The 1.5 m sensors were used to calculate the S_{b} term (to avoid snowpack effects in winter). Bole temperatures from the summers of 2011 and 2012 had a multiplexer problem, so these years were excluded from the storage term calculation. The needle temperature was estimated using the 8-m air temperature as a proxy for needle temperature. The storage terms in Eq. (5.2) were all calculated as described by Turnipseed et al. [2002] and interested readers should look there for additional details. The individual storage terms are shown over the diel cycle for each precipitation state in Fig. 5.15b1-b4. S_{tot} was at a maximum during dry conditions with a value near $100\,\mathrm{W\,m^{-2}}$ which corresponds to about 15 % of R_{net} (Fig. 5.15a1-a4).

The heat flux at the soil surface (G) was calculated from the average soil heat flux from the ≈ 10 cm deep heat-flux plates combined with the heat storage in the soil above the heat-flux plates S_{soil} [e.g., Oncley et al., 2007],

$$G \;=\; G_{\mathrm{plate}} \;+\; S_{\mathrm{soil}}. \tag{5.3}$$

The soil storage term was calculated with,

$$S_{\mathrm{soil}} \;=\; C_{\mathrm{soil}}\, z_p\, \frac{d\overline{T}_{\mathrm{soil}}}{dt}, \tag{5.4}$$

where C_{soil} is the volumetric heat capacity of the soil [$\mathrm{J\,m^{-3}\,K^{-1}}$], z_p is the depth of the heat-flux plates, and $\overline{T}_{\mathrm{soil}}$ is the average temperature of the soil layer above the heat-flux plates. For $\overline{T}_{\mathrm{soil}}$, the 107 thermistor sensor at a depth of 5 cm was used starting in summer of 2006. If the heat capacity of air within the soil matrix is neglected, then C_{soil} depends on the amount of water within the soil and can be calculated from,

$$C_{\mathrm{soil}} \;=\; \rho_{\mathrm{water}} c_{\mathrm{water}} \mathrm{VWC} \;+\; \rho_{\mathrm{soil.dry}} c_{\mathrm{soil.dry}}, \tag{5.5}$$

where the density of dry soil $\rho_{\mathrm{soil.dry}}$ was assumed to be $1700\,\mathrm{kg\,m^{-3}}$ with a specific heat capacity $c_{\mathrm{soil.dry}}$ of $900\,\mathrm{J\,kg^{-1}\,K^{-1}}$. For water, the values of ρ_{water} and c_{water} used were $998\,\mathrm{kg\,m^{-3}}$ and

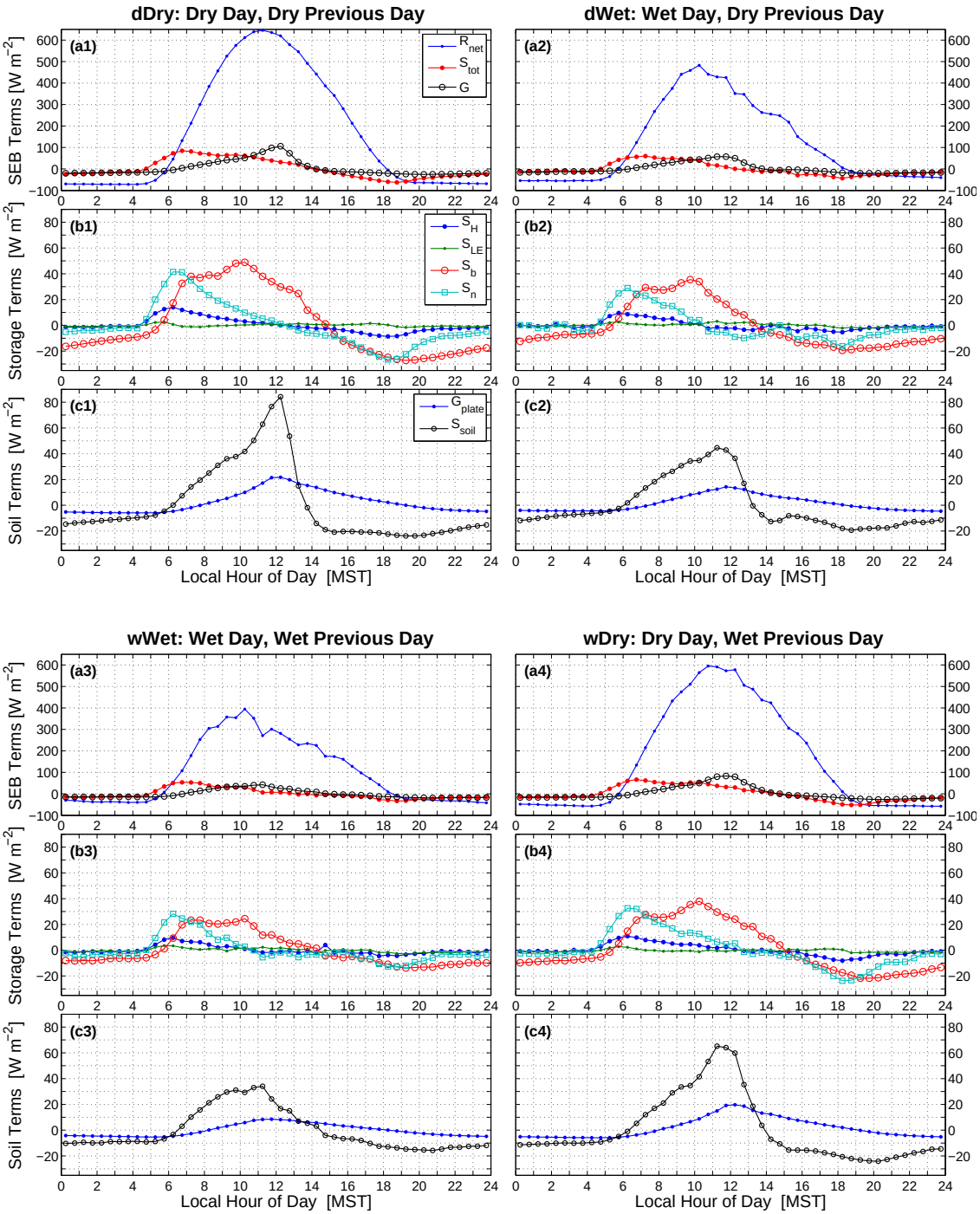

Figure 5.15: The warm-season mean diel cycle of **(a1-a4)** net radiation R_{net}, the sum of four storage terms S_{tot}, and soil surface heat flux G; **(b1-b4)** storage terms, sensible heat in the air column S_H, latent heat in the air column S_{LE}, heat storage in tree boles S_{b}, and heat storage in tree needles S_{n}; and **(c1-c4)** the average soil heat flux measured at 10 cm depth by several heat flux plates G_{plate} and the heat stored in the soil between the heat-flux plates depth and the ground surface S_{soil}. The diel cycles are shown for dDry, dWet, wWet, and wDry conditions. All panels use the legends shown for dDry conditions.

$4182\,\mathrm{J\,kg^{-1}\,K^{-1}}$, respectively. The volumetric water content VWC of the soil ranged between less than $0.1\,\mathrm{m^3\,m^{-3}}$ for dry soil to around $0.4\,\mathrm{m^3\,m^{-3}}$ for saturated soil. At mid-day, the soil storage term was found to be about twice as large as the measured soil heat flux (Fig. 5.15c1-c4). Therefore, the soil storage term has a significant contribution to the surface energy balance and should be included in future studies (note that S_{soil} was neglected by Turnipseed et al. [2002]).

5.4.10 Time series of measured fluxes

During the open-discussion portion of the *Biogeosciences* review of Burns et al. [2015a], it was suggested that a time series of the fluxes be provided. Bin-averaging can sometimes produce mis-leading results so we agreed with this suggestion. A time series of the measured fluxes is shown in Fig. 5.16. This period includes a large rain event between days 188-191. On the day following this rainy period, there was enhanced latent heat flux (Fig. 5.16c) which is a characteristic similar to what we found using the bin-averaged data.

5.5 Conclusions

The influence of warm-season precipitation on the scalars and fluxes at the US-NR1 site has been examined. Detailed conclusions on this topic can be found in Sect. 7.1.

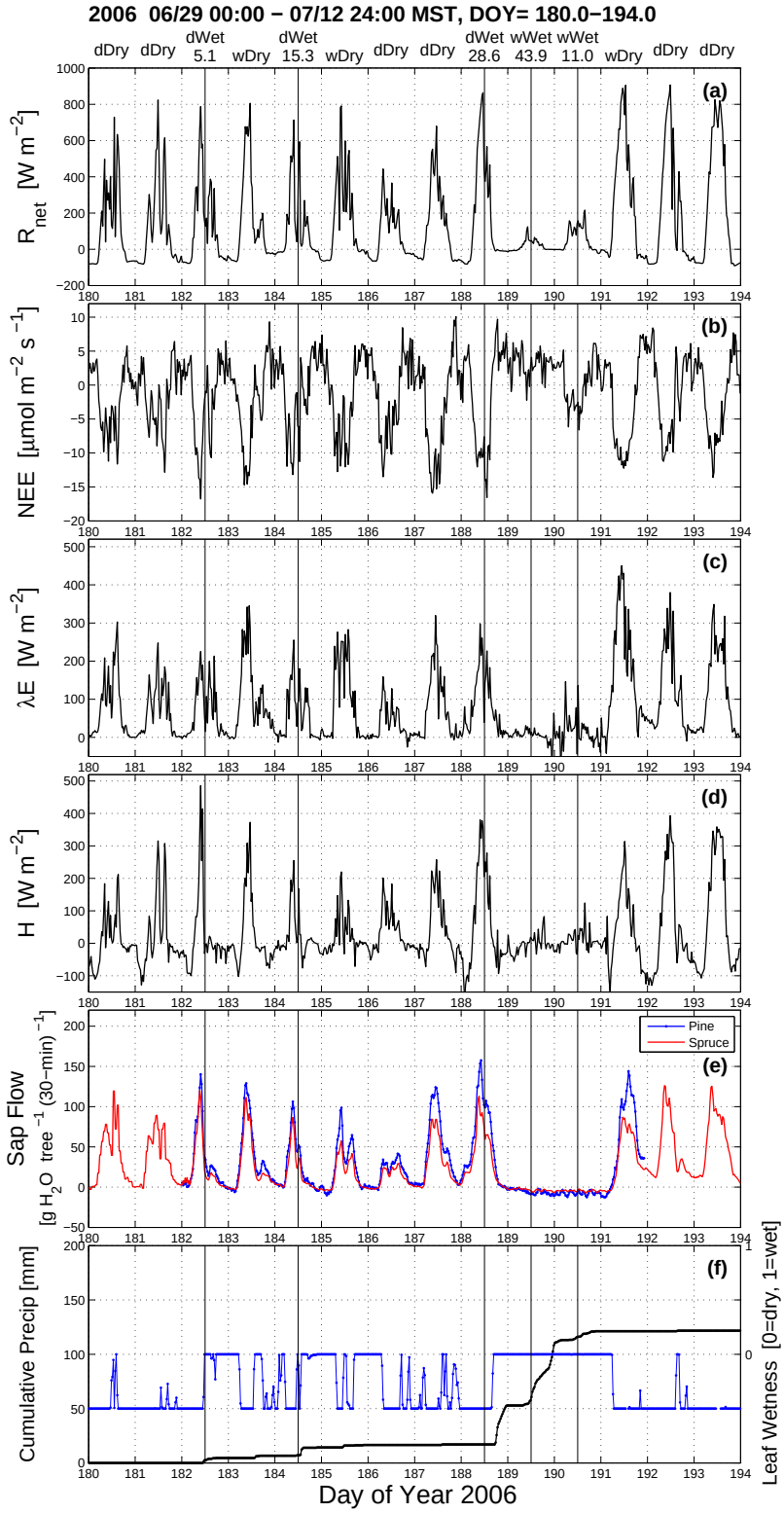

Figure 5.16: Fourteen-day time series of 30-min values of **(a)** net radiation R_{net}, **(b)** net ecosystem exchange of CO_2 NEE (without any u_* filter), **(c)** latent heat flux λE, **(d)** sensible heat flux H, **(e)** sap flow, and **(f)** cumulative precipitation (left axis) and leaf wetness (right axis). Above **(a)**, the time period is provided along with the precipitation state for each day. The wet days are identified by a thin vertical black line with the daily total precipitation (in mm) shown above panel **(a)**.

Chapter 6

A comparison of the diel cycle of modeled and measured latent heat flux during the warm season in a Colorado subalpine forest

Abstract

This work has recently been published in the AGU Journal of Advances in Modeling Earth Systems (JAMES) [Burns et al., 2018]. This chapter extends the observational analysis from Chapter 5 to include land-surface modeling of the warm-season ecosystem fluxes. Within this chapter we describe any additional analysis techniques used, followed by the results. Because land-surface models are often used to project changes in the hydrological cycle, modeling the effect of precipitation on the latent heat flux is an important aspect of land-surface models. In this chapter, we compare the conditionally-sampled diel composites of observed US-NR1 above-canopy sensible H and latent heat λE fluxes to those from the Community Land Model (CLM, version 4.5), where the model is driven using meteorological and radiation data measured from the US-NR1 micrometeorological tower. With respect to measured λE during the warm-season, we focus on two results from the previous chapter: for the day following above-average precipitation, λE was enhanced at mid-day by $\approx 40\,W\,m^{-2}$ (relative to dry conditions), and nocturnal λE increased from $\approx 10\,W\,m^{-2}$ in dry conditions to over $20\,W\,m^{-2}$ in wet conditions. With default settings, CLM4.5 did not successfully model these changes. By increasing the amount of time that rainwater was retained by the canopy/needles,

CLM was able to match the observed mid-day increase in λE on a dry day following a wet day. Stable nighttime conditions were problematic for CLM4.5. Nocturnal CLM λE had only a small ($\approx 3\,W\,m^{-2}$) increase during wet conditions, CLM nocturnal friction velocity u_* was smaller than observed u_*, and CLM canopy air temperature was $2\,^{\circ}C$ less than those measured at the site. Using observed u_* as input to CLM increased λE; however, this caused CLM λE to be increased during both wet and dry periods. We suggest that sloped topography and the ever-present drainage flow enhanced nocturnal u_* and λE. Such phenomena would not be properly captured by topographically blind land-surface models, such as CLM.

6.1 Introduction

Models of the earth system are tools used to evaluate what might happen to our planet in the future. Because observations are limited in time and space, one productive use of ecosystem observations is to verify the accuracy of models. Such information can help us to better understand the parameter space over which a model is valid; for example, certain features of models may only be applicable in the ecosystem where they were initially developed in. In this chapter we use a popular land-surface model to see if it can reproduce the influence of precipitation which we found in the observations (as presented in the previous chapter). Here, we focus on the ecosystem energy fluxes (sensible and latent heat), with particular attention to the evapotranspiration, or latent heat flux. We start the chapter by introducing the land-surface model, describe a few new analysis tools specific to the model-data comparisons, and introduce a second AmeriFlux site (in less complex terrain, Howland Forest) which is used as a contrast to US-NR1. In the rest of the chapter, the results from our comparison are shown.

6.2 Information related to the US-NR1/model comparison

6.2.1 The Community Land Model (CLM)

For our study, the Community Land Model (CLM) version 4.5 (CLM4.5, Oleson et al. [2013]) was run in single-point mode driven with satellite-derived phenology and 30-min US-NR1 tower observations. The above-canopy tower observations used for model input were: horizontal wind speed U, air temperature T_a, relative humidity RH, barometric pressure P, precipitation, and incoming shortwave and longwave radiation. The CLM soil texture was set to a loamy sand (72% sand, 27% silt, 1% clay), based on a soil sample taken near the tower (Appendix C). In CLM, the appropriate plant functional type for US-NR1 is a temperate needleleaf evergreen forest. For this plant type, CLM assumes a canopy height h of 17 m, momentum roughness length z_{0m} of $0.055h$, and displacement height d of $0.67h$ [Oleson et al., 2013]. Modifying the CLM4.5 value for h affected our our results; therefore, we chose a CLM4.5 h that was closer to that of the US-NR1 forest (details are in Appendix A). For ease of comparison, we use the same nomenclature as that of Oleson et al. [2013], and the symbols and variables used within this chapter are in Appendix B. Specific changes made to variables or settings for different CLM4.5 configurations used in our study are listed in Table 6.1.

6.2.2 Howland Forest information

The Howland Forest AmeriFlux site (site US-Ho1, Hollinger [1996-present]) was included in our study to serve as a contrast to the US-NR1 site. The US-Ho1 site is located in a spruce-hemlock forest in Maine with a tree density of around 2600 trees ha^{-1}, LAI of 5.5, and tree heights on the order of 20 m [Hollinger et al., 1999]. (The corresponding values for US-NR1 are 4000 trees ha^{-1} with a LAI of 3.8–4.2 $\mathrm{m}^2\mathrm{m}^{-2}$ and tree heights of 12–13 m with more details in Sect. 4.4). The landscape at the US-Ho1 site can be considered "rolling hills", with a maximum elevation change of less than 68 m within a 10 km area. The US-Ho1 site was chosen because it has a forest of comparable LAI to that of US-NR1, but without the nocturnal slope flow found at US-NR1 (US-

Table 6.1: Modifications made to CLM4.5 as part of the sensitivity experiments.

CLM4.5 Configuration Name	CLM4.5 Variables and Settings Used for each Configuration: Form of Universal Function	u_* Source[a]	(ζ_{stable}^{max})[b]	(f_{wet}^{max})[c]	S-Z[d]	$(C_{s,dense})$[e]	Notes / Long Description
A1:	Zeng et al. [1998]	CLM	2	1	S-Z	0.004	Changed default soil texture (43% sand, 21% clay) to a value more appropriate for the US-NR1 site (72% sand, 1% clay); the CLM4.5 canopy height was also set to 13 m (see Appendix A for details)
B0:	Zeng et al. [1998]	CLM	2	0.02	S-Z	0.004	Test the impact of varying f_{wet}^{max}
B1:	Zeng et al. [1998]	CLM	2	0.02	na	0.004	
B2:	Zeng et al. [1998]	Obs	100	0.02	na	0.004	
C0:	Zeng et al. [1998]	Obs	2	1	S-Z	0.004	Test the impact of using observed u_*
D0:	Zeng et al. [1998]	CLM	100	1	S-Z	0.004	Test the impact of varying *zetamaxstable* ζ_{stable}^{max}
D1:	Zeng et al. [1998]	Obs	100	1	na	0.004	Test the impact of varying the universal function form
D2:	Högström [1988]	Obs	100	1	na	0.004	
D3:	Handorf et al. [1999]	Obs	100	1	na	0.004	
E0:	Zeng et al. [1998]	CLM	2	1	na	0.004	Test the impact of turning off S-Z [Sakaguchi and Zeng, 2009]
F0:	Zeng et al. [1998]	CLM	2	1	S-Z	0.01	Test the impact of varying $C_{s,dense}$
F1:	Zeng et al. [1998]	CLM	2	1	na	0.01	
F2:	Zeng et al. [1998]	Obs	100	1	na	0.01	
G1:	Högström [1988]	Obs	100	0.02	na	0.01	Changes made to all variables

Note: The alphanumeric codes in the 1st column are used throughout the text and figures to specify the configuration used for CLM4.5. The default configuration is "CLM4.5 A1", and a numerical value of "0" indicates a single variable has been modified from the CLM4.5 A1 configuration. For the A1 configuration, LAI is varied as described in the text.

[a] "Obs" indicates that US-NR1 observed friction velocity u_* was used as input to CLM; "CLM" indicates CLM4.5-calculated u_* was used

[b] The value of *zetamaxstable* ζ_{stable}^{max} (CLM4.5 default: $\zeta_{stable}^{max} = 2$)

[c] The value of *maximum leaf wetted fraction* f_{wet}^{max} (CLM4.5 default: $f_{wet}^{max} = 1$)

[d] "S-Z" indicates that the subcanopy stability correction proposed by Sakaguchi and Zeng [2009] was used; "na" indicates it was not used

[e] The value of the subcanopy turbulent transfer coefficient $C_{s,dense}$ (CLM4.5 default: $C_{s,dense} = 0.004$)

Ho1 also has a long data record, measurements there started in 1996). Further details about the US-Ho1 site are in Hollinger et al. [1999, 2004].

6.2.3 Statistical evaluation of results

As will be shown more explicitly in Sect. 6.3, the focus in this chapter is on two specific aspects of the warm-season diel cycle during wet and dry conditions. First, for a wDry day, mid-day λE was enhanced by $\approx 40\,\mathrm{W\,m^{-2}}$ relative to dry conditions, with a concomitant reduction in sensible heat flux H. Second, nocturnal λE increased from $\approx 10\,\mathrm{W\,m^{-2}}$ in dry conditions to over $20\,\mathrm{W\,m^{-2}}$ in wet conditions. Based on these observations from the measured fluxes, we evaluate CLM4.5 using

the following statistics: (1) calculating the mean difference in mid-day composite energy fluxes on a wDry day compared to a dDry day, and (2) taking the difference in nocturnal energy fluxes between 0–4 LST for a dDry period compared to a wDry period. Using λE as an example, these statistics will be designated as "wDry−dDry λE " in our discussion. These simple statistics will be applied to both the US-NR1 and US-Ho1 measurements and CLM4.5 model output. By using the difference statistics we are not explicitly comparing the mean values of the observed and CLM4.5 fluxes, but instead checking that the model and observations are responding to precipitation events in a consistent way.

Air and soil temperatures are readily measured in the field and calculated by CLM4.5, making them useful to evaluate the model performance. At US-NR1, three levels of aspirated air temperature and 11 levels of thermocouple air temperature from near the ground to twice canopy height were measured [Burns et al., 2015a]. We compare these tower observations with various CLM4.5 temperatures, which are: canopy surface temperature T_v, canopy airspace temperature T_s, the "2-m" level air temperature T_{2m}, and ground surface T_g and subsurface soil temperatures T_{soil}. Because CLM4.5 is a simple single-leaf model, temperatures such as T_s and T_{2m} are attempting to represent an average temperature from many locations where the true temperature may widely differ (e.g., shady versus sunny portions of the canopy). Therefore, the precise vertical location of T_v, T_s and T_{2m} can be a bit vague. In the CLM4.5 manual T_{2m} is defined as being "2 m above the apparent sink for sensible heat" which is defined by the roughness length for heat and displacement height [Oleson et al., 2013]. Since T_{2m} and T_s are usually only separated by an offset, we will often only show T_s which should be comparable with air temperature observations within the canopy (at US-NR1, these are the thermocouples or aspirated temperature sensors at 2 m and 8 m).

6.2.4 Additional details

The dDry conditions are likely to provide the most robust comparison for the following reasons: (1) they are the most common precipitation state with approximately 1148 days (or over 3 years worth of 30-min time periods) available for analysis which provides good statistics, and (2) the

gap-filling of the fluxes due to sensor problems caused by precipitation are at a minimum in dDry and wDry conditions. For a list of the problems that precipitation causes with eddy covariance measurements, see, for example, van Dijk et al. [2015].

Our analysis examines the sensitivity of CLM fluxes and temperatures to changing certain variables or parameters within CLM4.5, using the nomenclature and alphanumeric descriptions in Table 6.1. For example, "CLM4.5 A1" will be considered the default configuration of CLM4.5. The leading letter describes changes to a specific variable (A is default, B is related to f_{wet}^{max}, C is related to u_*, and so on). Unless specified otherwise, the CLM4.5 results in our plots are shown as closed or filled symbols and the tower observations are shown as open circles.

6.3 Comparison between US-NR1 measurements and CLM

6.3.1 Net radiation and turbulent energy fluxes

After each day was organized into the precipitation categories described in Sect. 5.2.1, the mean diel cycle of net radiation, the turbulent energy fluxes, and precipitation are plotted side-by-side based on the precipitation state for a given day (Fig. 6.1). As one would expect, a majority of the rain occurred during dWet and wWet days (Fig. 6.1d) when clouds increased and mid-day net radiation was reduced (Fig. 6.1a). Our analysis is focused on two main features of Fig. 6.1: (i) in wDry conditions mid-day λE was enhanced by around $40\,\mathrm{W\,m^{-2}}$ compared to dDry conditions with a concomitant reduction in mid-day sensible heat flux (green arrows in Fig. 6.1b and c), and (ii) at night, in wet conditions, latent heat flux was enhanced by about $15\,\mathrm{W\,m^{-2}}$ relative to dDry conditions (highlighted by the blue arrows in Fig. 6.1c). Numerical values of dDry and wDry λE and H (as well as wDry−dDry) are listed in Table 6.2, with other aspects of the effect of precipitation on the composite diel cycle at US-NR1 discussed in the previous chapter (or in Burns et al. [2015a]).

In Fig. 6.2 the CLM4.5 A1 net radiative and turbulent fluxes are compared with the measurements. Because CLM4.5 used the measured incoming shortwave and longwave radiation as input to the model, it is to be expected that CLM4.5 net radiation agrees well with the observations.

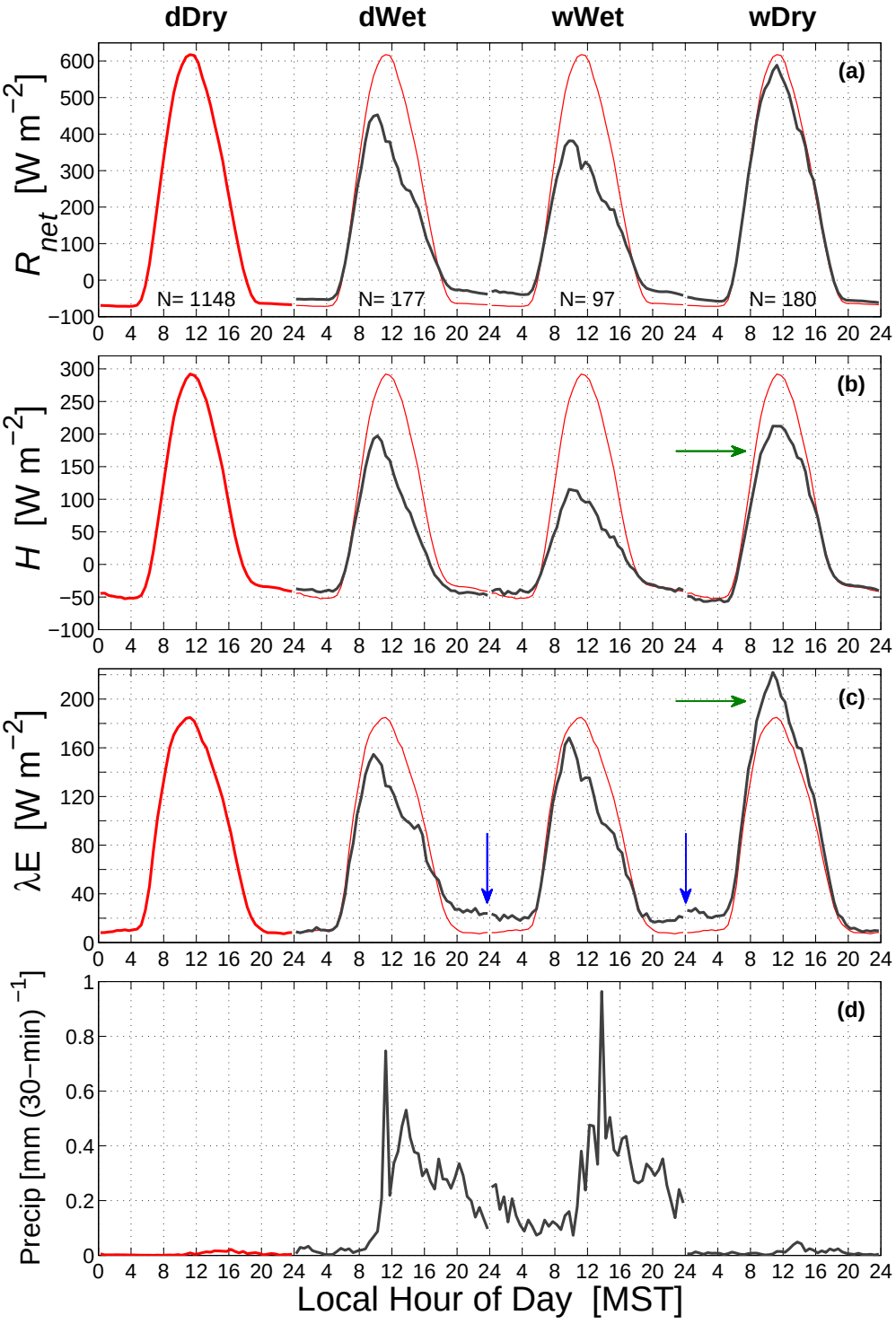

Figure 6.1: The mean warm-season composite diel cycle of **(a)** net radiation R_{net}, **(b)** sensible heat flux H, **(c)** latent heat flux λE, and **(d)** precipitation for each precipitation state (dDry, dWet, wWet, and wDry) where the precipitation state for each diel cycle is identified above panel **(a)**. For reference, the dDry diel cycle is repeated for all states as a red line. In panels **(b)** and **(c)**, the arrows refer to discussion points within the text. The diel cycle is calculated from 30 min measurements during the warm-season for years 1999–2003 and 2006–2014 with the approximate number of days (N) used to create each composite shown in panel **(a)**. More information on the measurements, precipitation state, and data compositing are within the text.

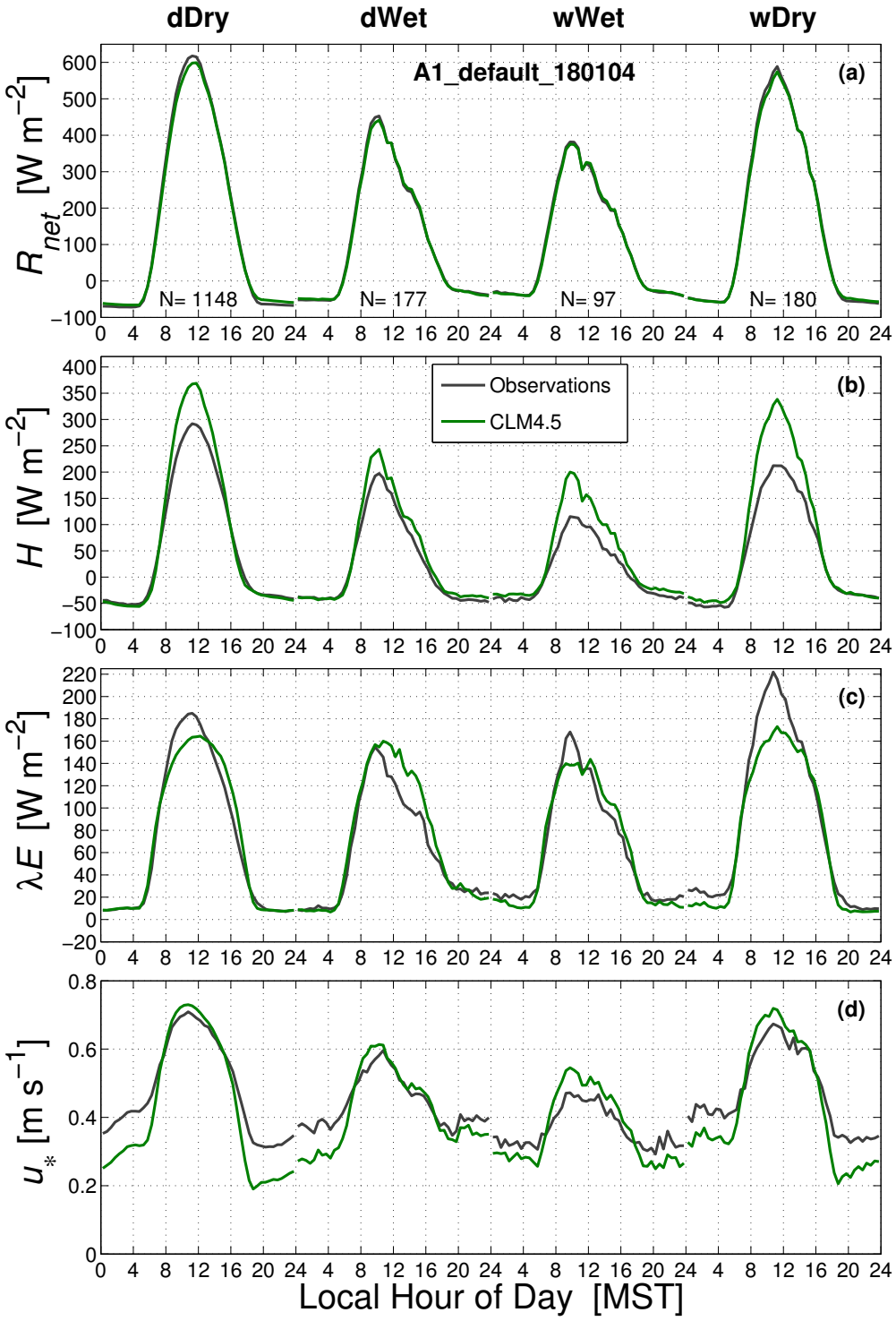

Figure 6.2: Similar to Fig. 6.1, but a comparison of the observations and CLM4.5 model output for **(a)** net radiation R_{net}, **(b)** sensible heat flux H, **(c)** latent heat flux λE, and **(d)** friction velocity u_*. The legend in panel **(b)** applies to all panels. The CLM results use the CLM4.5 A1 (default) configuration with a leaf area index (LAI) of 4 (Table 6.1).

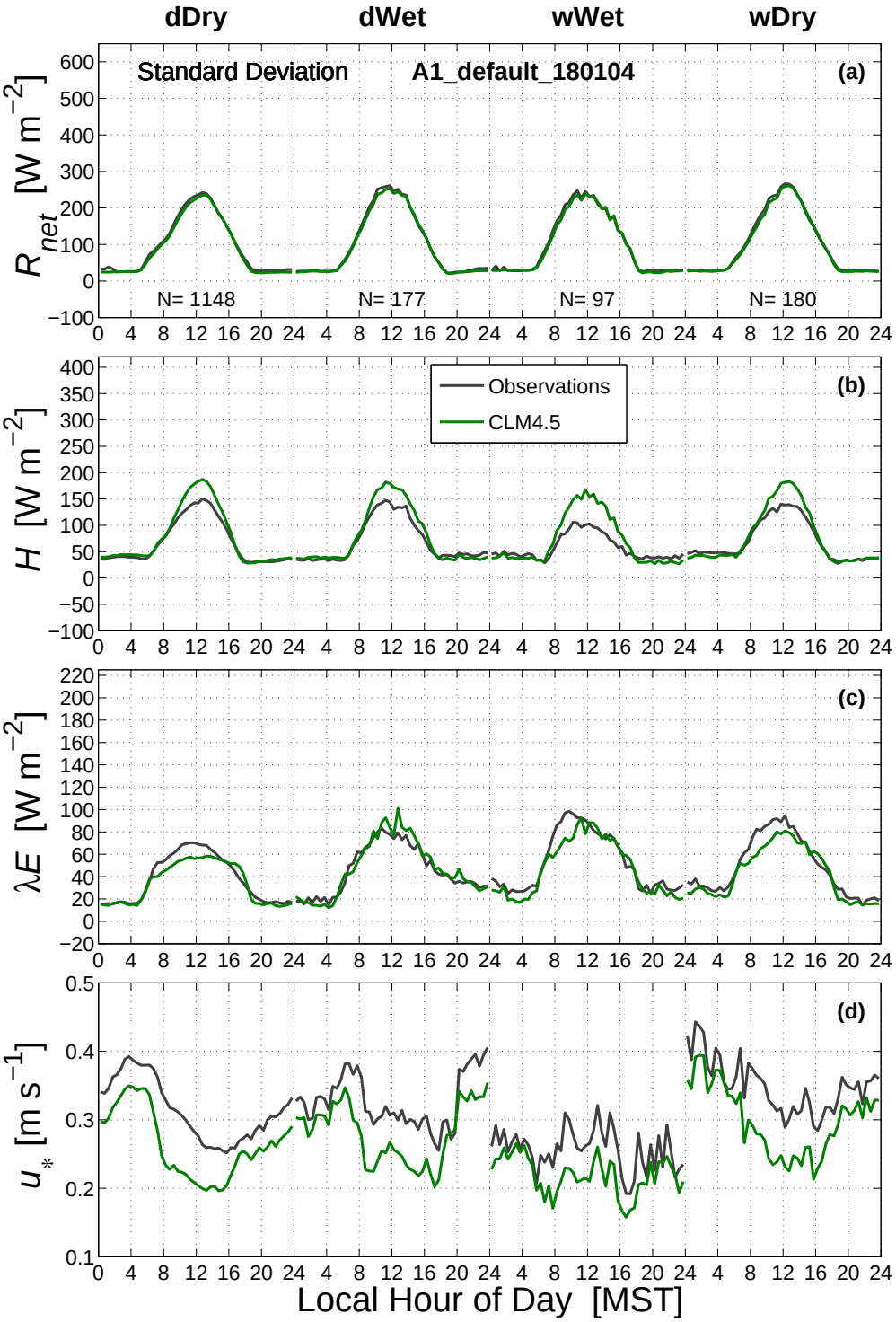

Figure 6.3: As in Fig. 6.2, except the standard deviation of the data within each bin are shown.

In general, during daytime, the CLM4.5 sensible heat flux was larger than the observations by anywhere from 50 to 100 $\mathrm{W\,m^{-2}}$ (Fig. 6.2b) whereas daytime CLM4.5 latent heat flux was similar or smaller than measured λE (Fig. 6.2c). With the exception of friction velocity, the variability or SD-Bin of the measured fluxes and CLM4.5 were of similar magnitude (Fig. 6.3). However, if we focus on the two items related to λE highlighted in the previous paragraph, we found that CLM did not properly reproduce either the increase in λE on wDry days or the enhanced latent heat flux at night in wet conditions. The CLM4.5 latent heat flux during mid-day and at night on wDry days was only slightly larger than λE during those same periods on dDry days (for numerical values, see the CLM4.5 A1 entry in Table 6.2).

6.3.2 Components of latent heat flux in CLM4.5

Latent heat flux is a combination of transpiration λE_v^t, and evaporation from the ground λE_g and vegetation/canopy λE_v^w surfaces. The component parts of CLM4.5 λE at three different LAI values are shown in Fig. 6.4. As LAI was increased, the components were affected as follows: (1) transpiration increased, (2) canopy evaporation increased slightly, and (3) ground evaporation decreased significantly. For all three LAI values in Fig. 6.4, CLM transpiration on a wDry day was similar to that of a dDry day. Therefore, if CLM is going to reproduce the enhanced λE during a wDry day observed at US-NR1, this "enhancement" needs to come from the canopy and ground evaporation. For LAI = 2, we can see that mid-day λE on a wDry day was larger than on a dDry day due to an increase in ground evaporation within a relatively more open forest (Fig. 6.4a). The increase in wDry λE qualitatively matches the US-NR1 observations shown in the upper panel of Fig. 6.4b, and we will discuss more about the LAI = 2 results in Sect. 6.3.3.

Next, we consider λE on the afternoon of wet (dWet and wWet) days in Fig. 6.4. At these times, US-NR1 λE was decreased relative to dDry λE. For CLM, the reduction in λE on the afternoon of wet days became larger as LAI increased; however, even for LAI= 6, the reduction was not as large as the US-NR1 observations. In contrast, the reduction of the CLM transpiration on wet-day afternoons looks qualitatively similar to the λE observations. The lack of diel symmetry

Table 6.2: Daytime and nighttime mean statistics of net radiation R_{net}, sensible heat flux H, and latent heat flux λE for dDry and wDry precipitation conditions for the warm-season for years 1999–2003 and 2006-2014. All R_{net}, H, and λE daytime and nighttime values in the table have units W m^{-2}, and those in bold are emphasized within the text. The two right-hand columns show the cumulative sum of R_{net}, H, and λE over the 2010 warm season (units: MW m^{-2}) and the percent difference relative to the US-NR1 measurements, respectively.

Site or Model	LAI	Variable	Daytime (10:00–14:00 MST) dDry	wDry	wDry-dDry	Night (00:00–04:00 MST) dDry	wDry	wDry-dDry	2010 Cumulative Sums[a] Total [MW m^{-2}]	Percent from US-NR1 [%]
US-NR1[b]	3.8-4.2	R_{net}	572.8	523.3	−49.5	−70.7	−52.6	18.1	1693.4	0
		H	270.5	197.1	−73.4	−48.7	−53.8	−5.1	693.0	0
		λE	172.6	195.3	**22.7**	9.2	24.0	**14.8**	**735.5**	0
US-Ho1[c]	≈ 5.5	R_{net}	471.5	460.3	−11.2	−37.3	−28.2	9.1	1353.9	−20.0
		H	210.5	175.6	−34.9	−17.6	−23.3	−5.6	593.2	−14.4
		λE	169.4	189.7	**20.3**	1.4	1.4	**0.02**	**646.0**	**−12.2**
A1	2	R_{net}	549.7	509.6	−40.0	−68.9	−56.9	12.0	1538.8	−9.1
		H	337.2	267.3	−69.9	−48.1	−39.9	8.2	834.4	20.4
		λE	132.6	169.0	**36.4**	9.7	15.6	**5.9**	**616.9**	**−16.1**
A1	4	R_{net}	557.9	514.3	−43.7	−64.2	−53.2	11.0	1593.5	−5.9
		H	337.4	298.0	−39.4	−51.7	−43.6	8.1	794.6	14.7
		λE	160.8	163.2	**2.4**	9.4	12.6	**3.1**	**719.5**	**−2.2**
A1	6	R_{net}	561.9	517.1	−44.8	−62.1	−51.7	10.4	1620.1	−4.3
		H	335.2	305.3	−29.9	−53.9	−47.0	6.9	766.0	10.5
		λE	178.6	170.8	**−7.8**	9.6	12.9	**3.3**	**763.2**	**3.8**
B0	4	R_{net}	558.0	515.1	−42.9	−64.4	−53.7	10.7	1591.4	-6.0
		H	335.9	286.1	−49.8	−51.8	−43.4	8.5	801.7	15.7
		λE	162.1	176.0	**13.9**	9.5	12.1	**2.6**	**707.1**	**−3.9**
B1	4	R_{net}	558.0	515.3	−42.7	−64.2	−53.6	10.6	1591.3	-6.0
		H	335.8	282.9	−53.0	−52.0	−43.5	8.4	797.5	15.1
		λE	164.2	181.3	**17.2**	9.4	12.3	**2.8**	**719.9**	**−2.1**
B2	4	R_{net}	556.8	514.3	−42.6	−71.7	−57.5	14.2	1528.9	-9.7
		H	341.7	285.7	−56.0	−65.3	−51.3	14.0	714.0	3.0
		λE	159.8	178.8	**19.0**	13.1	15.8	**2.7**	**746.3**	**1.5**
C0	4	R_{net}	557.2	514.2	−43.0	−72.7	−58.5	14.2	1524.3	-10.0
		H	337.8	288.4	−49.5	−66.5	−47.7	18.8	716.8	3.4
		λE	162.5	174.7	**12.2**	13.3	11.0	**−2.3**	**733.4**	**−0.3**

Table 6.2: Continued.

Site or Model	LAI	Variable	Daytime (10:00–14:00 MST) dDry	wDry	wDry-dDry	Night (00:00–04:00 MST) dDry	wDry	wDry-dDry	2010 Cumulative Sums[a] Total [MW m^{-2}]	Percent from US-NR1 [%]
		R_{net}	558.2	514.4	−43.8	−53.5	−47.2	6.3	1654.3	-2.3
D0	4	H	332.6	295.8	−36.8	−35.5	−36.3	−0.9	861.0	24.2
		λE	162.5	163.2	**0.7**	7.8	13.3	**5.5**	**709.2**	**−3.6**
		R_{net}	556.7	513.4	−43.2	−71.7	−57.1	14.5	1531.0	-9.6
D1	4	H	344.0	297.1	−46.9	−65.1	−52.0	13.2	707.7	2.1
		λE	157.6	166.3	**8.7**	12.8	16.6	**3.8**	**755.6**	**2.7**
		R_{net}	562.8	518.5	−44.3	−71.7	−56.9	14.8	1550.0	-8.5
D2	4	H	357.2	314.4	−42.8	−66.2	−51.9	14.3	741.7	7.0
		λE	152.5	157.0	**4.5**	13.0	15.9	**2.9**	**736.5**	**0.1**
		R_{net}	556.5	513.3	−43.2	−76.6	−59.5	17.1	1508.1	-10.9
D3	4	H	346.7	298.6	−48.0	−73.4	−56.2	17.2	681.0	-1.7
		λE	156.4	165.8	**9.4**	14.3	17.5	**3.2**	**759.3**	**3.2**
		R_{net}	557.8	514.4	−43.4	−64.1	−53.2	10.9	1593.2	-5.9
E0	4	H	337.9	295.2	−42.6	−51.8	−43.8	8.0	791.7	14.2
		λE	162.3	168.0	**5.7**	9.4	12.8	**3.5**	**730.8**	**−0.6**
		R_{net}	557.9	514.4	−43.5	−64.2	−53.3	10.9	1593.6	-5.9
F0	4	H	338.4	294.9	−43.5	−52.2	−44.5	7.7	785.5	13.3
		λE	161.4	167.4	**6.0**	10.0	14.2	**4.2**	**730.6**	**−0.7**
		R_{net}	557.6	514.5	−43.0	−64.3	−53.4	10.9	1592.7	-5.9
F1	4	H	342.0	290.6	−51.4	−52.2	−44.7	7.5	777.7	12.2
		λE	160.4	174.1	**13.7**	9.8	14.8	**5.0**	**745.3**	**1.3**
		R_{net}	555.9	513.1	−42.8	−72.0	−57.3	14.7	1529.9	-9.7
F2	4	H	355.2	298.0	−57.2	−65.0	−52.6	12.5	699.7	1.0
		λE	148.9	166.9	**18.0**	12.9	18.7	**5.8**	**765.1**	**4.0**
		R_{net}	562.7	519.2	−43.5	−71.9	−57.3	14.6	1547.6	-8.6
G1	4	H	359.6	298.0	−61.6	−66.9	−51.9	14.9	734.0	5.9
		λE	152.4	175.7	**23.4**	13.7	17.0	**3.3**	**742.0**	**0.9**

Note: Years 2004 and 2005 were not used because the 4-component radiometer on the US-NR1 tower was not available, which provided the incoming shortwave and longwave radiation used as input to drive CLM. At US-Ho1, statistics are from years 1996–2014. The CLM4.5 results are from US-NR1 for different configurations of the CLM4.5 software as shown by the alphanumeric code listed in column 1 and described in Table 6.1. Column 2 has the estimated leaf area index (LAI) for the flux sites or the LAI used by CLM4.5.

[a] Cumulative sums of each variable for the warm season of 2010 (June–September) are shown along with the percentage difference relative to the US-NR1 tower measurements. The cumulative sums of the energy terms have units of megawatt (MW) per square-meter of forest.

[b] For US-NR1, the number of 30-min samples within each of the precipitation categories are: dDry = 1148, dWet = 177, wWet = 97, and wDry = 180. The CLM statistics are from the same time periods as US-NR1.

[c] For US-Ho1, the number of 30-min samples within each of the precipitation categories are: dDry = 1029, dWet = 161, wWet = 50, and wDry = 214.

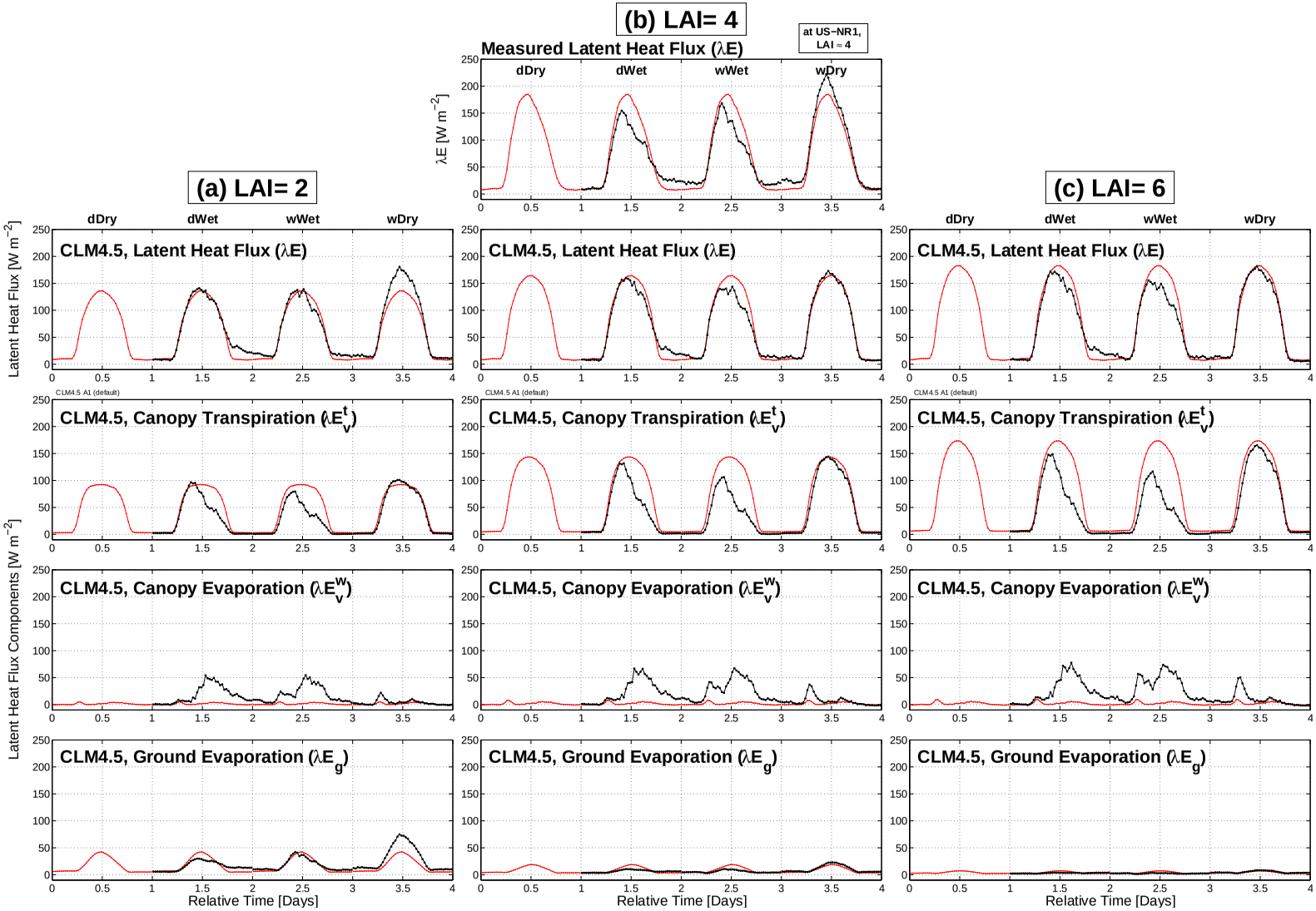

Figure 6.4: The mean diel cycle of latent heat flux λE separated into dDry, dWet, wWet, and wDry conditions for **(a)** leaf area index LAI=2, **(b)** LAI=4, and **(c)** LAI=6. The red line in each panel is the mean diel cycle for dDry conditions which is repeated for ease of comparison to the results from dWet, wWet, and wDry conditions. The upper, middle panel is λE measured at the US-NR1 tower which has an LAI of around 4. Below that are the CLM4.5 model output which are (from the 2nd to bottom row): total latent heat flux (λE); canopy transpiration (λE_v^t); canopy evaporation (λE_v^w), and ground evaporation (λE_g). Other than LAI, CLM uses the CLM4.5 A1 (default) configuration.

in CLM λE implies that the asymmetry in transpiration was offset by higher values of canopy evaporation on wet afternoons (soil evaporation being symmetric about mid-day). This suggests that the timing and/or magnitude of the CLM canopy evaporation term was problematic.

Another observation from Fig. 6.4 is that at night both the canopy and ground evaporation terms were small (less than $5\,\mathrm{W\,m^{-2}}$), regardless of whether it was a dry or wet period. Soil evaporation is thought to have two stages: one when soil moisture is high and atmospheric demand controls evaporation, and a second stage where the soil surface is relatively dry and diffusion of water vapor through the soil controls surface evaporation [Brutsaert, 1982]. For a crop, it has been shown that soil evaporation doubles when irrigation exists and nighttime evaporation can account for over 10 % of daily λE [Tolk et al., 2006]. In Fig. 6.4, CLM ground evaporation appears to be primarily controlled by LAI and there is little evidence that the existence of liquid water was playing a role in modifying the soil evaporation, especially at night. Furthermore, if soil evaporation is expected to be higher when the soil is wet, one would not expect near-perfect symmetry (around noon) on a wDry day.

From Fig. 6.4b, we can roughly estimate that the CLM canopy and ground evaporation terms both reached maximum values during mid-day of wet days, with values of 50–60 $\mathrm{W\,m^{-2}}$ and $10\,\mathrm{W\,m^{-2}}$, respectively. CLM λE peaked at similar times, at a value of around $150\,\mathrm{W\,m^{-2}}$. These values suggest that CLM canopy evaporation and ground evaporation were no higher than 36% and 6% of the total λE, respectively. In a pine-spruce forest of similar LAI to that of US-NR1, Grelle et al. [1997] found that the canopy and soil evaporation components of total λE accumulated over a growing season were ≈ 20 % and 15 %, respectively. Based on these numbers, canopy and ground evaporation should have similar magnitudes, and the CLM ground evaporation seems low.

In the observations, we have assumed that transpiration at night is small. CLM4.5 allows for a small level of nocturnal transpiration (λE_v^t on the order of $5\,\mathrm{W\,m^{-2}}$), and we will revisit this topic in Sect. 6.3.8.1. The separation of nocturnal λE into transpiration and evaporation is a complicated problem [e.g., Novick et al., 2009], and for more discussion about the possibility of nocturnal transpiration at the US-NR1 site see Turnipseed et al. [2009]. We hypothesize that

the topographically-induced nocturnal slope flow at US-NR1 resulted in a higher-than-expected nocturnal ground evaporation component (to be discussed in Sect. 6.3.9.4).

6.3.3 Sensitivity of CLM4.5 latent heat flux and temperature to leaf area index (LAI)

As LAI was increased from 2 to 6, we found that dDry mid-day latent heat flux increased from $\approx 133\,\mathrm{W\,m^{-2}}$ to $179\,\mathrm{W\,m^{-2}}$, while sensible heat flux stayed approximately the same (Fig. 6.5a1, Table 6.2). For the mid-day wDry−dDry fluxes, net radiation was nearly constant with changing LAI, while the λE difference became smaller and went slightly negative as LAI increased (Fig. 6.5b1). This means that the enhancement of λE at mid-day on a wDry day became smaller as LAI was increased (the observations at the US-NR1 tower suggest that wDry−dDry λE should be $22\,\mathrm{W\,m^{-2}}$). In Fig. 6.5b1, one can follow the blue dashed line for the observations and see it intersects the CLM wDry−dDry λE at a value of LAI$\approx$2.5. As discussed in the previous section, increased CLM wDry λE for LAI=2 was due to increased ground evaporation. While it makes sense that reducing LAI would lead to enhanced mid-day wDry λE, LAI is a fairly well-constrained variable, and it does not seem realistic to use such a low LAI value for the US-NR1 site. Therefore, we reject the possibility that LAI explains the mis-match in wDry−dDry λE between CLM and the observations.

The mid-day CLM4.5 canopy air temperature T_s was unaffected by increasing LAI, but vegetation surface temperature T_v decreased by around $2\,^{\circ}\mathrm{C}$ and T_g decreased by $8\,^{\circ}\mathrm{C}$ (Fig. 6.5c1). The dramatic decrease in ground surface temperature was, presumably, due to increased shading of the soil surfaces as LAI increased. The decrease in CLM T_g resulted in a smaller soil heat flux to keep the surface energy budget balanced (results not shown).

At night, the CLM4.5 dDry latent heat flux was very close to the observations (on the order of $10\,\mathrm{W\,m^{-2}}$) and insensitive to LAI changes, whereas net radiation decreased in magnitude as LAI increased and sensible heat flux increased in magnitude to compensate for the R_{net} changes (Fig. 6.5a2). For all the LAI values considered, the CLM4.5 nocturnal wDry−dDry latent heat flux was less than $6\,\mathrm{W\,m^{-2}}$, much less than the observed value of $15\,\mathrm{W\,m^{-2}}$ (Fig. 6.5b2). This suggests that LAI does not play a significant role in controlling the nocturnal latent heat flux (in

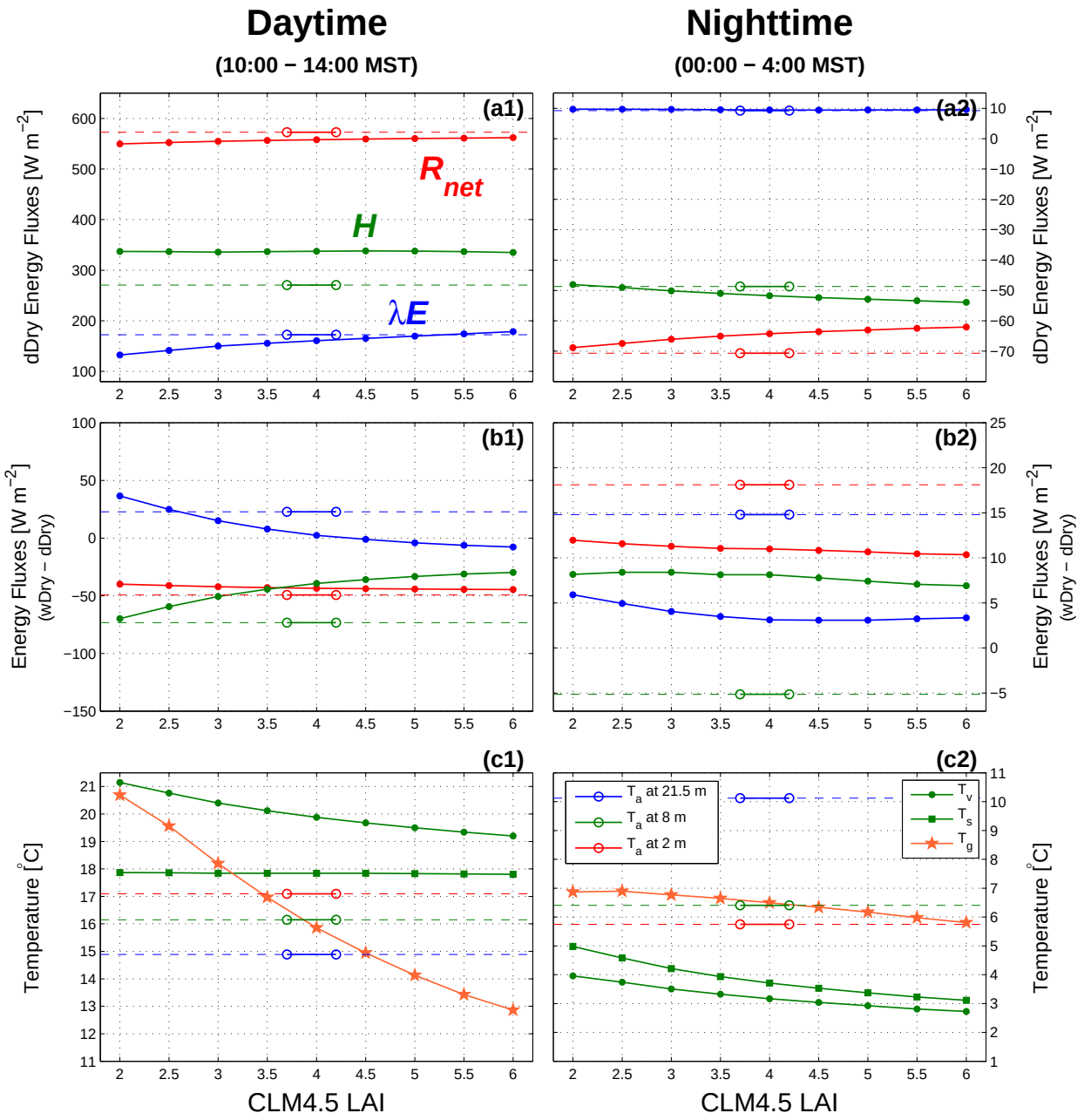

Figure 6.5: The **(a1, b1)** daytime and **(a2, b2)** nighttime energy fluxes versus CLM4.5 leaf area index (LAI) as it varies from 2 to 6. The 2 upper panels show the mean values for dDry conditions and the 2 middle panels show the mean differences between wDry and dDry conditions where the variables shown are: net radiation $R_{\rm net}$ (red), sensible heat flux H (green), and latent heat flux λE (blue). The solid lines with filled symbols are the CLM4.5 output, while the shorter lines with open circles are the US-NR1 above-canopy tower observations over an approximate range of the site LAI (3.7–4.2). In **(c1, c2)**, the US-NR1 observed air temperature T_a and the effect of varying LAI on CLM canopy surface T_v, canopy air T_s and ground T_g temperatures are shown (see legends). The CLM results use the CLM4.5 A1 (default) configuration (Table 6.1).

wet conditions). All the CLM4.5 nighttime temperatures decreased by around 1–2 °C as LAI was increased (Fig. 6.5c2)

6.3.4 Sensitivity of CLM4.5 latent heat flux to maximum leaf wetted fraction

When water is present on the canopy, the *maximum leaf wetted fraction* f_{wet}^{max} limits the area of the leaf surface that is wet. A larger f_{wet}^{max} value decreases the portion of the canopy undergoing transpiration and increases the direct evaporation of canopy water. For $f_{wet}^{max} = 1$, the entire leaf is covered in water, which is the CLM4.5 default value. This default setting is unlikely to be appropriate for needleleaf conifers, where rainwater accumulates at the tips of the needles that act as drip points [Moors, 2012].

For f_{wet}^{max} varied between 0.01 and 1, the CLM4.5 dDry fluxes were only minimally affected, as would be expected in dry conditions (Fig. 6.6a1, a2). However, when f_{wet}^{max} was smaller than 0.05, it had a significant effect on the wDry−dDry λE and H fluxes. For the mid-day wDry−dDry λE difference, the two smallest values of f_{wet}^{max} (0.01 and 0.02) approached the wDry−dDry λE difference of the US-NR1 observations (Fig. 6.6b1); however, these values also tended to decrease the nocturnal wDry−dDry λE difference toward zero (Fig. 6.6b2). As a compromise, we examined the effect of setting f_{wet}^{max} to 0.02 in our analysis (CLM4.5 B0, B1, and B2 in Table 6.1).

After setting f_{wet}^{max} to 0.02, CLM mid-day λE in wDry conditions (Fig. 6.7a) looked qualitatively similar to observed wDry λE (upper panel of Fig. 6.4b). Furthermore, CLM λE on the afternoon of wet days, was reduced (relative to dDry λE), similar to the observations. Transpiration and soil evaporation were relatively unchanged by decreasing f_{wet}^{max}, but the canopy evaporation term was smoother and decreased in magnitude, especially during the afternoon (Fig. 6.7a). Decreasing f_{wet}^{max} does not change the amount of intercepted water, but it does cause the intercepted water to evaporate at a slower rate, making it more likely for the water to build up in the canopy and drip to the ground (rather than evaporate to the atmosphere).

A good example of the effect of decreasing f_{wet}^{max} on the λE components can be seen in the wDry diel composite shown in Fig. 6.7c. With CLM4.5 A1, there was a sharp increase in the canopy

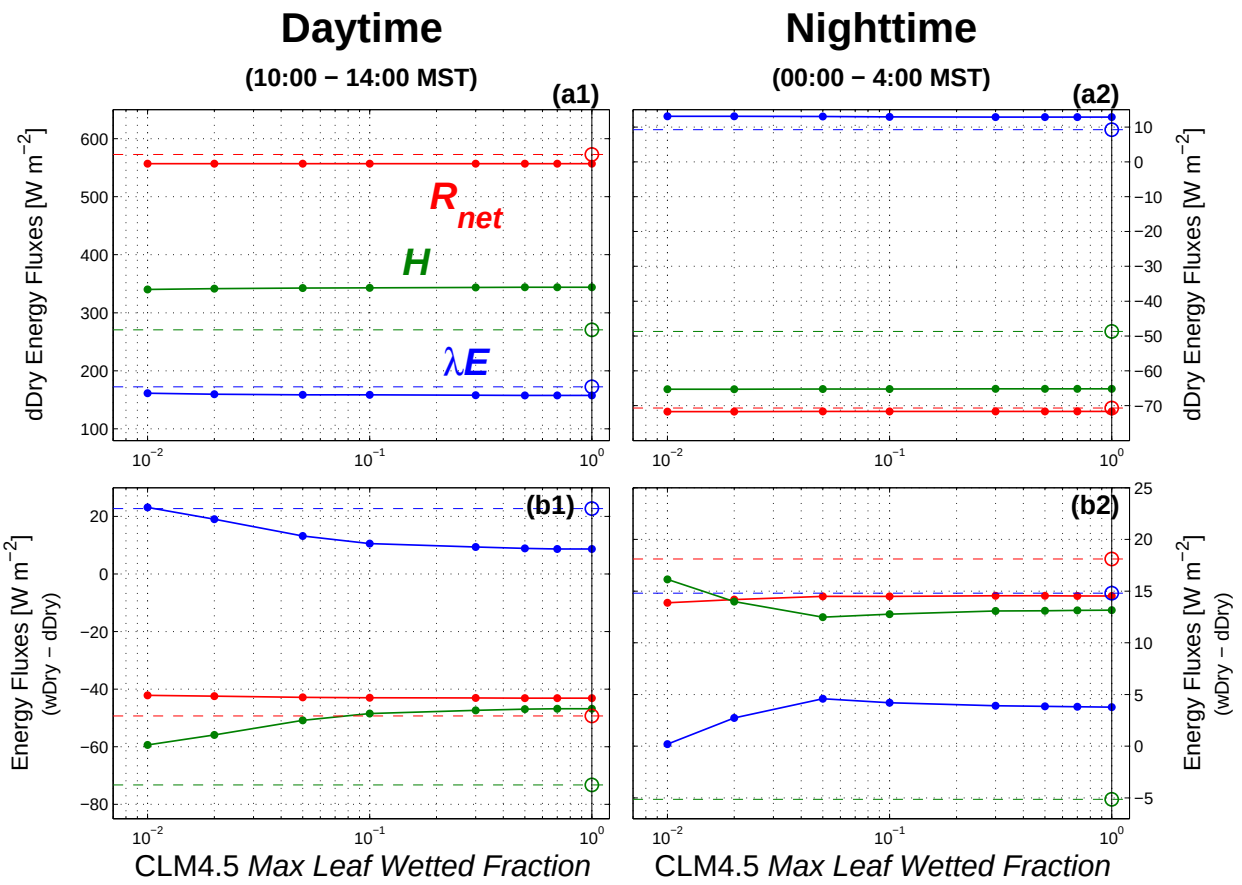

Figure 6.6: The **(a1, b1)** daytime and **(a2, b2)** nighttime energy fluxes versus changes to the CLM4.5 *maximum leaf wetted fraction* f_{wet}^{max} which has a default value of 1. The upper panels show the mean values for dDry conditions and the middle panels show the mean differences between wDry and dDry conditions where the variables shown are: net radiation R_{net} (red), sensible heat flux H (green), and latent heat flux λE (blue). The solid lines with filled symbols are the CLM4.5 output, while the horizontal dashed lines are the US-NR1 observations with an open circle placed near the default f_{wet}^{max} value. The CLM results use the CLM4.5 B2 configuration (Table 6.1).

evaporation term at sunrise from near zero up to 40 W m^{-2} which only lasted a few hours (between around 6:00 to 8:00 MST); in contrast, for CLM4.5 B0, the canopy evaporation term peaked at around 9:00 MST with a value of 40 W m^{-2} and the evaporation was spread over a much longer time period, between 6:00 and 13:00 MST. The other CLM4.5 configurations shown in Fig. 6.7c (B1 and B2) will be discussed later, but the important point is that these configurations are 2nd-order effects while the change to f_{wet}^{max} presents a fundamental change to the nature of CLM canopy evaporation. To extend this knowledge further, better knowledge of the true canopy evaporation

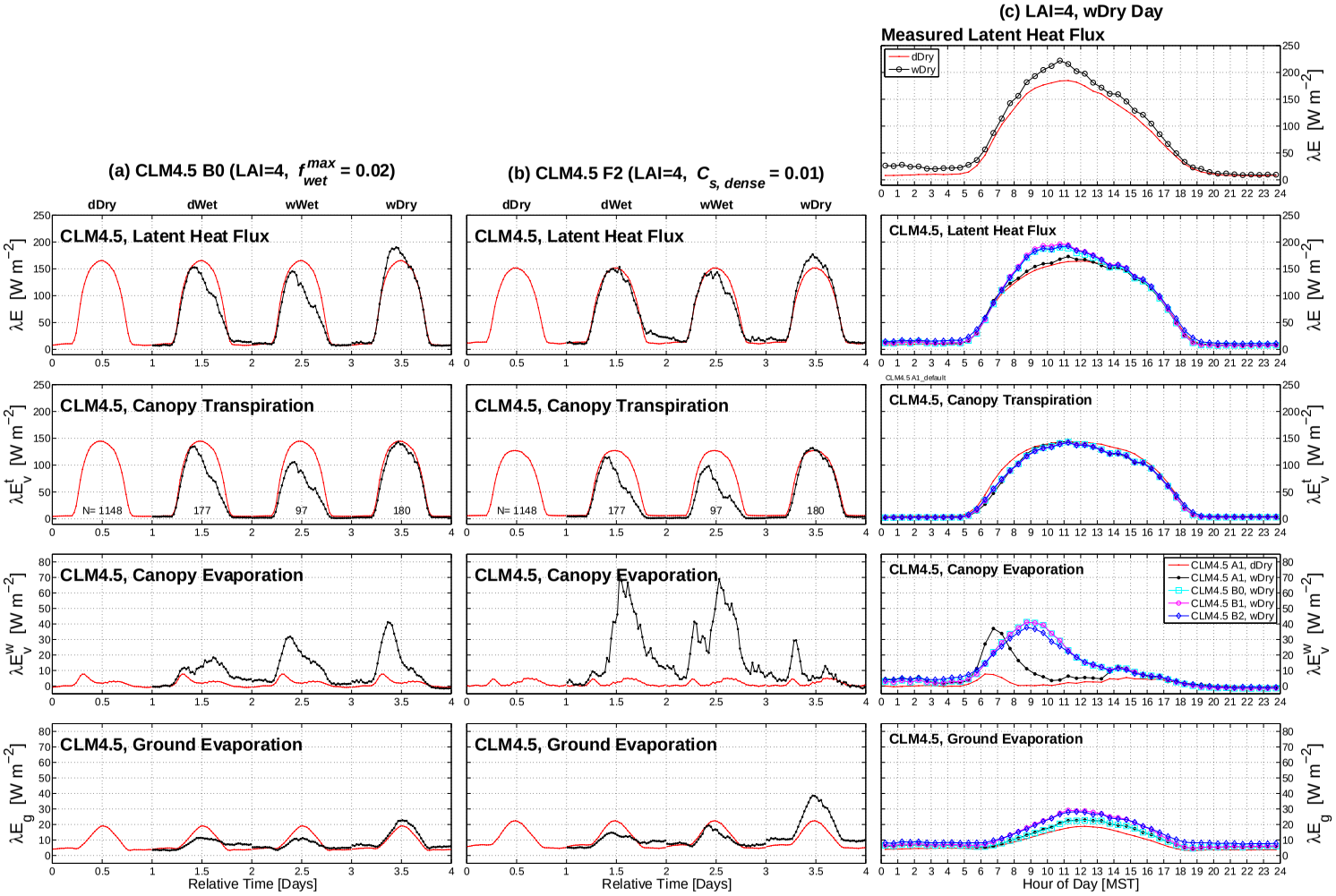

Figure 6.7: Components of the latent heat flux for (**a**) CLM4.5 using *maximum leaf wetted fraction* $f_{wet}^{max} = 0.02$ (CLM4.5 B0), (**b**) CLM4.5 with the subcanopy turbulent exchange coefficient $C_{s,dense} = 0.01$ (CLM4.5 F2), and (**c**) the results for a wDry day for the default settings (CLM4.5 A1) along with different cases of $f_{wet}^{max} = 0.02$ as listed in the legend. A detailed description of each CLM4.5 alphanumeric configuration is in Table 6.1. For (**a**) and (**b**), the mean diel cycles are separated into dDry, dWet, wWet, and wDry conditions where the red line in each panel is the mean diel cycle for dDry conditions which is repeated for ease of comparison to the results from dWet, wWet, and wDry conditions. CLM4.5 λE is broken down into individual components which are (from top to bottom row): total latent heat flux (λE); canopy transpiration (λE_v^t); canopy evaporation (λE_v^w), and ground evaporation (λE_g). In (**c**), US-NR1 observed λE is shown in the upper panel.

from the forest at US-NR1 would be required.

A final comment on Fig. 6.7a: it is curious that the mid-day ground evaporation during dWet, wWet, and wDry conditions was either smaller or only slightly larger than that in dDry conditions. This is suggestive that R_{net} plays a dominant role in controlling the CLM ground evaporation, as opposed to the availability of liquid water. One would expect that an important factor controlling the CLM ground evaporation term is the subcanopy turbulent transport, which will be discussed in Sect. 6.3.8.

6.3.5 Atmospheric turbulence and latent heat flux

6.3.5.1 Above-canopy friction velocity

Mechanical turbulence (characterized by the friction velocity u_*) plays a crucial role in the transport of water vapor between the forest and the atmosphere. At US-NR1, u_* generally follows a similar pattern to wind speed at night; however, during the daytime, the buoyancy generated by surface heating enhances u_* relative to nocturnal values [Burns et al., 2015a]. Observed u_* generally agrees well with CLM u_* during mid-day, but at night we found that observed nocturnal u_* was at around $0.4\,\mathrm{m\,s^{-1}}$ while the CLM u_* was closer to $0.3\,\mathrm{m\,s^{-1}}$ (Fig. 6.2d).

Another way to look at this issue, is to examine how CLM and observed u_* vary with bulk Richardson number $\mathrm{Ri_b}$ (Fig. 6.8). In general, it appears that CLM u_* has a low-bias relative to the observed u_* of around $0.1\,\mathrm{m\,s^{-1}}$. Many flux observations sites show a similar u_* bias with CLM4.5 [e.g., Bonan et al., 2017]. Because u_* is such an important variable, we circumvented this issue by using observed u_* as an input to CLM4.5 (see Table 6.1 for specific configurations). In general, using observed u_* increased the magnitude of the nocturnal fluxes (as one would expect). A more quantitative examination on the effect of using observed u_* is in Sect. 6.3.7.3.

6.3.5.2 Atmospheric stability effects on nocturnal latent heat flux

We used the bulk Richardson number $\mathrm{Ri_b}$ to examine how modeled and measured λE behaved

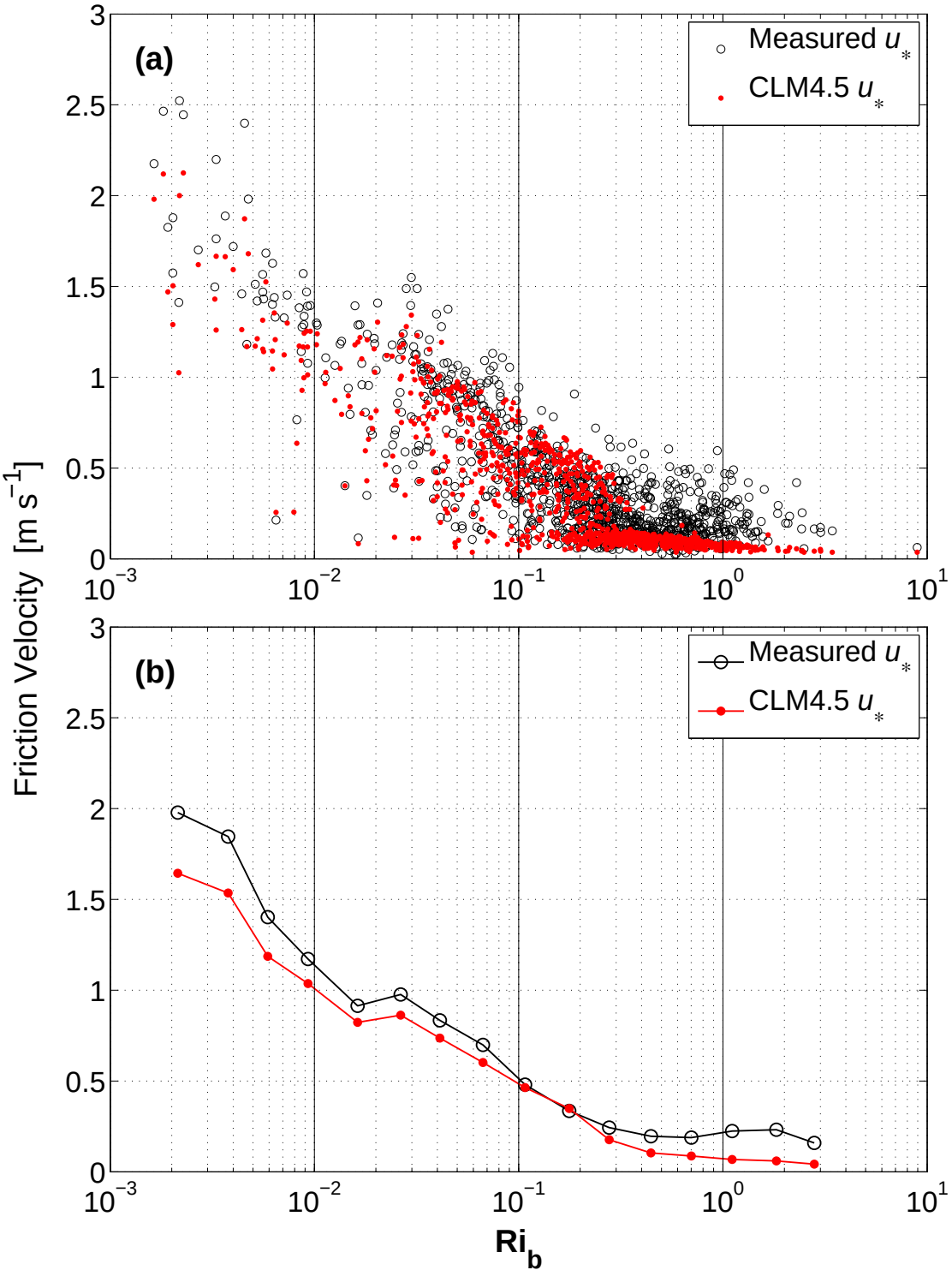

Figure 6.8: Observed and CLM4.5 friction velocity u_* during wDry periods between midnight and 4:00 MST versus the bulk Richardson number $\mathrm{Ri_b}$. In **(a)**, all the 30-min values are shown while **(b)** shows the $\mathrm{Ri_b}$-binned mean values. CLM results are from the CLM4.5 A1 (default) configuration (Table 6.1).

in strongly stable conditions (Fig. 6.9). Here, we observe that on wDry days the magnitude of λE was reduced in strongly stable conditions (i.e., $\mathrm{Ri_b} > 0.2$). In these strongly stable conditions, CLM λE had many negative 30-min periods, which suggests that there was net condensation on the canopy (not net evaporation). Based on the US-NR1 observations, net condensation ($\lambda E < 0$) was rare (Fig. 6.9a). This becomes more apparent when looking at the $\mathrm{Ri_b}$-binned averages in Fig. 6.9b. In strongly stable conditions, even though the ground evaporation term was slightly positive, the canopy evaporation term was negative, which led to CLM λE being slightly negative (on average). One explanation for condensation to dominate the CLM canopy evaporation term would be if the the CLM canopy surface temperature dropped below the dewpoint temperature. A comparison of observed and CLM temperatures is our next topic of discussion.

6.3.6 Vegetation, air, and soil temperature

At mid-day in dDry conditions, the air within the canopy and near the ground at the US-NR1 site was fairly uniform in temperature and, on average, was $\approx$1–2 °C warmer than the air just-above the forest (Fig. 6.10a). This compares fairly well with the mid-day CLM4.5 A1 temperatures. However, the nighttime temperatures show much less agreement (Fig. 6.10b). For CLM4.5 A1 at night, the canopy surface temperature T_v was around 3 °C colder than the ground surface and about 0.5 °C colder than the canopy air temperature T_s. Therefore, CLM considers the air within the canopy the coldest location within the forest. In contrast, the US-NR1 observations suggest that the coldest air was just above the ground surface, and near-ground T_a was only $\approx$1 °C cooler than T_{soil}. In a study at an evergreen forest using a thermal IR camera, Kim et al. [2016] showed that the nocturnal canopy skin temperature was typically $\approx$2 °C colder than the nearby air temperature. Recent work with IR cameras at US-NR1 have shown that the nighttime canopy IR and air temperatures are, on average, within about 1 °C of each other [Aubrecht et al., 2016, Bowling et al., 2018]. This seems similar to CLM $T_s - T_v$; however, the vertical temperature profiles in Fig. 6.10a clearly reveal that CLM T_s was over 2 °C colder than any level of the US-NR1 tower observations. If CLM was performing correctly, we would expect T_s to be closer to observed

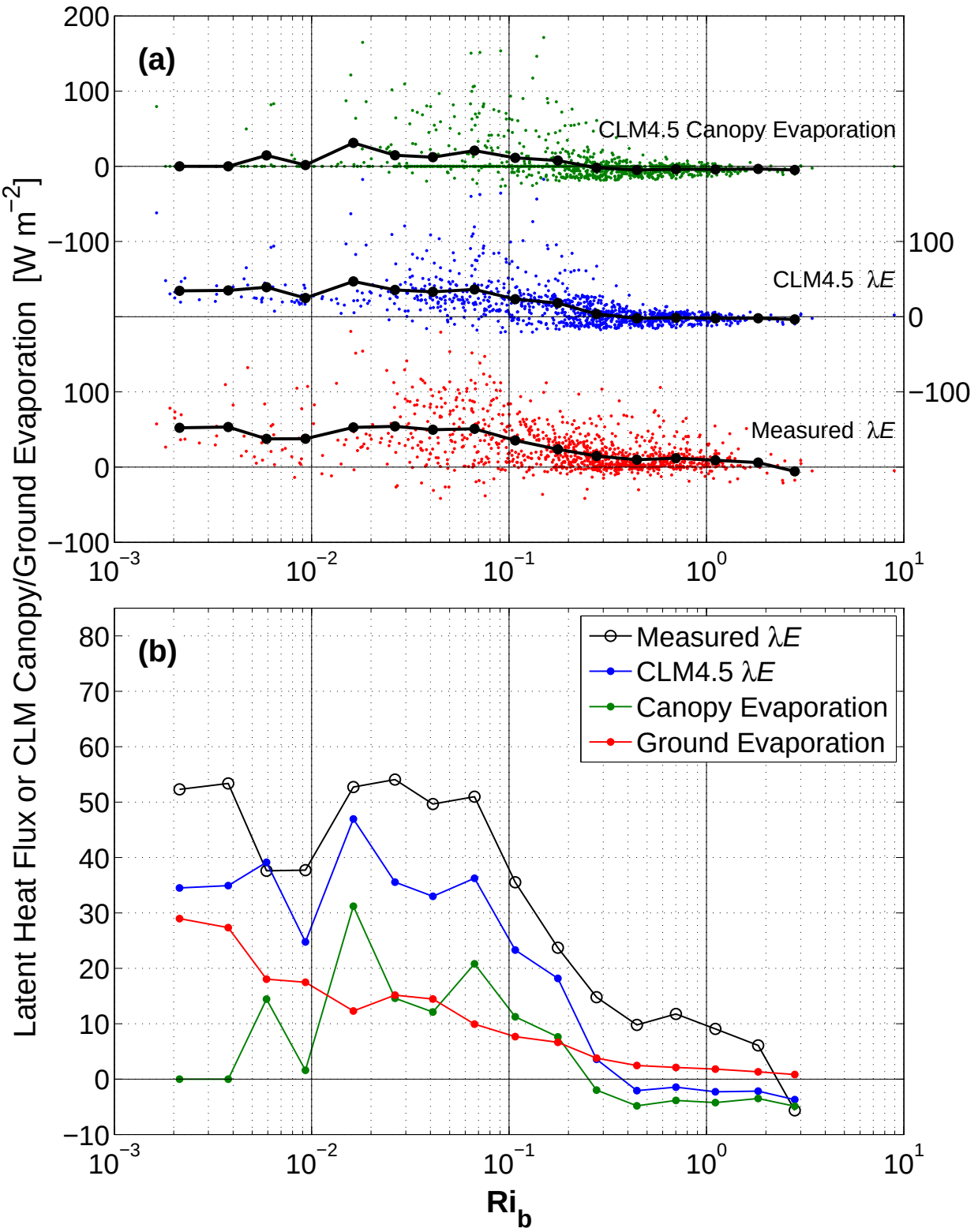

Figure 6.9: The US-NR1 and CLM4.5 latent heat flux λE and CLM4.5 canopy evaporation λE_v^w versus the bulk Richardson number $\mathrm{Ri_b}$ from wDry periods between midnight and 4:00 MST. In **(a)**, all the 30-min values including an $\mathrm{Ri_b}$-binned average of the 30-min data are shown. In **(b)**, the binned-averages of λE and CLM4.5 λE_v^w from **(a)** are shown along with the CLM4.5 ground evaporation term as described in the legend. CLM results are from the CLM4.5 A1 (default) configuration (Table 6.1).

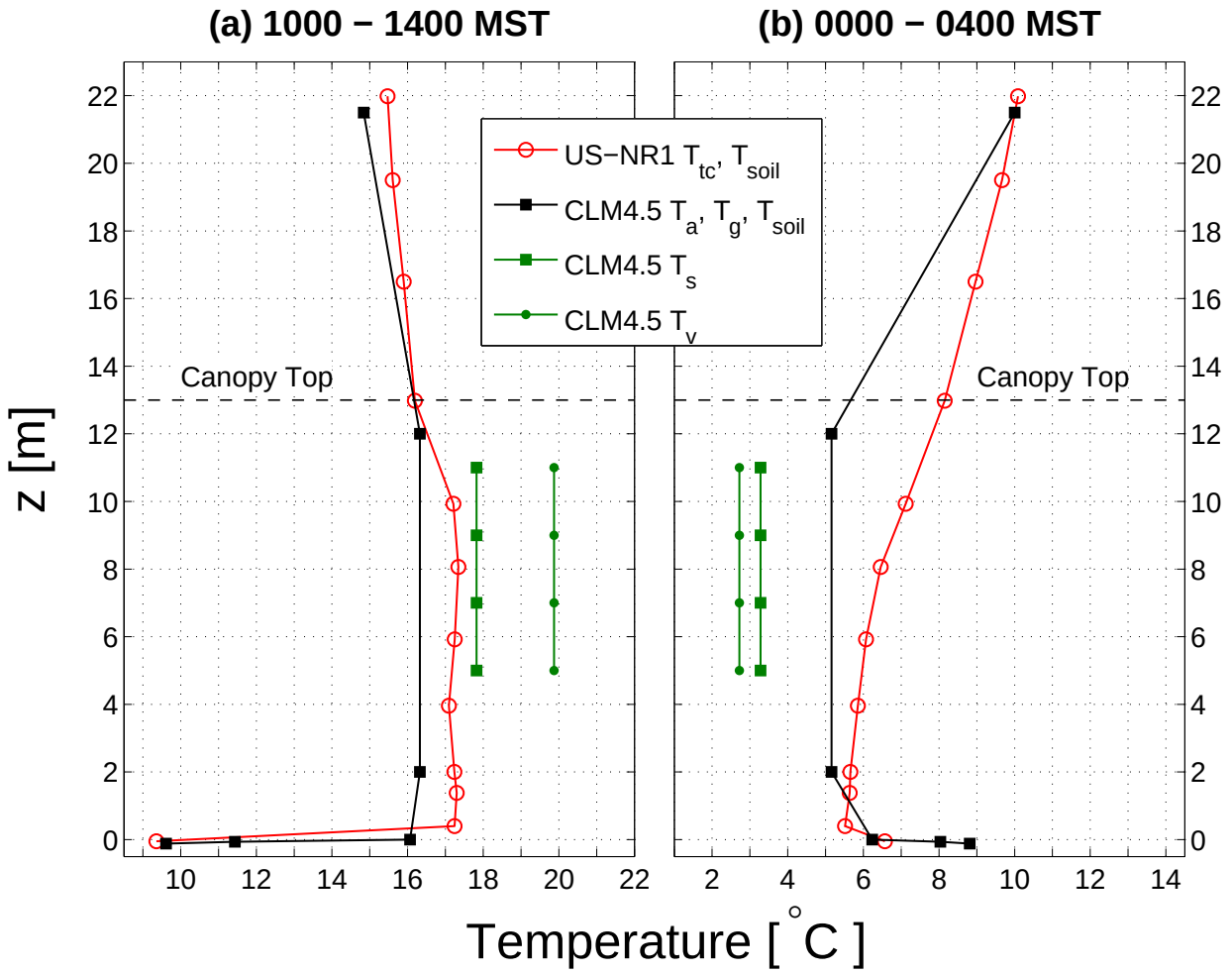

Figure 6.10: Average **(a)** daytime and **(b)** nighttime vertical temperature profiles in dDry conditions during the warm season for years 2006–2012. As shown in the legend, the US-NR1 air temperature T_a profile is from 11 levels of thermocouples T_{tc} and soil temperature at -5 cm depth. The CLM model includes temperature estimates of canopy vegetation T_v, the canopy air space T_s, and a 2-m air temperature T_{2m} defined as 2 m above the apparent sink for sensible heat [Oleson et al., 2013]. We show T_{2m} as the temperature between 2 m $\leq z \leq$ 12 m, and T_v and T_s are shown between 5 m $\leq z \leq$ 11 m. The approximate canopy top is shown as a horizontal dashed line at z = 13 m. CLM results are from the CLM4.5 A1 (default) configuration (Table 6.1).

subcanopy T_a.

For nocturnal air temperatures plotted versus $\mathrm{Ri_b}$ with CLM4.5 A1 (Fig. 6.11b1), the stronger the stability, the colder the CLM vegetation and canopy airspace temperatures became, such that $T_s - T_g$ was on the order of -6°C for the highest stabilities (Fig. 6.11b2). In contrast, US-NR1 T_a measured within the subcanopy air space appeared to reach a limit within strongly stable

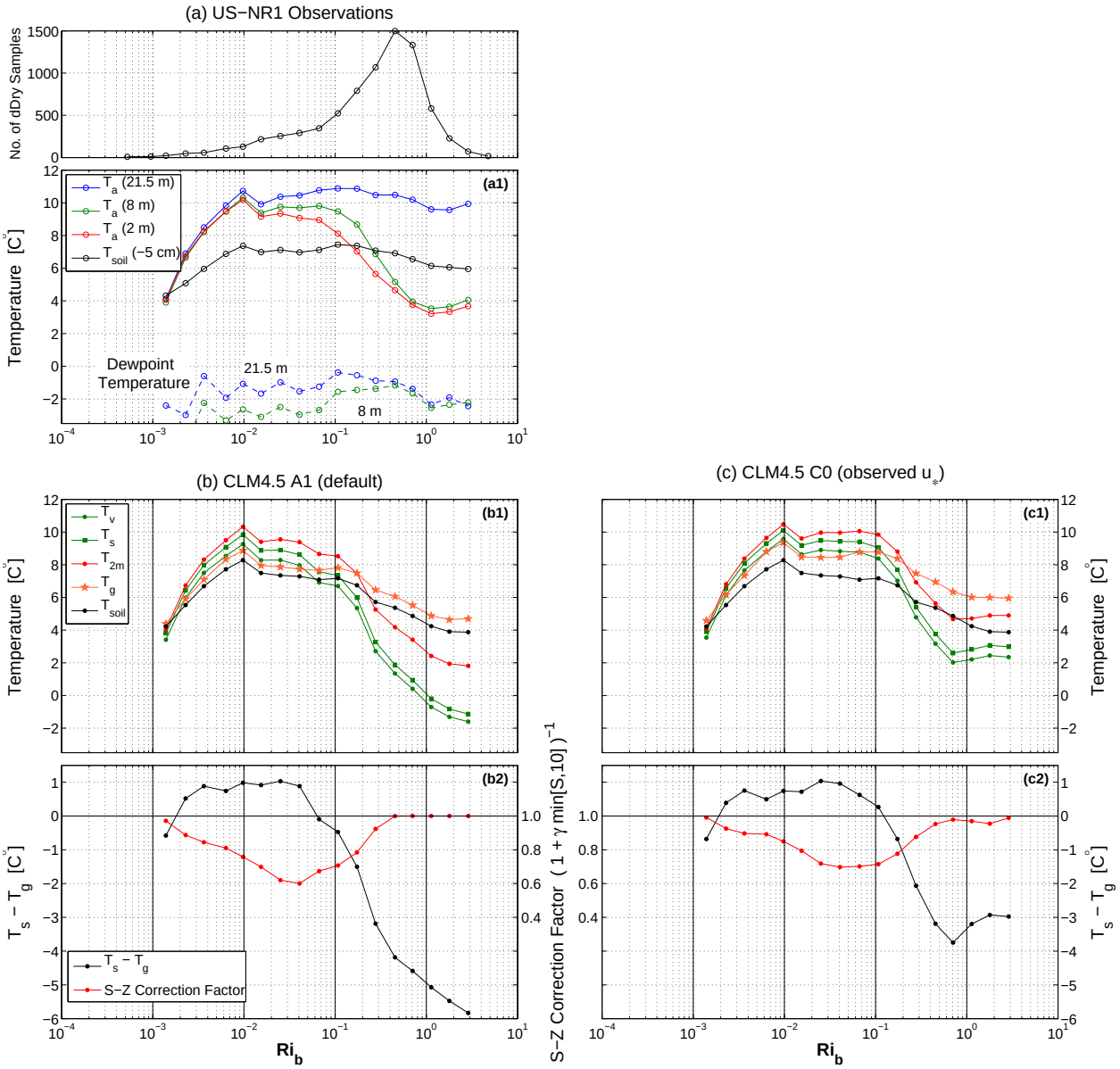

Figure 6.11: The **(a1)** US-NR1 observed air T_a, dewpoint T_d, and soil T_{soil} temperatures, **(b1)** CLM4.5 A1 (default configuration) temperatures, and **(c1)** CLM4.5 C0 (CLM using observed friction velocity u_*) temperatures versus the bulk Richardson number $\mathrm{Ri_b}$. The legends in **(b)** also applies to **(c)**, where the CLM temperatures shown are: canopy vegetation temperature T_v, canopy air space temperature T_s, "2-m" air temperature T_{2m}, ground surface temperature T_g, and T_{soil} at $-6.2\,\mathrm{cm}$ depth. In **(a)**, the upper panel shows the number of 30-min samples within each $\mathrm{Ri_b}$ bin, and only results with at least 20 samples in a bin are presented. In **(b2)** and **(c2)**, the CLM4.5 $T_s - T_g$ difference versus the bulk Richardson number $\mathrm{Ri_b}$ are shown in black along with the S–Z correction factor proposed by Sakaguchi and Zeng [2009] in red. For $T_s - T_g > 0$, the S–Z correction (based on the stability parameter S with $\gamma = 0.5$) is intended to reduce the value of the subcanopy turbulent transfer coefficient $C_{s,dense}$. The mean of the S–Z correction factor uses the y-axis between panels **(b2)** and **(c2)**. These data are from dDry periods between midnight and 4:00 MST.

conditions, as shown by the 2 m and 8 m T_a curves leveling off at $\approx$ 4°C for $\mathrm{Ri_b} > 0.8$ (Fig. 6.11a1). Presumably, this was due to the drainage flow forming in strongly stable conditions which increased turbulent mixing of (warmer) air aloft with air near the ground. The cold bias in CLM canopy temperatures and small values of friction velocity appear to be symptoms of runaway cooling, as discussed in the Introduction. In Sect. 6.3.7.3, we will discuss the effect of using observed u_* on the CLM temperatures.

In strongly stable conditions, the dewpoint temperature T_d measured at the US-NR1 site was ≈ -2°C, or 6°C below the air temperature (Fig. 6.11a1). The magnitude of this difference was fairly close to the CLM vegetation cold temperature bias, which suggests that the bias was likely contributing to condensation forming on the canopy in CLM (i.e., leading to $\lambda E_v^w < 0$).

6.3.7 Above-canopy turbulent exchange in CLM4.5

CLM4.5 uses Monin-Obukhov Similarity Theory (MOST) to calculate the turbulent fluxes between the atmosphere and the atmospheric surface layer, where the surface-layer fluxes approximate those near the ground [e.g., Businger et al., 1971, Panofsky and Dutton, 1984, Foken, 2006]. To model the turbulent fluxes, MOST utilizes the so-called universal similarity functions.

6.3.7.1 Universal similarity functions

One of the primary tenets of MOST is that, under specified conditions, there exists universal functions (ϕ_m, ϕ_h, and ϕ_w) that model the vertical gradients of wind, temperature and humidity, as

$$\phi_m(\zeta) = \frac{\kappa(z-d)}{u_*}\frac{\partial U}{\partial z}, \tag{6.1}$$

$$\phi_h(\zeta) = \frac{\kappa(z-d)}{\theta_*}\frac{\partial \theta}{\partial z}, \tag{6.2}$$

$$\phi_w(\zeta) = \frac{\kappa(z-d)}{q_*}\frac{\partial q}{\partial z}, \tag{6.3}$$

where κ is the von Karman constant, z is the height above the ground, d is the zero-plane displacement height, and other variables are defined in Table B1. The universal functions are a function

of only a single variable—the dimensionless stability parameter $\zeta = (z - d)/L$, where L is the Obukhov length (see Table B1 for details). For momentum, the displacement height represents the distance from the ground where the momentum of the above-canopy flow is completely absorbed [Raupach, 1994, Moene and Van Dam, 2014] (at US-NR1, the roughness length for momentum z_{0m} and displacement height were determined by Turnipseed et al. [2003] to be $z_{0m} = 1.6\,\mathrm{m}$ and $d = 7.8\,\mathrm{m}$.) After the form of the universal functions are empirically determined, they can be numerically integrated and the changes in horizontal wind speed and scalars with height in the surface layer can be calculated. Additional details can be found in any standard boundary-layer or micrometeorology textbook [e.g., Kaimal and Finnigan, 1994, Foken, 2008b]; for our purposes, we highlight that stability ζ and mechanical turbulence (represented by the friction velocity, u_*) are two of the primary variables controlling turbulent exchange which affects the degree of mixing that occurs between the ground surface and atmosphere. The fact that u_* is part of L is the so-called self-correlation issue with MOST [e.g., Baas et al., 2006, Moene and Van Dam, 2014]. Another possible issue using MOST over a forest exists if the tower measurement level is too close to the surface roughness elements (i.e., within the so-called roughness sublayer RSL), then the standard MOST universal functions can introduce a bias to the modeled canopy-atmosphere exchanges [e.g., Harman and Finnigan, 2007, 2008].

In Table 6.3 we list the universal functions used in CLM4.5 separated into different stability regimes. In stable conditions, the universal functions for momentum ϕ_m, heat ϕ_h, and moisture ϕ_w are identical. In unstable conditions, ϕ_h and ϕ_w are still identical, but the form of ϕ_m changes and occurs over a different stability range. The accuracy of the universal functions is typically on the order of 10-20 %, with larger uncertainty in strongly stable (i.e., z-less scaling) and unstable (i.e., free convection) conditions [Foken, 2008b]. In CLM4.5, the MOST equations are solved iteratively until a convergent solution is achieved (based on changes in vegetation temperature and transpiration being below a certain limit, or after 40 iterations have been carried out). Full details of the CLM4.5 methodology are provided in Oleson et al. [2013].

Over the years, many different forms of the universal functions have been proposed (see Foken

Table 6.3: Universal functions for momentum ϕ_m, heat ϕ_h, and moisture ϕ_w used in CLM4.5 listed by stability range based on the stability parameter, ζ.

Stability Range	CLM4.5 Manual Equation No.	Universal functions for momentum, heat, and moisture
Very unstable		
Momentum: $(\zeta < -1.574)$	Eq. 5.30	$\phi_m(\zeta) = 0.7k^{2/3}(-\zeta)^{1/3}$
Heat/Moist: $(\zeta < -0.465)$	Eq. 5.31	$\phi_h(\zeta) = \phi_w(\zeta) = 0.9k^{4/3}(-\zeta)^{-1/3}$
	Eq. 5.32	$V_a = \frac{u_*}{\kappa}\left\{\left[\ln\left(\frac{\zeta_m L}{z_{0m}}\right) - \psi_m(\zeta_m)\right] + 1.14\left[(-\zeta)^{1/3} - (-\zeta_m)^{1/3}\right]\psi_m\left(\frac{z_{0m}}{L}\right)\right\}$
Weakly unstable		
Momentum: $(-1.574 < \zeta < 0)$	Eq. 5.30	$\phi_m(\zeta) = (1 - 16\zeta)^{-1/4}$
Heat/Moist: $(-0.465 < \zeta < 0)$	Eq. 5.31	$\phi_h(\zeta) = \phi_w(\zeta) = (1 - 16\zeta)^{-1/2}$
	Eq. 5.33	$V_a = \frac{u_*}{\kappa}\left\{\left[\ln\left(\frac{z_{atm,m} - d}{z_{0m}}\right) - \psi_m(\zeta)\right] + \psi_m\left(\frac{z_{0m}}{L}\right)\right\}$
	Eq. 5.36	$\psi_m(\zeta) = 2\ln\left(\frac{1+x}{2}\right) + \ln\left(\frac{1+x^2}{2}\right) - 2\tan^{-1}x + \frac{\pi}{2}$
		where, $x = (1 - 16\zeta)^{1/4}$
Weakly stable		
Mom/Heat/Moist: $(0 < \zeta < 1)$	Eqs. 5.30, 5.31	$\phi_m(\zeta) = \phi_h(\zeta) = \phi_w(\zeta) = 1 + 5\zeta$
	Eq. 5.34	$V_a = \frac{u_*}{\kappa}\left\{\left[\ln\left(\frac{z_{atm,m} - d}{z_{0m}}\right) + 5(\zeta)\right] - 5\left(\frac{z_{0m}}{L}\right)\right\}$
Very stable		
Mom/Heat/Moist: $(1 < \zeta)$	Eqs. 5.30, 5.31	$\phi_m(\zeta) = \phi_h(\zeta) = \phi_w(\zeta) = 5 + \zeta$
	Eq. 5.35	$V_a = \frac{u_*}{\kappa}\left\{\left[\ln\left(\frac{L}{z_{0m}}\right) + 5\right] + [5\ln(\zeta) + \zeta - 1] - 5\left(\frac{z_{0m}}{L}\right)\right\}$

Note: In the unstable expressions, ψ_m is the diabatic term in the integrated momentum equation. Also shown is the full form of the integrated momentum equation used to calculate the above-canopy mean wind speed V_a.

[2008b] for a list of examples). It is natural to wonder how much of an effect the choice of universal function has on the model results. The universal functions that we consider within our study are listed in Table 6.4. In Fig. 6.12 we show the CLM4.5 universal functions (based on the work by Zeng et al. [1998]) along with the classical one from Högström [1988] versus ζ. In this figure we include the frequency distributions of ζ measured at 21.5 m on the US-NR1 tower—as one would expect, nocturnal conditions are typically stable (94% of the nighttime periods have $\zeta > 0$). Högström [1988] is only defined up to $\zeta = 1$ which is near the peak of the nocturnal ζ frequency distribution. For $\zeta > 1$, the form of the universal function is not well-understood, and the default CLM4.5 form for ϕ suggests it should increase sharply. However, the work by Handorf et al. [1999] and others

Table 6.4: Universal similarity functions for momentum ϕ_m, heat ϕ_h, and moisture ϕ_w examined in our study as a function of the stability parameter, ζ.

Universal functions for momentum, heat, and moisture			Stability Range		
CLM4.5 ([Zeng et al., 1998])					
Momentum:	$\phi_m(\zeta)$	$= 0.7k^{2/3}(-\zeta)^{1/3}$		ζ	< -1.574
	$\phi_m(\zeta)$	$= (1-16\zeta)^{-1/4}$	$-1.574 \leq$	ζ	< 0
	$\phi_m(\zeta)$	$= 1+5\zeta$	$0 \leq$	ζ	≤ 1
	$\phi_m(\zeta)$	$= 5+\zeta$	$1 <$	ζ	
Heat/Moisture:	$\phi_h(\zeta) = \phi_w(\zeta)$	$= 0.9k^{4/3}(-\zeta)^{-1/3}$		ζ	< -0.465
	$\phi_h(\zeta) = \phi_w(\zeta)$	$= (1-16\zeta)^{-1/2}$	$-0.465 \leq$	ζ	< 0
	$\phi_h(\zeta) = \phi_w(\zeta)$	$= 1+5\zeta$	$0 \leq$	ζ	≤ 1
	$\phi_h(\zeta) = \phi_w(\zeta)$	$= 5+\zeta$	$1 <$	ζ	
Högström [1988] (based on Businger et al. [1971])					
Momentum:	$\phi_m(\zeta)$	$= (1-19.3\zeta)^{-1/4}$	$-2 <$	ζ	< 0
	$\phi_m(\zeta)$	$= 1+6\zeta$	$0 <$	ζ	< 1
Heat/Moisture:	$\phi_h(\zeta) = \phi_w(\zeta)$	$= 0.95(1-11.6\zeta)^{-1/2}$	$-2 <$	ζ	< 0
	$\phi_h(\zeta) = \phi_w(\zeta)$	$= 0.95+7.8\zeta$	$0 <$	ζ	< 1
Handorf et al. [1999]					
Momentum:	$\phi_m(\zeta)$	$= 1+5\zeta$	$0 <$	ζ	< 0.6
	$\phi_m(\zeta)$	$= 4$	$0.6 <$	ζ	
Heat/Moisture:	$\phi_h(\zeta) = \phi_w(\zeta)$	$= 1+5\zeta$	$0 <$	ζ	< 0.6
	$\phi_h(\zeta) = \phi_w(\zeta)$	$= 4$	$0.6 <$	ζ	

suggest that ϕ should be capped at a fixed value within the strongly stable regime. One of our objectives is to test which formulation of ϕ leads to CLM4.5 fluxes that agree best with the US-NR1 measured fluxes. On the unstable side ($\zeta < 0$), the differences between the CLM4.5 and Högström [1988] ϕ functions are less dramatic (Fig. 6.12a2, a3).

CLM4.5 has an internal variable (*zetamaxstable*, ζ_{stable}^{max}) that sets a limit on how large ζ can become. The CLM4.5 default value is 2 (shown as a dashed vertical line in Fig. 6.12), and we will discuss the effect of changes to ζ_{stable}^{max} on the CLM4.5 output in Sect. 6.3.7.4.

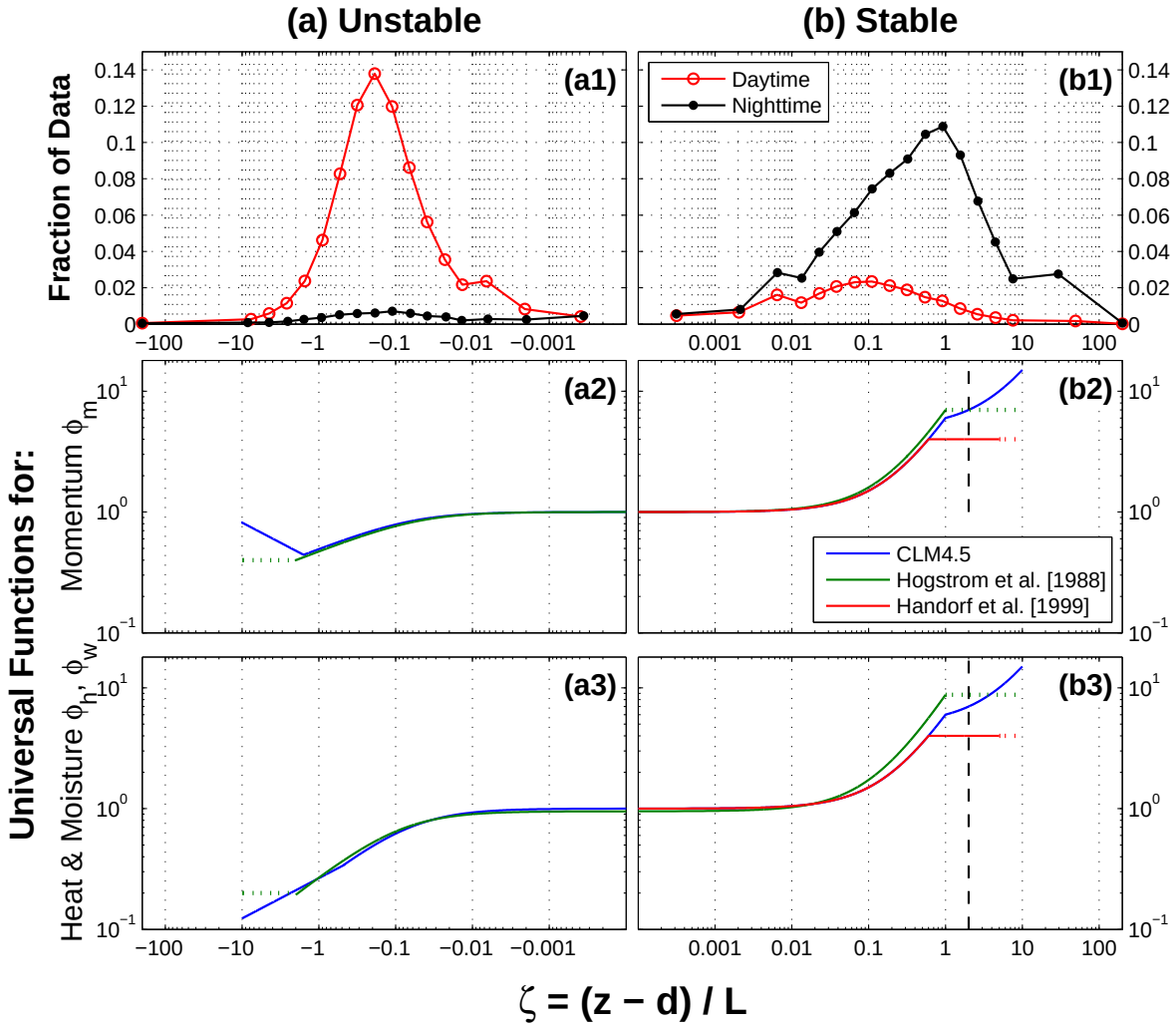

Figure 6.12: The frequency distribution of the dimensionless stability parameter $\zeta = (z-d)/L$ at the US-NR1 site measured at 21.5 m above the ground for **(a1)** unstable and **(b1)** stable conditions. These data are from 16 years of tower measurements (1999–2014) between June and September. The results are shown as the fraction of the total points for daytime (incoming PAR $> 50\,\mu\mathrm{mol\,m^{-2}\,s^{-1}}$) and nighttime (incoming PAR $< 1\mu\mathrm{mol\,m^{-2}\,s^{-1}}$) periods, as specified in the legend of **(b1)**. For the daytime data, 78.7% of the periods are unstable, and for nighttime data, 94.0% of the periods are stable. Below that, the universal similarity functions for **(a2, b2)** momentum ϕ_m and **(a3, b3)** heat ϕ_h and moisture ϕ_w are shown as a function of ζ. The relationships shown are from: CLM4.5 [i.e., Zeng et al., 1998], Högström [1988] (based on Businger et al. [1971]), and Handorf et al. [1999], as specified in the legend of panel **(b2)**. Handorf et al. [1999] is only defined in stable conditions and the ϕ values used outside of the defined ζ range are shown as dotted lines. In panels **(b2)** and **(b3)**, the vertical dashed line is the default value of *zetamaxstable*, $\zeta_{stable}^{max} = 2$. Note that $\phi_h = \phi_w$ for all formulations shown.

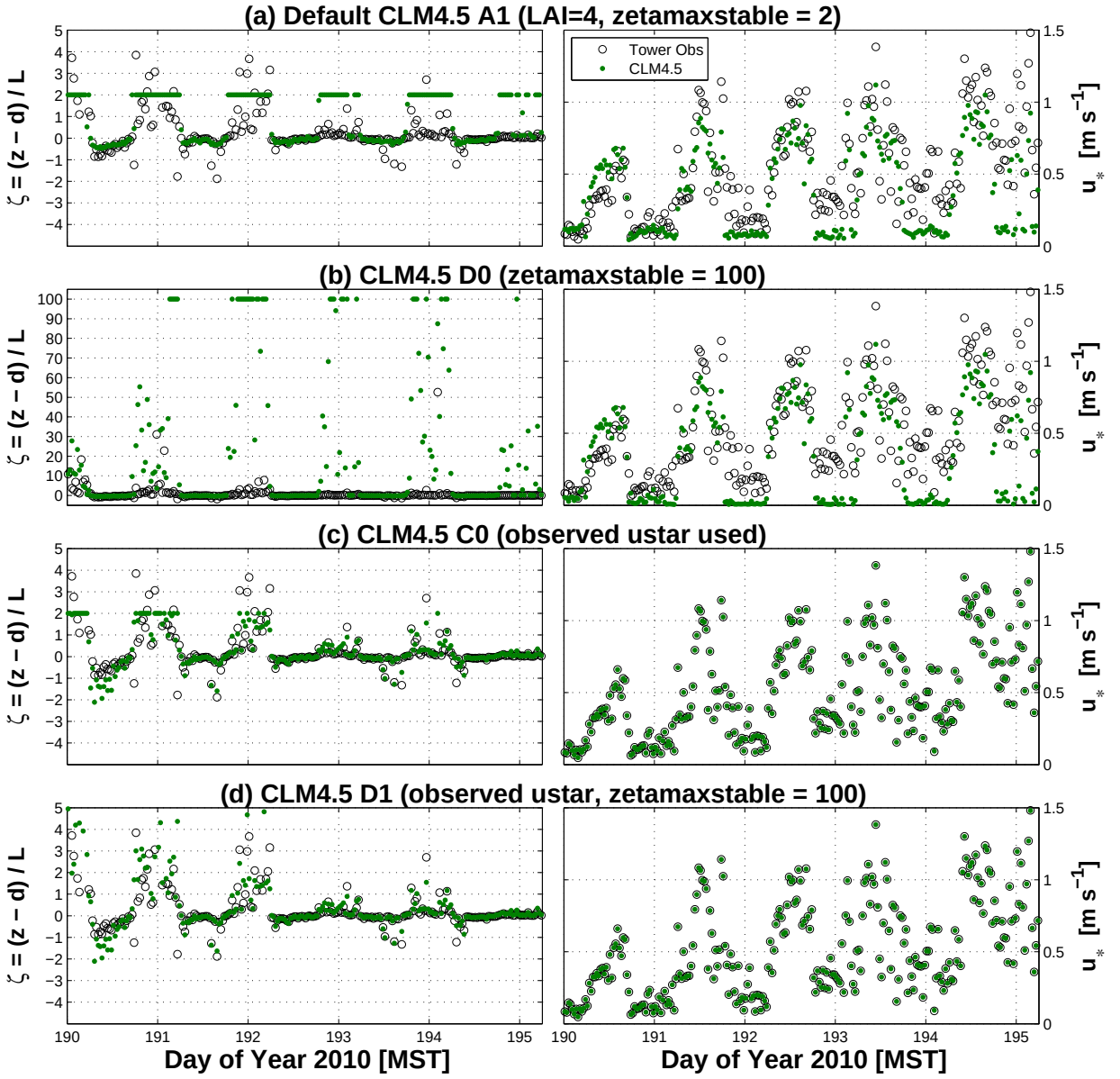

Figure 6.13: Time series of the 30-min observed and CLM4.5 **(left-side)** dimensionless stability parameter $\zeta = (z-d)/L$ and **(right-side)** friction velocity u_* during July 2010 (see legend in upper-right panel). Each row **(a)**-**(d)** corresponds to CLM4.5 run with changes to variables described in the text above that panel where the letters (A1, D0, C0, and D1) corresponds to a specific CLM configuration, as described in Table 6.1. In **(b)**, the y-axis limits for ζ have been increased so all data are shown.

6.3.7.2 Stable conditions in CLM4.5

The value chosen for the CLM4.5 variable *zetamaxstable* ζ_{stable}^{max} strongly impacts u_* and the stability parameter ζ. For the CLM4.5 A1 configuration, a time series of ζ shows that ζ was

almost always fixed at a value of $\zeta_{stable}^{max} = 2$, which determines the value of the universal function (Fig. 6.13a). Here, it can also be observed that CLM-calculated u_* was smaller than the observed u_* at night, as discussed in Sect. 6.3.5.1. If ζ_{stable}^{max} was changed to a value of 100, then ζ became fixed at 100, and u_* was very small (CLM4.5 D0; Fig. 6.13b). This is a signature of the positive feedback between ζ and u_* at night—where a large value of ζ reduces the turbulence which then leads to even more stable conditions. By using observed u_* we eliminated the possibility of this happening; however with ζ_{stable}^{max} set to 2 there were still some nights where ζ was fixed at ζ_{stable}^{max} (CLM4.5 C0; Fig. 6.13c). When the observed u_* was used and ζ_{stable}^{max} was set to 100, then the values of ζ were approximately the same as observed ζ (CLM4.5 D1; Fig. 6.13d). The value of $\zeta_{stable}^{max} = 100$ was chosen since this is near the upper-limit of observed ζ (Fig. 6.12b1). This example shows the complex interactions between these variables.

6.3.7.3 Sensitivity of CLM4.5 latent heat flux to u_* and the universal function

We first examine how using observed u_* (CLM4.5 C0 or D1) affected the default CLM4.5 A1 fluxes and temperatures (from Table 6.2, the results for C0 and D1 were similar so they will be used interchangeably within our discussion). During the daytime, the difference between CLM4.5 A1 and D1 fluxes (Fig. 6.14a1, b1) and temperatures (Fig. 6.14c1) were small. This is expected because the CLM4.5-derived and observed u_* agree well during the daytime (i.e., Fig. 6.2d).

At night, using observed u_* led to an increase in the magnitude of the net radiation R_{net} as well as the sensible and latent heat fluxes (Fig. 6.14a2). This is expected, since increased u_* should result in increased turbulent mixing and fluxes. Due to these increased fluxes, the nocturnal CLM4.5 canopy and 2-m temperatures increased by $\approx 1.5\,^{\circ}\text{C}$ (Fig. 6.14c2). When the CLM4.5 C0 temperatures are plotted versus Ri_b in Fig. 6.11c1, it can be seen that observed u_* helped limit the continual decrease in CLM temperature in strongly stable conditions in a manner similar to the US-NR1 air temperature (Fig. 6.11a1), as discussed in Sect. 6.3.6. Furthermore, the general shape of the CLM4.5 C0 temperature versus Ri_b curves look similar to the curves from the observations. Using observed u_* in CLM was a first-step toward eliminating the nocturnal cold bias in the vegetation

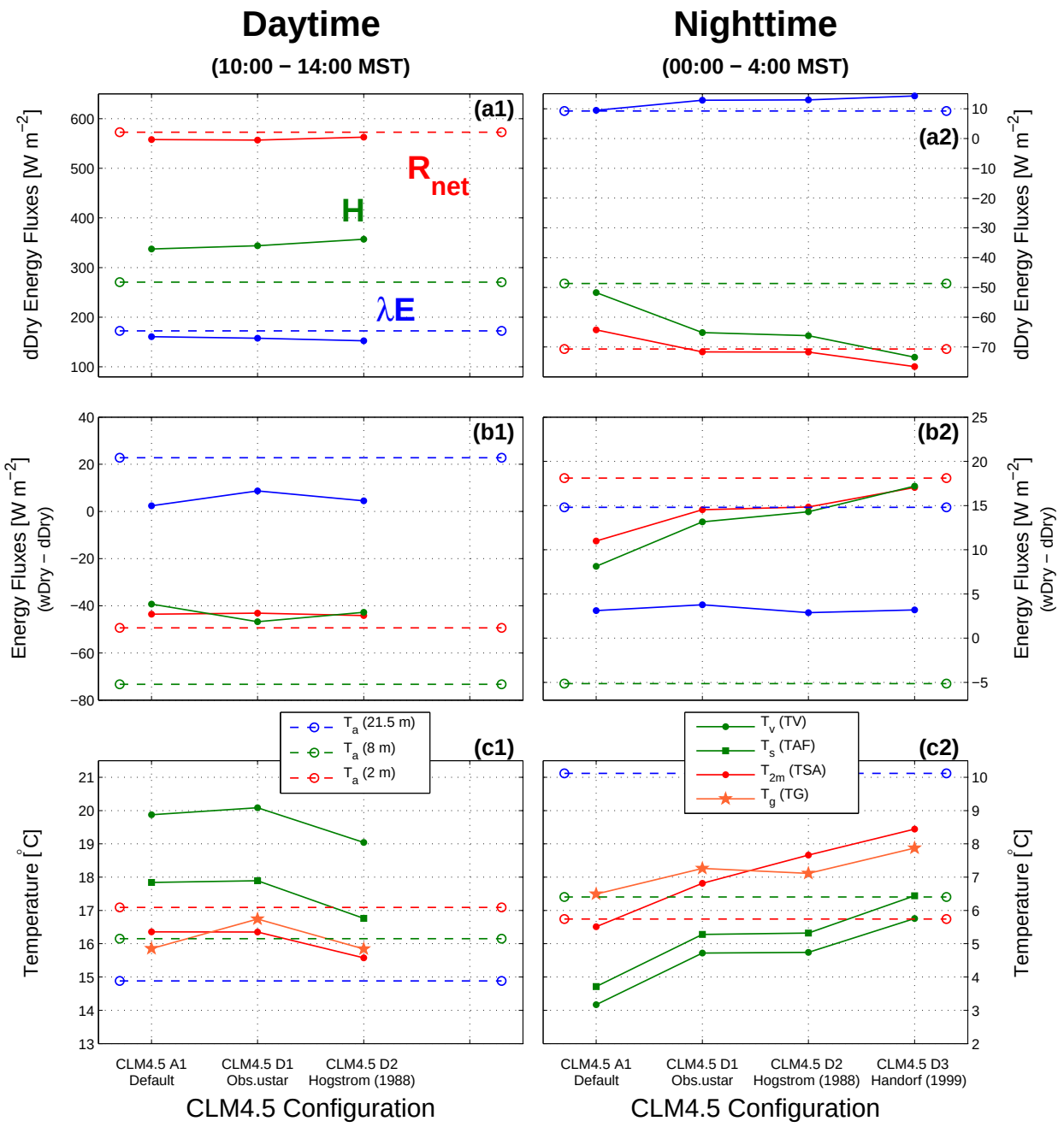

Figure 6.14: The changes in **(a1, b1)** daytime and **(a2, b2)** nighttime above-canopy energy fluxes as the CLM4.5 configuration is changed. The 2 upper panels show the mean values for dDry conditions and the 2 middle panels show the mean differences between wDry and dDry conditions where the variables shown are: net radiation $R_{\rm net}$ (red), sensible heat flux H (green), and latent heat flux λE (blue). The solid lines with filled symbols are the CLM4.5 output, while the dashed lines with open circles are the US-NR1 tower observations. In **(c1, c2)** the observed and CLM4.5 temperatures are shown as described in the two legends. Using the alphanumeric code described in Table 6.1, the CLM4.5 configurations shown from left-to-right are: the default A1, which uses the universal function of Zeng et al. [1998]; D1 which uses observed u_*; D2 which uses the universal function of Högström [1988]; and D3 which uses the universal function of Handorf et al. [1999] (only defined in stable conditions).

temperature and controlling runaway cooling in CLM. This point emphasizes the importance of modeling the basic turbulence variables, such as u_*, correctly.

Using the Högström [1988] (CLM4.5 D2) and Handorf et al. [1999] (CLM4.5 D3) universal functions increased the nocturnal temperatures (especially T_{2m}, Fig. 6.14c2) and magnitude of the fluxes even more than CLM5.4 D1. Using observed u_* had a larger effect on the CLM fluxes and temperatures than the choice of universal function.

Though using observed u_* increased the CLM4.5 A1 nocturnal dDry λE value of $9.5\,\mathrm{W\,m^{-2}}$ to over $13\,\mathrm{W\,m^{-2}}$, there was also a corresponding increase in λE during wDry conditions (see the entries for CLM4.5 D1, D2, or D3 in Table 6.2). Therefore, using observed u_* or a different form of the universal function increased λE in both wet and dry conditions, and only produced a wDry–dDry λE value of around $3\,\mathrm{W\,m^{-2}}$, rather than the $15\,\mathrm{W\,m^{-2}}$ from the US-NR1 observations (Fig. 6.14b2, Table 6.2).

6.3.7.4 Sensitivity of CLM4.5 latent heat flux and temperature to *zetamaxstable* ζ_{stable}^{max}

Another factor which changes the CLM4.5 fluxes and temperatures is the value of ζ_{stable}^{max}. In Fig. 6.15, we examine the effect of systematically varying ζ_{stable}^{max} between 0.1 and 100. Of course, the daytime CLM fluxes and temperatures were not affected very much (Figs. 6.15a1, b1, c1). For the nighttime periods, as ζ_{stable}^{max} was increased, the magnitude of the nocturnal dDry fluxes generally became smaller (Fig. 6.15a2) and the CLM4.5 temperatures decreased by $\approx 2\,^{\circ}\mathrm{C}$ (Fig. 6.15c2). Also, there was almost no change in the CLM4.5 fluxes or temperature for $\zeta_{stable}^{max} > 10$. This makes sense if we revisit Fig. 6.12 and realize that only a small percentage of data exist for $\zeta > 10$.

The purpose of ζ_{stable}^{max} is to limit the CLM4.5 universal functions in strongly stable conditions. This is, for all practical purposes, exactly what the universal function suggested by Handorf et al. [1999] was designed to do—but instead of putting the limit on ζ, the modification was made to the universal functions themselves. As we have shown in the time series of Fig. 6.13, reasonable values of ζ can be achieved if u_* is accurate. For this reason, it seems more logical to eliminate the use of ζ_{stable}^{max} in CLM4.5, and instead use a universal function that becomes a constant in the strongly

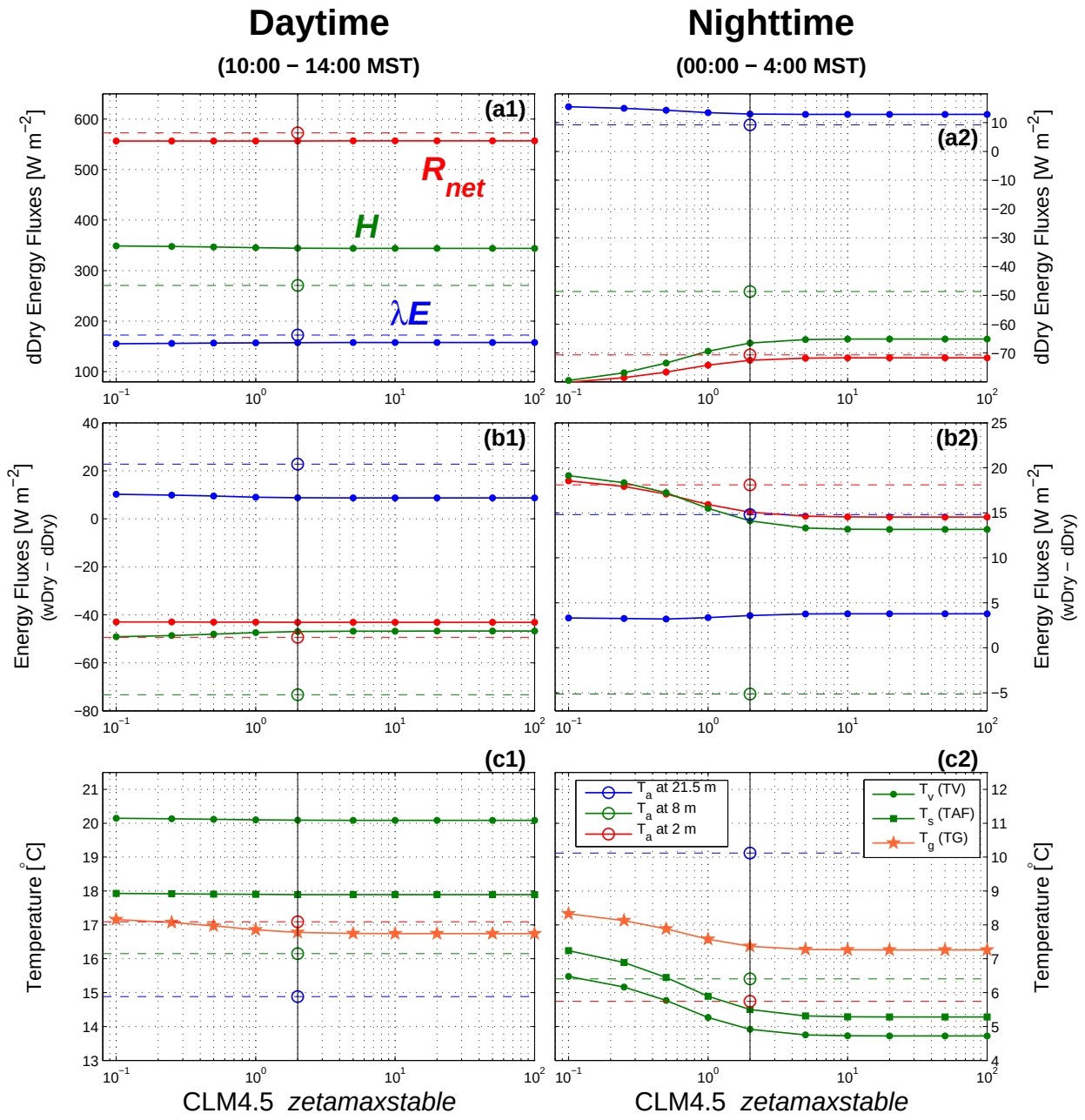

Figure 6.15: The **(a1, b1)** daytime and **(a2, b2)** nighttime energy fluxes versus the CLM4.5 variable *zetamaxstable* ζ_{stable}^{max} as it varies from 0.1 to 100. The upper panels show the mean values for dDry conditions and the middle panels show the mean differences between wDry and dDry conditions where the variables shown are: net radiation $R_{\rm net}$ (red), sensible heat flux H (green), and latent heat flux λE (blue). The solid lines with filled symbols are the CLM4.5 output, while the horizontal dashed lines are the US-NR1 tower observations with open circles placed at the CLM4.5 default value of $\zeta_{stable}^{max} = 2$. In **(c1, c2)**, the US-NR1 observed air temperature T_a and the effect of varying ζ_{stable}^{max} on CLM canopy surface T_v, canopy air T_s and ground T_g temperatures are shown (see legends). The CLM results use the CLM4.5 D1 configuration (Table 6.1), with ζ_{stable}^{max} being varied.

stable regime, such as that proposed by Handorf et al. [1999].

The other question related to both ζ_{stable}^{max} and/or a revised universal function is which value of ζ to use for the cut-off value. It would be logical to have this occur where there is a change in the flow characteristics. In terms of bulk Richardson number, the transition from fully turbulent to stable flow has traditionally been thought to occur at $Ri_b \approx 0.25$. At the US-NR1 site, Burns et al. [2011] found that, for $0.01 < Ri_b < 0.5$, there was a nearly linear relationship between Ri_b and ζ, and for $Ri_b > 0.5$, ζ became nearly constant at $\zeta \approx 1$. This suggests that (for US-NR1) the universal function should become a constant at $\zeta \approx 1$. This cut-off value agrees well with the universal function of Högström [1988], which, in stable conditions, is only defined for $\zeta < 1$ (Fig. 6.12b2, b3; Table 6.4). Handorf et al. [1999] chose a cut-off value of $\zeta = 0.6$ for the stable boundary layer over an Antarctic ice shelf. One would expect this cut-off value to be landscape-dependent and a possible range of values would best be determined by comparing results from many sites.

The variation of ζ_{stable}^{max} shown in Fig. 6.15 is equivalent to changing the ζ cut-off value for a universal function. Here, we can get some idea of the sensitivity of the CLM fluxes and temperature to changing this cut-off value. When the cut-off value was changed from the default value of 2 to 1, the following can be observed: there was a small effect on λE, dDry H decreased on the order of 10-15%, and the CLM temperatures increased by ≈ 0.5°C (Fig. 6.15). Though a more focused study may be needed, our initial results suggest that eliminating ζ_{stable}^{max} from CLM and using the universal function of Högström [1988], with a constant universal functions for $\zeta > 1$, should produce reasonable CLM results.

6.3.8 Subcanopy turbulent exchange in CLM4.5

For forested locations, CLM4.5 includes an additional resistance that represents the turbulent exchange of heat and moisture between the ground surface and the overlying canopy air-space. This turbulent energy exchange is controlled by the aerodynamic resistances for heat ${r_{ah}}'$ and water vapor

${r_{aw}}'$, which are assumed to be equivalent, and follow,

$$ {r_{ah}}' = {r_{aw}}' = \frac{1}{C_s U_{av}}, \tag{6.4} $$

where U_{av} is the magnitude of the wind velocity on the vegetation and C_s is the turbulent transfer coefficient between the underlying soil and the canopy air. Following Dickinson et al. [1993], U_{av} is roughly estimated based on the above-canopy friction velocity (i.e., $U_{av} = u_*$). Because there are wind speed and turbulence measurements within the subcanopy at US-NR1, we will test/validate the $U_{av} = u_*$ relationship at the US-NR1 site in Sect. 6.3.8.3.

Subcanopy exchange is known to depend on the canopy density profile within a forest [Zeng et al., 2005]. In CLM4.5, C_s is calculated from a linear combination of bare-soil $C_{s,bare}$ and dense canopy $C_{s,dense}$ turbulent transfer coefficients,

$$ C_s = C_{s,bare} W + C_{s,dense}(1 - W), \tag{6.5} $$

where W is an exponential function of the leaf and stem-area index. For the US-NR1 site with LAI≈4, W is around 0.018 and $C_{s,dense}$ is the dominant contributor to C_s.

Sakaguchi and Zeng [2009] proposed that $C_{s,dense}$ should depend on the local stability beneath the canopy. This accounts for situations where a dense overstory can lead to a stable understory during the daytime and an unstable understory at night. In extreme cases, such a situation can produce thermotopographic flows within the subcanopy [e.g., Froelich and Schmid, 2006]. Sakaguchi and Zeng [2009] assumed that $C_{s,dense} = 0.004$ was appropriate for locally unstable conditions in the subcanopy. To account for locally stable conditions (i.e., a canopy air temperature T_s warmer than the ground T_g), Sakaguchi and Zeng [2009] decreased the default $C_{s,dense}$ value of 0.004 following,

$$ C_{s,dense} = \begin{cases} 0.004 & T_s - T_g \leq 0 \text{ (locally unstable)}, \\ \dfrac{0.004}{1 + \gamma \min(S, 10)} & T_s - T_g > 0 \text{ (locally stable)}, \end{cases} \tag{6.6} $$

where γ is an empirical constant (chosen to be 0.5 by Sakaguchi and Zeng [2009]). S is a stability parameter with a form similar to $\mathrm{Ri_b}$, calculated by,

$$ S = \frac{gh(T_s - T_g)}{T_s u_*^2}, \tag{6.7} $$

where h is the canopy height and u_* is evaluated above the canopy (but also represents an average wind speed within the subcanopy airspace, as discussed in Sect. 6.3.8.3). The upper value of 0.004 for $C_{s,dense}$ was originally proposed by Dickinson et al. [1993], and it is not entirely clear how that specific value was determined. As discussed by Zeng et al. [2005], values for $C_{s,dense}$ on the order of ≈ 0.04 have been proposed by others [e.g., Bonan, 1996, Lo Seen et al., 1997]. Next, we examine the sensitivity of CLM4.5 output to variations in $C_{s,dense}$ and discuss the appropriateness of the Sakaguchi and Zeng [2009] correction (hereafter, labeled the "S–Z" correction).

6.3.8.1 Sensitivity of CLM4.5 latent heat flux and temperature to $C_{s,dense}$

During the daytime, as $C_{s,dense}$ was increased from 0.001 to 40 (the CLM4.5 default value is 0.004), changes to R_{net} (Figs. 6.16a1, b1) and T_v and T_s temperatures (Fig. 6.16c1) were generally small. However, as $C_{s,dense}$ was increased from 0.004 to ≈0.1, the ground temperature T_g increased and became very close to the canopy air temperature T_s. This implies that larger values of $C_{s,dense}$ increased the turbulent heat exchange between the atmosphere and the ground, warming the soil. During the daytime we have shown that T_a within the US-NR1 subcanopy was nearly constant with height, suggesting that air within the subcanopy was well-mixed. This implies that increasing $C_{s,dense}$ to the point where $T_g \approx T_s$ might be realistic.

The effect of increased $C_{s,dense}$ on the CLM mid-day fluxes is shown in Fig. 6.16a1, where dDry sensible heat flux increased at the expense of the latent heat flux. As $C_{s,dense}$ was increased, wDry−dDry λE increased from just-above zero for $C_{s,dense} = 0.001$, to a value of around $70\,\mathrm{W\,m^{-2}}$ at $C_{s,dense}$≈0.4 (Fig. 6.16b1). This was much larger than the US-NR1 wDry−dDry λE value of $\approx 25\,\mathrm{W\,m^{-2}}$ (shown as a blue dashed line in Fig. 6.16b1). This suggests that during a wDry day water was available to evaporate in CLM4.5, but $C_{s,dense}$ set at 0.004 limited this evaporation.

At night, as $C_{s,dense}$ was increased, the wDry−dDry λE difference increased dramatically to $\approx 16\,\mathrm{W\,m^{-2}}$ (for $C_{s,dense} > 4$) which was just-above the observed wDry−dDry λE value (Fig. 6.16b2). While we do not necessarily advocate that $C_{s,dense}$ should be increased from 0.004 to 4 (a factor of 1000), this example shows that changes to $C_{s,dense}$ can significantly impact nocturnal λE in wet

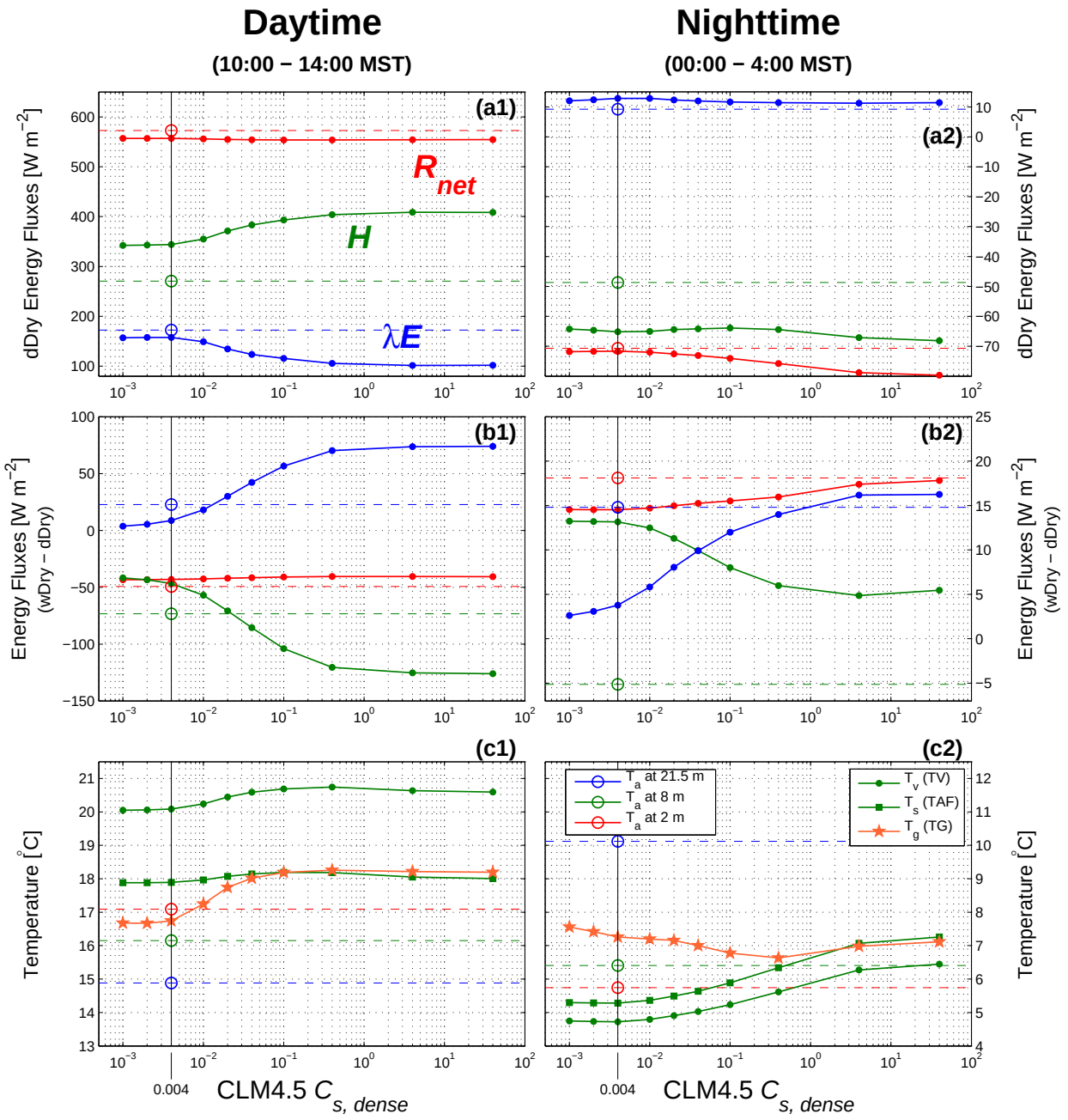

Figure 6.16: Similar to Fig. 6.15, except that the CLM4.5 dense canopy turbulent transfer coefficient $C_{s,dense}$ is varied from 0.001 to 40 (the CLM4.5 default value is $C_{s,dense} = 0.004$). The CLM results use the CLM4.5 F2 configuration (see Table 6.1 for details), with $C_{s,dense}$ being varied.

conditions.

For increased $C_{s,dense}$, the CLM4.5 nocturnal air and canopy temperatures all increased, while T_g decreased (Fig. 6.16c2), suggesting that heat was extracted from the soil and added to the atmosphere. (As discussed previously, the CLM nocturnal temperatures seemed more reasonable using observed u_*, so in Fig. 6.16 observed u_* was used.) If we look at the US-NR1 vertical T_a profile in Fig. 6.10b, the coldest air was located near the ground which implies that the ground surface was the coldest location, not the canopy as suggested by CLM. From Fig. 6.16c2, it is clear that $C_{s,dense}$ affects the relationship between T_g and T_s, and, at $C_{s,dense} \approx 0.4$, T_s approaches T_g.

In order to better understand how $C_{s,dense}$ affected the CLM latent heat flux, the components of λE are plotted in Fig. 6.17 as $C_{s,dense}$ was varied. In dDry mid-day conditions, there was a decrease in λE as $C_{s,dense}$ was increased due to changes in H (as discussed above, and shown in Fig. 6.16a1). The ground evaporation term increased slightly as $C_{s,dense}$ increased from 0.001 to 0.01, and then leveled off for $C_{s,dense} > 0.01$ (Fig. 6.17a1). However, for mid-day wDry−dDry, it was the ground evaporation term that contributed most to λE, and the magnitude of the ground evaporation was highly dependent on the value of $C_{s,dense}$ (Fig. 6.17b1). At night, the transpiration and ground evaporation in dDry conditions were both at around $5\,\mathrm{W\,m^{-2}}$ with only a weak dependence on $C_{s,dense}$ (Fig. 6.17a2). In wet conditions, the nocturnal transpiration decreased (which is why wDry−dDry for transpiration is negative in Fig. 6.17b2), and ground evaporation increased. Similar to the daytime, the magnitude of nocturnal ground evaporation was very sensitive to the choice of $C_{s,dense}$.

For our study, we were conservative, and examined the effect of increasing $C_{s,dense}$ from the default value of 0.004 to 0.01 (i.e., CLM4.5 F0, F1, and F2 in Table 6.1). The value of 0.01 was chosen because it produced a mid-day wDry−dDry λE value that was close to the observations (Fig. 6.16b1); however, the nighttime data suggest that $C_{s,dense}$ could be increased even further. As discussed by others [e.g., Zeng et al., 2005, Sakaguchi and Zeng, 2009], the real issue is that $C_{s,dense}$ cannot be assumed a constant and should depend on the conditions at the site. For simplicity and consistency we have left $C_{s,dense}$ as a constant in our study, but the validity of using a constant

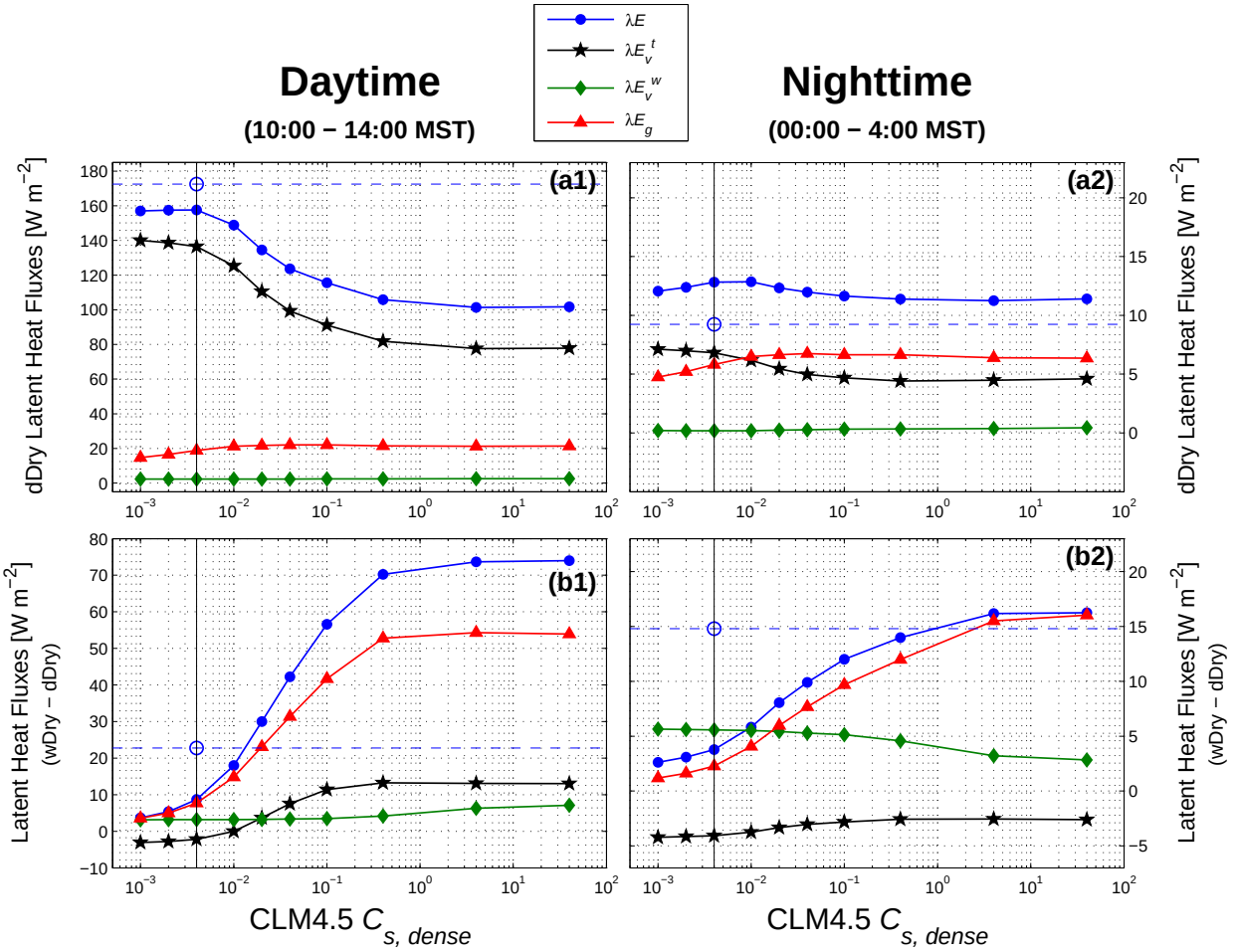

Figure 6.17: The **(a1, b1)** daytime and **(a2, b2)** nighttime CLM4.5 latent heat flux components as the CLM4.5 dense canopy turbulent transfer coefficient $C_{s,dense}$ as it is varied from 0.001 to 40. (top panels) The mean values for dDry conditions and (lower panels) the mean differences between wDry and dDry conditions where the λE components (as described in the legend) are: total latent heat flux λE; canopy transpiration λE_v^t; canopy evaporation λE_v^w; and ground evaporation λE_g. The solid lines with filled symbols are the CLM4.5 output, while the horizontal dashed lines are the US-NR1 observed λE with open circles (and vertical black line) placed at the CLM4.5 default value of $C_{s,dense} = 0.004$. The CLM results use the CLM4.5 F2 configuration (Table 6.1), with $C_{s,dense}$ being varied.

$C_{s,dense}$ needs further examination.

6.3.8.2 Correction of Sakaguchi and Zeng [2009]

For US-NR1, the S–Z correction (Eq. 6.6) does not achieve satisfactory results for reasons we explain herein. First, the subcanopy air (and thus T_a) was, on average, well-mixed during the

daytime, and the ground surface was directly cooled by longwave radiation at night (Fig. 6.10). The S–Z correction was designed for situations where a drastic temperature difference between the canopy and ground exists, which US-NR1 does not have. Second, the S–Z correction did not work well at US-NR1 at night due to the unreasonably cold canopy bias (using CLM4.5 A1) which created very unstable (and unrealistic) conditions in the subcanopy (Fig. 6.11). However, even after the CLM temperatures were made more reasonable (e.g., by using observed u_*), the S–Z correction still seems problematic because it was very small in the most stable conditions (Fig. 6.11c2).

We also need to consider the magnitude and direction of the S-Z correction. As mentioned by Sakaguchi and Zeng [2009], the S–Z correction that they proposed is "conservative". On average, the S–Z correction reduced $C_{s,dense}$ by about a factor 0.7 at night (red line in Fig. 6.11c2) and 0.6 during the daytime (red line in Fig. 6.18c2). This means that, in general, the S–Z correction reduced $C_{s,dense}$ from 0.004 to somewhere between 0.0016 to 0.0028. In Fig. 6.16, one can observe that such changes to $C_{s,dense}$ would lead to very small changes to the CLM fluxes and/or temperatures. Furthermore, as shown in Fig. 6.16 (and discussed in the previous section), it is by increasing $C_{s,dense}$ that significant changes to CLM output occurred. While the value of 0.004 might be appropriate for certain forest types, it does not appear to work well at the US-NR1 coniferous forest site. In short, it should be considered whether 0.004 is an appropriate upper value of $C_{s,dense}$ (or not). For more discussion, see Sect. 6.3.9.1.

6.3.8.3 Relationship between u_* and subcanopy wind

As part of the subcanopy turbulent parameterization, it is assumed that the wind velocity on the vegetation U_{av} is linearly related to above-canopy friction velocity, i.e., $U_{av} = u_*$. Surprisingly, we could not find any study that checked or confirmed this relationship. This expression was first suggested by Dickinson et al. [1993] and then adopted into CLM4.5. At the US-NR1 site, we used two sonic anemometers located in the mid- and lower-portion of the canopy to show that the subcanopy mean wind speed U has very little connection to above-canopy u_* (Fig. 6.19). If we make an assumption that subcanopy $U \approx U_{av}$, then using $U_{av} = u_*$ will lead to an overestimate

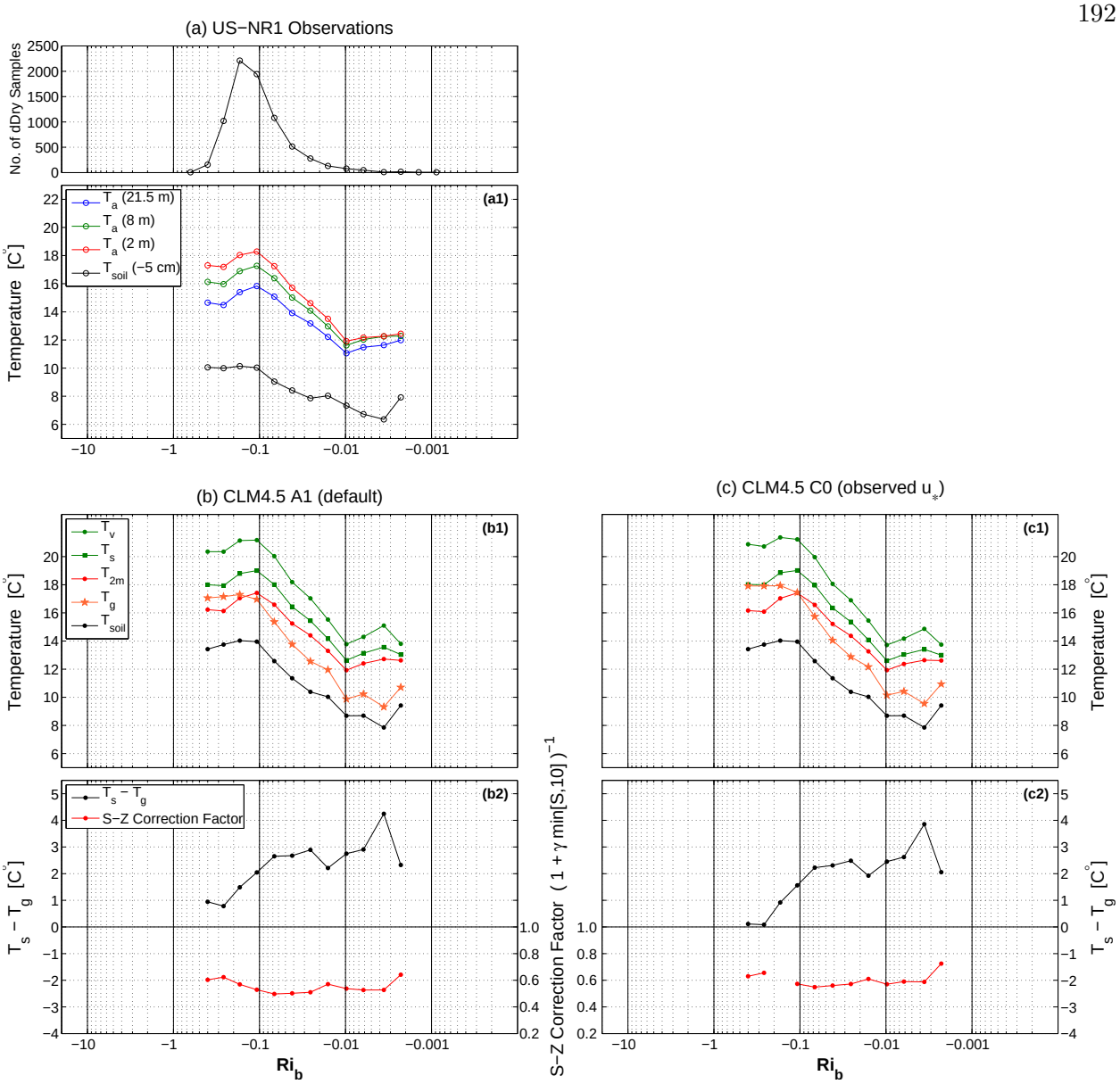

Figure 6.18: As in Fig. 6.11, except for unstable conditions.

of U_{av} by about a factor of 2 in high above-canopy winds, and an underestimation of U_{av} in low winds. Somewhere in the upper canopy it is possible that $U_{av} = u_*$ is appropriate. Mean wind profiles in canopies are known to primarily follow an exponential profiles with height [e.g., Inoue, 1963, Cionco, 1965]. This is an example of the complexity of flow within a forest canopy and one of the challenges of using a simple big-leaf type of model to represent this complexity.

Air motions in the subcanopy are largely controlled by the canopy-generated coherent struc-

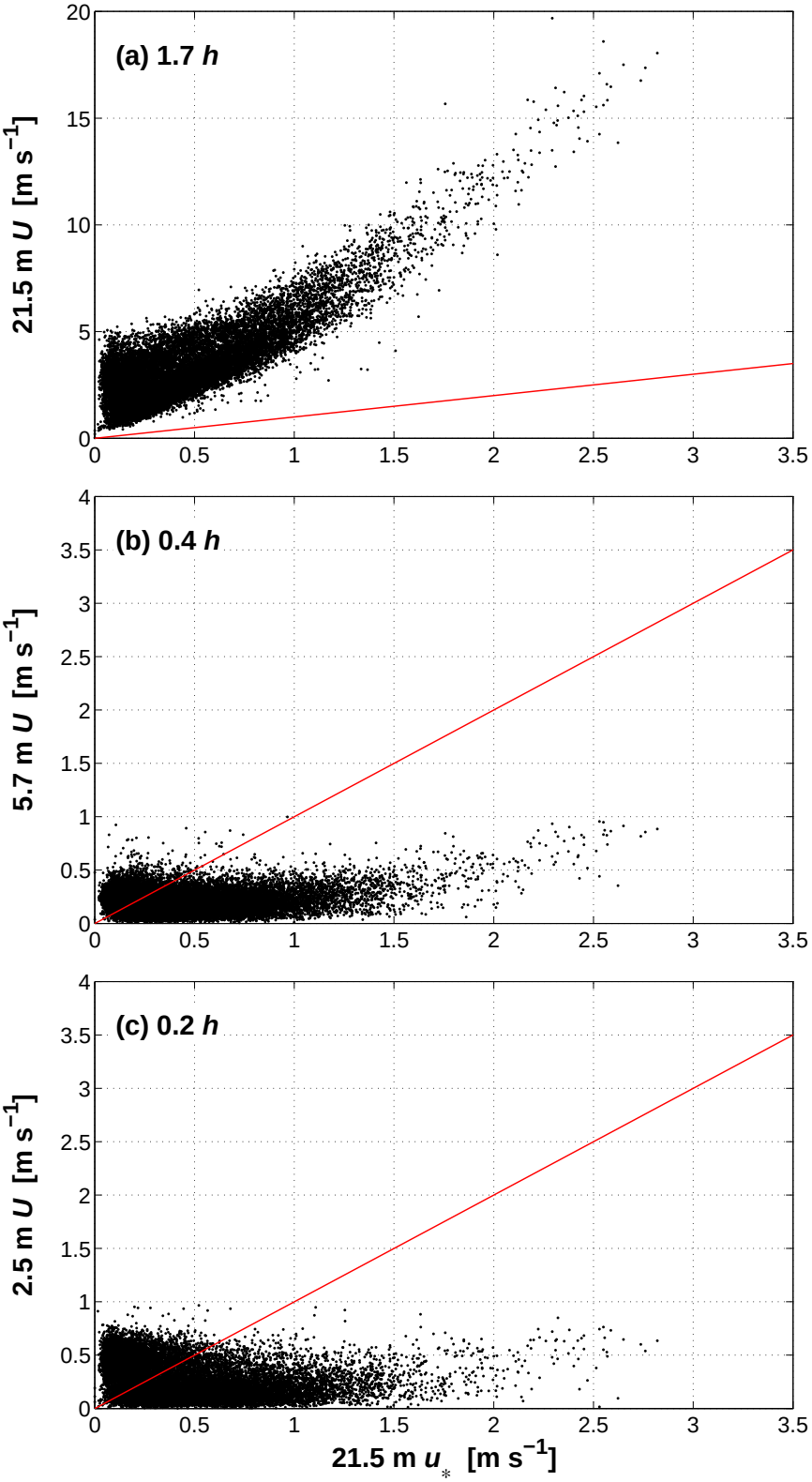

Figure 6.19: The above-canopy friction velocity u_* versus the mean horizontal wind speed U at **(a)** 21.5 m, **(b)** 5.7 m, and **(c)** 2.5 m above the ground. The canopy height h ranges between 12 and 15 m; the percentage of h for each level is shown in the upper-left corner of each panel assuming $h = 13$ m. The red line shows the relationship, $U = u_*$. Each point is a 30-min mean value from the warm season (1 June to 30 September) for years 2005–2012. Note that the y-axis range in **(a)** is a factor of 5 larger than that of **(b)** and **(c)**.

tures just-above canopy top [Raupach et al., 1996] and associated pressure fronts [Shaw and Zhang, 1992]. Or, in complex terrain, by the local topography [Burns et al., 2011]. Such flows often result in subcanopy fluxes that are opposite to the scalar gradient [Denmead and Bradley, 1985]. For a big-leaf model, the meaning of U_{av} is difficult to define because the wind velocity varies from some finite value in the forest gaps to zero at the leaf and branch surfaces. This subject goes beyond the scope of this thesis, but is a possible future topic of study.

6.3.9 Final comments and speculations

6.3.9.1 Contrasting the effect of decreasing f_{wet}^{max} versus increasing to $C_{s,dense}$ on λE

We found that increased mid-day wDry−dDry λE can be achieved by either decreasing f_{wet}^{max} from 1 to 0.02 (Fig. 6.6b1) or by increasing $C_{s,dense}$ from 0.004 to 0.01 (Fig. 6.16b1). Modified f_{wet}^{max} increased CLM wDry λE by modifying the timing and magnitude of the canopy evaporation term, whereas modified $C_{s,dense}$ increased the ground evaporation term. In order to better understand any non-linear or confounding effects of the S–Z correction or using observed u_*, we have plotted the λE components for CLM4.5 B0, B1, and B2 in Fig. 6.20, and those for CLM4.5 F0, F1, and F2 in Fig. 6.21. As discussed in Sect. 6.3.4, the changes to f_{wet}^{max} nicely reproduced two aspects of the observations: (1) the timing and magnitude of the increase of mid-day λE on a wDry day, and (2) the shape of λE on the afternoon of a wet day (relative to a dDry day). These features remain regardless of the S-Z correction (Fig. 6.20b) or the use of observed u_* (Fig. 6.20c). For increased $C_{s,dense}$, the increase of mid-day wDry−dDry λE occurred most strongly when observed u_* was used (Fig. 6.21c). In addition, for CLM4.5 F0, F1, and F2, λE on the afternoons of dWet and wWet days does not look very much like the observations (i.e., Fig. 6.4b).

If we only consider a wDry day (Fig. 6.7c) we can see that observed λE between 0-4 MST was about $10\,\mathrm{W\,m^{-2}}$ larger than the dDry value, whereas between 19–24 MST λE approached the dDry value. This means that the contribution of evaporation to the enhancement of λE, on average, lasts about 18 hours following a wet day [Burns et al., 2015a]. This implies that CLM

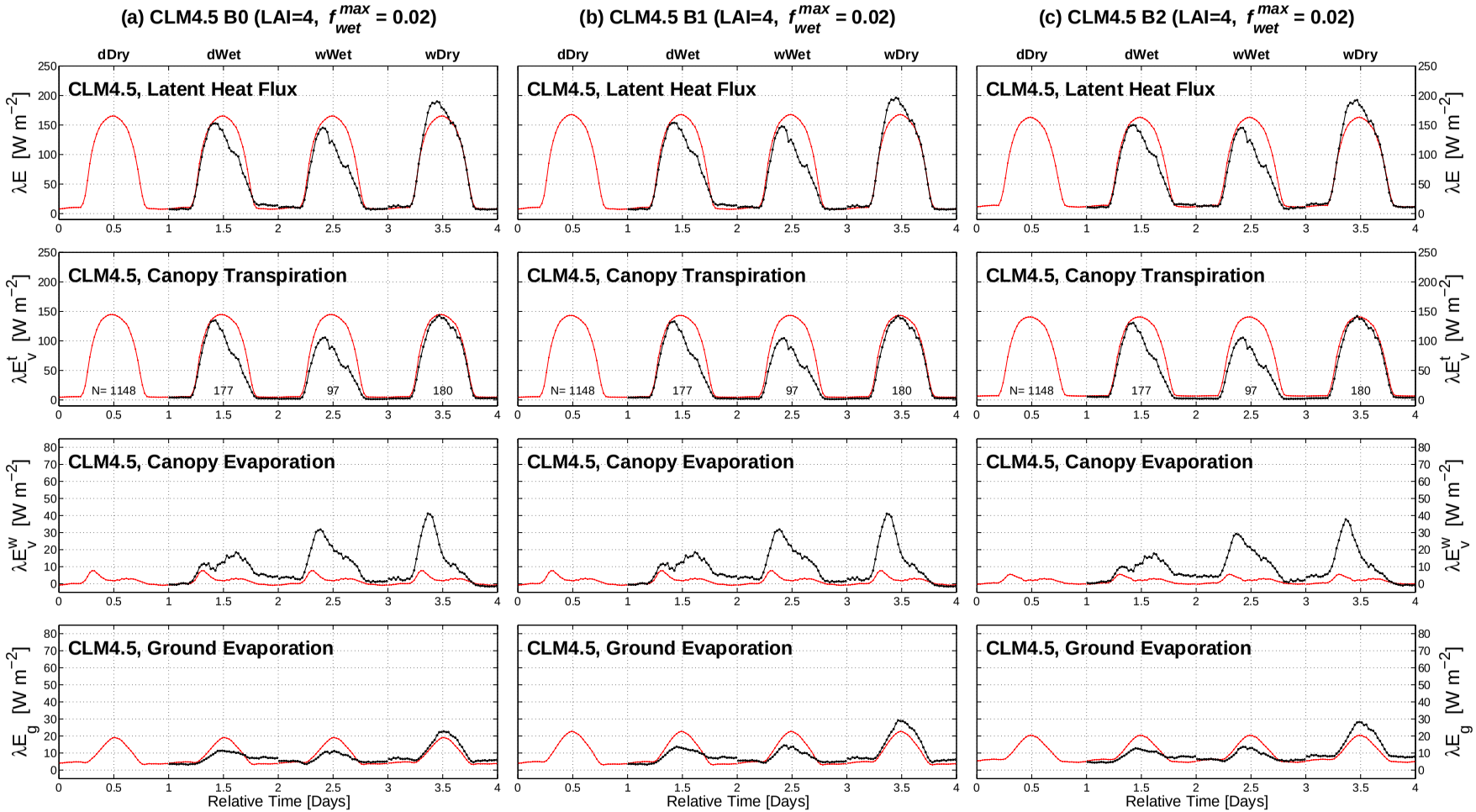

Figure 6.20: The mean diel cycle of CLM4.5 components of latent heat flux λE with LAI=4 and *maximum leaf wetted fraction* $f_{wet}^{max} = 0.02$ for different CLM4.5 configurations: (**a**) CLM4.5 B0, (**b**) CLM4.5 B1, and (**c**) CLM4.5 B2 where the settings for each alphanumeric code are described in Table 6.1. The mean diel cycles are separated into dDry, dWet, wWet, and wDry conditions where the red line in each panel is the mean diel cycle for dDry conditions which is repeated for ease of comparison to the results from dWet, wWet, and wDry conditions. CLM4.5 λE is broken down into individual components which are (from top to bottom row): total latent heat flux (λE); canopy transpiration (λE_v^t); canopy evaporation (λE_v^w), and ground evaporation (λE_g).

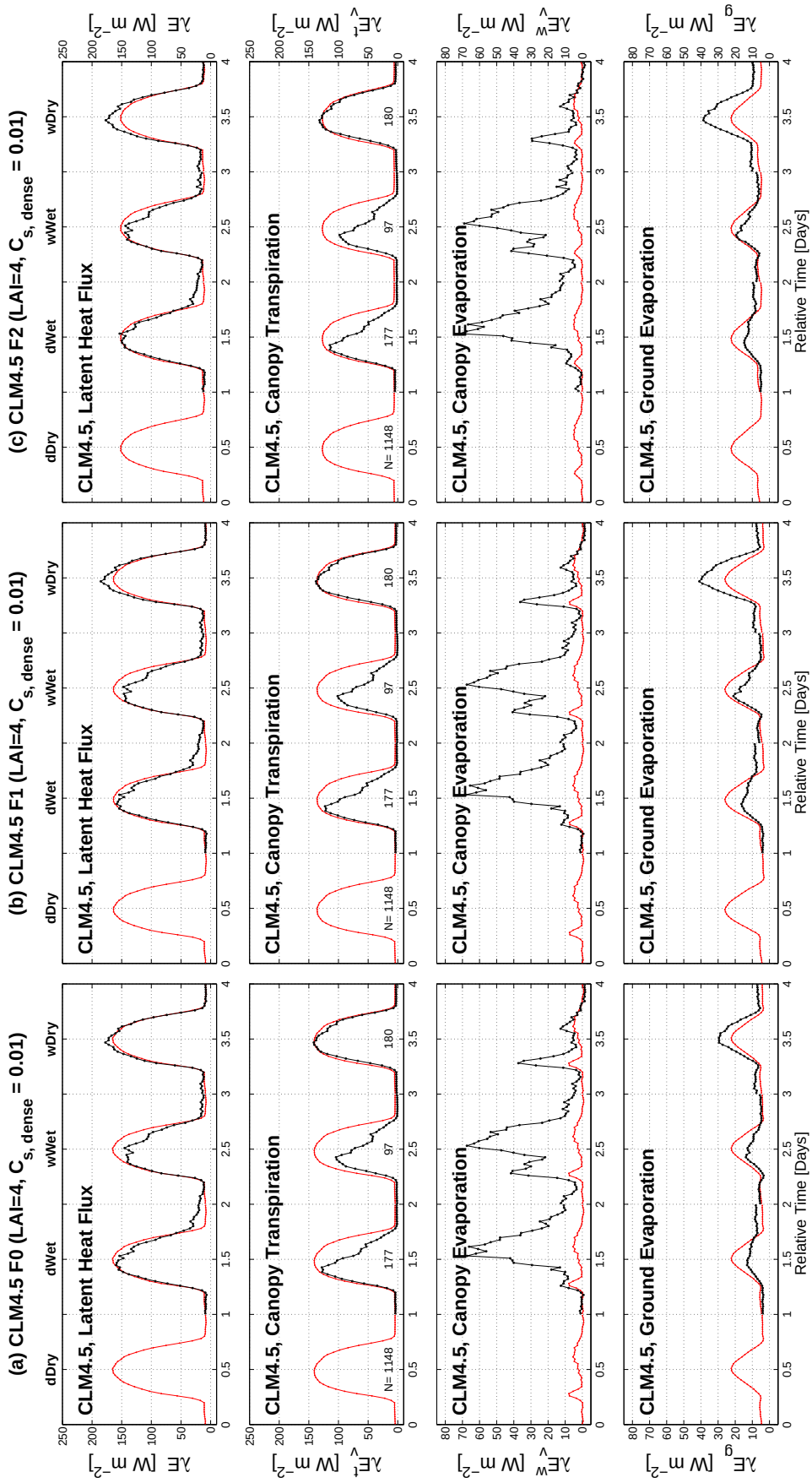

Figure 6.21: Similar to Fig. 6.20, except here the subcanopy turbulent exchange coefficient $C_{s,dense}$ =0.01 and different CLM4.5 configurations are: (**a**) CLM4.5 F0, (**b**) CLM4.5 F1, and (**c**) CLM4.5 F2. The settings for each alphanumeric code are described in Table 6.1.

canopy and ground evaporation terms should be higher on a wDry early morning and smaller on a wDry evening. As shown in Fig. 6.7c, the canopy evaporation term behaved that way for the CLM4.5 B1 and B2 configurations. In contrast, for ground evaporation, the magnitude of early morning and evening λE_g were almost the same. This, coupled with the fairly symmetric shape of the ground evaporation around noon, suggest that the ground evaporation term in CLM is unrealistic during a wDry day.

As discussed in Sect. 6.3.8.1, CLM ground evaporation is sensitive to the value of $C_{s,dense}$. These analyses suggest that the parameterization of subcanopy turbulent transfer (i.e., $C_{s,dense}$) and the related S–Z correction could be revisited and/or improved in CLM. This would best be achieved by looking at different forest types in a variety of terrain (flat, simple slopes, mountainous) and over a wide range of stabilities, similar to what was done by Zeng et al. [2005]. Such a study would determine the site characteristics and atmospheric conditions that most affect $C_{s,dense}$, as well as whether using a constant value for $C_{s,dense}$ is appropriate.

To examine the effect of changing $C_{s,dense}$ and f_{wet}^{max} at the same time, we included the CLM4.5 G1 configuration in our study (Table 6.2). In Figs. 6.22–6.24, we have repeated Figs. 6.2, 6.9, and 6.10 using the CLM4.5 G1 configuration. From Fig. 6.23, it is apparent that CLM λE can be increased in strongly stable conditions. Figure 6.24 shows how the CLM nocturnal temperatures increase by around 1.5 °C with the G1 settings.

6.3.9.2 Cumulative effects of revised CLM4.5 parameters

In our study we have examined 14 different CLM4.5 configurations (Table 6.1) with the statistics for each configuration shown in Table 6.2. Since we have focused on the diel cycle, an obvious question is how different are the long term, cumulative fluxes for these 14 possible changes to CLM. Such knowledge, for example, has implications related to the total amount of water transported from an ecosystem to the atmosphere over a season [e.g., Knowles et al., 2015b]. The far right-hand column of Table 6.2 shows (in bold font for λE) the percent difference between the CLM4.5 cumulative water loss relative to the US-NR1 observed water loss over the 2010 warm

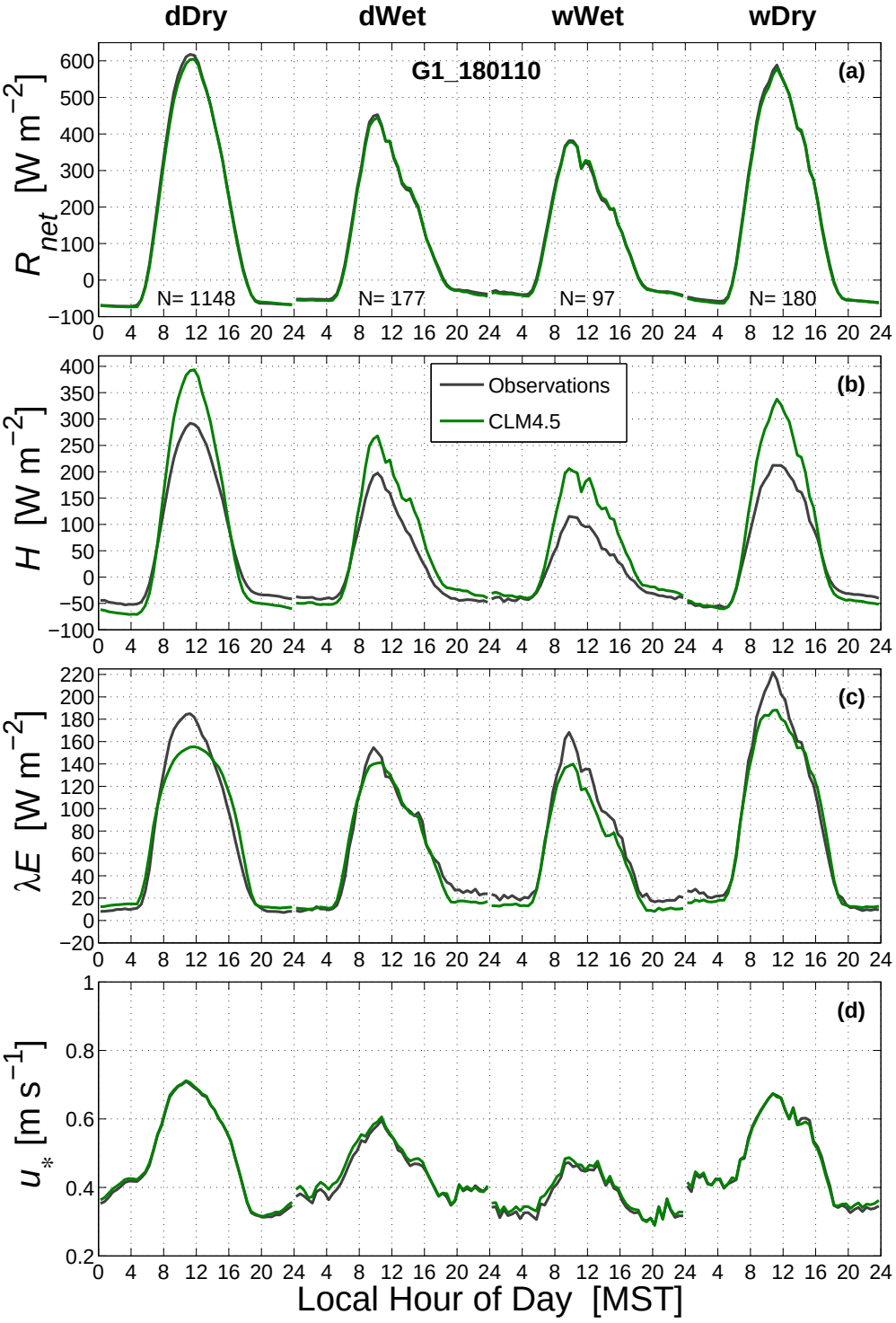

Figure 6.22: As in Fig. 6.2, except for the CLM4.5 G1 configuration (i.e., with LAI = 4, observed u_*, $C_{s,dense} = 0.01$, $f_{wet}^{max} = 0.02$, and using universal function from Högström [1988]).

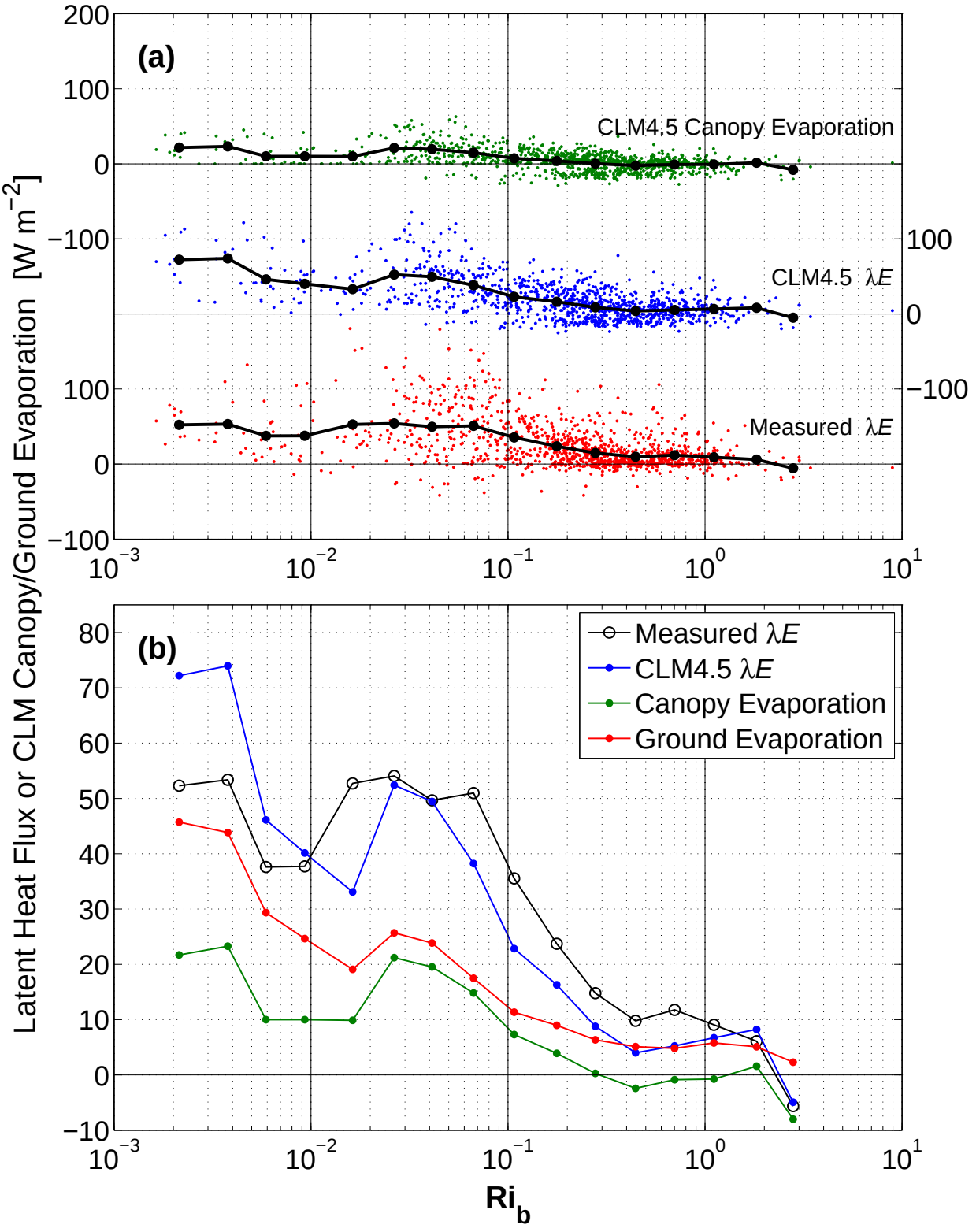

Figure 6.23: As in Fig. 6.9, except for the CLM4.5 G1 configuration (i.e., with LAI = 4, observed u_*, $C_{s,dense} = 0.01$, $f_{wet}^{max} = 0.02$, and using universal function from Högström [1988]).

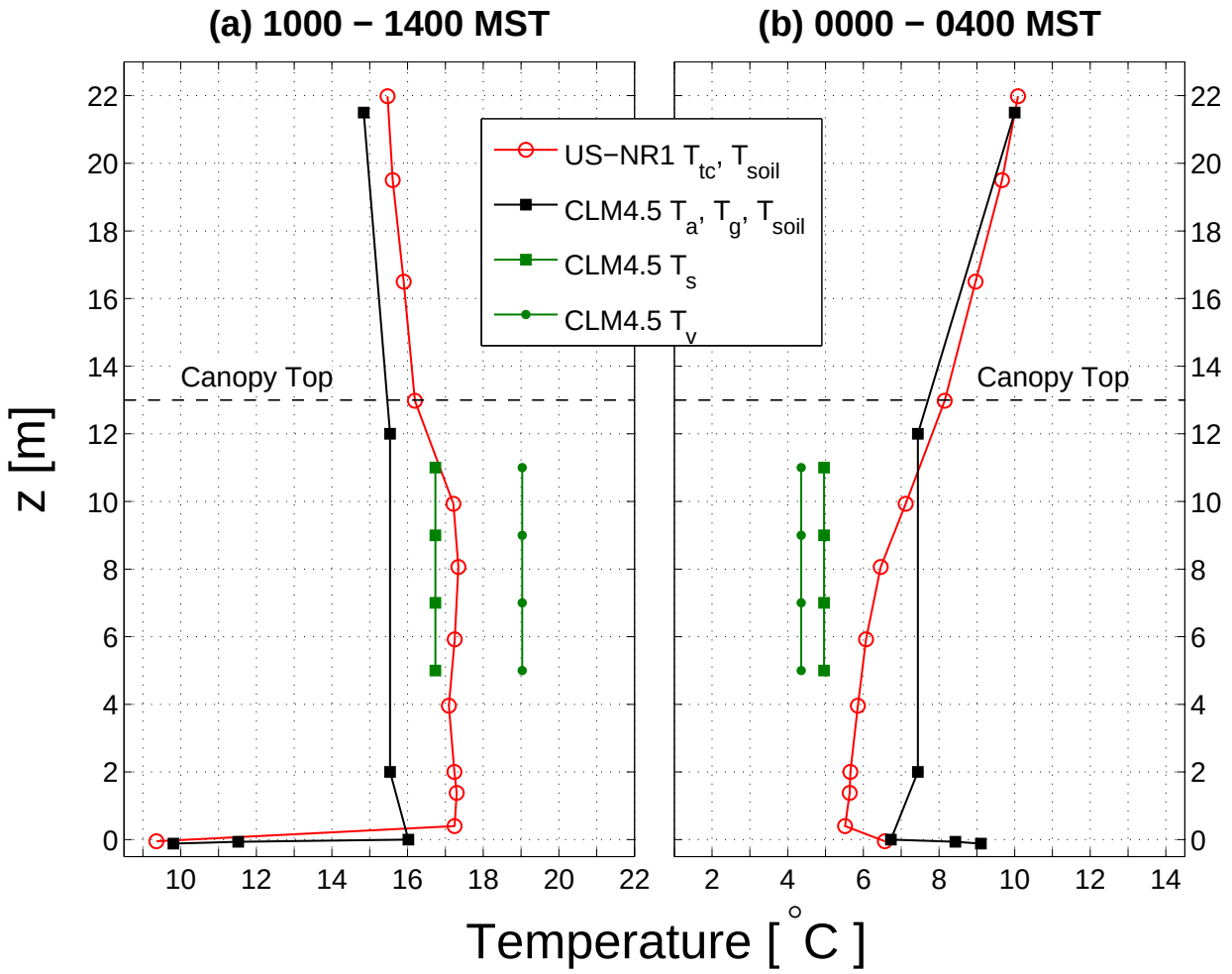

Figure 6.24: As in Fig. 6.10, except for the CLM4.5 G1 configuration (i.e., with LAI = 4, observed u_*, $C_{s,dense} = 0.01$, $f_{wet}^{max} = 0.02$, and using universal function from Högström [1988]).

season (for US-NR1, this was 735.5 MJ m^{-2}, or around 298 mm of water lost for every square meter of the forest). CLM4.5 A1 with LAI=4 had a 2010 warm-season cumulative λE value of 719.5 MJ m^{-2}, which was 2.2% smaller than the US-NR1 observations. For all 14 combinations, the difference from US-NR1 ranged from 4% lower then US-NR1 to around 4% larger. For the configuration with all variables modified (CLM4.5 G1), cumulative λE was 0.9% larger than the US-NR1 observations. Though our focus is on λE, we note that changes to cumulative CLM H were on the order of 25% different from US-NR1 and more sensitive to the choice of CLM configuration (Table 6.2).

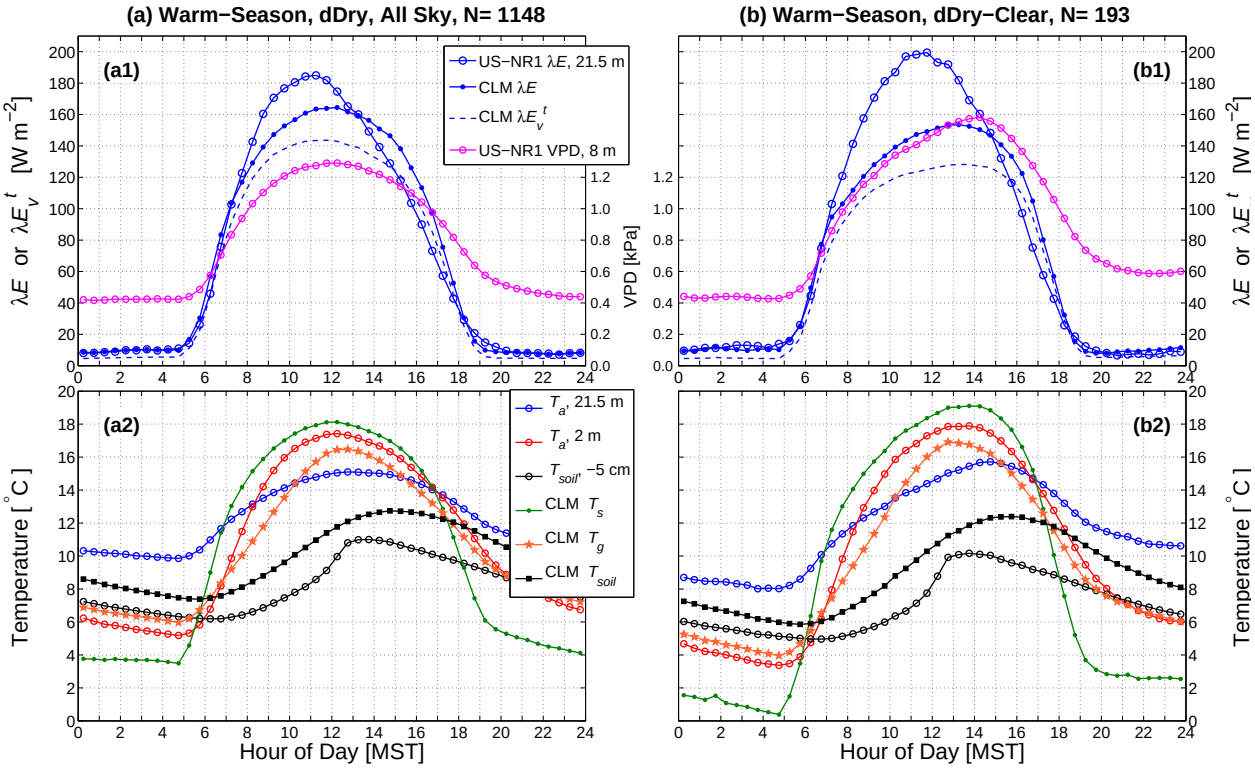

Figure 6.25: The dDry warm-season composite diel cycle of **(a1, b1)** the US-NR1 above-canopy latent heat flux λE and vapor pressure deficit VPD (middle axis) with CLM4.5 λE and canopy transpiration λE_v^t, and **(a2, b2)** US-NR1 observed 21.5 m and 2 m air temperature T_a and soil temperature T_{soil} at −5 cm depth, along with CLM4.5 canopy air temperature T_s, ground temperature T_g, and T_{soil} at −6.5 cm depth. Panels **(a1, a2)** are for all dDry conditions while **(b1, b2)** are dDry days with clear skies; the number of days (N) that satisfy each condition are listed above the upper panel. The legends in the **(a)** panels also apply to the **(b)** panels.

6.3.9.3 Asymmetry in the diel pattern of latent heat flux

Because we are interested in the diel cycle, a close look at Fig. 6.2 reveals that, for dDry conditions, observed R_{net}, H, and λE all peaked just before noon. Burns et al. [2015a] showed that the primary reason the observed fluxes peaked prior to noon was due to the common occurrence of afternoon clouds at the US-NR1 site (generated by the dynamics of the mountain-plain circulation). If only days with clear skies were examined, then these variables peak close to noon. While CLM4.5 does a fairly good job on the timing of the peak for R_{net} and H, CLM λE peaks near noon, rather than before noon (Fig. 6.2c). In Fig. 6.25 we have separated the dDry diel cycle into periods with any sky condition (left-side panels) and those with clear skies (right-side panels). In the upper

panels of Fig. 6.25, we have included the vapor pressure deficit (VPD) measured at the site along with λE. Here, we can see the the peaks in CLM λE and VPD were both at around noon in all-sky conditions (Fig. 6.25a1) and shifted toward around 14:00 MST for clear skies (Fig. 6.25b1). In contrast, the timing of the peak in observed λE shifted from around 11:00 MST in all-sky conditions to just before noon with clear skies. It seems that the peak in CLM λE follows observed VPD, while observed λE does not. There are several possible explanations for this mismatch in the timing of the CLM λE peak: observed λE is affected by larger-scale atmospheric processes which are unknown to CLM, such as entrainment of dry air at the top of the boundary layer [Betts, 2009, van Heerwaarden et al., 2010, Gentine et al., 2011] or large eddies that impact the near-surface turbulence [Patton et al., 2016]; or, it could be related to improper modeling of the US-NR1 tree hydrodynamics [e.g., Matheny et al., 2014].

If we compare the timing of the temperatures peaks in all-sky (Fig. 6.25a2) versus clear-sky (Fig. 6.25b2) conditions, we can make the following conclusion: the peak in above-canopy air temperature during clear-sky conditions was later (at $\approx$15:00 MST), the peak in soil temperature (at -5 cm) was relatively unaffected by the sky conditions, the peak in observed 2-m air temperature was shifted to a later time, somewhere between the peaks in T_{soil} and above-canopy T_a, and the timing of VPD peaks followed T_a. The shift in timing of the above-canopy T_a is presumably due to the biomass of the forest accumulating heat when the incoming shortwave irradiance is highest (i.e., on clear-sky days), and then slowly releasing it back to the atmosphere. The CLM4.5 canopy air temperature T_s generally followed the pattern of observed T_a. However, observed T_{soil} peaked at around 13:00 MST, while CLM T_{soil} peaked at around 15:00 MST, suggesting that the CLM soil thermal properties or amount of shading is incorrect. The heat capacity of vegetation biomass and soil is an important consideration to properly balance the surface energy budget [e.g., Lindroth et al., 2010, Leuning et al., 2012].

6.3.9.4 The effect of sloped terrain on latent heat flux

CLM4.5 could not simulate the enhanced latent heat flux at night during wet conditions

at US-NR1. Our hypothesis is that enhanced nocturnal λE was due to two phenomena: (1) the presence of liquid water, providing a source for evaporation, and (2) the ever-present slope/drainage flow supplying additional energy to drive the evaporation.

To explore this possibility, we examined data from the Howland Forest AmeriFlux site (US-Ho1). Howland forest was chosen because it has a forest similar to that of US-NR1, but with flatter, rolling terrain. The results from US-Ho1 showed that while US-Ho1 has enhanced λE at mid-day on a wDry day, it did not show increased λE on wet nights (Fig. 6.26). US-Ho1 nocturnal λE was very small for both wet and dry conditions which was similar to CLM nocturnal λE from US-NR1. Though our discussion here is focused on the possible effects of slope flow on λE, we cannot rule out the possibility that the larger LAI at US-Ho1 (US-Ho1 LAI ≈ 5.5 versus US-NR1 LAI ≈ 4) also contributes to a smaller US-Ho1 nocturnal λE. One way to better explore this parameter space would be to look at many sites with a wide range of LAI values and topographic slopes.

Are there features we can examine to highlight something unique about sloped terrain? It is known that the relationship between u_* and wind speed depends on the underlying surface type and roughness [e.g., Blanken et al., 2003]. We explored this relationship for both US-NR1 and US-Ho1 and found that US-Ho1 (and CLM for that matter) exhibited a nearly monotonic increase in u_* with increasing wind speed during mid-day and at night (Fig. 6.27). At US-NR1, however, nocturnal u_* was enhanced for low winds (shown as a "hump" at $U \approx 2\,\mathrm{m\,s^{-1}}$ in Fig. 6.27b2). This, we suspect, is a signature of the drainage flow. At night, CLM-calculated u_* shows a monotonic increase with wind speed, as well as the low-bias discussed in Sect. 6.3.5.1 (Fig. 6.27b2). MOST should not be expected to calculate an accurate value of u_* during light winds in sloping terrain.

Since we used observed u_* as an input into CLM, should that account for the turbulence in the drainage flow? One might expect this, however the turbulence measured above the canopy is not necessarily the same as what is happening near the ground. This is especially true in a slope flow which can be seen in Fig. 6.19c, where the lowest values of above-canopy u_* ($< 0.25\,\mathrm{m\,s^{-1}}$) led to an increase in the 2.5 m horizontal wind speed U. This provides evidence that what is happening above the canopy is not representative of the ground surface, where drainage winds are

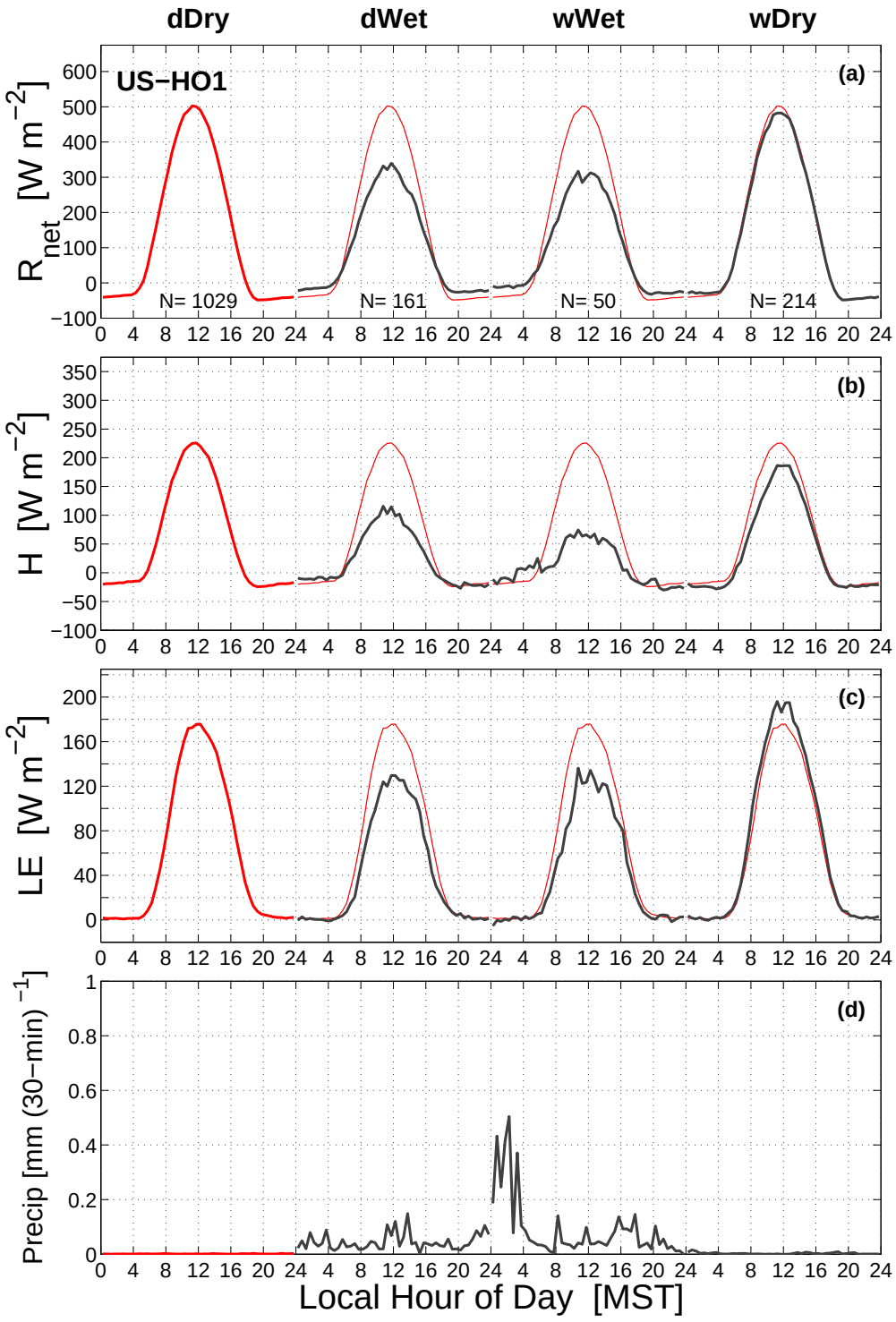

Figure 6.26: As in Fig. 6.1, except for the Howland Forest (US-Ho1) in Maine which is a northern boreal spruce-dominated transitional forest consisting primarily of a hemlock-spruce-fir mixture with an LAI ≈5.5. Measurements are from the warm-season between years 1996 to 2012.

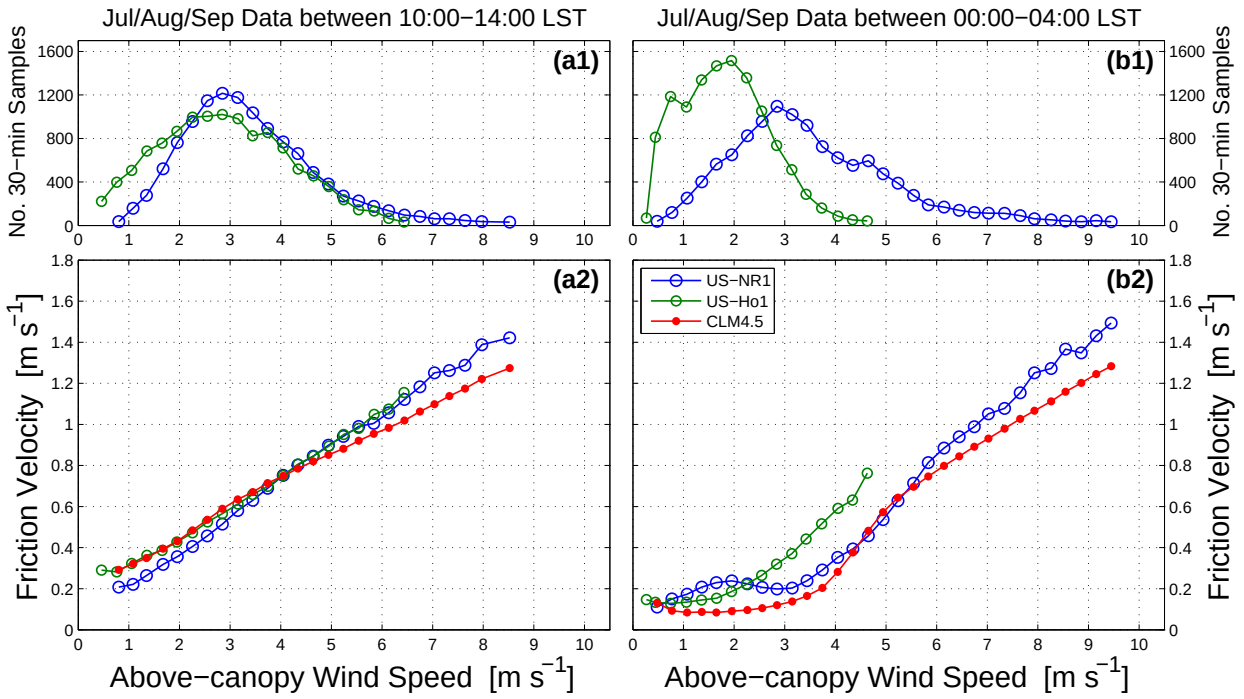

Figure 6.27: Friction velocity u_* versus above-canopy wind speed U for the observations from Howland Forest (US-Ho1), Niwot Ridge (US-NR1) along with CLM4.5 A1 u_* from US-NR1 for **(a2)** daytime and **(b2)** nighttime conditions during the warm-season months. The legend in **(b2)** applies to all panels and only bins with at least 30 samples are shown.. The frequency distribution of 30-min average U is shown in the upper panels for **(a1)** daytime and **(b1)** nighttime conditions.

likely stronger and promoting surface evaporation. Despite several previous studies related to the horizontal advection at US-NR1 [e.g., Yi et al., 2005, Sun et al., 2007, Yi et al., 2008] how the drainage flow affects the above-canopy fluxes and how representative the above-canopy flux is of the actual flux at the ground surface remains poorly understood.

6.4 Conclusions

The influence of warm-season precipitation on a model of the scalars and fluxes at the US-NR1 site have been examined by comparison to the observations. Detailed conclusions from this chapter are in Sect. 7.2.

Chapter 7

Conclusions and future research ideas

This thesis uses and describes measurements made since 1 November 1998 at a high-elevation subalpine forest AmeriFlux research site (US-NR1) located at 3050 m elevation on the east side of Arapaho moraine in western Boulder County, Colorado. First, the history of the forest around the US-NR1 site was examined (Chapter 2). Logging to support mining and building activities was found to have occurred in the area between the late 1880s to the early 1900s (possibly as late as 1920). However, any logging done in the immediate vicinity of the US-NR1 main tower appears to be done selectively, and the forest was primarily left intact. Many trees at the site are over 200 years old, corroborating this description. This information clarifies and corrects previous reports that have suggested logging at the US-NR1 site was at the 99% (clear-cut) level [e.g., Thornton et al., 2002, Bradford et al., 2008]. Understanding the true age of the forest can affect attempts to establish relationships between the forest age and forest productivity or water usage [Bradford et al., 2008].

Chapter 3 is a summary of all the primary variables measured at the US-NR1 site (especially on the main tower). This information was included not only to explain the measurements used in the subsequent data analysis sections, but also to document (in detail) what and how the measurements have been made on the US-NR1 tower (this description is intended to be published as part of a 3-part paper on the US-NR1 site, which is described in the abstract of Chapter 3). In order to assess the quality of the US-NR1 flux measurements, we included the results from a sensor (IRGA) intercomparison that was performed on the US-NR1 tower (conclusions are described in

Sect. 3.23). For long-term measurements such as those at US-NR1, documentation and knowledge of how measurements change over time is an important (and surprisingly difficult) task. An important take-home lesson for other long-term research projects—documentation procedures and strategies should be implemented in the early stages of data collection. In this regard, more work is still needed at US-NR1 to make the historical record complete.

Chapter 4 provided some of the general site characteristics (related to topography, geology, soil, forest structure, and weather/climate). Preliminary results and analysis from lidar and UAV overflights were presented, which showed the enormous power and potential that these platforms have in determining the forest characteristics. In the future, such information can (hopefully) be useful for footprint analysis [Xu et al., 2017] and/or land-surface modeling efforts that might require fine-scale surface characteristics.

Within this thesis, the US-NR1 site observations were focused on answering one simple question (Chapter 5): *How did warm-season precipitation affect the tower measurements?* This observational work was followed with a similar simple question using land-surface modeling (Chapter 6): *If modeled fluxes are calculated using the US-NR1 site meteorological variables as input, can the model reproduce the effect of warm-season precipitation similar to that in the observed surface energy fluxes?* Though the questions we asked are simple, the answers are complex. In the two sections that follow, the conclusions and recommendations for each of these topics will be summarized.

7.1 The influence of warm-season precipitation on US-NR1 observations

Here, we summarize our conclusions from Chapter 5. These results were based on fourteen years of 30-minute measurements at US-NR1. In order to put the warm-season in context, the typical seasonal cycle and interannual variability of turbulent fluxes of sensible and latent heat and NEE from just-above a high-elevation subalpine forest were presented. The snowpack ablation date was used to determine the start of the warm-season. The warm-season was further analyzed to determine how precipitation perturbed the ecosystem fluxes on a diel (i.e., hourly) time-scale. A simple, novel conditional sampling method based on whether the mean daily precipitation was

greater than $3\,\mathrm{mm\,day^{-1}}$ was used which essentially created a four day composite of a cold front passing by the tower (the dry days prior to the cold front, a day when the precipitation started, a day with precipitation on the preceding day, and the day following the precipitation event). Though the wet days comprised only 17 % of the warm-season days, they accounted for around 85 % of the total precipitation.

The results showed what might be expected for a cold-front passage in a mountainous location: an afternoon peak in precipitation, a 6 °C drop in air temperature, and a 50 % increase in specific humidity. Changing from dry conditions to the wet, cool period of the composite front, we found the following changes during mid-day: net radiation decreased from around 585 to $275\,\mathrm{W\,m^{-2}}$ (over 50 %), sensible heat flux decreased from 280 to $85\,\mathrm{W\,m^{-2}}$ (around 70 %), latent heat flux was reduced from 170 to $125\,\mathrm{W\,m^{-2}}$ (around 25 %), and the magnitude of NEE was reduced from -7.8 to $-5.4\,\mu\mathrm{mol\,m^{-2}\,s^{-1}}$ (around 30 %). Despite these dramatic changes to the individual component energy fluxes, the surface energy balance (SEB) closure during the daytime was between 90–110 % throughout the 4 day composite frontal passage (Fig. 5.14a1). There was only a slight dependence of the SEB on the precipitation state. In our study, most of the storage terms were calculated based on biomass properties in the lower part of the canopy. Several recommendations of potential improvements with regard to the SEB are: (1) take into account the vertical variation of biomass properties, (2) use canopy and needle temperatures based on radiometric temperature measurements, (3) calculate storage terms using temperature lags in the soil and biomass [e.g., Lindroth et al., 2010], (4) improve our knowledge of soil properties (especially how they vary with depth), (5) examine the effect of flow distortion on the turbulent fluxes [e.g., Horst et al., 2015], and (6) explore calculating the sensible heat flux using a thermocouple rather than sonic temperature for warm-season conditions [e.g., Burns et al., 2012b].

For a typical day following a rain event, net radiation and sensible heat flux both recovered to slightly below dry-day values. Latent heat flux, however, increased from a dry-day value of $170\,\mathrm{W\,m^{-2}}$ to nearly $200\,\mathrm{W\,m^{-2}}$. Because λE also increased at night we conclude that λE primarily increased due to evaporation of liquid water from within the soil. The enhanced λE due to

evaporation lasted at least 18 hours, after which time it returned to a value similar to that of dry conditions (Fig. 5.9c). Another example of the effect of increased evaporation was the creation of a mid-day stable temperature layer within the forest sub-canopy (Fig. 5.4e). We conclude that the stable layer formed due to a combination of the vegetation being warmed by solar radiation and evaporative cooling near the ground. For NEE, we found that the subalpine forest at the US-NR1 site was most effective in assimilating CO_2 on the day following a significant rain event. A closer look at the diel cycle reveals that increased NEE occurred during the afternoon of a day following rain (Fig. 5.9b).

Any effect of precipitation on nocturnal NEE and SEB closure was overshadowed by the influence of low winds and drainage flows. Precipitation also disrupted the typical dry-day diel pattern in several distinct ways: (1) it eliminated the dip of $\approx 1\,\mathrm{m\,s^{-1}}$ in above-canopy horizontal wind speed during the morning and evening transitions (Fig. 5.3d), (2) it generally led to lower overall levels of mechanical turbulence (Fig. 5.3e), and (3) it decreased the magnitude of subcanopy/above-canopy vertical air temperature differences (Fig. 5.4). These effects resulted in weakly stable conditions in the late evening during wet periods (bulk Richardson Number $\mathrm{Ri_b} \approx 0.1$) compared to the more strongly stable dry periods ($\mathrm{Ri_b} \approx 0.2$). These stability differences contributed to smaller CO_2 vertical differences (relative to above-canopy CO_2) in the wet (less stable) conditions. After midnight, stability increased for both wet and dry conditions which created CO_2 vertical differences that were similar in both wet and dry conditions. Despite the stronger stability after midnight there was also increased wind speed and mechanical turbulence (especially in dry conditions) which should result in increased vertical mixing. Further examination of these nighttime phenomena are beyond the scope of this thesis but are recommended for future investigations.

By comparing cloudy and cloud-free days during dry periods we found that clouds changed the diel maximum in sensible heat flux and net radiation from 11:00 MST on cloudy days to around 12:00 MST on clear days (Fig. 5.12a, d). Latent heat flux peaked at around 11:00 MST on cloudy days, but just prior to noon on clear days (Fig. 5.12c). Also, mid-day net radiation and sensible heat flux were enhanced by about 20 % on clear days relative to cloudy days. In contrast, the timing

of the peak in NEE (at around 10:00 MST) was relatively unaffected by clouds and the forest was more efficient at assimilating CO_2 on cloudy days than clear days (Fig. 5.12b). Air temperature also differs on clear and cloudy days (Fig. 5.13), which might also be affecting NEE, and requires more investigation.

Our study has provided an example of one way to look at the complex interconnections between variables that make modeling ecosystems so challenging. We have centered our study on precipitation, but these techniques could easily be adapted to focus on a different variable (such as temperature or wind speed). Furthermore, this type of analysis could be used to evaluate models at the hourly time-scale, such as what is presented in Chapter 6. We have shown that precipitation is intrinsically linked to changes in air temperature, pressure, and atmospheric humidity. Our focus was on the local near-ground and source effects on the scalars and fluxes relative to precipitation during the warm-season. Three items that we did not fully consider in our analysis are: (1) there are undoubtedly sub-seasonal variations within the warm season that might reveal different responses to precipitation, (2) we did not examine the effect of the magnitude of precipitation events on our results, and (3) the atmospheric boundary layer, and specifically the boundary layer height and entrainment, will also have an impact on the near-surface scalar concentrations and fluxes [e.g., Culf et al., 1997, Freedman et al., 2001, van Heerwaarden et al., 2009, Pino et al., 2012, Pietersen et al., 2015]. Characteristics such as boundary-layer height are linked to the larger-scale flows at the mountainous US-NR1 research site.

7.2 Modeling of US-NR1 ecosystem fluxes

Here, we summarize our conclusions from Chapter 6. These results were based on over a decade of 30-minute measurements at US-NR1 with a focus on how precipitation perturbed the ecosystem-scale fluxes on a diel time-scale and how well a land-surface model represented these changes. The analysis methodology followed the same as that of Chapter 5 where each day was classified as either wet or dry. From the tower measurements, two results related to the effect of warm-season precipitation on the latent λE and sensible H heat flux were highlighted: (i) for a day

following an above-average wet day, mid-day latent heat flux was enhanced by around $40\,\mathrm{W\,m^{-2}}$ relative to dry conditions, with a concomitant reduction in sensible heat flux, and (ii) in wet conditions, nocturnal latent heat flux increased by about $15\,\mathrm{W\,m^{-2}}$ relative to latent heat flux in dry conditions (Fig. 6.1).

We used these two features of the measured turbulent fluxes as a framework for testing the Community Land Model (CLM), version 4.5 [Oleson et al., 2013]. Investigation into what controlled CLM latent heat flux necessitated examination of several other aspects of CLM4.5: the maximum permissible amount of water captured by the vegetation, the assumptions and parameterization of the subcanopy turbulent transport, and the MOST universal similarity functions. An additional tool used to evaluate CLM was from a vertical air temperature profile (11 levels), which revealed that CLM nocturnal temperatures had a cold bias of around 2–4 °C and evidence of runaway cooling (Figs. 6.10 and 6.11). Conclusions from our comparison between the US-NR1 tower observations and CLM4.5 modeled fluxes and temperature are the following:

(1) Using the default CLM configuration, mid-day latent heat flux did not increase for a dry day following an above-average wet day as seen in the observations and described in (i) above (thus, CLM sensible heat flux did not decrease as in the observations). By decreasing the *maximum leaf wetted fraction* f_{wet}^{max} from a default value of 1 to 0.02 the timing and magnitude of the canopy evaporation in CLM was modified in such a way that CLM was able to mimic the observations described in (i). It also resulted in λE on the afternoon of wet days that looked similar to observed λE.

(2) CLM ground evaporation was found to (primarily) be controlled by the subcanopy turbulent transfer coefficient $C_{s,dense}$. When $C_{s,dense}$ was increased from a default value of 0.004 to 0.01, CLM λE behaved as observed λE described in (i) above (Fig. 6.16b1). A comparison of the effect of increasing $C_{s,dense}$ or decreasing f_{wet}^{max} on overall λE suggested that the changes to f_{wet}^{max} were closer to the observed λE (Fig. 6.7). There were also indications that the timing and magnitude of ground evaporation were incorrect (Sect. 6.3.9.1), so we conclude that some

adjustment to the subcanopy ground evaporation (via modifications to $C_{s,dense}$) are needed.

(3) The stability correction to $C_{s,dense}$ suggested by Sakaguchi and Zeng [2009] was found to produce small changes in the CLM fluxes and temperature for the US-NR1 site. Furthermore, this correction only decreases $C_{s,dense}$, whereas our results suggest that increasing $C_{s,dense}$ would be justified (Fig. 6.16).

(4) The measured and modeled friction velocity u_* agreed well during daytime, however, CLM nocturnal u_* was $\approx 0.3\,\mathrm{m\,s^{-1}}$ whereas observed u_* was $\approx 0.4\,\mathrm{m\,s^{-1}}$. We circumvented this issue by using observed u_* as an input to CLM, which increased the magnitude of the turbulent fluxes and increased the nocturnal CLM temperatures (thus reducing the issue of a cold canopy temperature bias and runaway cooling).

(5) CLM nocturnal latent heat flux in both dry and wet conditions was $\approx 10\,\mathrm{W\,m^{-2}}$ (i.e., there was not a large increase in λE during wet conditions, as described in (ii) above). Further investigation found that CLM canopy and ground evaporation at night were both very small (Fig. 6.4). Though using observed u_* as input into CLM increased nocturnal λE, it did so for both wet and dry conditions. Increasing $C_{s,dense}$ by a factor of 1000 led to larger nocturnal λE fluxes in wet conditions, that approached the observations. Based on a comparison with a forested site in relatively flat terrain (Howland Forest), we hypothesize that the enhanced nocturnal λE at US-NR1 is related to the drainage flow which is not represented within CLM.

(6) The comparison with Howland Forest brought to light an important effect of mountainous terrain: slope-generated drainage flows contribute additional turbulent energy which we speculate promotes evaporation and enhances US-NR1 nocturnal latent heat flux.

(7) With regard to the universal similarity functions used in CLM4.5: we suggest that rather than limiting the dimensionless stability parameter ζ with the variable *zetamaxstable*, it would be more appropriate to use a form of the universal function that is constant in strongly stable conditions (as recommended by Handorf et al. [1999]). For US-NR1, we suggest that the

universal function should be constant for $\zeta > 1$.

(8) We tested the portion of the CLM4.5 subcanopy parameterization that assumes a linear relationship between velocity on the vegetation U_{av} and above-canopy u_*. We found it generally overestimated U_{av} by about a factor of 2 (Fig. 6.19).

(9) In dry conditions, the timing of the diel cycle peak in CLM λE and soil temperatures were inconsistent with those of the observations (Fig. 6.25). In general, CLM λE followed VPD whereas the peak in observed λE was affected by other phenomena (we suspect entrainment at the top of the boundary layer). Also, the peak in CLM soil temperature was several hours later than the peak in observed T_{soil}.

(10) From the US-NR1 observations, the cumulative warm-season fluxes suggest that this subalpine forest releases about 300 mm of water and 700 MJ m^{-2} of sensible heat into the atmosphere. Among the 14 CLM configurations considered in our study, the warm-season cumulative water vapor varied by about 8% and sensible heat by 25%.

Chapter 6 describes a method of testing land-surface models for appropriate representation of the diel changes in surface energy fluxes when precipitation occurs. This analysis led to further insight into the measurements as well as pin-pointing areas for future model improvement in forested areas. On the measurement side, improved understanding of canopy temperature, better estimates of soil and vegetation evaporation and interception (especially at night), controls on subcanopy turbulent exchange [e.g., Thomas et al., 2013], slope flow dynamics (or more comparisons between flat and sloped sites), as well as better estimates of forest and soil physical properties would be useful. On the modeling side, possible improvements and suggested areas for future work are: (1) revisiting the subcanopy turbulent parameterization [e.g., Zeng et al., 2005], (2) taking into account the effect of forest biomass heat capacity on the turbulent fluxes and the surface energy budget [e.g., Leuning et al., 2012], (3) including modifications to the MOST universal functions that take into account the possibility that the uppermost measurement level is within the roughness sublayer

[e.g., Harman and Finnigan, 2008], and (4) the inclusion of slope-effects and drainage air flows in complex terrain that lead to increased nocturnal turbulence and surface evaporation. Model development will only progress if data from multiple measurement sites with a wide variety of canopy types and forest densities situated in different landscapes are brought together to create better understanding over a wide parameter space. Observational networks such as FLUXNET [Baldocchi et al., 2001] are well positioned to help in these efforts and much work has already been made in this direction [e.g., Stöckli et al., 2008, Abramowitz et al., 2008, Chen and Zhang, 2009, Williams et al., 2009, Blyth et al., 2010, Bonan et al., 2011, 2012, Ukkola et al., 2017].

7.3 Future research plans and ideas

We conclude this thesis with some ideas for future work that would improve our understanding of the topics presented herein. This list could easily be made much longer, and several other ideas of future needs have already been presented within the previous two sections. Here are a few ideas for future research topics of study at US-NR1:

- We have presented our analysis of precipitation influence over the warm season. The warm season itself includes several distinct ecological periods such as the soil dry-down in late June, the start of the North American monsoon in late July, and there are often periods of several weeks without any precipitation in September and October. Not to mention that snow dominates the landscape for over half of the year. Previous research has shown the snowmelt period to be important for the subalpine ecosystem [e.g., Monson et al., 2005, Winchell et al., 2016]. Because we have the tools already in place, it would be interesting to extend the precipitation-based analysis with a focus on different "ecological periods" throughout the entire year. Similar concepts were recently used by Albert et al. [2017].

- The work presented in this thesis has focused on the near-ground processes, while ignoring any effects of atmospheric exchanges that might be occurring at the top of the boundary layer (e.g., entrainment). Knowing the boundary-layer height and how it changes with time would

open up the possibility for examining the effect of entrainment by using models such as those described by van Heerwaarden et al. [2009], Pino et al. [2012]. The software to do such analysis is readily available as part of Vilà–Guerau de Arellano et al. [2015].

- The CLM comparison suggested that soil evaporation is sensitive to the chosen value of the subcanopy turbulent transfer coefficient. Actually measuring soil evaporation with microlysimeters [e.g., Heusinkveld et al., 2006, Uclés et al., 2013, Hirschi et al., 2017] would provide some guidance on how big the soil evaporation term might be. We have tentative plans to deploy a microlysimeter at the site in summer of 2018.

- This thesis has not delved much into the fluid mechanics driving the ecosystem exchanges within the canopy—these exchanges depend heavily on the coherent structures which form just-above the canopy top and the resulting pressure fields [e.g., Gao et al., 1989, 1992, Shaw et al., 1990, Shaw and Zhang, 1992, Raupach et al., 1996, Thomas and Foken, 2007, Dupont and Brunet, 2009, Finnigan et al., 2009]. We initially planned to include a chapter on this topic, but instead chose to focus on the precipitation-based analysis presented herein. Some initial work on this topic has been completed [Burns et al., 2017], with more analysis planned in the future.

- There is a long record of subcanopy flux measurements that could be analyzed to help determine soil evaporation contributions to the ecosystem latent heat flux, as well as the distinctive subcanopy flow pattern that is known as the "spectral shortcut" where energy of the flow is shifted from mid-range frequencies to higher frequencies due to the shedding off of tree elements. Can we understand this phenomena better?

- Finally, as mentioned in Sect. 3.10, there was a full year with 7 additional sonic anemometer wind measurements added to the US-NR1 main tower [Burns et al., 2016a]. These data can be analyzed to better understand the nocturnal slope flow, and how such flows might affect the above-canopy turbulent fluxes.

Bibliography

G. Abramowitz, R. Leuning, M. Clark, and A. Pitman. Evaluating the performance of land surface models. Journal Of Climate, 21:5468–5481, 2008.

O. C. Acevedo, O. L. L. Moraes, G. A. Degrazia, D. R. Fitzjarrald, A. O. Manzi, and J. G. Campos. Is friction velocity the most appropriate scale for correcting nocturnal carbon dioxide fluxes? Agric. For. Meteor., 149:1–10, 2009.

D. K. Adams and A. C. Comrie. The North American monsoon. Bulletin Of The American Meteorological Society, 78:2197–2213, 1997.

L. P. Albert, T. F. Keenan, S. P. Burns, T. E. Huxman, and R. K. Monson. Climate controls over ecosystem metabolism: Insights from a fifteen-year inductive artificial neural network synthesis for a subalpine forest. Oecologia, 184:25–41, 2017. doi: 10.1007/s00442-017-3853-0.

P. Alekseychik, I. Mammarella, S. Launiainen, Ü. Rannik, and T. Vesala. Evolution of the nocturnal decoupled layer in a pine forest canopy. Agric. For. Meteor., 174-175:15–27, 2013.

R. R. Alexander. Ecology, silviculture, and management of the engelmann spruce - subalpine fir type in the central and southern rocky mountains, USDA Forest Service, Agriculture Handbook No. 659, 1987. 144 pp.

C. C. Amundsen. The subalpine forest of Wild Basin, Front Range, Colorado. PhD thesis, University of Colorado, Boulder, Boulder, CO, USA, 129 pp., 1967.

S. P. Anderson, G. Qinghua, and E. G. Parrish. Snow-on and snow-off LiDAR point cloud data and digital elevation models for study of topography, snow, ecosystems and environmental change at Boulder Creek Critical Zone Observatory. Colorado: Boulder Creek CZO, INSTAAR, University of Colorado at Boulder, digital media., 2012.

R. A. Andrus, B. J. Harvey, K. C. Rodman, S. J. Hart, and T. T. Veblen. Moisture availability limits subalpine tree establishment. Ecology, 99(3):567–575, 2018. doi: 10.1002/ecy.2134.

M. Aubinet. Eddy covariance CO_2 flux measurements in nocturnal conditions: An analysis of the problem. Ecol. Appl., 18:1368–1378, 2008.

M. Aubinet, A. Grelle, A. Ibrom, U. Rannik, J. Moncrieff, T. Foken, A. S. Kowalski, P. H. Martin, P. Berbigier, C. Bernhofer, R. Clement, J. Elbers, A. Granier, T. Grunwald, K. Morgenstern, K. Pilegaard, C. Rebmann, W. Snijders, R. Valentini, and T. Vesala. Estimates of the annual net carbon and water exchange of forests: The euroflux methodology. Advances In Ecological Research, Vol 30, 30:113–175, 2000.

M. Aubinet, P. Berbigier, C. H. Bernhofer, A. Cescatti, C. Feigenwinter, A. Granier, T. H. Grunwald, K. Havrankova, B. Heinesch, B. Longdoz, B. Marcolla, L. Montagnani, and P. Sedlak. Comparing co2 storage and advection conditions at night at different carboeuroflux sites. Bound.-Layer Meteor., 116:63–94, 2005.

M. Aubinet, T. Vesala, and D. Papale. Eddy Covariance: A Practical Guide to Measurement and Data Analysis. Springer Atmospheric Sciences, Dordrecht, The Netherlands, 2012. 438 pp.

D. M. Aubrecht, B. R. Helliker, M. L. Goulden, D. A. Roberts, C. J. Still, and A. D. Richardson. Continuous, long-term, high-frequency thermal imaging of vegetation: Uncertainties and recommended best practices. Agric. For. Meteor., 228-229:315–326, 2016. doi: 10.1016/j.agrformet.2016.07.017.

A. T. Austin, L. Yahdjian, J. M. Stark, J. Belnap, A. Porporato, U. Norton, D. A. Ravetta, and S. M. Schaeffer. Water pulses and biogeochemical cycles in arid and semiarid ecosystems. Oecologia, 141:221–235, 2004.

T. E. Avery and H. E. Burkhart. Forest Measurements. Series in forest resources. McGraw-Hill, Fifth edition, 2002. 456 pp.

P. Baas, G. J. Steeneveld, B. J. H. van de Wiel, and A. A. M. Holtslag. Exploring self-correlation in flux-gradient relationships for stably stratified conditions. J. Atmos. Sci., 63:3045–3054, 2006. doi: 10.1175/JAS3778.1.

D. Baldocchi, J. Finnigan, K. Wilson, K. T. Paw U, and E. Falge. On measuring net ecosystem carbon exchange over tall vegetation on complex terrain. Bound.-Layer Meteor., 96:257–291, 2000.

D. Baldocchi, E. Falge, L. Gu, R. Olson, D. Hollinger, S. Running, P. Anthoni, C. Bernhofer, K. Davis, R. Evans, J. Fuentes, A. Goldstein, G. Katul, B. Law, X. H. Lee, Y. Malhi, T. Meyers, W. Munger, W. Oechel, K. T. Paw, K. Pilegaard, H. P. Schmid, R. Valentini, S. Verma, T. Vesala, K. Wilson, and S. Wofsy. FLUXNET: A new tool to study the temporal and spatial variability of ecosystem-scale carbon dioxide, water vapor, and energy flux densities. Bull. Amer. Meteor. Soc., 82:2415–2434, 2001.

D. D. Baldocchi. Assessing the eddy covariance technique for evaluating carbon dioxide exchange rates of ecosystems: past, present and future. Global Change Biology, 9:479–492, 2003.

D. D. Baldocchi and T. P. Meyers. Trace gas-exchange above the floor of a deciduous forest .1. evaporation and CO_2 efflux. J. Geophys. Res., 96:7271–7285, 1991.

D. D. Baldocchi, B. B. Hicks, and T. P. Meyers. Measuring biosphere-atmosphere exchanges of biologically related gases with micrometeorological methods. Ecology, 69(5):1331–1340, 1988.

R. M. Banta. Daytime boundary-layer evolution over mountainous terrain. Part 1: Observations of the dry circulations. Monthly Weather Review, 112(2):340–356, 1984. doi: 10.1175/1520-0493(1984)112¡0340:DBLEOM¿2.0.CO;2.

R. G. Barry. A climatological transect on the east slope of the Front Range, Colorado. Arctic and Alpine Research, pages 89–110, 1973.

D. J. Beerling. Gas valves, forests and global change: A commentary on Jarvis (1976) 'the interpretation of the variations in leaf water potential and stomatal conductance found in canopies in the field'. Philos. T. Roy. Soc. B, 370:20140311, 2015. doi: 10.1098/rstb.2014.0311.

S. E. Belcher, J. J. Finnigan, and I. N. Harman. Flows through forest canopies in complex terrain. Ecol. Appl., 18:1436–1453, 2008.

J. B. Benedict and B. L. Olson. The Mount Albion Complex: A Study of Prehistoric Man and the Altithermal. Research report No. 1, Center for Mountain Archeology, Ward, Colorado, 213 pp., 1978.

M. Berkelhammer, J. Hu, A. Bailey, D. C. Noone, C. J. Still, H. Barnard, D. Gochis, G. S. Hsiao, T. Rahn, and A. Turnipseed. The nocturnal water cycle in an open-canopy forest. J. Geophys. Res., 118:1–18, 2013.

M. Berkelhammer, D. C. Noone, T. E. Wong, S. P. Burns, J. F. Knowles, A. Kaushik, P. D. Blanken, and M. W. Williams. Convergent approaches to determine an ecosystem's transpiration fraction. Global Biogeochemical Cycles, 30:933–951, 2016.

A. K. Betts. Land-surface-atmosphere coupling in observations and models. Journal of Advances in Modeling Earth Systems, 1, 2009. doi: 10.3894/JAMES.2009.1.4.

A. K. Betts and J. H. Ball. The FIFE surface diurnal cycle climate. J. Geophys. Res., 100: 25679–25693, 1995.

P. D. Blanken, T. A. Black, P. C. Yang, H. H. Neumann, Z. Nesic, R. Staebler, G. den Hartog, M. D. Novak, and X. Lee. Energy balance and canopy conductance of a boreal aspen forest: Partitioning overstory and understory components. Journal of Geophysical Research-Atmospheres, 102:28915–28927, 1997.

P. D. Blanken, T. A. Black, H. H. Neumann, G. den Hartog, P. C. Yang, Z. Nesic, and X. Lee. The seasonal water and energy exchange above and within a boreal aspen forest. Journal of Hydrology, 245:118–136, 2001.

P. D. Blanken, W. R. Rouse, and W. M. Schertzer. Enhancement of evaporation from a large northern lake by the entrainment of warm, dry air. J. Hydrometeor., 4:680–693, 2003.

P. D. Blanken, M. W. Williams, S. P. Burns, R. K. Monson, J. Knowles, K. Chowanski, and T. Ackerman. A comparison of water and carbon dioxide exchange at a windy alpine tundra and subalpine forest site near Niwot Ridge, Colorado. Biogeochemistry, 95:61–76, 2009. doi: 10.1007/s10533-009-9325-9.

E. Blyth, J. Gash, A. Lloyd, M. Pryor, G. P. Weedon, and J. Shuttleworth. Evaluating the JULES land surface model energy fluxes using FLUXNET data. Journal Of Hydrometeorology, 11: 509–519, 2010.

T. A. Boden, M. Krassovski, and B. Yang. The AmeriFlux data activity and data system: an evolving collection of data management techniques, tools, products and services. Geosci. Instrum. Method. Data Syst., 2:165–176, 2013. doi: 10.5194/gi-2-165-2013.

G. B. Bonan. A Land Surface Model (LSM version 1.0) for ecological, hydrological, and atmospheric studies: Technical description and user's guide. Technical Report NCAR/TN-417+STR, NCAR Technical Note, 1996. 150 pp.

G. B. Bonan. Forests and climate change: forcings, feedbacks, and the climate benefits of forests. Science, 320:1444–1449, 2008a.

G. B. Bonan. Ecological Climatology: Concepts and Applications. Cambridge University Press, Cambridge, UK, 2nd edition, 2008b. 550 pp.

G. B. Bonan, P. J. Lawrence, K. W. Oleson, S. Levis, M. Jung, M. Reichstein, D. M. Lawrence, and S. C. Swenson. Improving canopy processes in the Community Land Model version 4 (CLM4) using global flux fields empirically inferred from FLUXNET data. J. Geophys. Res., 116:G02014, 2011. doi: 10.1029/2010JG001593.

G. B. Bonan, K. W. Oleson, R. A. Fisher, G. Lasslop, and M. Reichstein. Reconciling leaf physiological traits and canopy flux data: Use of the TRY and FLUXNET databases in the Community Land Model version 4. J. Geophys. Res., 117:G02026, 2012. doi: 10.1029/2011JG001913.

G. B. Bonan, M. Williams, R. A. Fisher, and K. W. Oleson. Modeling stomatal conductance in the earth system: linking leaf water-use efficiency and water transport along the soil-plant-atmosphere continuum. Geoscientific Model Development, 7:2193–2222, 2014.

G. B. Bonan, E. G. Patton, I. N. Harman, K. W. Oleson, J. J. Finnigan, Y. Lu, and E. A. Burakowski. Modeling canopy-induced turbulence in the Earth system: a unified parameterization of turbulent exchange within plant canopies and the roughness sublayer (CLM-ml v0). Geoscientific Model Development Discussions, In Review:1–80, 2017. doi: 10.5194/gmd-2017-261.

W. Borken and E. Matzner. Reappraisal of drying and wetting effects on C and N mineralization and fluxes in soils. Global Change Biology, 15:808–824, 2009.

F. C. Bosveld and W. Bouten. Evaluating a model of evaporation and transpiration with observations in a partially wet Douglas-fir forest. Bound.-Layer Meteor., 108:365–396, 2003.

D. R. Bowling, S. P. Burns, T. J. Conway, R. K. Monson, and J. W. C. White. Extensive observations of CO_2 carbon isotope content in and above a high-elevation subalpine forest. Global Biogeochem. Cycle, 19:GB3023, 2005. doi: 10.1029/2004GB002394.

D. R. Bowling, J. B. Miller, M. E. Rhodes, S. P. Burns, R. K. Monson, and D. Baer. Soil, plant, and transport influences on methane in a subalpine forest under high ultraviolet irradiance. Biogeosciences, 6:1311–1324, 2009.

D. R. Bowling, E. E. Grote, and J. Belnap. Rain pulse response of soil CO_2 exchange by biological soil crusts and grasslands of the semiarid Colorado Plateau, United States. J. Geophys. Res., 116:G03028, 2011. doi: 10.1029/2011JG001643.

D. R. Bowling, A. P. Ballantyne, J. B. Miller, S. P. Burns, T. J. Conway, O. Menzer, B. B. Stephens, and B. H. Vaughn. Ecological processes dominate the ^{13}C land disequilibrium in a Rocky Mountain subalpine forest. Global Biogeochem. Cycle, 28:352–370, 2014. doi: 10.1002/2013GB004686.

D. R. Bowling, J. E. Egan, S. J. Hall, and D. A. Risk. Environmental forcing does not induce diel or synoptic variation in the carbon isotope content of forest soil respiration. Biogeosciences, 12: 5143–5160, 2015.

D. R. Bowling, B. A. Logan, K. Hufkens, D. M. Aubrecht, A. D. Richardson, S. P. Burns, W. R. L. Anderegg, P. D. Blanken, and D. Eiriksson. Limitations to winter and spring photosynthesis of a Rocky Mountain subalpine forest. Agric. For. Meteor., 252:241–255, 2018. doi: 10.1016/j.agrformet.2018.01.025.

J. B. Bradford, R. A. Birdsey, L. A. Joyce, and M. G. Ryan. Tree age, disturbance history, and carbon stocks and fluxes in subalpine Rocky Mountain forests. Global Change Biol., 14(12): 2882–2897, 2008.

A. J. Brazel and S. W. Brazel. Summer diurnal wind patterns at 3,000 m surface level, Front Range, Colorado, U.S.A. Phys. Geog., 4:53–61, 1983.

H. Brean. Dry start to winter prompts ugly forecast for Colorado River. Las Vegas Review-Journal, 3 January, 2018. URL `https://www.reviewjournal.com`. [Online; last access, March 2018].

J. A. Brotzge and C. E. Duchon. A field comparison among a domeless net radiometer, two four-component net radiometers, and a domed net radiometer. Journal of Atmospheric and Oceanic Technology, 17:1569–1582, 2000. doi: 10.1175/1520-0426(2000)017¡1569:AFCAAD¿2.0.CO;2.

P. D. Broxton, A. A. Harpold, J. A. Biederman, P. A. Troch, N. P. Molotch, and P. D. Brooks. Quantifying the effects of vegetation structure on snow accumulation and ablation in mixed-conifer forests. Ecohydrology, 8:1073–1094, 2015.

W Brutsaert. Evaporation into the Atmosphere. Kluwer Academic Publishers, Dordrecht, The Netherlands, 1982. 299 pp.

C. W. Buchholtz. Rocky Mountain National Park: A History. Colorado Associated University Press, Boulder, Colorado, 255 pp., 1983.

A. Buechling and W. L. Baker. A fire history from tree rings in a high-elevation forest of Rocky Mountain National Park. Canadian Journal of Forest Research, 34(6):1259–1273, 2004. doi: 10.1139/x04-012.

G. Burba. Eddy Covariance Method for Scientific, Industrial, Agricultural, and Regulatory Applications: A Field Book on Measuring Ecosystem Gas Exchange and Areal Emission Rates. LI-COR Biosciences, Lincoln, Nebraska, USA, 2013. 331 pp.

G. Burba, A. Schmidt, R. L. Scott, T. Nakai, J. Kathilankal, G. Fratini, C. Hanson, B. Law, D. K. McDermitt, R. Eckles, M. Furtaw, and M. Velgersdyk. Calculating CO_2 and H_2O eddy covariance fluxes from an enclosed gas analyzer using an instantaneous mixing ratio. Global Change Biology, 18:385–399, 2012.

G. G. Burba, D. K. Mcdermitt, D. J. Anderson, M. D. Furtaw, and R. D. Eckles. Novel design of an enclosed CO_2/H_2O gas analyser for eddy covariance flux measurements. Tellus Series B-Chemical And Physical Meteorology, 62:743–748, 2010.

Bureau of Reclamation. Colorado River Basin Water Supply and Demand Study: Executive summary. Technical report, U.S. Department of the Interior, Bureau of Reclamation, 34 pp., 2012.

S. P. Burns and J. Sun. Thermocouple temperature measurements from the CASES-99 main tower. In Proceedings of the 14th Symposium on Boundary Layer and Turbulence, Snowmass, Colorado, 7-11 August 2000, 358-361, 2000. Amer. Meteor. Soc.

S. P. Burns, A. C. Delany, J. Sun, B. B. Stephens, S. P. Oncley, G. D. Maclean, S. R. Semmer, J. Schröter, and J. Ruppert. An evaluation of calibration techniques for in situ carbon dioxide measurements using a programmable portable trace-gas measuring system. J. Atmos. Oceanic Technol., 26:291–316, 2009a. doi: 10.1175/2008JTECHA1080.1.

S. P. Burns, A. A. Turnipseed, D. R. Bowling, J. Hu, and R. K. Monson. Ten-year variability in fluxes, meteorology, and environmental conditions at a Colorado subalpine forest. In 2009 AGU Fall Meeting, American Geophysical Union. San Francisco, California, 14–18 December 2009, B51A-0290, 2009b.

S. P. Burns, J. Sun, D. H. Lenschow, S. P. Oncley, B. B. Stephens, C. Yi, D. E. Anderson, J. Hu, and R. K. Monson. Atmospheric stability effects on wind fields and scalar mixing within and just above a subalpine forest in sloping terrain. Bound.-Layer Meteor., 138:231–262, 2011. doi: 10.1007/s10546-010-9560-6.

S. P. Burns, T. W. Horst, P. D. Blanken, and R. K. Monson. Using sonic anemometer temperature to measure sensible heat flux in strong winds. Atmospheric Measurement Techniques Discussions, 5:447–469, 2012a. doi: 10.5194/amtd-5-447-2012.

S. P. Burns, T. W. Horst, L. Jacobsen, P. D. Blanken, and R. K. Monson. Using sonic anemometer temperature to measure sensible heat flux in strong winds. Atmos. Meas. Tech., 5:2095–2111, 2012b. doi: 10.5194/amt-5-2095-2012.

S. P. Burns, N. P. Molotch, M. W. Williams, J. F. Knowles, B. Seok, R. K. Monson, A. A. Turnipseed, and P. D. Blanken. Snow temperature changes within a seasonal snowpack and their relationship to turbulent fluxes of sensible and latent heat. J. Hydrometeor., 15:117–142, 2013. doi: 10.1175/JHM-D-13-026.1.

S. P. Burns, S. Metzger, P. D. Blanken, G. G. Burba, E. Swiatek, J. Li, B. Conrad, H. Luo, and J. Taylor. A comparison of infrared gas analyzers above a subalpine forest in complex terrain. In 17th Symposium on Meteorological Observation and Instrumentation, American Meteorological Society. Westminister, Colorado, 9-13 June 2014, paper 13, 2014. available at: https://ams.confex.com/ams/21Applied17SMOI/webprogram/, last access: 26 September 2016.

S. P. Burns, P. D. Blanken, A. A. Turnipseed, J. Hu, and R. K. Monson. The influence of warm-season precipitation on the diel cycle of the surface energy balance and carbon dioxide at a Colorado subalpine forest site. Biogeosciences, 12:7349–7377, 2015a. doi: 10.5194/bg-12-7349-2015.

S. P. Burns, P. D. Blanken, A. A. Turnipseed, and R. K. Monson. The effect of warm-season precipitation on the diel cycle of the surface energy balance and carbon dioxide at a Colorado subalpine forest site. Biogeosciences Discussions, 12(12):8939–9004, 2015b. doi: 10.5194/bgd-12-8939-2015.

S. P. Burns, T. W. Horst, S. P. Oncley, G. Maclean, S. Semmer, D. H. Lenschow, and P. D. Blanken. Characteristics of wind and turbulence just-above and within a subalpine forest in complex terrain. In Proceedings of the 22nd Symposium on Boundary Layer and

Turbulence. Salt Lake City, UT. American Meteorological Society, 2016a. poster 117, URL: https://ams.confex.com/ams/32AgF22BLT3BG/.

S. P. Burns, G. D. Maclean, P. D. Blanken, S. P. Oncley, S. R. Semmer, and R. K. Monson. The Niwot Ridge Subalpine Forest US-NR1 AmeriFlux site – Part 1: Data acquisition and site record-keeping. Geosci. Instrum. Method. Data Syst., 5:451–471, 2016b. doi: 10.5194/gi-5-451-2016.

S. P. Burns, J. M. Frank, W. J. Massman, E. G. Patton, and P. D. Blanken. Static pressure-wind covariance and coherent structures at two subalpine forest sites. In FLUXNET Conference 2017. Berkeley, CA. 7-9 June, 2017.

S. P. Burns, S. C. Swenson, W. R. Wieder, D. M. Lawrence, G. B. Bonan, J. F. Knowles, and P. D. Blanken. A comparison of the diel cycle of modeled and measured latent heat flux during the warm season in a Colorado subalpine forest. J. Adv. Model Earth Sys., 10:617–651, 2018. doi: 10.1002/2017MS001248.

S. P. Burns, P. D. Blanken, A. A. Harpold, D. E. Weibel, N. P. Molotch, D. J. P. Moore, M. W. Williams, and R. K. Monson. The Niwot Ridge Subalpine Forest US-NR1 AmeriFlux site – Part II: Vegetation, soil, and topographic characteristics. Hydrol. Earth Syst. Sc., 2019. to be submitted.

J. A. Businger, J. C. Wyngaard, Y. Izumi, and E. F. Bradley. Flux-profile relationships in atmospheric surface layer. J. Atmos. Sci., 28:181–189, 1971.

S. A. Cain and G. M. de Oliveira Castro. Manual of vegetation analysis. Harper, New York, 325 pp., 1959.

G. S. Campbell. 'measurement of air temperature fluctuations with thermocouples'. Technical Report ECOM-5273, Atmospheric Sciences Laboratory, White Sands Missile Range, 10 pp., 1969.

Campbell Scientific. TGA100A Trace Gas Analyzer Overview, 2004. 14 pp., (Available at www.campbellsci.com).

Campbell Scientific. CSAT3 Three Dimensional Sonic Anemometer Manual, 2010. Revision 6/10, 70 pp., (Available at www.campbellsci.com).

Campbell Scientific. CPEC200 Closed-Path Eddy-Covariance System Instruction Manual, 2013a. Revision 12/13, 106 pp., (Available at www.campbellsci.com).

Campbell Scientific. EC155 CO_2 and H_2O Closed-Path Gas Analyzer Instruction Manual, 2013b. Revision 5/13, 66 pp., (Available at www.campbellsci.com).

E. S. Cassells. This Land of Shining Mountains: Archeological Studies in Colorado's Indian Peaks Wilderness Area. Research report No. 8, Center for Mountain Archeology, Ward, Colorado, 215 pp., 2000.

S. Chan, S. Biraud, and D. Billesbach. AmeriFlux QA/QC Report on US-NR1/PECS Comparison between 29 July and 3 August 2013. Technical report, Earth Sciences Division, Lawerence Berkeley National Laboratory, Berkeley, California, 48 pp., 2014.

F. Chen and Y. Zhang. On the coupling strength between the land surface and the atmosphere: From viewpoint of surface exchange coefficients. Geophysical Research Letters, 36:L10404, 2009.

N. S. Christensen and D. P. Lettenmaier. A multimodel ensemble approach to assessment of climate change impacts on the hydrology and water resources of the colorado river basin. Hydrol. Earth Syst. Sci., 11:1417–1434, 2007.

R. M. Cionco. A mathematical model for air flow in a vegetative canopy. Journal of Applied Meteorology, 4:517–522, 1965. doi: 10.1175/1520-0450(1965)004¡0517:AMMFAF¿2.0.CO;2.

M. P. Clark, Y. Fan, D. M. Lawrence, J. C. Adam, D. Bolster, D. J. Gochis, R. P. Hooper, M. Kumar, L. R. Leung, D. S. Mackay, R. M. Maxwell, C. P. Shen, S. C. Swenson, and X. Zeng. Improving the representation of hydrologic processes in Earth System Models. Water Resources Research, 51:5929–5956, 2015.

Clason Map Company. *Mining Districts In Boulder County Colorado*. map. 1:25340, 1916.

R. J. Clement, G. G. Burba, A. Grelle, D. J. Anderson, and J. B. Moncrieff. Improved trace gas flux estimation through IRGA sampling optimization. Agric. For. Meteor., 149:623–638, 2009.

A. M. J. Coenders-Gerrits, R. J. van der Ent, T. A. Bogaard, L. Wang-Erlandsson, M. Hrachowitz, and H. H. G. Savenije. Uncertainties in transpiration estimates. Nature, 506:E1–E2, 2014.

F. Crossen. The Switzerland Trail of America. Robinson Press, Inc. Fort Collins, Colorado, 422 pp., 1978.

A. D. Culf, G. Fisch, Y. Malhi, and C. A. Nobre. The influence of the atmospheric boundary layer on carbon dioxide concentrations over a tropical forest. Agric. For. Meteor., 85:149–158, 1997.

K. R. Dailey. Streamflow and groundwater response to precipitation variability in a snow-dominated, subalpine headwater catchment, Colorado Rocky Mountains, USA. Master's thesis, University of Colorado, Boulder, Boulder, CO, USA, 89 pp., 2016.

J. Dalton. Experimental essays on the constitution of mixed gases; on the force of steam or vapour from water and other liquids at different temperatures, both in a Torricellian vacuum and in air; on evaporation and on the expansion of gas by heat. Mem. Manchester Lit. and Phil. Soc., 5: 535–602, 1802.

O. T. Denmead and E. F. Bradley. Flux-gradient relationships in a forest canopy. In B. A. Hutchison and B. B. Hicks, editors, The Forest-Atmosphere Interaction, pages 421–442. D. Reidel Publishing Company, Dordrecht, 1985.

J. L. Devore. Probability and Statistics for Engineering and the Sciences. Brooks/Cole Publishing Company, Monterey, California, 1987.

H. J. Diamond, T. R. Karl, M. A. Palecki, C. B. Baker, J. E. Bell, R. D. Leeper, D. R. Easterling, J. H. Lawrimore, T. P. Meyers, M. R. Helfert, G. Goodge, and P. W. Thorne. U.S. Climate Reference Network after one decade of operations: status and assessment. Bull. Amer. Meteor. Soc., 94:485–498, 2013.

R. E. Dickinson, A. Henderson-Sellers, and P. J. Kennedy. Biosphere-Atmosphere Transfer Scheme (BATS) Version 1e as coupled to the NCAR Community Climate Model. Technical Report NCAR/TN-387+STR, NCAR Technical Note, 1993. 72 pp.

M. M. Douglass. Ecology of forest succession on a ridge in the subalpine forest of northern Colorado. Master's thesis, University of Colorado, Boulder, Boulder, CO, USA, 134 pp., 1954.

H. A. Drumm. Drumm's pocket map of Boulder County Colorado. 1:96000, 1908.

H. A. Drumm. Drumm's revised edition pocket map of Boulder County Colorado. 1:96000, 1932.

H. A. Drumm. The autobiography of Henry A. Drumm: First graduate of the University of Colorado. Unfinished manuscript, [available from the Boulder Carnegie Library for Local History], 1971.

R. O. Dubayah and J. B. Drake. Lidar remote sensing for forestry. Journal Of Forestry, 98:44–46, 2000.

S. Dupont and Y. Brunet. Coherent structures in canopy edge flow: a large-eddy simulation study. Journal Of Fluid Mechanics, 630:93–128, 2009.

S. Dupont, M. R. Irvine, J. M. Bonnefond, E. Lamaud, and Y. Brunet. Turbulent structures in a pine forest with a deep and sparse trunk space: Stand and edge regions. Bound.-Layer Meteor., 143:309–336, 2012.

S. L. Edburg, D. Stock, B. K. Lamb, and E. G. Patton. The effect of the vertical source distribution on scalar statistics within and above a forest canopy. Bound.-Layer Meteor., 142:365–382, 2012.

J. Egger and K. P. Hoinka. Fronts and orography. Meteorol. Atmos. Phys., 48:3–36, 1992.

P. M. Ellsworth. Ecological seaonal cycles in a Colorado mountain pond. Journal Of Freshwater Ecology, 2:225–237, 1983.

J. Everaerts. The use of unmanned aerial vehicles (UAVs) for remote sensing and mapping. The International Archives of the Photogrammetry, Remote Sensing and Spatial Information Sciences, 37:1187–1192, 2008.

J. Finnigan. An introduction to flux measurements in difficult conditions. Ecol. Appl., 18:1340–1350, 2008.

J. J. Finnigan. A re-evaluation of long-term flux measurement techniques. Part II: Coordinate systems. Bound.-Layer Meteor., 113:1–41, 2004.

J. J. Finnigan, R. H. Shaw, and E. G. Patton. Turbulence structure above a vegetation canopy. Journal Of Fluid Mechanics, 637:387–424, 2009.

T. Foken. 50 years of the Monin-Obukhov similarity theory. Bound.-Layer Meteor., 119:431–447, 2006.

T. Foken. The energy balance closure problem: An overview. Ecol. Appl., 18:1351–1367, 2008a.

T. Foken. Micrometeorology. Springer, Heidelberg, 2008b. 308 pp.

T. Foken and H. Falke. Technical note: Calibration device for the krypton hygrometer KH20. Atmos. Meas. Tech., 5(8):1861–1867, 2012. doi: 10.5194/amt-5-1861-2012.

T. Foken, M. Aubinet, J. J. Finnigan, M. Y. Leclerc, M. Mauder, and K. T. Paw U. Results of a panel discussion about the energy balance closure correction for trace gases. Bull. Amer. Meteor. Soc., 92:ES13–ES18, 2011.

T. Foken, R. Leuning, S. Oncley, M. Mauder, and M. Aubinet. Corrections and data quality control. In M. Aubinet, T. Vesala, and D. Papale, editors, Eddy Covariance: A Practical Guide to Measurement and Data Analysis, pages 85–131. Springer Atmospheric Sciences, Dordrecht, The Netherlands, 2012.

H. J. Hendricks Franssen, R. Stöckli, I. Lehner, E. Rotenberg, and S. I. Seneviratne. Energy balance closure of eddy-covariance data: A multisite analysis for european FLUXNET stations. Agric. For. Meteor., 150:1553–1567, 2010. doi: 10.1016/j.agrformet.2010.08.005.

G. Fratini, A. Ibrom, N. Arriga, G. Burba, and D. Papale. Relative humidity effects on water vapour fluxes measured with closed-path eddy-covariance systems with short sampling lines. Agric. For. Meteor., 165:53–63, 2012.

G. Fratini, D. K. McDermitt, and D. Papale. Eddy-covariance flux errors due to biases in gas concentration measurements: origins, quantification and correction. Biogeosciences, 11:1037–1051, 2014.

J. M. Freedman, D. R. Fitzjarrald, K. E. Moore, and R. K. Sakai. Boundary layer clouds and vegetation-atmosphere feedbacks. Journal of Climate, 14:180–197, 2001.

C. A. Friehe, W. J. Shaw, D. P. Rogers, K. L. Davidson, W. G. Large, S. A. Stage, G. H. Crescenti, S. J. S. Khalsa, G. K. Greenhut, and F. Li. Air-sea fluxes and surface-layer turbulence around a sea-surface temperature front. J. Geophys. Res., 96:8593–8609, 1991.

N. J. Froelich and H. P. Schmid. Flow divergence and density flows above and below a deciduous forest. Part II: below-canopy thermotopographic flows. Agric. For. Meteor., 138:29–43, 2006.

N. J. Froelich, C. S. B. Grimmond, and H. P. Schmid. Nocturnal cooling below a forest canopy: Model and evaluation. Agric. For. Meteor., 151:957–968, 2011.

P. L. Fuehrer and C. A. Friehe. Flux corrections revisited. Bound.-Layer Meteor., 102:415–457, 2002.

D. J. Gable. Vegetation map of the Ward quadrangle, Boulder County, Colorado. U.S. Geological Survey Miscellaneous Field Studies Map MF-940; scale 1:24,000, digital media., 1978.

D. J. Gable and R. F. Madole. Geologic map of the Ward quadrangle, Boulder County, Colorado. U.S. Geological Survey Geologic Quadrangle Map GQ-1277; scale 1:24,000, digital media., 1976.

W. Gao, R. H. Shaw, and K. T. Paw. Observation of organized structure in turbulent-flow within and above a forest canopy. Boundary-Layer Meteorology, 47:349–377, 1989.

W. Gao, R. H. Shaw, and K. T. Paw. Conditional analysis of temperature and humidity microfronts and ejection sweep motions within and above a deciduous forest. Boundary-Layer Meteorology, 59:35–57, 1992.

J. R. Garratt. The Atmospheric Boundary Layer. Cambridge University Press, Cambridge, 1992. 316 pp.

R. Geiger, R. H. Aron, and P. Todhunter. The Climate Near the Ground. Rowman & Littlefield, Oxford, sixth edition, 2003. 584 pp.

P. Gentine, D. Entekhabi, and J. Polcher. The diurnal behavior of evaporative fraction in the soil-vegetation-atmospheric boundary layer continuum. J. Hydrometeor., 12:1530–1546, 2011. doi: 10.1175/2011JHM1261.1.

P. J. Gleichman. A literature review and summary of Albion. Native Cutural Services,, Boulder, Colorado, 19 pp. [available from the Boulder Carnegie Library for Local History], 2005.

J. A. Goff and S. Gratch. Low-pressure properties of water from 160 to 212 °F. In Transactions of the American Society of Heating and Ventilating Engineers. 52nd annual meeting of the American Society of Heating and Ventilating Engineers, New York, pp. 95–122, 1946.

M. Golub. Footprint heterogeneity effect on evapotranspiration and net ecosystem exchange in a subalpine forest: Scaling sap flux measurements to the tower. Master's thesis, King's College London, London, England, 40 pp., 2010.

B. E. Goodison, P. Y. T. Louie, and D. Yang. WMO solid precipitation measurement intercomparison: Final report. Instruments and Observing Methods Report No. 67, WMO/TD No. 872. World Meteorological Organization, Geneva, Switzerland, 212 pp., 1998.

M. L. Goulden, J. W. Munger, S. M. Fan, B. C. Daube, and S. C. Wofsy. Measurements of carbon sequestration by long-term eddy covariance: Methods and a critical evaluation of accuracy. Global Change Biology, 2:169–182, 1996.

E. R. Grant, A. N. Ross, B. A. Gardiner, and S. D. Mobbs. Field observations of canopy flows over complex terrain. Bound.-Layer Meteor., 156:231–251, 2015.

C. M. Gray, R. K. Monson, and N. Fierer. Emissions of volatile organic compounds during the decomposition of plant litter. Journal of Geophysical Research (Biogeosciences), 115:G03015, 2010.

C. M. Gray, R. K. Monson, and N. Fierer. Biotic and abiotic controls on biogenic volatile organic compound fluxes from a subalpine forest floor. Journal of Geophysical Research (Biogeosciences), 119:547–556, 2014.

C. M. Gray, D. Helmig, and N. Fierer. Bacteria and fungi associated with isoprene consumption in soil. Elementa Science of the Anthropocene, 3, 2015. doi: 10.12952.

D. Greenland. The climate of Niwot Ridge, Front Range, Colorado, USA. Arctic and Alpine Research, 21:380–391, 1989.

D. Greenland. Mountain climates. In J. E. Oliver, editor, Encyclopedia of World Climatology, Encyclopedia of Earth Sciences Series, pages 517–523. Springer, Dordrecht, the Netherlands, 2005. doi: 10.1007/1-4020-3266-8_145.

A. Grelle, A. Lundberg, A. Lindroth, A. S. Moren, and E. Cienciala. Evaporation components of a boreal forest: variations during the growing season. Journal of Hydrology, 197:70–87, 1997.

G. J. Grenzdörffer, A. Engel, and B. Teichert. The photogrammetric potential of low-cost UAVs in forestry and agriculture. The International Archives of the Photogrammetry, Remote Sensing and Spatial Information Sciences, 31(B3):1207–1214, 2008.

C. S. B. Grimmond, S. A. Isard, and M. J. Belding. Development and evaluation of continuously weighing mini-lysimeters. Agric. For. Meteor., 62:205–218, 1992.

L. Gu, J. D. Fuentes, H. H. Shugart, R. M. Staebler, and T. A. Black. Responses of net ecosystem exchanges of carbon dioxide to changes in cloudiness: Results from two north american deciduous forests. J. Geophys. Res., 104:31421–31434, 1999.

L. Gu, D. Baldocchi, S. B. Verma, T. A. Black, T. Vesala, E. M. Falge, and P. R. Dowty. Advantages of diffuse radiation for terrestrial ecosystem productivity. J. Geophys. Res., 107:4050, 2002. doi: 10.1029/2001JD001242.

J. C. Halfpenny. Ecological studies in the Colorado Alpine: A festschrift for John W. Marr. Occasional Paper 37, Institute of Arctic and Alpine Research, University of Colorado at Boulder, 147 pp., 1982.

J. C. Halfpenny, K. P. Ingraham, J. Mattysse, and P. J. Lehr. Bibliography of Alpine and Subalpine areas of the Front Range, Colorado. Occasional Paper 43, Institute of Arctic and Alpine Research, University of Colorado at Boulder, 114 pp., 1986.

B. D. Hall, A. Engel, J. Mühle, J. W. Elkins, F. Artuso, E. Atlas, M. Aydin, D. Blake, E.-G. Brunke, S. Chiavarini, and many others. Results from the International Halocarbons in Air Comparison Experiment (IHALACE). Atmospheric Measurement Techniques, 7(2):469–490, 2014. doi: 10.5194/amt-7-469-2014.

S. Halldin and A. Lindroth. Errors in net radiometry: Comparison and evaluation of 6 radiometer designs. Journal Of Atmospheric And Oceanic Technology, 9:762–783, 1992.

D. Handorf, T. Foken, and C. Kottmeier. The stable atmospheric boundary layer over an Antarctic ice sheet. Bound.-Layer Meteor., 91:165–189, 1999.

H. P. Handy. Map of Boulder County Colorado. 1:31680, 1888. Board of County Commissioners, [In collection: Boulder County Map, University of Colorado, Digital Library].

I. N. Harman and J. J. Finnigan. A simple unified theory for flow in the canopy and roughness sublayer. Bound.-Layer Meteor., 123:339–363, 2007.

I. N. Harman and J. J. Finnigan. Scalar concentration profiles in the canopy and roughness sublayer. Bound.-Layer Meteor., 129:323–351, 2008.

A. A. Harpold, J. A. Marshall, S. W. Lyon, T. B. Barnhart, B. A. Fisher, M. Donovan, K. M. Brubaker, C. J. Crosby, N. F. Glenn, C. L. Glennie, P. B. Kirchner, N. Lam, K. D. Mankoff, J. L. McCreight, N. P. Molotch, K. N. Musselman, J. Pelletier, T. Russo, H. Sangireddy, Y. Sjoberg, T. Swetnam, and N. West. Laser vision: lidar as a transformative tool to advance critical zone science. Hydrology And Earth System Sciences, 19:2881–2897, 2015.

B. D. Haugen, T. A. Scambos, Pfeffer W. T., and R. S. Anderson. Twentieth-century changes in the thickness and extent of Arapaho Glacier, Front Range, Colorado. Arctic, Antarctic, and Alpine Research, 42:198–209, 2010.

B. G. Heusinkveld, S. M. Berkowicz, A. F. G. Jacobs, A. A. M. Holtslag, and W. C. A. M. Hillen. An automated microlysimeter to study dew formation and evaporation in arid and semiarid regions. Journal Of Hydrometeorology, 7:825–832, 2006.

P. Hignett. Corrections to temperature-measurements with a sonic anemometer. Bound.-Layer Meteor., 61:175–187, 1992.

T. Hirano, H. Kim, and Y. Tanaka. Long-term half-hourly measurement of soil CO_2 concentration and soil respiration in a temperate deciduous forest. J. Geophys. Res., 108(D20):4631, 2003. doi: 10.1029/2003JD003766.

M. Hirschi, D. Michel, I. Lehner, and S. I. Seneviratne. A site-level comparison of lysimeter and eddy covariance flux measurements of evapotranspiration. Hydrology and Earth System Sciences, 21:1809–1825, 2017. doi: 10.5194/hess-21-1809-2017.

D. C. Hoaglin, F. Mosteller, and J. W. Tukey. Understanding Robust and Exploratory Data Analysis. John Wiley & Sons, New York, 1983. 447 pp.

M. J Hoffman, A. G. Fountain, and J. M. Achuff. 20th-century variations in area of cirque glaciers and glacierets, Rocky Mountain National Park, Rocky Mountains, Colorado, USA. Annals of Glaciology, 46:349–354, 2007.

E. H. Hogg, T. A. Black, G. den Hartog, H. H. Neumann, R. Zimmermann, P. A. Hurdle, P. D. Blanken, Z. Nesic, P. C. Yang, R. M. Staebler, K. C. McDonald, and R. Oren. A comparison of sap flow and eddy fluxes of water vapor from a boreal deciduous forest. J. Geophys. Res., 102: 28929–28937, 1997.

U. Högström. Non-dimensional wind and temperature profiles in the atmospheric surface layer: A re-evaluation. Bound.-Layer Meteor., 42:55–78, 1988.

D. Hollinger. Data and Information for the AmeriFlux US-Ho1 Howland Forest (main tower) Site, AmeriFlux Management Project, Lawrence Berkeley National Laboratory, California. doi:10.17190/AMF/1246061, 1996-present.

D. Y. Hollinger, S. M. Goltz, E. A. Davidson, J. T. Lee, K. Tu, and H. T. Valentine. Seasonal patterns and environmental control of carbon dioxide and water vapour exchange in an ecotonal boreal forest. Global Change Biology, 5:891–902, 1999.

D. Y. Hollinger, J. Aber, B. Dail, E. A. Davidson, S. M. Goltz, H. Hughes, M. Y. Leclerc, J. T. Lee, A. D. Richardson, C. Rodrigues, N. A. Scott, D. Achuatavarier, and J. Walsh. Spatial and temporal variability in forest-atmosphere CO_2 exchange. Global Change Biology, 10:1689–1706, 2004.

A. A. M. Holtslag and H. A. R. De Bruin. Applied modeling of the nighttime Surface Energy Balance over land. Journal Of Applied Meteorology, 27:689–704, 1988.

A. A. M. Holtslag, G. Svensson, P. Baas, S. Basu, B. Beare, A. C. M. Beljaars, F. C. Bosveld, J. Cuxart, J. Lindvall, G. J. Steeneveld, M. Tjernstrom, and B. J. H. Van de Wiel. Stable atmospheric boundary layers and diurnal cycles: Challenges for weather and climate models. Bull. Amer. Meteor. Soc., 94:1691–1706, 2013.

T. W. Horst, S. R. Semmer, and G. Maclean. Correction of a non-orthogonal, three-component sonic anemometer for flow distortion by transducer shadowing. Bound.-Layer Meteor., 155:371–395, 2015. doi: 10.1007/s10546-015-0010-3.

R. A. Jr. Houze. Orographic effects on precipitating clouds. Reviews of Geophysics, 50:RG1001, 2012. doi: 10.1029/2011RG000365.

B. Hu, J. Li, L. Jing, and A. Judah. Improving the efficiency and accuracy of individual tree crown delineation from high-density LiDAR data. International Journal of Applied Earth Observation and Geoinformation, 26:145–155, 2014.

J. Hu, D. J. P. Moore, S. P. Burns, and R. K. Monson. Longer growing seasons lead to less carbon sequestration by a subalpine forest. Global Change Biol., 16:771–783, 2010a. doi: 10.1111/j.1365-2486.2009.01967.x.

J. Hu, D. J. P. Moore, D. A. Riveros-Iregui, S. P. Burns, and R. K. Monson. Modeling whole-tree carbon assimilation rate using observed transpiration rates and needle sugar carbon isotope ratios. New Phytologist, 185(4):1000–1015, 2010b. doi: 10.1111/j.1469-8137.2009.03154.x.

T. E. Huxman, A. A. Turnipseed, J. P. Sparks, P. C. Harley, and R. K. Monson. Temperature as a control over ecosystem CO_2 fluxes in a high-elevation, subalpine forest. Oecologia, 134:537–546, 2003.

T. E. Huxman, K. A. Snyder, D. Tissue, A. J. Leffler, K. Ogle, W. T. Pockman, D. R. Sandquist, D. L. Potts, and S. Schwinning. Precipitation pulses and carbon fluxes in semiarid and arid ecosystems. Oecologia, 141:254–268, 2004.

A. Ibrom, E. Dellwik, S. E. Larsen, and K. Pilegaard. On the use of the Webb-Pearman-Leuning theory for closed-path eddy correlation measurements. Tellus Series B-Chemical And Physical Meteorology, 59:937–946, 2007.

I. Inglima, G. Alberti, T. Bertolini, F. P. Vaccari, B. Gioli, F. Miglietta, M. F. Cotrufo, and A. Peressotti. Precipitation pulses enhance respiration of mediterranean ecosystems: the balance between organic and inorganic components of increased soil CO_2 efflux. Global Change Biology, 15:1289–1301, 2009.

E. Inoue. On the turbulent structure of airflow within crop canopies. J. Meteor. Soc. Japan, 41: 317–326, 1963.

INSTAAR. 50th anniversary: the Institute of Arctic and Alpine Research (INSTAAR) 1951-2001, 2001. University of Colorado at Boulder, 107 pp.

J. Irvine and B. E. Law. Contrasting soil respiration in young and old-growth ponderosa pine forests. Global Change Biology, 8:1183–1194, 2002.

S. Ivans, L. Hipps, A. J. Leffler, and C. Y. Ivans. Response of water vapor and CO_2 fluxes in semiarid lands to seasonal and intermittent precipitation pulses. Journal Of Hydrometeorology, 7:995–1010, 2006.

J. D. Ives. The development of a Front Range Mountain Research Station. In J. D. Ives, editor, Geoecology of the Colorado Front Range: A study of alpine and subalpine environments, pages xv–xx. Westview Press, Boulder, Colorado, 1980.

R. L. Ives. Modern glaciers of the Arapaho massif. The Scientific Monthly, 73(1):25–36, 1951.

R. L. Ives. Later Pleistocene glaciation in the Silver Lake Valley, Colorado. Geographical Review, 43(2):229–252, 1953.

J. Jacobs. The sustainability of water resources in the Colorado River Basin. The Bridge, National Academy of Engineering (NAE), 41:6–12, 2011.

P. Jarvis, A. Rey, C. Petsikos, L. Wingate, M. Rayment, J. Pereira, J. Banza, J. David, F. Miglietta, M. Borghetti, G. Manca, and R. Valentini. Drying and wetting of mediterranean soils stimulates decomposition and carbon dioxide emission: the "birch effect". Tree Physiology, 27:929–940 ER, 2007.

P. G. Jarvis and K. G. McNaughton. Stomatal control of transpiration: Scaling up from leaf to region. Advances In Ecological Research, 15:1–49, 1986.

S. Jasechko, Z. D. Sharp, J. J. Gibson, S. J. Birks, Y. Yi, and P. J. Fawcett. Terrestrial water fluxes dominated by transpiration. Nature, 496:347–351, 2013.

G. D. Jenerette, R. L. Scott, and T. E. Huxman. Whole ecosystem metabolic pulses following precipitation events. Functional Ecology, 22:924–930, 2008.

A. W. Johnson. Ecology of subalpine forest communities in the Silver Lake Valley of the Front Range of Colorado. PhD thesis, University of Colorado, Boulder, Boulder, CO, USA, 121 pp., 1956.

J. B. Johnson. Stand structure and vegetation dynamics of a subalpine wooded fen in Rocky Mountain National Park, Colorado. Journal of Vegetation Science, 8(3):337–342, 1987. doi: 10.2307/3237322.

J. C. Kaimal and J. J. Finnigan. Atmospheric Boundary Layer Flows: Their Structure and Measurement. Oxford University Press, New York, 1994. 289 pp.

J. C. Kaimal and J. E. Gaynor. Another look at sonic thermometry. Bound.-Layer Meteor., 56: 401–410, 1991.

M. Kang, H. Kwon, J. H. Cheon, and J. Kim. On estimating wet canopy evaporation from deciduous and coniferous forests in the Asian monsoon climate. J. Hydrometeor., 13:950–965, 2012.

T. G. Karl, C. Spirig, J. Rinne, C. Stroud, P. Prevost, J. Greenberg, R. Fall, and A. Guenther. Virtual disjunct eddy covariance measurements of organic compound fluxes from a subalpine forest using proton transfer reaction mass spectrometry. Atmos. Chem. Phys, 2:279–291, 2002.

G. G. Katul, J. J. Finnigan, D. Poggi, R. Leuning, and S. E. Belcher. The influence of hilly terrain on canopy-atmosphere carbon dioxide exchange. Bound.-Layer Meteor., 118:189–216, 2006.

G. G. Katul, R. Oren, S. Manzoni, C. Higgins, and M. B. Parlange. Evapotranspiration: a process driving mass transport and energy exchange in the soil-plant-atmosphere-climate system. Reviews of Geophysics, 50:RG3002, 2012. doi: 10.1029/2011RG000366.

F. Kienast and F. H. Schweingruber. Dendroecological studies in the Front Range, Colorado, U.S.A. Arctic and Alpine Research, 18:277–288, 1986. doi: 10.1080/00040851.1986.12004089.

D. Kim, R. Oren, A. C. Oishi, C. I. Hsieh, N Phillips, K. A. Novick, and P. C. Stoy. Sensitivity of stand transpiration to wind velocity in a mixed broadleaved deciduous forest. Agric. For. Meteor., 187:62–71, 2014.

Y. Kim, C. J. Still, C. V. Hanson, H. Kwon, B. T. Greer, and B. E. Law. Canopy skin temperature variations in relation to climate, soil temperature, and carbon flux at a ponderosa pine forest in central Oregon. Agric. For. Meteor., 226:161–173, 2016.

J. M. Kindig. A research station with an altitude: a history of the Mountain Research Station, 2000. Institute of Arctic and Alpine Research, University of Colorado at Boulder, 61 pp.

D. J. Kirshbaum, B. Adler, N. Kalthoff, C. Barthlott, and S. Serafin. Moist orographic convection: Physical mechanisms and links to surface-exchange processes. Atmosphere, 9, 2018.

T. G. F. Kittel, M. W. Williams, K. Chowanski, M. Hartman, T. Ackerman, M. Losleben, and P. D. Blanken. Contrasting long-term alpine and subalpine precipitation trends in a mid-latitude North American mountain system, Colorado Front Range, USA. Plant Ecology & Diversity, 8: 607–624, 2015.

W. Klaassen. Evaporation from rain-wetted forest in relation to canopy wetness, canopy cover, and net radiation. Water Resour. Res., 37:3227–3236, 2001.

J. F. Knowles, P. D. Blanken, M. W. Williams, and K. M. Chowanski. Energy and surface moisture seasonally limit evaporation and sublimation from snow-free alpine tundra. Agric. For. Meteor., 157:106–115, 2012.

J. F. Knowles, S. P. Burns, P. D. Blanken, and R. K. Monson. Fluxes of energy, water, and carbon dioxide from mountain ecosystems at Niwot Ridge, Colorado. Plant Ecology & Diversity, 8: 663–676, 2015a. doi: 10.1080/17550874.2014.904950.

J. F. Knowles, A. A. Harpold, R. Cowie, M. Zeliff, H. R. Barnard, S. P. Burns, P. D. Blanken, J. F. Morse, and M. W. Williams. The relative contributions of alpine and subalpine ecosystems to the water balance of a mountainous, headwater catchment. Hydrological Processes, 29:4794–4808, 2015b. doi: 10.1002/hyp.10526.

J. Kochendorfer, R. Rasmussen, M. Wolff, B. Baker, M. E. Hall, T. Meyers, S. Landolt, A. Jachcik, K. Isaksen, R. Brækkan, and R. Leeper. The quantification and correction of wind-induced precipitation measurement errors. Hydrology and Earth System Sciences, 21:1973–1989, 2017. doi: 10.5194/hess-21-1973-2017.

R. D. Koster, Z. Guo, R. Yang, P. A. Dirmeyer, K. Mitchell, and M. J. Puma. On the nature of soil moisture in Land Surface Models. Journal of Climate, 22(16):4322–4335, 2009. doi: 10.1175/2009JCLI2832.1.

M. Kottek, J. Grieser, C. Beck, B. Rudolf, and F. Rubel. World map of the Köppen-Geiger climate classification updated. Meteor. Z., 15:259–263, 2006. doi: 10.1127/0941-2948/2006/0130.

A. S. Kowalski and P. Serrano-Ortiz. On the relationship between the eddy covariance, the turbulent flux, and surface exchange for a trace gas such as CO_2. Boundary-Layer Meteorology, 124:129–141, 2007.

T. Kume, O. J. Manfroi, M. Suzuki, K. Tanaka, K. Kuraji, M. Nakagawa, H. Komatsu, and T. Kumagai. Estimation of vertical profiles of leaf drying times after daytime rainfall within a bornean tropical rainforest. Hydrological Processes, 22:3689–3696, 2008. doi: 10.1002/hyp.6972.

G. Lasslop, M. Reichstein, D. Papale, A. D. Richardson, A. Arneth, A. Barr, P. Stoy, and G. Wohlfahrt. Separation of net ecosystem exchange into assimilation and respiration using a light response curve approach: critical issues and global evaluation. Global Change Biology, 16:187–208, 2010.

B. E. Law, M. Williams, P. M. Anthoni, D. D. Baldocchi, and M. H. Unsworth. Measuring and modelling seasonal variation of carbon dioxide and water vapour exchange of a pinus ponderosa forest subject to soil water deficit. Global Change Biol., 6:613–630, 2000.

B. E. Law, E. Falge, L. Gu, D. D. Baldocchi, P. Bakwin, P. Berbigier, K. Davis, A. J. Dolman, M. Falk, J. D. Fuentes, A. Goldstein, A. Granier, A. Grelle, D. Hollinger, I. A. Janssens, P. Jarvis, N. O. Jensen, G. Katul, Y. Mahli, G. Matteucci, T. Meyers, R. Monson, W. Munger, W. Oechel, R. Olson, K. Pilegaard, K. T. Paw, H. Thorgeirsson, R. Valentini, S. Verma, T. Vesala, K. Wilson, and S. Wofsy. Environmental controls over carbon dioxide and water vapor exchange of terrestrial vegetation. Agric. For. Meteor., 113:97–120, 2002.

D. M. Lawrence, P. E. Thornton, K. W. Oleson, and G. B. Bonan. The partitioning of evapotranspiration into transpiration, soil evaporation, and canopy evaporation in a GCM: Impacts on land-atmosphere interaction. J. Hydrometeor., 8:862–880, 2007.

D. M. Lawrence, K. W. Oleson, M. G. Flanner, P. E. Thornton, S. C. Swenson, P. J. Lawrence, X. Zeng, Z. L. Yang, S. Levis, K. Sakaguchi, G. B. Bonan, and A. G. Slater. Parameterization improvements and functional and structural advances in version 4 of the Community Land Model. Journal Of Advances In Modeling Earth Systems, 3:M03001, 2011. doi: 10.1029/2011MS000045.

T. R. Lee, S. F. J. De Wekker, A. E. Andrews, J. Kofler, and J. Williams. Carbon dioxide variability during cold front passages and fair weather days at a forested mountaintop site. Atmos. Environ., 46:405–416, 2012.

X. Lee, H. J. Wu, J. Sigler, C. Oishi, and T. Siccama. Rapid and transient response of soil respiration to rain. Global Change Biology, 10:1017–1026, 2004.

M. A. Lefsky, W. B. Cohen, G. G. Parker, and D. J. Harding. Lidar remote sensing for ecosystem studies. Bioscience, 52:19–30, 2002.

D. H. Lenschow and M. R. Raupach. The attenuation of fluctuations in scalar concentrations through sampling tubes. J. Geophys. Res., 96:15259–15268, 1991.

R. Leuning and M. J. Judd. The relative merits of open- and closed-path analysers for measurement of eddy fluxes. Global Change Biology, 2:241–253, 1996.

R. Leuning, E. van Gorsel, W. J. Massman, and P. R. Isaac. Reflections on the surface energy imbalance problem. Agric. For. Meteor., 156:65–74, 2012. doi: 10.1016/j.agrformet.2011.12.002.

W. K. Li, Q. H. Guo, M. K. Jakubowski, and M. Kelly. A new method for segmenting individual trees from the lidar point cloud. Photogrammetric Engineering And Remote Sensing, 78:75–84, 2012.

LI-COR. LI-6262 CO_2/H_2O Analyzer Operating and Service Manual, 1996. Publication Number 9003-59, 3rd Printing, 120 pp., (Available at www.licor.com).

LI-COR. LI-7200 CO_2/H_2O Analyzer Instruction Manual, 2013. Publication Number 984-10564, 5th Printing, 194 pp., (Available at www.licor.com).

A. Lindroth. Seasonal and diurnal-variation of energy budget components in coniferous forests. Journal Of Hydrology, 82:1–15, 1985.

A. Lindroth, M. Molder, and F. Lagergren. Heat storage in forest biomass improves energy balance closure. Biogeosciences, 7:301–313, 2010.

R. S. Lindzen and S. Chapman. Atmospheric tides. Space Science Reviews, 10:3–188, 1969.

D. Lo Seen, A. Chehbouni, E. Njoku, S. Saatchi, E. Mougin, and G. Monteny. An approach to couple vegetation functioning and soil-vegetation-atmosphere-transfer models for semiarid grasslands during the HAPEX-Sahel experiment. Agric. For. Meteor., 83:49–74, 1997.

J. Lobeck. More water shortages on tap in Desert Southwest? Western Farm Press, 15 March, 2018. URL `http://www.westernfarmpress.com`. [Online; last access, March 2018].

H. Loescher. AmeriFlux-Niwot Comparison between 22–30 July, 2003. Technical report, Department of Forest Science, Oregon State University, Corvallis, Oregon, 5 pp., 2004.

M. Lothon, F. Lohou, D. Pino, F. Couvreux, E. R. Pardyjak, and many others. The BLLAST field experiment: Boundary-Layer Late Afternoon and Sunset Turbulence. Atmospheric Chemistry and Physics, 14:10931–10960, 2014. doi: 10.5194/acp-14-10931-2014.

J. L. Lovell, D. L. B. Jupp, D. S. Culvenor, and N. C. Coops. Using airborne and ground-based ranging lidar to measure canopy structure in australian forests. Canadian Journal Of Remote Sensing, 29:607–622, 2003.

G. Maclean and C. Webster. NCAR in-situ data acquisition software for airborne and surface measurements. In 16th Symposium on Meteorological Observation and Instrumentation, American Meteorological Society. New Orleans, Louisiana, 21-26 January 2012, paper 10.1, 2012. available at: https://ams.confex.com/ams/92Annual/webprogram/, last access: 26 September 2016.

R. F. Madole. Pinedale and Bull Lake glaciation in Upper St. Vrain drainage basin, Boulder County, Colorado. Arctic, Antarctic, and Alpine Research, 4:279–287, 1969.

L. Mahrt. Stratified atmospheric boundary layers. Bound.-Layer Meteor., 90:375–396, 1999.

Y. Malhi, E. Pegoraro, A. D. Nobre, M. G. P. Pereira, J. Grace, A. D. Culf, and R. Clement. Energy and water dynamics of a central amazonian rain forest. Journal Of Geophysical Research-Atmospheres, 107:8061, 2002. doi: 10.1029/2001JD000623.

J. W. Marr. Ecosystems on the east slope of the Front Range in Colorado, Series in Biology, No. 8, University of Colorado Press, Boulder, Colorado, 1961. 144 pp.

J. W. Marr. Data on mountain environments: I. Front Range, Colorado, sixteen sites, 1952–1953, Series in Biology, No. 27, University of Colorado Press, Boulder, Colorado, 110 pp., 1967.

J. W. Marr, J. M. Clark, W. S. Osburn, and M. W. Paddock. Data on mountain environments: III. Front Range, Colorado, four climax regions, 1959–1964, Series in Biology, No. 29, University of Colorado Press, Boulder, Colorado, 181 pp., 1968a.

J. W. Marr, A. W. Johnson, W. S. Osburn, and O. A. Knorr. Data on mountain environments: II. Front Range, Colorado, four climax regions, 1953–1958, Series in Biology, No. 28, University of Colorado Press, Boulder, Colorado, 170 pp., 1968b.

W. J. Massman. The attenuation of concentration fluctuations in turbulent-flow through a tube. J. Geophys. Res., 96:15269–15273, 1991.

W. J. Massman and X. Lee. Eddy covariance flux corrections and uncertainties in long term studies of carbon and energy exchanges. Agric. For. Meteor., 113:121–144, 2002.

A. M. Matheny, G. Bohrer, P. C. Stoy, I. T. Baker, A. T. Black, A. R. Desai, M. C. Dietze, C. M. Gough, V. Y. Ivanov, R. S. Jassal, K. A. Novick, K. V. R. Schafer, and H. Verbeeck. Characterizing the diurnal patterns of errors in the prediction of evapotranspiration by several land-surface models: An NACP analysis. J. Geophys. Res., 119:1458–1473, 2014.

M. Mauder, T. Foken, R. Clement, J. A. Elbers, W. Eugster, T. Grunwald, B. Heusinkveld, and O. Kolle. Quality control of carboeurope flux data - part 2: Inter-comparison of eddy-covariance software. Biogeosciences, 5:451–462, 2008.

Max Planck Institute for Biogeochemistry. Eddy covariance gap-filling and flux-partitioning tool. http://www.bgc-jena.mpg.de/~MDIwork/eddyproc/ [Last access: June 2015], 2013.

G. J. McCabe and D. M. Wolock. Warming may create substantial water supply shortages in the Colorado River basin. Geophys. Res. Lett., 34, 2007.

D. K. McDermitt. Some recommendations for using LI-COR Gas Analyzers in Eddy Correlation Measurements. Topics discussed at Ameriflux Workshop, 1996. Application Note #118, LI-COR Inc., 1997. Lincoln, Nebraska, 7pp., (Available at www.licor.com).

R. McKie. Why fresh water shortages will cause the next great global crisis. The Guardian, 7 March, 2015. URL `https://www.theguardian.com/environment/2015/mar/08/`. [Online; last access, November 2015].

K. G. McNaughton and P. G. Jarvis. Effects of spatial scale on stomatal control of transpiration. Agric. For. Meteor., 54:279–302, 1991.

S. Metzger, G. Burba, S. P. Burns, P. D. Blanken, J. Li, H. Luo, and R. C. Zulueta. Optimization of an enclosed gas analyzer sampling system for measuring eddy covariance fluxes of H_2O and CO_2. Atmos. Meas. Tech., 9:1341–1359, 2016. doi: 10.5194/amt-9-1341-2016.

D. Michel, R. Philipona, C. Ruckstuhl, R. Vogt, and L. Vuilleumier. Performance and uncertainty of CNR1 net radiometers during a one-year field comparison. Journal Of Atmospheric And Oceanic Technology, 25:442–451, 2008.

N. L. Miles, S. J. Richardson, K. J. Davis, T. Lauvaux, A. E. Andrews, T. O. West, V. Bandaru, and E. R. Crosson. Large amplitude spatial and temporal gradients in atmospheric boundary layer CO_2 mole fractions detected with a tower-based network in the U.S. upper Midwest. J. Geophys. Res., 117:G01019, 2012. doi: 10.1029/2011JG001781.

R. C. Mills. A study of near climax conditions in a spruce-fir ecosystem. Master's thesis, University of Colorado, Boulder, Boulder, CO, USA, 68 pp., 1962.

L. Misson, A. Gershenson, J. W. Tang, M. McKay, W. X. Cheng, and A. Goldstein. Influences of canopy photosynthesis and summer rain pulses on root dynamics and soil respiration in a young ponderosa pine forest. Tree Physiology, 26:833–844, 2006.

L. Misson, D. D. Baldocchi, T. A. Black, P. D. Blanken, Y. Brunet, J. C. Yuste, J. R. Dorsey, M. Falk, A. Granier, M. R. Irvine, N. Jarosz, E. Lamaud, S. Launiainen, B. E. Law, B. Longdoz, D. Loustau, M. Mckay, K. T. Paw, T. Vesala, D. Vickers, K. B. Wilson, and A. H. Goldstein. Partitioning forest carbon fluxes with overstory and understory eddy-covariance measurements: A synthesis based on FLUXNET data. Agric. For. Meteor., 144:14–31, 2007.

A. F. Moene and J. C. Van Dam. Transport in the Atmosphere-Vegetation-Soil Continuum. Cambridge University Press, New York, 2014. 458 pp.

N. P. Molotch, P. D. Blanken, M. W. Williams, A. A. Turnipseed, R. K. Monson, and S. A. Margulis. Estimating sublimation of intercepted and sub-canopy snow using eddy covariance systems. Hydrological Processes, 21:1567–1575, 2007.

N. P. Molotch, P. D. Brooks, S. P. Burns, M. Litvak, R. K. Monson, J. R. McConnell, and K. Musselman. Ecohydrological controls on snowmelt partitioning in mixed-conifer sub-alpine forests. Ecohydrology, 2:129–142, 2009. doi: 10.1002/eco.48.

R. K. Monson, A. A. Turnipseed, J. P. Sparks, P. C. Harley, L. E. Scott-Denton, K. Sparks, and T. E. Huxman. Carbon sequestration in a high-elevation, subalpine forest. Global Change Biol., 8:459–478, 2002.

R. K. Monson, J. P. Sparks, T. N. Rosenstiel, L. E. Scott-Denton, T. E. Huxman, P. C. Harley, A. A. Turnipseed, S. P. Burns, B. Backlund, and J. Hu. Climatic influences on net ecosystem CO_2 exchange during the transition from wintertime carbon source to springtime carbon sink in a high-elevation, subalpine forest. Oecologia, 146:130–147, 2005.

R. K. Monson, S. P. Burns, M. W. Williams, A. C. Delany, M. Weintraub, and D. A. Lipson. The contribution of beneath-snow soil respiration to total ecosystem respiration in a high-elevation, subalpine forest. Global Biogeochem. Cycle, 20:GB3030, 2006a. doi:10.1029/2005GB002684.

R. K. Monson, D. L. Lipson, S. P. Burns, A. A. Turnipseed, A. C. Delany, M. W. Williams, and S. K. Schmidt. Winter forest soil respiration controlled by climate and microbial community composition. Nature, 439:711–714, 2006b. doi: 10.1038/nature04555.

R. K. Monson, M. R. Prater, J. Hu, S. P. Burns, J. P. Sparks, K. L. Sparks, and L. E. Scott-Denton. Tree species effects on ecosystem water-use efficiency in a high-elevation, subalpine forest. Oecologia, 162:491–504, 2010. doi: 10.1007/s00442-009-1465-z.

F. Montané, A. M. Fox, A. F. Arellano, N. MacBean, M. R. Alexander, A. Dye, D. A. Bishop, V. Trouet, F. Babst, A. E. Hessl, N. Pederson, P. D. Blanken, G. Bohrer, C. M. Gough, M. E. Litvak, K. A. Novick, R. P. Phillips, J. D. Wood, and D. J. P. Moore. Evaluating the effect of alternative carbon allocation schemes in a land surface model (CLM4.5) on carbon fluxes, pools, and turnover in temperate forests. Geoscientific Model Development, 10:3499–3517, 2017. doi: 10.5194/gmd-10-3499-2017.

J. L. Monteith. Evaporation and environment. In G. E. Fogg, editor, The State and Movement of Water in Living Organisms, pages 205–234. Academic Press, New York, 1965.

J. L. Monteith. A reinterpretation of stomatal responses to humidity. Plant Cell And Environment, 18:357–364, 1995.

D. J. P. Moore, J. Hu, W. J. Sacks, D. S. Schimel, and R. K. Monson. Estimating transpiration and the sensitivity of carbon uptake to water availability in a subalpine forest using a simple ecosystem process model informed by measured net CO_2 and H_2O fluxes. Agric. For. Meteor., 148:1467–1477, 2008.

D. J. P. Moore, N. A. Trahan, P. Wilkes, T. Quaife, B. B. Stephens, K. Elder, A. R. Desai, J. Negron, and R. K. Monson. Persistent reduced ecosystem respiration after insect disturbance in high elevation forests. Ecology Letters, 16:731–737, 2013.

E. J. Moors. Water use of forests in the Netherlands. PhD thesis, Vrije Universiteit, Amsterdam, the Netherlands, 290 pp., 2012.

D. R. Muhs and J. B. Benedict. Eolian additions to late quaternary alpine soils, Indian Peaks wilderness area, Colorado front range. Arctic, Antarctic, and Alpine Research, 38:120–130, 2006.

S. M. Munson, T. J. Benton, W. K. Lauenroth, and I. C. Burke. Soil carbon flux following pulse precipitation events in the shortgrass steppe. Ecological Research, 25:205–211, 2010.

T. Nakai, H. Iwata, and Y. Harazono. Importance of mixing ratio for a long-term CO_2 flux measurement with a closed-path system. Tellus Series B-Chemical And Physical Meteorology, 63:302–308, 2011.

K. A. Novick, P. C. Stoy, G. G. Katul, D. S. Ellsworth, M. B. S. Siqueira, J. Juang, and R. Oren. Carbon dioxide and water vapor exchange in a warm temperate grassland. Oecologia, 138:259–274, 2004.

K. A. Novick, R. Oren, P. C. Stoy, M. B. S. Siqueira, and G. G. Katul. Nocturnal evapotranspiration in eddy-covariance records from three co-located ecosystems in the Southeastern U.S.: Implications for annual fluxes. Agric. For. Meteor., 149:1491–1504, 2009.

K. A. Novick, J. Walker, W. S. Chan, A. Schmidt, C. Sobek, and J. M. Vose. Eddy covariance measurements with a new fast-response, enclosed-path analyzer: Spectral characteristics and cross-system comparisons. Agric. For. Meteor., 181:17–32, 2013.

A. C. Oishi, R. Oren, and P. C. Stoy. Estimating components of forest evapotranspiration: A footprint approach for scaling sap flux measurements. Agric. For. Meteor., 148:1719–1732, 2008.

K. W. Oleson, G. Y. Niu, Z. L. Yang, D. M. Lawrence, P. E. Thornton, P. J. Lawrence, R. Stockli, R. E. Dickinson, G. B. Bonan, S. Levis, A. Dai, and T. Qian. Improvements to the Community Land Model and their impact on the hydrological cycle. J. Geophys. Res., 113:G01021, 2008. doi: 10.1029/2007JG000563.

K. W. Oleson, D. M. Lawrence, G. B. Bonan, B. Drewniak, M. Huang, C. D. Koven, S. Levis, F. Li, W. J. Riley, Z. M. Subin, S. Swenson, P. E. Thornton, A. Bozbiyik, R. Fisher, C. L. Heald, E. Kluzek, J.-F. Lamarque, P. J. Lawrence, L. R. Leung, S. P. Lipscomb, W. Muszala, D. M.

Ricciuto, W. J. Sacks, Y. Sun, J. Tang, and Z.-L. Yang. Technical description of version 4.5 of the Community Land Model (CLM). Technical Report NCAR/TN-503+STR, NCAR Technical Note, 2013. 420 pp.

P. E. S. Oliveira, O. C. Acevedo, O. L. L. Moraes, H. R. Zimermann, and C. Teichrieb. Nocturnal intermittent coupling between the interior of a pine forest and the air above it. Bound.-Layer Meteor., 146:45–64, 2013.

S. P. Oncley. 'CME04 Report', NCAR Earth Observing Laboratory (EOL) Integrated Surface Flux Facility (ISFF), 2004. URL `http://www.eol.ucar.edu/cme04/`.

S. P. Oncley, T. Foken, R. Vogt, W. Kohsiek, H. A. R. DeBruin, C. Bernhofer, A. Christen, E. van Gorsel, D. Grantz, C. Feigenwinter, I. Lehner, C. Liebethal, H. Liu, M. Mauder, A. Pitacco, L. Ribeiro, and T. Weidinger. The energy balance experiment EBEX-2000. Part I: Overview and energy balance. Bound.-Layer Meteor., 123:1–28, 2007.

H. A. Panofsky and J. A. Dutton. Atmospheric turbulence: models and methods for engineering applications. Wiley Interscience, New York, 1984. 397 pp.

D. D. Parrish, C. H. Hahn, D. W. Fahey, E. J. Williams, M. J. Bollinger, G. Hubler, M. P. Buhr, P. C. Murphy, M. Trainer, E. Y. Hsie, S. C. Liu, and F. C. Fehsenfeld. Systematic variations in the concentration of NO_x (NO plus NO_2) at Niwot Ridge, Colorado. J. Geophys. Res., 95: 1817–1836, 1990.

W. Parton, J. Morgan, D. Smith, S. Del Grosso, L. Prihodko, D. Lecain, R. Kelly, and S. Lutz. Impact of precipitation dynamics on net ecosystem productivity. Global Change Biology, 18: 915–927, 2012.

M. Pattantyús-Ábrahám and I. M. Jánosi. What determines the nocturnal cooling timescale at 2 m? Geophysical Research Letters, 31:L05109, 2004. doi: 10.1029/2003GL019137.

E. G. Patton, P. P. Sullivan, R. H. Shaw, J. J. Finnigan, and J. C. Weil. Atmospheric stability influences on coupled boundary layer and canopy turbulence. J. Atmos. Sci., 73:1621–1647, 2016.

J. L. H. Paulhus. Record snowfall of April 14–15, 1921, at Silver Lake, Colorado. Monthly Weather Review, 81:38–40, 1953.

R. C. Pearson and G. Johnson. Mineral resources of the Indian Peaks Study Area, Boulder and Grand counties, Colorado. Technical Report *Geological Survey Bulletin 1463*, US Government Printing Office, 110 pp., 1980.

R. K. Peet. Forest vegetation of the Colorado Front Range. Vegetatio, 45:3–75, 1981. doi: 10.1007/BF00240202.

H. L. Penman. Natural evaporation from open water, bare soil and grass. Proceedings of the Royal Society of London A: Mathematical, Physical and Engineering Sciences, 193(1032):120–145, 1948. doi: 10.1098/rspa.1948.0037.

S. Pettem and C. Ellinghouse. Boulder's Waterworks Past & Present. City of Boulder, Boulder, Colorado, 149 pp., 2014.

R. Pieruschka, G. Huber, and J. A. Berry. Control of transpiration by radiation. Proc. Nat. Acad. Sci. USA, 107:13372–13377, 2010.

H. P. Pietersen, J. Vilà-Guerau de Arellano, P. Augustin, A. van de Boer, O. de Coster, H. Delbarre, P. Durand, M. Fourmentin, B. Gioli, O. Hartogensis, F. Lohou, M. Lothon, H. G. Ouwersloot, D. Pino, and J. Reuder. Study of a prototypical convective boundary layer observed during BLLAST: Contributions by large-scale forcings. Atmos. Chem. Phys, 15:4241–4257, 2015.

D. Pino, J. Vilà-Guerau de Arellano, W. Peters, J. Schröter, C. C. van Heerwaarden, and M. Krol. A conceptual framework to quantify the influence of convective boundary layer development on carbon dioxide mixing ratios. Atmos. Chem. Phys, 12:2969–2985, 2012.

J. Pitt, E. Kendy, K. Schlatter, O. Hinojosa-Huerta, K. Flessa, P. B. Shafroth, J. Ramirez-Hernandez, P. Nagler, and E. P. Glenn. It takes more than water: Restoring the colorado river delta. Ecological Engineering, 106:629–632, 2017.

H. W. Polley, W. Emmerich, J. A. Bradford, P. L. Sims, D. A. Johnson, N. Z. Sallendra, T. Svejcar, R. Angell, A. B. Frank, R. L. Phillips, K. A. Snyder, J. A. Morgan, J. Sanabria, P. C. Mielnick, and W. A. Dugas. Precipitation regulates the response of net ecosystem CO_2 exchange to environmental variation on United States rangelands. Rangeland Ecology & Management, 63: 176–186, 2010.

S. C. Popescu and R. H. Wynne. Seeing the trees in the forest: Using lidar and multispectral data fusion with local filtering and variable window size for estimating tree height. Photogrammetric Engineering And Remote Sensing, 70:589–604, 2004.

S. Postel. Landmark cooperation brings the Colorado River home. National Geographic, 5 April, 2013. URL `https://blog.nationalgeographic.org/`. [Online; last access, March 2018].

R. D. Pyles, B. C. Weare, and K. T. Paw U. The UCD Advanced Canopy-Atmosphere-Soil Algorithm: Comparisons with observations from different climate and vegetation regimes. Quart. J. Roy. Meteor. Soc., 126:2951–2980, 2000.

B. Raczka, H. F. Duarte, C. D. Koven, D. Ricciuto, P. E. Thornton, J. C. Lin, and D. R. Bowling. An observational constraint on stomatal function in forests: evaluating coupled carbon and water vapor exchange with carbon isotopes in the Community Land Model (CLM4.5). Biogeosciences, 13(18):5183–5204, 2016. doi: 10.5194/bg-13-5183-2016.

F. Ramaley. The University of Colorado Mountain Laboratory. University of Colorado Studies, 7: 91–95, 1909.

G. Rana and N. Katerji. Measurement and estimation of actual evapotranspiration in the field under mediterranean climate: a review. European Journal of Agronomy, 13:125–153, 2000.

U. Rannik, T. Vesala, and R. Keskinen. On the damping of temperature fluctuations in a circular tube relevant to the eddy covariance measurement technique. J. Geophys. Res., 102:12789–12794, 1997.

R. Rasmussen, B. Baker, J. Kochendorfer, T. Meyers, S. Landolt, A. P. Fischer, J. Black, J. M. Theriault, P. Kucera, D. Gochis, C. Smith, R. Nitu, M. Hall, K. Ikeda, and E. Gutmann. How well are we measuring snow? The NOAA/FAA/NCAR winter precipitation test bed. Bull. Amer. Meteor. Soc., 93:811–829, 2012.

M. R. Raupach. Simplified expressions for vegetation roughness length and zero-plane displacement as functions of canopy height and area index. Bound.-Layer Meteor., 71:211–216, 1994.

M. R. Raupach and J. J. Finnigan. Single-layer models of evaporation from plant canopies are incorrect but useful, whereas multilayer models are correct but useless: Discuss. Australian Journal Of Plant Physiology, 15:705–716, 1988.

M. R. Raupach, J. J. Finnigan, and Y. Brunet. Coherent eddies and turbulence in vegetation canopies: the mixing-layer analogy. Bound.-Layer Meteor., 78:351–382, 1996.

M. Reichstein, E. Falge, D. Baldocchi, D. Papale, M. Aubinet, P. Berbigier, C. Bernhofer, N. Buchmann, T. Gilmanov, A. Granier, T. Grunwald, K. Havrankova, H. Ilvesniemi, D. Janous, A. Knohl, T. Laurila, A. Lohila, D. Loustau, G. Matteucci, T. Meyers, F. Miglietta, J. M. Ourcival, J. Pumpanen, S. Rambal, E. Rotenberg, M. Sanz, J. Tenhunen, G. Seufert, F. Vaccari, T. Vesala, D. Yakir, and R. Valentini. On the separation of net ecosystem exchange into assimilation and ecosystem respiration: review and improved algorithm. Global Change Biol., 11:1424–1439, 2005.

J. Reitberger, P. Krzystek, and U. Stilla. Analysis of full waveform lidar data for the classification of deciduous and coniferous trees. International Journal Of Remote Sensing, 29:1407–1431, 2008.

A. D. Richardson, K. Hufkens, T. Milliman, D. M. Aubrecht, M. Chen, J. M. Gray, M. R. Johnston, T. F. Keenan, S. T. Klosterman, M. Kosmala, E. K. Melaas, M. A. Friedl, and S. Frolking. Tracking vegetation phenology across diverse North American biomes using PhenoCam imagery. Scientific Data, 5:180028, 2018.

W. J. Ripple, C. Wolf, T. M. Newsome, M. Galetti, M. Alamgir, E. Crist, M. I. Mahmoud, W. F. Laurance, and 15,364 scientist signatories from 184 countries. World scientists warning to humanity: A second notice. BioScience, 67(12):1026–1028, 2017. doi: 10.1093/biosci/bix125.

D. A. Riveros-Iregui, J. Hu, S. P. Burns, D. R. Bowling, and R. K. Monson. An interannual assessment of the relationship between the stable carbon isotopic composition of ecosystem respiration and climate in a high-elevation subalpine forest. J. Geophys. Res., 116:G02005, 2011. doi: 10.1029/2010JG001556.

L. Runyon. Scarce Rocky Mountain snowpack deepens Southwest water supply concerns. Community Radio for Northern Colorado (KUNC), Greeley, CO, 13 March, 2018. URL `http://www.kunc.org`. [Online; last access, March 2018].

A. J. Rutter, A. J. Morton, and P. C. Robins. A predictive model of rainfall interception in forests. II. Generalization of model and comparison with observations in some coniferous and hardwood stands. Journal of Applied Ecology, 12:367–380, 1975.

M. G. Ryan and B. Law. Interpreting, measuring, and modeling soil respiration. Biogeochem, 73: 3–27, 2005.

M. G. Ryan and B. J. Yoder. Hydraulic limits to tree height and tree growth. Bioscience, 47: 235–242, 1997.

E. Sahlee and W. M. Drennan. Measurements of damping of temperature fluctuations in a tube. Bound.-Layer Meteor., 132:339–348, 2009.

K. Sakaguchi and X. Zeng. Effects of soil wetness, plant litter, and under-canopy atmospheric stability on ground evaporation in the Community Land Model (CLM3.5). J. Geophys. Res., 114, 2009.

E. P. Sánchez-Cañete, A. S. Kowalski, P. Serrano-Ortiz, O. Pérez-Priego, and F. Domingo. Deep CO_2 soil inhalation / exhalation induced by synoptic pressure changes and atmospheric tides in a carbonated semiarid steppe. Biogeosciences, 10:6591–6600, 2013. doi: 10.5194/bg-10-6591-2013.

S. Sargent. Quantifying frequency response of a low-power, closed-path CO_2 and H_2O eddy-covariance system, 2012. 10 pp., (Available at www.campbellsci.com).

K. Savage, E. A. Davidson, A. D. Richardson, and D. Y. Hollinger. Three scales of temporal resolution from automated soil respiration measurements. Agric. For. Meteor., 149:2012–2021, 2009.

T. M. Scanlon and W. P. Kustas. Partitioning carbon dioxide and water vapor fluxes using correlation analysis. Agric. For. Meteor., 150:89–99, 2010.

S. M. Schaeffer, D. E. Anderson, S. P. Burns, R. K. Monson, J. Sun, and D. R. Bowling. Canopy structure and atmospheric flows in relation to the $\delta^{13}C$ of respired CO_2 in a subalpine coniferous forest. Agric. For. Meteorol., 148:592–605, 2008a. doi: 10.1016/j.agrformet.2007.11.003.

S. M. Schaeffer, J. B. Miller, B. H. Vaughn, J. W. C. White, and D. R. Bowling. Long-term field performance of a tunable diode laser absorption spectrometer for analysis of carbon isotopes of CO_2 in forest air. Atmospheric Chemistry And Physics, 8:5263–5277, 2008b.

D. R. Schlaepfer, B. E. Ewers, B. N. Shuman, D. G. Williams, J. M. Frank, W. J. Massman, and W. K. Lauenroth. Terrestrial water fluxes dominated by transpiration: Comment. Ecosphere, 5(5):61, 2014. doi: 10.1890/ES13-00391.1.

W. H. Schlesinger and S. Jasechko. Transpiration in the global water cycle. Agric. For. Meteor., 189:115–117, 2014.

A. Schmidt, C. Hanson, W. S. Chan, and B. E. Law. Empirical assessment of uncertainties of meteorological parameters and turbulent fluxes in the AmeriFlux network. J. Geophys. Res., 117:G04014, 2012. doi: 10.1029/2012JG002100.

T. Schoennagel, T. T. Veblen, and W. H. Romme. The interaction of fire, fuels, and climate across rocky mountain forests. Bioscience, 54:661–676, 2004.

P. Schotanus, F. T. M. Nieuwstadt, and H. A. R. De Bruin. Temperature-measurement with a sonic anemometer and its application to heat and moisture fluxes. Bound.-Layer Meteor., 26: 81–93, 1983.

D. M. Schultz. A review of cold fronts with prefrontal troughs and wind shifts. Monthly Weather Review, 133:2449–2472, 2005.

L. E. Scott-Denton, K. L. Sparks, and R. K. Monson. Spatial and temporal controls of soil respiration rate in a high-elevation, subalpine forest. Soil Biol. Biochem., 35:525–534, 2003.

L. E. Scott-Denton, T. N. Rosenstiel, and R. K. Monson. Differential controls by climate and substrate over the heterotrophic and rhizospheric components of soil respiration. Global Change Biol., 12:205–216, 2006.

R. H. Shaw and X. J. Zhang. Evidence of pressure-forced turbulent-flow in a forest. Boundary-Layer Meteorology, 58:273–288, 1992.

R. H. Shaw, K. T. Paw, X. J. Zhang, W. Gao, G. Denhartog, and H. H. Neumann. Retrieval of turbulent pressure-fluctuations at the ground surface beneath a forest. Boundary-Layer Meteorology, 50:319–338, 1990.

K. L. Shea. Demographic aspects of coexistence in Engelmann spruce and subalpine fir. American Journal of Botany, 72:1823–1833, 1985.

R. L. Sherriff, T. T. Veblen, and J. S. Sibold. Fire history in high elevation subalpine forests in the Colorado Front Range. Ecoscience, 8:369–380, 2001.

W. J. Shuttleworth. Experimental evidence for the failure of the Penman-Monteith equation in partially wet conditions. Bound.-Layer Meteor., 10:91–94, 1976.

W. J. Shuttleworth. Putting the 'vap' into evaporation. Hydrology And Earth System Sciences, 11:210–244, 2007.

J. S. Sibold and T. T. Veblen. Relationships of subalpine forest fires in the Colorado Front Range with interannual and multidecadal-scale climatic variation. J. Biogeogr., 33:833–842, 2006.

H. Sievering, T. Tomaszewski, and J. Torizzo. Canopy uptake of atmospheric N deposition at a conifer forest: Part I—canopy N budget, photosynthetic efficiency and net ecosystem exchange. Tellus Series B-Chemical And Physical Meteorology, 59:483–492, 2007.

J. Sievers, T. Papakyriakou, S. E. Larsen, M. M. Jammet, S. Rysgaard, M. K. Sejr, and L. L. Sørensen. Estimating surface fluxes using eddy covariance and numerical ogive optimization. Atmospheric Chemistry and Physics, 15:2081–2103, 2015. doi: 10.5194/acp-15-2081-2015.

J. M. Smith, J. Paritsis, T. T. Veblen, and T. B. Chapman. Permanent forest plots show accelerating tree mortality in subalpine forests of the Colorado Front Range from 1982 to 2013. For. Ecol. Manage., 341:8–17, 2015.

R. M. Staebler and D. R. Fitzjarrald. Observing subcanopy CO_2 advection. Agric. For. Meteor., 122:139–156, 2004.

K. Staudt, A. Serafimovich, L. Siebicke, R. D. Pyles, and E. Falge. Vertical structure of evapotranspiration at a forest site (a case study). Agric. For. Meteor., 151:709–729, 2011.

B. B. Stephens, N. L. Miles, S. J. Richardson, A. S. Watt, and K. J. Davis. Atmospheric CO_2 monitoring with single-cell NDIR-based analyzers. Atmos. Meas. Tech., 4:2737–2748, 2011.

J. B. Stewart. Evaporation from wet canopy of a pine forest. Water Resour. Res., 13:915–921, 1977.

J. B. Stewart and A. S. Thom. Energy budgets in pine forest. Quart. J. Roy. Meteor. Soc., 99: 154–170, 1973.

R. Stöckli, D. M. Lawrence, G. Y. Niu, K. W. Oleson, P. E. Thornton, Z. L. Yang, G. B. Bonan, A. S. Denning, and S. W. Running. Use of FLUXNET in the Community Land Model development. J. Geophys. Res., 113:G01025, 2008. doi: 10.1029/2007JG000562.

P. C. Stoy, G. G. Katul, M. B. S. Siqueira, J. Y. Juang, K. A. Novick, J. M. Uebelherr, and R. Oren. An evaluation of models for partitioning eddy covariance-measured net ecosystem exchange into photosynthesis and respiration. Agric. For. Meteor., 141:2–18, 2006.

J. Sun, S. P. Burns, A. C. Delany, S. P. Oncley, A. A. Turnipseed, B. B. Stephens, D. H. Lenschow, M. A. LeMone, R. K. Monson, and D. E. Anderson. CO_2 transport over complex terrain. Agric. For. Meteor., 145:1–21, 2007. doi: 10.1016/j.agrformet.2007.02.007.

J. Sun, S. P. Oncley, S. P. Burns, B. B. Stephens, D. H. Lenschow, T. Campos, R. K. Monson, D. S. Schimel, W. J. Sacks, S. F. J. De Wekker, C.-T. Lai, B. Lamb, D. Ojima, P. Z. Ellsworth, L. S. L. Sternberg, S. Zhong, C. Clements, D. J. P. Moore, D. E. Anderson, A. S. Watt, J. Hu, M. Tschudi, S. Aulenbach, E. Allwine, and T. Coons. A multiscale and multidisciplinary investigation of ecosystem-atmosphere CO_2 exchange over the Rocky Mountains of Colorado. Bull. Amer. Meteor. Soc., 91:209–230, 2010. doi: 10.1175/2009BAMS2733.1.

S. C. Swenson and D. M. Lawrence. Assessing a dry surface layer-based soil resistance parameterization for the Community Land Model using GRACE and FLUXNET-MTE data. J. Geophys. Res., 119:10299–10312, 2014. doi: 10.1002/2014JD022314.

C. S. Tan and T. A. Black. Factors affecting the canopy resistance of a Douglas-fir forest. Bound.-Layer Meteor., 10:475–488, 1976.

J. W. Tang, L. Misson, A. Gershenson, W. X. Cheng, and A. H. Goldstein. Continuous measurements of soil respiration with and without roots in a ponderosa pine plantation in the Sierra Nevada Mountains. Agric. For. Meteor., 132:212–227, 2005.

S. Tao, Q. Guo, L. Li, B. Xue, M. Kelly, W. Li, G. Xu, and Y. Su. Airborne Lidar-derived volume metrics for aboveground biomass estimation: A comparative assessment for conifer stands. Agricultural And Forest Meteorology, 198–199:24–32, 2014.

H. F. M. Ten Berge. Heat and water transfer in bare topsoil and the lower atmosphere. Centre for Agricultural Publishing and Documentation (Pudoc), Wageningen, the Netherlands, 1990. 207 pp.

C. Thomas and T. Foken. Flux contribution of coherent structures and its implications for the exchange of energy and matter in a tall spruce canopy. Bound.-Layer Meteor., 123:317–337, 2007.

C. K. Thomas. Niwot Ridge and AmeriFlux portable eddy covariance system comparison between 30 June and 9 July 2006. Technical report, Department of Forest Science, Oregon State University, Corvallis, Oregon, 23 pp., 2007.

C. K. Thomas, B. E. Law, J. Irvine, J. G. Martin, J. C. Pettijohn, and K. J. Davis. Seasonal hydrology explains interannual and seasonal variation in carbon and water exchange in a semiarid mature ponderosa pine forest in central Oregon. J. Geophys. Res., 114:G04006, 2009. doi: 10.1029/2009JG001010.

C. K Thomas, J. G. Martin, B. E. Law, and K. Davis. Toward biologically meaningful net carbon exchange estimates for tall, dense canopies: Multi-level eddy covariance observations and canopy coupling regimes in a mature Douglas-fir forest in Oregon. Agric. For. Meteor., 173:14–27, 2013. doi: 10.1016/j.agrformet.2013.01.001.

P. E. Thornton, B. E. Law, H. L. Gholz, K. L. Clark, E. Falge, D. S. Ellsworth, A. H. Golstein, R. K. Monson, D. Hollinger, M. Falk, J. Chen, and J. P. Sparks. Modeling and measuring the effects of disturbance history and climate on carbon and water budgets in evergreen needleleaf forests. Agric. For. Meteor., 113:185–222, 2002.

F. Timouk, L. Kergoat, E. Mougin, C. R. Lloyd, E. Ceschia, J. M. Cohard, P. de Rosnay, P. Hiernaux, V. Demarez, and C. M. Taylor. Response of surface energy balance to water regime and vegetation development in a sahelian landscape. J. Hydrol., 375:178–189, 2009.

J. A. Tolk, T. A. Howell, and S. R. Evett. Nighttime evapotranspiration from alfalfa and cotton in a semiarid climate. Agronomy Journal, 98:730–736, 2006.

T. Tomaszewski and H. Sievering. Canopy uptake of atmospheric N deposition at a conifer forest: Part II—response of chlorophyll fluorescence and gas exchange parameters. Tellus Series B-Chemical And Physical Meteorology, 59:493–501, 2007.

T. Tomaszewski, R. L. Boyce, and H. Sievering. Canopy uptake of atmospheric nitrogen and new growth nitrogen requirement at a Colorado subalpine forest. Canadian Journal Of Forest Research, 33:2221–2227, 2003.

N. Trivett and A. Köhler. Guide on sampling and analysis techniques for chemical constituents and physical properties in air and precipitation as applied at stations of the Global Atmosphere Watch. Part I: Carbon dioxide. Technical report, WMO Tech. Doc. No. 980; Global Atmosphere Watch (GAW) Report No. 134, 1999.

A. A. Turnipseed, P. D. Blanken, D. E. Anderson, and R. K. Monson. Energy budget above a high-elevation subalpine forest in complex topography. Agric. For. Meteor., 110:177–201, 2002.

A. A. Turnipseed, D. E. Anderson, P. D. Blanken, W. M. Baugh, and R. K. Monson. Airflows and turbulent flux measurements in mountainous terrain. Part 1. Canopy and local effects. Agric. For. Meteor., 119:1–21, 2003.

A. A. Turnipseed, D. E. Anderson, S. Burns, P. D. Blanken, and R. K. Monson. Airflows and turbulent flux measurements in mountainous terrain. Part 2: mesoscale effects. Agric. For. Meteor., 125:187–205, 2004.

A. A. Turnipseed, S. P. Burns, D. J. P. Moore, J. Hu, A. B. Guenther, and R. K. Monson. Controls over ozone deposition to a high elevation subalpine forest. Agric. For. Meteor., 149:1447–1459, 2009. doi: 10.1016/j.agrformet.2009.04.001.

O. Uclés, L. Villagarcía, Y. Cantón, and F. Domingo. Microlysimeter station for long term non-rainfall water input and evaporation studies. Agric. For. Meteor., 182–183:13–20, 2013. doi: 10.1016/j.agrformet.2013.07.017.

B. Udall and J. Overpeck. The twenty-first century colorado river hot drought and implications for the future. Water Resources Research, 53:2404–2418, 2017.

A. M. Ukkola, N. Haughton, M. G. De Kauwe, G. Abramowitz, and A. J. Pitman. FluxnetLSM R package (v1.0): a community tool for processing FLUXNET data for use in land surface modelling. Geoscientific Model Development, 10:3379–3390, 2017. doi: 10.5194/gmd-10-3379-2017.

S. Unger, C. Maguas, J. S. Pereira, T. S. David, and C. Werner. The influence of precipitation pulses on soil respiration - assessing the "birch effect" by stable carbon isotopes. Soil Biology & Biochemistry, 42:1800–1810, 2010.

United States Forest Service. *Aeriel Photograph, BOW 21-71 (26 October 1938)*. 1:20000, 1938. [In collection: Aerial Photographs of Colorado, University of Colorado, Digital Library].

United States Forest Service. *Motor Vehicle Use Map, Boulder Ranger District, Roosevelt National Forest*. map., 2016.

A. I. J. M. van Dijk, J. H. Gash, E. van Gorsel, P. D. Blanken, A. Cescatti, C. Emmel, B. Gielen, I. N. Harman, G. Kiely, L. Merbold, L. Montagnani, E. Moors, M. Sottocornola, A. Varlagin, C. A. Williams, and G. Wohlfahrt. Rainfall interception and the coupled surface water and energy balance. Agric. For. Meteor., 214:402–415, 2015.

C. C. van Heerwaarden, J. Vilà-Guerau de Arellano, A. F. Moene, and A. A. M. Holtslag. Interactions between dry-air entrainment, surface evaporation and convective boundary-layer development. Quart. J. Roy. Meteor. Soc., 135:1277–1291, 2009. doi: 10.1002/qj.431.

C. C. van Heerwaarden, J. Vilà-Guerau de Arellano, A. Gounou, F. Guichard, and F. Couvreux. Understanding the daily cycle of evapotranspiration: a new method to quantify the influence of forcings and feedbacks. J. Hydrometeor., 11:1405–1422, 2010. doi: 10.1175/2010JHM1272.1.

M. van Leeuwen, T. Hilker, N. C. Coops, G. Frazer, M. A. Wulder, G. J. Newnham, and D. S. Culvenor. Assessment of standing wood and fiber quality using ground and airborne laser scanning: A review. Forest Ecology And Management, 261:1467–1478, 2011.

T. T. Veblen. Age and size structure of subalpine forests in the Colorado Front Range. Bull. Torrey Bot. Club, 113:225–240, 1986.

T. T. Veblen and D. C. Lorenz. The Colorado Front Range: A century of ecological change. University of Utah Press, 186 pp., 1991.

T. T. Veblen, K. S. Hadley, and M. S. Reid. Disturbance and stand development of a Colorado subalpine forest. J. Biogeogr., 18:707–716, 1991.

T. T. Veblen, K. S. Hadley, E. M. Nel, T. Kitzberger, M. Reid, and R. Villalba. Disturbance regime and disturbance interactions in a Rocky Mountain subalpine forest. J. Ecol., 82:125–135, 1994.

J. Vilà–Guerau de Arellano, C. C. van Heerwaarden, B. J. H. van Stratum, and K. van den Dries. Atmospheric Boundary Layer: Integrating Air Chemistry and Land Interactions. Cambridge University Press, New York, 265 pp., 2015.

R. Villalba, T. T. Veblen, and J. Ogden. Climatic influences on the growth of subalpine trees in the Colorado Front Range. Ecology, 75:1450–1462, 1994.

M. K. Vollmer, J. Mühle, C. M. Trudinger, M. Rigby, S. A. Montzka, C. M. Harth, and many others. Atmospheric histories and global emissions of halons H-1211 (CBrClF2), H-1301 (CBrF3), and H-2402 (CBrF2CBrF2). Journal of Geophysical Research: Atmospheres, 121:3663–3686, 2016. doi: 10.1002/2015JD024488.

L. Wallace, A. Lucieer, C. Watson, and D. Turner. Development of a UAV-LiDAR system with application to forest inventory. Remote Sensing, 4:1519–1543, 2012.

K. C. Wang and R. E. Dickinson. A review of global terrestrial evapotranspiration: observation, modeling, climatology, and climatic variability. Reviews Of Geophysics, 50, 2012.

K. C. Wang, R. E. Dickinson, and S. L. Liang. Observational evidence on the effects of clouds and aerosols on net ecosystem exchange and evapotranspiration. Geophysical Research Letters, 35: L10401, 2008. doi: 10.1029/2008GL034167.

L. Wang, S. P. Good, and K. K. Caylor. Global synthesis of vegetation control on evapotranspiration partitioning. Geophysical Research Letters, 41:6753–6757, 2014.

J. Waterman. Record drought reveals stunning changes along the Colorado River. National Geographic, 23 November, 2014. URL `https://news.nationalgeographic.com`. [Online; last access, March 2018].

E. K. Webb, G. I. Pearman, and R. Leuning. Correction of flux measurements for density effects due to heat and water-vapor transfer. Quarterly Journal Of The Royal Meteorological Society, 106:85–100, 1980.

M. N. Weintraub, L. E. Scott-Denton, S. K. Schmidt, and R. K. Monson. The effects of tree rhizodeposition on soil exoenzyme activity, dissolved organic carbon, and nutrient availability in a subalpine forest ecosystem. Oecologia, 154:327–338, 2007.

J. M. Welles and D. K. McDermitt. Measuring carbon dioxide in the atmosphere. In Micrometeorology in Agricultural Systems, pages 287–320. 2005. (Available at www.licor.com).

C. Werner, H. Schnyder, M. Cuntz, C. Keitel, M. J. Zeeman, T. E. Dawson, F. W. Badeck, E. Brugnoli, J. Ghashghaie, T. E. E. Grams, Z. E. Kayler, M. Lakatos, X. Lee, C. Maguas, J. Ogee, K. G. Rascher, R. T. W. Siegwolf, S. Unger, J. Welker, L. Wingate, and A. Gessler. Progress and challenges in using stable isotopes to trace plant carbon and water relations across scales. Biogeosciences, 9:3083–3111, 2012.

P. W. West. Tree and Forest Measurements. Springer-Verlag, Berlin, Germany, Second edition, 2009. 192 pp.

C. D. Whiteman. Mountain meteorology: fundamentals and applications. Oxford University Press, New York, 2000. 355 pp.

J. M. Wilczak, S. P. Oncley, and S. A. Stage. Sonic anemometer tilt correction algorithms. Bound.-Layer Meteor., 99:127–150, 2001.

D. G. Williams, W. Cable, K. Hultine, J. C. B. Hoedjes, E. A. Yepez, V. Simonneaux, S. Er-Raki, G. Boulet, H. A. R. de Bruin, A. Chehbouni, O. K. Hartogensis, and F. Timouk. Evapotranspiration components determined by stable isotope, sap flow and eddy covariance techniques. Agric. For. Meteor., 125:241–258, 2004.

M. Williams, A. D. Richardson, M. Reichstein, P. C. Stoy, P. Peylin, H. Verbeeck, N. Carvalhais, M. Jung, D. Y. Hollinger, J. Kattge, R. Leuning, Y. Luo, E. Tomelleri, C. M. Trudinger, and Y. P. Wang. Improving land surface models with FLUXNET data. Biogeosciences, 6:1341–1359, 2009.

M. W. Williams, M. Losleben, N. Caine, and D. Greenland. Changes in climate and hydrochemical responses in a high-elevation catchment in the Rocky Mountains, USA. Limnology And Oceanography, 41:939–946, 1996.

M. W. Williams, T. R. Seastedt, W. D. Bowman, D. M. McKnight, and K. N. Suding. An overview of research from a high elevation landscape: the Niwot Ridge, Colorado Long Term Ecological Research programme. Plant Ecology & Diversity, 8:597–605, 2015.

K. Wilson, A. Goldstein, E. Falge, M. Aubinet, D. Baldocchi, P. Berbigier, C. Bernhofer, R. Ceulemans, H. Dolman, C. Field, A. Grelle, A. Ibrom, B. E. Law, A. Kowalski, T. Meyers, J. Moncrieff, R. Monson, W. Oechel, J. Tenhunen, R. Valentini, and S. Verma. Energy balance closure at fluxnet sites. Agric. For. Meteor., 113:223–243, 2002.

K. B. Wilson, P. J. Hanson, P. J. Mulholland, D. D. Baldocchi, and S. D. Wullschleger. A comparison of methods for determining forest evapotranspiration and its components: sap-flow, soil water budget, eddy covariance and catchment water balance. Agric. For. Meteor., 106:153–168, 2001.

T. S. Winchell, D. M. Barnard, R. K. Monson, S. P. Burns, and N. P. Molotch. Earlier snowmelt reduces atmospheric carbon uptake in midlatitude subalpine forests. Geophysical Research Letters, 43:8160–8168, 2016. doi: 10.1002/2016GL069769.

P. G. Worcester. The geology of the Ward Region, Boulder County, Colorado. Technical Report *Bulletin 21*, Colorado Geological Survey, 74 pp., 1920.

K. Xu, S. Metzger, and A. R. Desai. Upscaling tower-observed turbulent exchange at fine spatio-temporal resolution using environmental response functions. Agric. For. Meteor., 232:10–22, 2017. doi: 10.1016/j.agrformet.2016.07.019.

L. Xu, D. D. Baldocchi, and J. W. Tang. How soil moisture, rain pulses, and growth alter the response of ecosystem respiration to temperature. Global Biogeochem. Cycle, 18:GB4002, 2004. doi: 10.1029/2004GB002281.

D. Yakir and L. daS. L. Sternberg. The use of stable isotopes to study ecosystem gas exchange. Oecologia, 123:297–311, 2000.

C. Yi, R. Z. Li, P. S. Bakwin, A. Desai, D. M. Ricciuto, S. P. Burns, A. A. Turnipseed, S. C. Wofsy, J. W. Munger, K. Wilson, and R. K. Monson. A nonparametric method for separating photosynthesis and respiration components in CO_2 flux measurements. Geophys. Res. Lett., 31: L17107, 2004. doi: 10.1029/2004GL020490.

C. Yi, R. K. Monson, Z. Q. Zhai, D. E. Anderson, B. Lamb, G. Allwine, A. A. Turnipseed, and S. P. Burns. Modeling and measuring the nocturnal drainage flow in a high-elevation, subalpine forest with complex terrain. J. Geophys. Res., 110:D22303, 2005. doi: 10.1029/2005JD006282.

C. Yi, D. E. Anderson, A. A. Turnipseed, S. P. Burns, J. P. Sparks, D. I. Stannard, and R. K. Monson. The contribution of advective fluxes to net ecosystem exchange in a high-elevation, subalpine forest. Ecol. Appl., 18:1379–1390, 2008. doi: 10.1890/06-0908.1.

R. T. Young. The forest formations of Boulder County, Colorado. Botanical Gazette, 44(5):321–352, 1907. URL `http://www.jstor.org/stable/2466600`.

D. Zardi and C. D. Whiteman. Diurnal mountain wind systems. In F. K. Chow, S. F. J. De Wekker, and B. J. Snyder, editors, Mountain Weather Research and Forecasting, Springer Atmospheric Sciences, Springer, Dordrecht, the Netherlands, pages 35–119. Springer Netherlands, 2013. doi: 10.1007/978-94-007-4098-3_2.

I. I. Zawadzki. Statistical properties of precipitation patterns. J. Appl. Meteor., 12:459–472, 1973.

X. Zeng, M. Zhao, and R. E. Dickinson. Intercomparison of bulk aerodynamic algorithms for the computation of sea surface fluxes using TOGA COARE and TAO data. Journal of Climate, 11: 2628–2644, 1998. doi: 10.1175/1520-0442(1998)011¡2628:IOBAAF¿2.0.CO;2.

X. Zeng, R. E. Dickinson, M. Barlage, Y. J. Dai, G. L. Wang, and K. Oleson. Treatment of undercanopy turbulence in land models. J. Clim., 18:5086–5094, 2005.

S. Zhang, X. Wen, J. Wang, G. Yu, and X. Sun. The use of stable isotopes to partition evapotranspiration fluxes into evaporation and transpiration. Acta Ecologica Sinica, 30:201 – 209, 2010. doi: 10.1016/j.chnaes.2010.06.003.

C. Zhao and P. P. Tans. Estimating uncertainty of the WMO mole fraction scale for carbon dioxide in air. J. Geophys. Res., 111:D08S09, 2006. doi: 10.1029/2005JD006003.

S. Zielinski. The Colorado River runs dry. Smithsonian Magazine, Ocotober, 2010. URL `http://www.smithsonianmag.com`. [Online; last access, March 2018].

J. M. Zobitz, J. P. Keener, H. Schnyder, and D. R. Bowling. Sensitivity analysis and quantification of uncertainty for isotopic mixing relationships in carbon cycle research. Agric. For. Meteor., 136:56–75, 2006.

J. M. Zobitz, S. P. Burns, M. Reichstein, and D. R. Bowling. Partitioning net ecosystem carbon exchange and the carbon isotopic disequilibrium in a subalpine forest. Glob. Change Biol., 14: 1785–1800, 2008. doi: 10.1111/j.1365-2486.2008.01609.x.

Appendix A

Site-specific adjustments to CLM4.5

For the US-NR1 plant type (temperate needleleaf evergreen forest), CLM assumes a canopy height h of 17 m. We found that fine-tuning the canopy and observation height (to better match the actual US-NR1 forest) resulted in slightly different results compared to using the default version of CLM4.5. To tune CLM4.5 for use with a specific flux site, the CLM4.5 FORTRAN program "CanopyTemperatureMod.F90" was modified in the following 2 ways:

(1) The US-NR1 canopy height of 13 m (*htop* in CLM4.5 source code) was specified and added to the following DO LOOP of CanopyTemperatureMod.F90. This replaces the default value (17 m), which is based on the vegetation type:

```
do fp = 1,num_nolakep
   p = filter_nolakep(fp)
      !scs: from burns et al 15
      htop(p) = 13.0_r8
      !scs
      z0m(p)    = z0mr(patch%itype(p)) * htop(p)
      displa(p) = displar(patch%itype(p)) * htop(p)
end do
```

(2) The following lines,

```
if (frac_veg_nosno(p) == 0) then
   forc_hgt_u_patch(p) = forc_hgt_u(g) + z0mg(c) + displa(p)
```

```
            forc_hgt_t_patch(p) = forc_hgt_t(g) + z0mg(c) + displa(p)
            forc_hgt_q_patch(p) = forc_hgt_q(g) + z0mg(c) + displa(p)
         else
            forc_hgt_u_patch(p) = forc_hgt_u(g) + z0m(p) + displa(p)
            forc_hgt_t_patch(p) = forc_hgt_t(g) + z0m(p) + displa(p)
            forc_hgt_q_patch(p) = forc_hgt_q(g) + z0m(p) + displa(p)
         end if
```

are modified so that the forcing height is not adjusted by the displacement and roughness heights. For US-NR1, the observational height is 21.5 m so these lines become:

```
!scs: don't adjust forcing height
         if (frac_veg_nosno(p) == 0) then
            forc_hgt_u_patch(p) = max(forc_hgt_u(g),21.5)
            forc_hgt_t_patch(p) = max(forc_hgt_t(g),21.5)
            forc_hgt_q_patch(p) = max(forc_hgt_q(g),21.5)
         else
            forc_hgt_u_patch(p) = max(forc_hgt_u(g),21.5)
            forc_hgt_t_patch(p) = max(forc_hgt_t(g),21.5)
            forc_hgt_q_patch(p) = max(forc_hgt_q(g),21.5)
         end if
!scs
```

Our modified version of CanopyTemperatureMod.F90 (along with all other modified programs) are included in a ZIP file as described in Appendix C. The modified version of CanopyTemperatureMod.F90 should be placed in the "SourceMods/src.clm/" subdirectory for any particular case where it is to be used.

The effect of varying the canopy height and specifying the observation height of the fluxes and CLM temperatures is shown in Fig. A1. Here, the CLM4.5 A1 settings are those described in Table 6.1. CLM4.5 with the "A0" settings uses the default values of a canopy height of 17 m and an observational height that has been adjusted using the momentum roughness and displacement

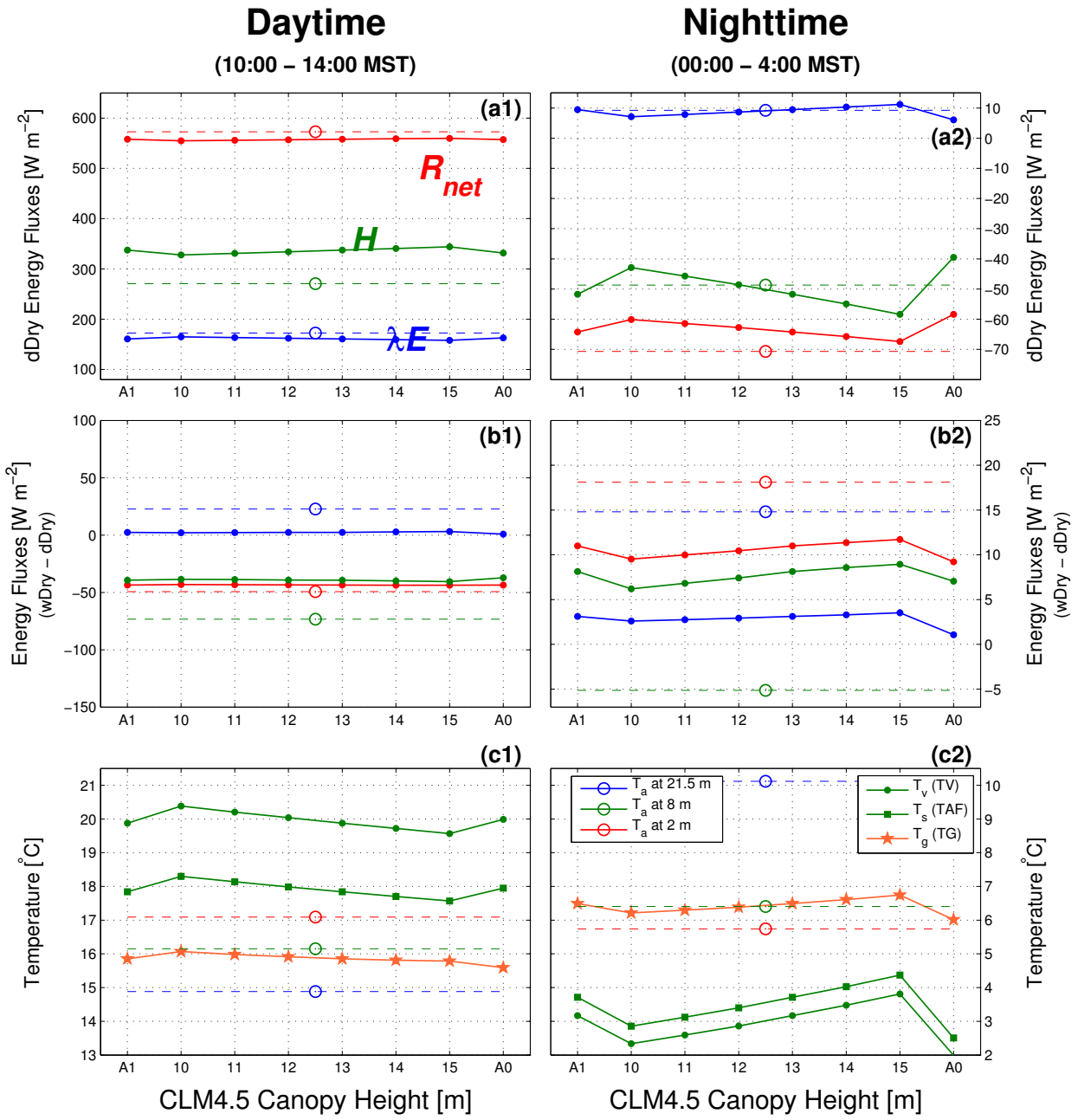

Figure A1: The **(a1, b1)** daytime and **(a2, b2)** nighttime energy fluxes versus changes to the CLM4.5 canopy height h which has a default value of 17 m. The upper panels show the mean values for dDry conditions and the middle panels show the mean differences between wDry and dDry conditions where the variables shown are: net radiation $R_{\rm net}$ (red), sensible heat flux H (green), and latent heat flux λE (blue). The solid lines with filled symbols are the CLM4.5 output, while the horizontal dashed lines are the US-NR1 observations with an open circle placed at $h = 12.5$ m. In **(c1, c2)**, the US-NR1 observed air temperature T_a and the effect of varying h on CLM canopy surface T_v, canopy air T_s and ground T_g temperatures are shown (see legends). The A1 column uses the default CLM4.5 settings (see Table 6.1), whereas the A0 column (on the far-right side) uses the default version of CanopyTemperatureMod.F90, as described in Appendix A.

height, as described in (2) above. In general, the nocturnal data were more affected than the daytime data by changes to the canopy height, with the changes to nocturnal fluxes on the order of 10-15% (Fig. A1a2) and the temperatures changed by around 2 °C (Fig. A1c2). One of the primary reasons for these changes is that the nocturnal values of friction velocity were increased by around $0.1\,\mathrm{m\,s^{-1}}$ after fine-tuning the CLM forest properties for US-NR1.

Appendix B

Nomenclature

Table B1 contains the nomenclature, units, and variable descriptions used within Chapter 6 of this thesis. It also includes a list of some of the variables measured at US-NR1. In some cases, these measured variables are used as input to CLM, as noted in the right column of Table B1.

Table B1: A list of variables in CLM4.5 and nomenclature related to Chapter 6 in this thesis. Where appropriate, equation numbers from the CLM4.5 manual [Oleson et al., 2013] are listed. If the variable is measured at the US-NR1 site, then "Measured" is included within this same column. Mean values are shown with an overbar ($\overline{x}$) and turbulent fluctuations from a mean are indicated by a prime (x'); if neither are shown a total or mean value should be assumed.

Variable Name	CLM4.5 Manual Equation Number	units	Description and/or Equation
Roman symbols:			
C_s	Eq. 5.115	dimensionless	Turbulent transfer coefficient between ground and canopy air space
$C_{s,dense}$	Eq. 5.115	dimensionless	Turbulent transfer coefficient between ground and canopy air space for a dense canopy
d	Eq. 5.127	m	Displacement height, prescribed in CLM based on surface type
H	Measured, Eqs. 5.83–5.95	$\mathrm{W\,m^{-2}}$	Above-canopy vertical sensible heat flux
L	Eq. 5.16	m	Obukhov length, $L = -(u_*^3\,\overline{\theta})\ /\ (\kappa g\,\overline{w'\theta'})$
LAI		$\mathrm{m^2\,m^{-2}}$	Projected leaf area index, prescribed in CLM based on surface type and satellite data
P	Measured	kPa	Barometric pressure (supplied as an input variable to CLM4.5)
R_{net}	Measured, Eqs. 4.4, 4.17	$\mathrm{W\,m^{-2}}$	Above-canopy net irradiance (incoming shortware and longwave irradiance are supplied as input variables to CLM4.5)
RH	Measured	%	Above-canopy relative humidity (supplied as an input variable to CLM4.5)
${r_{ah}}'$	Eq. 5.113	$\mathrm{s\,m^{-1}}$	Aerodynamic resistance for heat exchange between between ground and canopy
${r_{aw}}'$	Eq. 5.113	$\mathrm{s\,m^{-1}}$	Aerodynamic resistance for water vapor exchange between between ground and canopy (${r_{ah}}' = {r_{aw}}'$)
T_{tc}	Measured	°C	Thermocouple temperature (at US-NR1, measured at 11 levels)
T_a	Measured	K or °C	Air temperature (measured at US-NR1; the above-canopy air temperature (TBOT) is used as an input variable to CLM4.5)
T_g	Eqs. 6.29–6.32	K or °C	Ground surface temperature
T_{2m}	Eq. 5.58	K or °C	Air temperature at 2 m above the apparent sink for sensible heat ($z_{0h} + d$)
T_s	Eq. 5.90	K or °C	Surface temperature (at height ($z_{0h} + d$)), or canopy air temperature
T_{soil}	Measured, Eq. 6.12	K or °C	Soil temperature (measured at −5 cm at US-NR1; in CLM4.5, calculated at 15 depths below the surface)
T_v		K or °C	Vegetation temperature
q	Measured	$\mathrm{g\,kg^{-1}}$	Atmospheric specific humidity (at US-NR1, measured at 21.5 m)
q_*	Eq. 5.15	$\mathrm{g\,kg^{-1}}$	Humidity scale
u_*	Measured, Eqs. 5.32–5.35	$\mathrm{m\,s^{-1}}$	Above-canopy friction velocity, $u_* = ((\overline{u'w'})^2 + (\overline{v'w'})^2)^{0.25}$
U_{av}	Eq. 5.114	$\mathrm{m\,s^{-1}}$	Velocity of air within foliage ($U_{av} = u_*$)
U	Measured,	$\mathrm{m\,s^{-1}}$	Horizontal wind velocity (at US-NR1, measured at 3 heights (21.5 m, 5.7 m, 2.5 m); above-canopy (21.5 m) U is an input variable to CLM4.5)
u, v, w	Measured	$\mathrm{m\,s^{-1}}$	streamwise, crosswise, and vertical planar-fit wind components (at US-NR1, measured at 3 heights: 21.5 m, 5.7 m, 2.5 m)
VPD	Measured	kPa	Vapor pressure deficit
z		m	Height above the ground
z_{0m}	Eq. 5.126	m	Roughness length for momementum
Greek symbols:			
κ		dimensionless	von Kármán constant; in CLM4.5 $\kappa = 0.4$
λ	Table 2.6	$\mathrm{kJ\,kg^{-1}}$	Latent heat of vaporization of water vapor; for US-NR1, λ was calculated with $\lambda = 1000000\,(2.501 - 0.00237\,T_a)$ which is for liquid water, with T_a in °C

Table B1: Continued.

Variable Name	CLM4.5 Manual Equation Number	units	Description and/or Equation
λE	Measured, Eqs. 5.96, 5.97	$\mathrm{W\,m^{-2}}$	Above-canopy vertical latent heat flux ($\lambda E = \lambda E_v^t + \lambda E_v^w + \lambda E_g$)
λE_v^t	Eq. 5.135	$\mathrm{W\,m^{-2}}$	Canopy transpiration
λE_v^w	Eq. 5.111	$\mathrm{W\,m^{-2}}$	Canopy evaporation
λE_g	Eq. 5.112	$\mathrm{W\,m^{-2}}$	Ground evaporation
ϕ_m, ϕ_h, ϕ_w	Eqs. 5.30–5.31	dimensionless	Universal functions for momentum, heat, and moisture (see Table 6.3)
ψ_m, ψ_h, ψ_w	Eqs. 5.36–5.45	dimensionless	Integral of the universal function for momentum, heat, and moisture (see Table 6.3)
θ		K or °C	Potential temperature
θ_*	Eq. 5.14	K or °C	Temperature scale
ζ	Measured, Eqs. 5.48–5.49	dimensionless	Above-canopy stability parameter ($\zeta = (z-d)/L$)

Appendix C

Soil report from CSU

In 2011, Nicole Trahan and Ben Braydon collected soil samples from between the US-NR1 tower and Como Creek and had them analyzed by the Soil, Water and Plant Testing Laboratory at Colorado State University. They collected soil from both the organic and mineral layer which had the following texture properties: organic soil (sand 62 %, silt 25 %, clay 13 %) so it is a sandy loam; mineral soil (sand 73.5 % silt 26.42 %, clay 0.08 %) so it is a loamy sand.). The full report is shown below in Fig. C1.

Ben Brayden/University of Colorado-Boulder
Campus Box: 260 UCB GUGG 110
Boulder CO 80304

DATE RECEIVED: 02-24-2012
DATE REPORTED: 03-08-2012

Colorado State University
Soil, Water and Plant Testing Laboratory
Natural & Environmental Sciences Bldg - A319
Fort Collins, CO 80523-1120

(970) 491-5061 FAX: 491-2930

BILLING: **CC05073**

RESEARCH SOIL ANALYSIS

Lab #	Sample ID #	paste pH	paste EC mmhos/cm	Lime Estimate	% OM	AB-DTPA Extract ppm NO_3-N	P	K	Zn	Fe	Mn	Cu	Texture Estimate
R4231	BHB1 O	4.7	0.2	Low	22.8	1.0	4.0	220	11.9	215	125	2.54	Loam
R4232	BHB1 M	4.7	0.3	Low	3.2	0.5	10.0	125	1.75	221	27.1	1.20	Sandy Clay Loam
R4233	BHB2 O	4.3	0.4	Low	36.9	1.3	12.3	300	8.59	300	142	2.33	Loam
R4234	BHB2 M	4.4	0.3	Low	4.8	0.5	7.2	106	0.81	333	22.3	1.66	Sandy Loam
R4235	BHB3 O	4.8	0.3	Low	28.8	0.9	16.8	334	6.47	268	119	4.24	Loam
R4236	BHB3 M	4.8	0.3	Low	2.9	0.2	6.8	66.8	0.42	120	9.17	1.01	Sandy Clay Loam
R4237	BHB4 O	4.7	0.3	Low	42.6	1.7	24.0	522	12.9	303	221	4.28	Loam
R4238	BHB4 M	4.7	0.3	Low	2.8	0.4	4.0	138	0.47	253	20.3	1.28	Sandy Loam
R4239	BHB5 O	4.7	0.2	Low	40.6	1.4	25.8	519	11.2	278	237	4.32	Loam
R4240	BHB5 M	4.9	0.2	Low	3.1	0.4	10.2	150	0.60	248	31.0	1.51	Sandy Loam
R4241	BHB6 O	4.7	0.2	Low	24.6	1.6	11.6	262	9.73	243	75.7	2.48	Loam
R4242	BHB6 M	5.0	0.1	Low	3.9	0.4	10.4	158	1.70	211	18.1	1.28	Sandy Clay Loam
R4243	BHB7 O	5.0	0.1	Low	17.3	0.8	7.2	196	9.60	198	37.5	1.42	Loam
R4244	BHB7 M	5.0	0.1	Low	2.6	0.3	6.4	93.8	0.92	179	6.01	0.56	Sandy Loam
R4245	BHB8 O	5.1	0.2	Low	32.0	1.3	12.6	293	9.90	279	110	3.90	Loam
R4246	BHB8 M	5.0	0.1	Low	3.8	0.4	9.2	120	1.17	231	13.6	0.85	Sandy Clay Loam
R4247	BHB9 O	4.8	0.2	Low	24.6	1.4	12.0	275	9.35	291	70.4	5.30	Loam
R4248	BHB9 M	4.7	0.1	Low	2.1	0.5	10.2	114	0.79	297	7.79	2.08	Sandy Loam
R4249	BHB10 O	4.9	0.2	Low	11.0	0.5	6.2	194	3.53	156	33.2	2.74	Loam
R4250	BHB10 M	4.9	0.2	Low	3.3	0.3	4.2	106	0.69	195	8.19	1.77	Sandy Loam
R4251	BHB11 O	4.3	0.2	Low	38.3	3.3	36.0	337	9.83	255	183	4.75	Loam
R4252	BHB11 M	4.1	0.2	Low	2.5	0.5	28.4	78.3	0.67	299	14.8	1.80	Sandy Clay Loam

Ben Brayden/University of Colorado-Boulder
Campus Box: 260 UCB GUGG 110
Boulder CO 80304

DATE RECEIVED: 02-24-2012
DATE REPORTED: 03-08-2012

Colorado State University
Soil, Water and Plant Testing Laboratory
Natural & Environmental Sciences Bldg - A319
Fort Collins, CO 80523-1120

(970) 491-5061 FAX: 491-2930

BILLING: **CC05073**

RESEARCH SOIL ANALYSIS

Lab #	Sample ID #	paste pH	paste EC mmhos/cm	Lime Estimate	% OM	AB-DTPA Extract ppm NO_3-N	P	K	Zn	Fe	Mn	Cu	Texture Estimate
R4253	BHB12 O	4.3	0.2	Low	28.2	1.3	21.0	287	9.70	227	141	4.50	Loam
R4254	BHB12 M	4.7	0.1	Low	3.8	0.4	8.0	115	1.19	236	24.5	0.83	Sandy Loam
R4255	BHB13 O	4.6	0.2	Low	40.3	2.9	17.6	468	12.7	299	177	4.91	Loam
R4256	BHB13 M	4.6	0.2	Low	3.4	0.6	14.6	133	0.90	287	19.9	2.58	Sandy Clay Loam
R4257	BHB14 O	4.8	0.2	Low	24.8	4.2	0.6	294	14.4	195	133	5.45	Loam
R4258	BHB14 M	4.3	0.2	Low	3.0	1.2	40.0	106	1.50	449	25.0	2.25	Sandy Loam
R4259	BHB15 O	4.9	0.2	Low	36.0	3.1	30.3	401	16.7	206	149	3.16	Loam
R4260	BHB15 M	4.7	0.2	Low	2.6	0.6	22.4	120	1.10	181	14.6	0.69	Sandy Loam
R4261	BHB16 O	4.9	0.2	Low	30.3	1.1	19.8	340	9.74	248	95.5	6.47	Loam
R4262	BHB16 M	4.8	0.2	Low	2.2	0.3	13.2	109	0.42	151	5.14	0.68	Sandy Clay Loam
R4263	BHB17 O	4.7	0.2	Low	22.8	1.1	11.2	192	5.69	175	90.7	2.06	Loam
R4264	BHB17 M	4.4	0.1	Low	2.3	0.5	8.4	85	0.54	234	14.0	0.89	Sandy Loam
R4265	BHB18 O	5.1	0.2	Low	33.0	1.2	19.8	356	3.90	296	119	2.73	Loam
R4266	BHB18 M	5.2	0.1	Low	4.0	0.4	3.2	116	0.35	142	12.9	1.47	Sandy Clay Loam
R4267	BHB19 O	4.4	0.2	Low	30.2	1.3	18.6	252	5.77	233	113	3.22	Loam
R4268	BHB19 M	4.6	0.1	Low	3.1	0.4	5.0	121	0.50	208	8.65	1.06	Sandy Loam
R4269	BHB20 O	4.7	0.3	Low	29.1	1.1	11.6	177	7.02	198	69.4	3.27	Loam
R4270	BHB20 M	4.7	0.2	Low	3.4	0.6	13.2	126	1.03	253	15.9	1.16	Sandy Loam

Figure C1: Soil report on US-NR1 soil samples from Colorado State University.

Appendix D

People from Niwot Ridge

Over the many years that the US-NR1 data used in this thesis have been collected, I have had the good fortune to collaborate and interact with many different researchers. As everyone that works at the site knows, I have taken many photos during my trips there (around 15,000 photos and counting). Here, I acknowledge some of the people I have met on this journey in the attached photo gallery. Additional photos from the site are available on-line at http://urquell.colorado.edu/calendar/. While these photos do not represent all of the collaborators I have had, it does cover many of them. May the spirt of the forest be with you all!

Figure D1: Photos of people that I worked with during my time at the Niwot Ridge AmeriFlux site.

Figure D1: Cont'd.

Figure D1: Cont'd.

Appendix E

Niwot Ridge Subalpine Forest US-NR1 AmeriFlux data details

A few additional details about the data collected at the US-NR1 AmeriFlux site and used in this thesis are included here. Much of this information is available on the urquell website,

http://urquell.colorado.edu/data_ameriflux/

however, it is unknown how long this website will be available so it is our hope that providing a snapshot of the information here will be useful. In addition to the AmeriFlux website (http://ameriflux.lbl.gov/), details about the site and data documentation, archived logbook files, and the CLM software can be found in Burns et al. [2016b] and Burns et al. [2018]. More information about the measurements is also in Chapter 3.

The next several pages provide details about the version of the US-NR1 30-min processed data files used in this thesis (ver.2015.11.10), and includes a listing of the header of the climate, flux, and soil data files which describes the data within each 30-min data file, data issues, and some of the data processing details.

To: <ameriflux@lbl.gov>, <bodenta@ornl.gov>, <yangb@ornl.gov>, Dario Papale <darpap@unitus.it>, Deb Agarwal <daagarwal@lbl.gov>, Gilberto Pastorello <gzpastorello@lbl.gov>, Carlo Trotta <trottacarlo@unitus.it>, "Eleonora Canfora" <e.canfora@unitus.it>, Housen Chu <hchu@berkeley.edu>, "Diego Polidori" <diego.p@unitus.it>
From: Sean Burns <sean.burns@Colorado.EDU>
CC: <sean.burns@colorado.edu>, Peter Blanken <blanken@colorado.edu>, <Russell.Monson@colorado.edu>
Subject: Updated US-NR1 ameriflux data...
Date: Tue, 10 Nov 2015 12:43:49 -0700

Hi All,

We have updated the US-NR1 AmeriFlux data (including adding year 2014)...Bai, I just uploaded these data (as a zip file) to the AmeriFlux website and was told the data will reach you that way. The website says "your upload was successful", but I'm not sure the zip file was actually uploaded or not?, ie:

http://urquell.colorado.edu/sean/ameriflux_upload.png

it shows a green check mark near the description, but there isn't any green check mark near the actual data file...Deb (or someone), can you confirm the zip file was uploaded...

I have also posted the data files to our data webpage which is:

http://urquell.colorado.edu/data_ameriflux/

All the updated data files (listed at the end of this email) can be downloaded as a single zip file from:

http://urquell.colorado.edu/data_ameriflux/data_30min/ameriflux_data_ver.2015.11.10.zip

For this release, we did not re-calculate any fluxes from the hi-rate data. The primary objective was to clean-up/correct some descrepancies between years (that many of you have noticed). At the end of this email, I will include a header from the data files that more fully describes the changes/updates we made.

I am happy to discuss any of these changes in more detail or provide more information. Also, if you see problems with the data please let me know because I am limited in how much I can check things and I'm sure that I have missed somethings. . .any feedback you give me is extremely helpful...At some point, we will be making a major change to the data-output file-format to be more consistent with the standard ameriflux file structure.

As usual, much more information about the data can be found here:

http://urquell.colorado.edu/data_ameriflux/docs/

and, if you have a question about a specific date, please refer to the on-line site calendar, ie:

http://urquell.colorado.edu/calendar/

If you want to scan an entire year, this can be done with, for example
using year 2013 (or pick the year of interest),

  http://urquell.colorado.edu/calendar/2013.html

Finally, if you no longer want to receive these emails, please let me
know so I can remove you from the list...

cheers,

SpB.

Sean Burns
Department of Geography
Campus Box 260
University of Colorado
Boulder, CO 80309-0260

for FEDex: Guggenheim 110

Internet: sean.burns@colorado.edu
http://www2.mmm.ucar.edu/people/burns/
Phone: (303) 497-8934   Fax: (303) 492-8699

Example File Header:

```
%  -- Niwot Ridge Subalpine Forest AmeriFlux Data (site ID:  US-NR1) --
% MST Time Period: 2008  01/01 00:00:00 - 2009  01/01 00:00:00, JD 1.000-367.000 (MST)
% UTC Time Period: 2008  01/01 07:00:00 - 2009  01/01 07:00:00, JD 1.292-367.292 (UTC)
% File Name: flux_2008_ver.2015.11.10.dat
% File Created by: Sean Burns (sean.burns@colorado.edu)
% File Created for: CU Ameriflux Web Site (http://urquell.colorado.edu/data_ameriflux/)
% Date: 10-Nov-2015
% --------
%
%  Data Version: ver.2015.11.10
%
%
%    NOTES:
%
%
%  Info about ver.2015.11.10:
%
%    * Unless noted otherwise, all information listed below for recent
%      versions also applies to the current version.
%
%    * ver.2015.11.10 includes data from 2014
%
%    * Changes to data in ver.2015.11.10 were applied to data from all
%      years (1998-2014).  No turbulent fluxes were re-calculated.
%
%    * Rsw_out CNR1 data prior to 2005 have been corrected using a correction
%      factor of 0.6 (ie, s_Rsw_out_25m_KZ = 0.6*s_Rsw_out_25m_KZ_raw)
%
%      We chose to correct the older CNR1 data based on two inter-comparisons
%      with the AmeriFlux QA/QC team (Cristoph Thomas in 2006 and Stephen
```

```
%      Chan/Sebastien Biraud in 2013) that showed the recent CNR1 data to be
%      fairly close to the reference CNR1 they used.
%
%    * in climate_2013_ver.2015.01.28.dat, the barometric pressure had an
%      incorrect offset applied (this has now been fixed)
%
%    * QA/QC cut-off limits have been adjusted/changed for:
%
%         Qe_21m:  Latent Heat Flux
%        Qh_soil:  Soil Heat Flux
%        Strg_Qh:  Sensible Heat Storage
%    Strg_needle:  Needle Heat Storage
%
%    * Erroneous night-time Rppfd_in_25m from 1999-2002 have been fixed
%
%    * Ensured VPD is calculated with 8-m TRH sensor
%
%    * replaced the binary wet_b data with leaf_wet_scaled which is an
%      average leaf wetness between 0 (dry) and 1 (wet) where values between
%      0 and 1 are considered partially-wet
%
%    * Ensured that T_bole is from a consistent sensor depth, this is:
%
%                 Fir = 2 cm into bole
%                Pine = 3 cm into bole
%              Spruce = 2 cm into bole
%
%    * re-calculated Strg_bole:  this is now done using only the pine
%      trees.  It is important to note that due to equipment failures
%      different trees are sampled for different periods.  The trees
%      sampled are:
%
%           1 Jan 2004 - 17 July 2006:  pine2 and pine3
%          24 Oct 2006 - 31 Dec 2010:  pine2, pine3, pine11, pine16
%           1 Jan 2011 - 21 Sep 2015:  pine11, pine16
%
%    * a future data release will include the individual bole temperature
%      measurements
%
%    * For 2011 on-ward, added a new column to the flux data file which is:
%
%      Qh_Ttc_21m :  Sensible Heat Flux using a co-located Thermocouple
%
%      For more details see Burns, et al (2012) "Using sonic anemometer
%      temperature to measure sensible heat flux in strong winds", Atmos.
%      Measurement Techniques
%
%  Info about ver.2015.01.30: ----------------------------------------------
%
%    * Bai Yang noticed two issues with ver.2014.12.02 which are corrected
%      for in ver.2015.01.28:
%
%        - the picarro Deuterium data (dD_picarro) were the delta-O-18
%          (d180_picarro) data (this was due to a typo in my code).
%
%        - there were some anomolous Rnet (REBS) data at night.  These were
%          removed and gap-filled with Rnet from the KZ CNR1 sensor
%
%    * even though both these issues were with the climate data files, I
%      re-created both the flux and climate files so they have a consistent
```

```
%      file name.
%
%  Info about ver.2014.12.02 (notes below also apply to current version):
%
%    * to remove spikes in flux data, applied a very light 5-point median
%      filter to Fco2_21m_nee_*, Qe_21m, Qh_21m
%
%    * It is recommended that an empirical correction (of around 0.25C) be
%      applied to the Ta_8m data.  The correction has NOT been applied,
%      but one possible form could be:
%
%               Ta = Ta_raw + T_corr,  where T_corr=0.25 degC
%
%      - The correction was determined based on (1) temperature comparisons
%        with the oregon state prt in Sept 2005, (2) comparisons with
%        unaspirated thermocouples, (3) comparisons with other temperature
%        measurements at high WS.
%
%     * a krypton hygrometer is used as the primary latent heat flux (Qe)
%       instrument; however when the krypton data are missing, an "enhanced"
%       Qe from the closed-path LI-6262 are used.  The enhancement factor
%       takes into account Qe information lost in the tubing.
%
%     * the tipping bucket Met One precipitation data measured at the
%       AmeriFlux tower should not be used after 2011.  Starting in 2011, we
%       have replaced the precip data with those from the USCRN Boulder W14
%       site (http://www.ncdc.noaa.gov/crn/) which is less than 1km from the
%       AmeriFlux tower.   It should also be noted that the Met One gauge is
%       unshielded, so winter-time precipitation will have a large undercatch
%       due to snow blowing past the entrance/opening of the gauge.
%
%    * an empirical correction (of the form T_corr = A*T_raw + B) has been
%       applied to the 107L raw soil temperature data. The correction
%       was determined at the NCAR Calibration Lab (EOL) and the result is to
%       decrease the raw soil temperature by approx 0.2-0.5 degC.
%
%    * the mean co2 data were measured with a tunable diode laser (TDL)
%       using an inlet at 21.5m on the CU tower.  These data are supplied
%       courtesy of Dave Bowling (david.bowling@utah.edu).  To obtain
%       more information about these data, and to get mean co2 and stable
%       isotope (del13c) data from other levels on the tower, please visit
%       the webpage:
%
%        http://www.biology.utah.edu/bowling/
%
%    * From Nov 2011-present, a vertical profile (8 levels) of water vapor
%      isotopes was measured with a Picarro l2120-i gas analyzer.  Water
%      vapor dry mole fraction and the isotopic ratio (d18O and dD, reported
%      relative to VSMOW) from the 24.3m inlet are provided here.  The
%      calibration and sampling protocol closely follows that described in
%      Berkelhammer et al., (2013), "The nocturnal water cycle in an open
%      canopy", Journal of Geophysical Research. These data are supplied
%      courtesy of David Noone (dcn@coas.oregonstate.edu) and Max Berkelhammer
%      (berkelha@uic.edu).  To get more information about these data and
%      to obtain the data from other tower levels, please contact David
%      or Max directly.  When these data are unavailable, the column is set
%      to NaN.
%
%
%    * For other specific details please see:
```

```
%
%        http://urquell.colorado.edu/calendar/
%
%        http://urquell.colorado.edu/data_ameriflux/docs/
%

List of Updated Files:
----------------------
-rw-r--r-- 1 sburns aster 1030105 Nov 10 11:34 climate_1998_ver.2015.11.10.dat
-rw-r--r-- 1 sburns aster 6078949 Nov 10 11:35 climate_1999_ver.2015.11.10.dat
-rw-r--r-- 1 sburns aster 6095560 Nov 10 11:38 climate_2000_ver.2015.11.10.dat
-rw-r--r-- 1 sburns aster 6078952 Nov 10 11:40 climate_2001_ver.2015.11.10.dat
-rw-r--r-- 1 sburns aster 6078948 Nov 10 11:43 climate_2002_ver.2015.11.10.dat
-rw-r--r-- 1 sburns aster 6078950 Nov 10 11:45 climate_2003_ver.2015.11.10.dat
-rw-r--r-- 1 sburns aster 6095553 Nov 10 11:48 climate_2004_ver.2015.11.10.dat
-rw-r--r-- 1 sburns aster 6078942 Nov 10 11:50 climate_2005_ver.2015.11.10.dat
-rw-r--r-- 1 sburns aster 6078956 Nov 10 11:53 climate_2006_ver.2015.11.10.dat
-rw-r--r-- 1 sburns aster 6078956 Nov 10 11:55 climate_2007_ver.2015.11.10.dat
-rw-r--r-- 1 sburns aster 6095571 Nov 10 11:58 climate_2008_ver.2015.11.10.dat
-rw-r--r-- 1 sburns aster 6078966 Nov 10 12:00 climate_2009_ver.2015.11.10.dat
-rw-r--r-- 1 sburns aster 6078963 Nov 10 12:03 climate_2010_ver.2015.11.10.dat
-rw-r--r-- 1 sburns aster 6078974 Nov 10 12:05 climate_2011_ver.2015.11.10.dat
-rw-r--r-- 1 sburns aster 6095578 Nov 10 12:09 climate_2012_ver.2015.11.10.dat
-rw-r--r-- 1 sburns aster 6078970 Nov 10 12:12 climate_2013_ver.2015.11.10.dat
-rw-r--r-- 1 sburns aster 6078965 Nov 10 12:15 climate_2014_ver.2015.11.10.dat

-rw-r--r-- 1 sburns aster  486717 Nov 10 11:34 climate_flags_1998_ver.2015.11.10.dat
-rw-r--r-- 1 sburns aster 2836049 Nov 10 11:36 climate_flags_1999_ver.2015.11.10.dat
-rw-r--r-- 1 sburns aster 2843778 Nov 10 11:39 climate_flags_2000_ver.2015.11.10.dat
-rw-r--r-- 1 sburns aster 2836050 Nov 10 11:41 climate_flags_2001_ver.2015.11.10.dat
-rw-r--r-- 1 sburns aster 2836050 Nov 10 11:44 climate_flags_2002_ver.2015.11.10.dat
-rw-r--r-- 1 sburns aster 2836050 Nov 10 11:46 climate_flags_2003_ver.2015.11.10.dat
-rw-r--r-- 1 sburns aster 2843778 Nov 10 11:49 climate_flags_2004_ver.2015.11.10.dat
-rw-r--r-- 1 sburns aster 2836049 Nov 10 11:51 climate_flags_2005_ver.2015.11.10.dat
-rw-r--r-- 1 sburns aster 2836050 Nov 10 11:54 climate_flags_2006_ver.2015.11.10.dat
-rw-r--r-- 1 sburns aster 2836049 Nov 10 11:56 climate_flags_2007_ver.2015.11.10.dat
-rw-r--r-- 1 sburns aster 2843777 Nov 10 11:58 climate_flags_2008_ver.2015.11.10.dat
-rw-r--r-- 1 sburns aster 2836049 Nov 10 12:01 climate_flags_2009_ver.2015.11.10.dat
-rw-r--r-- 1 sburns aster 2836050 Nov 10 12:03 climate_flags_2010_ver.2015.11.10.dat
-rw-r--r-- 1 sburns aster 2836048 Nov 10 12:06 climate_flags_2011_ver.2015.11.10.dat
-rw-r--r-- 1 sburns aster 2843776 Nov 10 12:09 climate_flags_2012_ver.2015.11.10.dat
-rw-r--r-- 1 sburns aster 2836050 Nov 10 12:13 climate_flags_2013_ver.2015.11.10.dat
-rw-r--r-- 1 sburns aster 2836050 Nov 10 12:16 climate_flags_2014_ver.2015.11.10.dat

-rw-r--r-- 1 sburns aster  529798 Nov 10 11:34 flux_1998_ver.2015.11.10.dat
-rw-r--r-- 1 sburns aster 3097990 Nov 10 11:37 flux_1999_ver.2015.11.10.dat
-rw-r--r-- 1 sburns aster 3106443 Nov 10 11:39 flux_2000_ver.2015.11.10.dat
-rw-r--r-- 1 sburns aster 3097992 Nov 10 11:42 flux_2001_ver.2015.11.10.dat
-rw-r--r-- 1 sburns aster 3097995 Nov 10 11:44 flux_2002_ver.2015.11.10.dat
-rw-r--r-- 1 sburns aster 3097995 Nov 10 11:47 flux_2003_ver.2015.11.10.dat
-rw-r--r-- 1 sburns aster 3106447 Nov 10 11:49 flux_2004_ver.2015.11.10.dat
-rw-r--r-- 1 sburns aster 3097996 Nov 10 11:52 flux_2005_ver.2015.11.10.dat
-rw-r--r-- 1 sburns aster 3097998 Nov 10 11:54 flux_2006_ver.2015.11.10.dat
-rw-r--r-- 1 sburns aster 3097997 Nov 10 11:56 flux_2007_ver.2015.11.10.dat
-rw-r--r-- 1 sburns aster 3106448 Nov 10 11:59 flux_2008_ver.2015.11.10.dat
-rw-r--r-- 1 sburns aster 3098003 Nov 10 12:01 flux_2009_ver.2015.11.10.dat
-rw-r--r-- 1 sburns aster 3097992 Nov 10 12:04 flux_2010_ver.2015.11.10.dat
-rw-r--r-- 1 sburns aster 3097994 Nov 10 12:07 flux_2011_ver.2015.11.10.dat
-rw-r--r-- 1 sburns aster 3106444 Nov 10 12:10 flux_2012_ver.2015.11.10.dat
-rw-r--r-- 1 sburns aster 3097988 Nov 10 12:13 flux_2013_ver.2015.11.10.dat
```

```
-rw-r--r-- 1 sburns aster 3097999 Nov 10 12:16 flux_2014_ver.2015.11.10.dat

-rw-r--r-- 1 sburns aster  339474 Nov 10 11:35 flux_flags_1998_ver.2015.11.10.dat
-rw-r--r-- 1 sburns aster 1959191 Nov 10 11:37 flux_flags_1999_ver.2015.11.10.dat
-rw-r--r-- 1 sburns aster 1964525 Nov 10 11:40 flux_flags_2000_ver.2015.11.10.dat
-rw-r--r-- 1 sburns aster 1959197 Nov 10 11:42 flux_flags_2001_ver.2015.11.10.dat
-rw-r--r-- 1 sburns aster 1959197 Nov 10 11:45 flux_flags_2002_ver.2015.11.10.dat
-rw-r--r-- 1 sburns aster 1959197 Nov 10 11:47 flux_flags_2003_ver.2015.11.10.dat
-rw-r--r-- 1 sburns aster 1964525 Nov 10 11:50 flux_flags_2004_ver.2015.11.10.dat
-rw-r--r-- 1 sburns aster 1959197 Nov 10 11:52 flux_flags_2005_ver.2015.11.10.dat
-rw-r--r-- 1 sburns aster 1959197 Nov 10 11:55 flux_flags_2006_ver.2015.11.10.dat
-rw-r--r-- 1 sburns aster 1959197 Nov 10 11:57 flux_flags_2007_ver.2015.11.10.dat
-rw-r--r-- 1 sburns aster 1964525 Nov 10 11:59 flux_flags_2008_ver.2015.11.10.dat
-rw-r--r-- 1 sburns aster 1959197 Nov 10 12:02 flux_flags_2009_ver.2015.11.10.dat
-rw-r--r-- 1 sburns aster 1959197 Nov 10 12:04 flux_flags_2010_ver.2015.11.10.dat
-rw-r--r-- 1 sburns aster 1959196 Nov 10 12:08 flux_flags_2011_ver.2015.11.10.dat
-rw-r--r-- 1 sburns aster 1964525 Nov 10 12:11 flux_flags_2012_ver.2015.11.10.dat
-rw-r--r-- 1 sburns aster 1959197 Nov 10 12:14 flux_flags_2013_ver.2015.11.10.dat
-rw-r--r-- 1 sburns aster 1959197 Nov 10 12:17 flux_flags_2014_ver.2015.11.10.dat


Soil data files:

-rw-r--r-- 1 sburns aster  6628864 Jul  9  2009 soil_2005.dat
-rw-r--r-- 1 sburns aster  4359018 Jul  9  2009 soil_2006.dat
-rw-r--r-- 1 sburns aster  4180299 Jul  9  2009 soil_2007.dat
-rw-r--r-- 1 sburns aster  7546749 Jul  9  2009 soil_2008.dat
-rw-r--r-- 1 sburns aster  5591008 Oct 15  2010 soil_2009_ver.2010.10.15.dat
-rw-rw-r-- 1 sburns aster  5586196 Mar 23  2012 soil_2010_ver.2012.03.23.dat
-rw-rw-r-- 1 sburns aster  5586944 Mar 23  2012 soil_2011_ver.2012.03.23.dat

_____________________________________________________________________
```

```
--------------------------------------------------------------------------
Data File Headers:

%
% --------
%
%  Flux Data Files Columns are:
%
%  1-6. Year, Month, Day, Hour, Minute, Sec -- in MST, Time Stamp Corresponds to center of Averaging Time Period
%  07. Decimal Day of Year (MST)
%  08. Fco2_21m_nee    umol/m2/s       21.5m             C02 Flux (NEE = w'co2' + storage flux)                 CSAT3 Sonic + LI-6262
%  09. Fco2_21m_nee_wust   umol/m2/s       21.5m         C02 Flux (same as above but w/ ustar filter)           CSAT3 Sonic + LI-6262
%  10. Strg_co2        umol/m2/s       0.5-21.5m         C02 Canopy Storage                                     LI-COR LI-6251 (or TGA100)
%  11. u_w_21m         m2/s2           21.5m             Momentum Flux (kinematic units)                        CSAT3 Sonic
%  12. Taua_21m        kg/m/s2         21.5m             Momentum Flux                                          CSAT3 Sonic
%  13. Qh_21m          W/m2            21.5m             Sensible Heat Flux                                     CSAT3 Sonic
%  14. Qe_21m          W/m2            21.5m             Latent Heat Flux                                       CSAT3 Sonic + Krypton Hygrometer (or LI-6262)
%  15. w_h2o_21m       mmol(H2O)/m2/s   21.5m           Water Vapor Flux (same as Qe_21m)                      CSAT3 Sonic + Krypton Hygrometer
%  16. Qh_soil         W/m2            0 to -10cm        Soil Heat Flux                                         REBS HFT-1
%  17. Strg_Qh         W/m2            2m+8m+21.5m       Sensible Heat Storage                                  Vaisala HMP-35D
%  18. Strg_Qe         W/m2            2m+8m+21.5m       Latent Heat Storage                                    Vaisala HMP-35D
%  19. Strg_bole       W/m2            1.5m (3cm depth)  Bole Heat Storage (Pine trees)                         Campbell A3537 (T-type Thermocouples)
%  20. Strg_needle     W/m2            8m                Needle Heat Storage                                    Vaisala HMP-35D
%  21. Qh_Ttc_21m      W/m2            21.5m             Sensible Heat Flux (from Thermocouple)                 CSAT3 Sonic + E-type Thermocouple
% --------
%
%
% --------
%
%  Climate Data Files Columns are:
%
%  1-6. Year, Month, Day, Hour, Minute, Sec -- in MST, Time Stamp Corresponds to center of Averaging Time Period
%  07. Decimal Day of Year (MST)
%  08. T_21m           degC            21.5m             Air Temperature                                        Vaisala HMP-35D
%  09. RH_21m          percent         21.5m             Relative Humidity                                      Vaisala HMP-35D
%  10. P_bar_12m       kPa             12m               Barometric Pressure                                    Vaisala PTB-101B
%  11. ws_21m          m/s             21.5m             Wind Speed                                             Campbell Scientific CSAT3 Sonic
%  12. wd_21m          deg from N      21.5m             Wind Direction (from true North)                       Campbell Scientific CSAT3 Sonic
%  13. ustar_21m       m/s             21.5m             friction velocity                                      Campbell Scientific CSAT3 Sonic
%  14. z_L_21m         NA              21.5m             Stability Parameter                                    Campbell Scientific CSAT3 Sonic
%  15. precip_mm       mm              10.5m             Precipitation                                          Met One Model 385 (or USCNR)
%  16. Td_21m          degC            21.5m             Dewpoint Temperature                                   Vaisala HMP-35D
%  17. vpd             kPa             8m                Vapor Pressure Deficit                                 Vaisala HMP-35D
%  18. leaf_wetness    0=dry 1=wet     13.5m             Wetness                                                Campbell Model 237
%  19. T_soil          degC            -5cm              Soil Temperature                                       Campbell 107L (thermistor)
%  20. T_bole_pine     degC            3 cm in bole      Pine Bole Temperature                                  Campbell A3537 (T-type Thermocouples)
%  21. T_bole_fir      degC            2 cm in bole      Fir Bole Temperature                                   Campbell A3537 (T-type Thermocouples)
%  22. T_bole_spruce   degC            2 cm in bole      Spruce Bole Temperature                                Campbell A3537 (T-type Thermocouples)
%  23. Rppfd_in_25m    umol/m2/s       25.5m             Incoming Photosynthetic Active Photon Flux Density (PPFD) LI-COR 190-SA
%  24. Rppfd_out_25m   umol/m2/s       25.5m             Outgoing PPFD                                          LI-COR 190-SA
%  25. Rnet_25m_REBS   W/m2            25.5m             Net Radiation                                          REBS Q-7.1
%  26. Rsw_in_25m_KZ   W/m2            25.5m             Incoming Shortwave Radiation                           Kipp and Zonen CNR1
%  27. Rsw_out_25m_KZ   W/m2            25.5m             Outgoing Shortwave Radiation                          Kipp and Zonen CNR1
%  28. Rlw_in_25m_KZ   W/m2            25.5m             Incoming Longwave Radiation                            Kipp and Zonen CNR1
%  29. Rlw_out_25m_KZ   W/m2            25.5m             Outgoing Longwave Radiation                           Kipp and Zonen CNR1
%  30. T_2m            degC            2m                Air Temperature                                        Vaisala HMP-35D or HMP-45D
%  31. T_8m            degC            8m                Air Temperature                                        Vaisala HMP-35D
%  32. RH_2m           percent         2m                Relative Humidity                                      Vaisala HMP-35D
%  33. RH_8m           percent         8m                Relative Humidity                                      Vaisala HMP-35D
%  34. h2o_soil        m3/m3           -5cm              Volumetric Soil Moisture                               Campbell CS616 (or CS615)
%  35. co2_21m         umol/mol        21.5m             Carbon Dioxide Mixing Ratio                            Campbell TGA100
%  36. h2o_picarro     mmol/mol        24.3m             Water Vapor Mixing Ratio                               Picarro L2120i
%  37. dD_picarro      per mil         24.3m             Deuterium                                              Picarro L2120i
%  38. d180_picarro    per mil         24.3m             delta-O-18 (ratio of oxygen-18:oxygen-16)              Picarro L2120i
% --------
%
%
% Soil data file Information:
%
% -- Niwot Ridge Ameriflux Data --
% MST Time Period: 2011  01/01 00:15:00 - 12/31 23:45:00, JD 1.010-365.990 (MST)
% UTC Time Period: 2011  01/01 07:15:00 - 01/01 06:45:00, JD 1.302-366.281 (UTC)
% File Creation Date: 23-Mar-2012
% File Created by: Sean Burns (sean.burns@colorado.edu)
% File Created for: CU/Monson Ameriflux Tower, Supplemental Soil Data
% Current Version: ver.2012.03.23
%
%   note: soil sensors were moved in Oct 2008 (locations used in 2008 are removed starting with "soil_2009_XXXX.dat")
%
%--------
%
% NOTES:
%              * If you use these data please contact Sean Burns (sean.burns@colorado.edu) or Russ Monson (russell.monson@colorado.edu)
%
%              * Acronyms:
%                       CSI = Campbell Scientific Instruments
%                      REBS = Radiation and Energy Balance Systems
%                       RTD = (Platinum) Resistance Temperature Detector
%                     horiz = sensor is oriented horizontally (ie, parallel to the ground)
%                      vert = sensor is oriented vertically (ie, either perpendicular or at 45 deg relative to the ground)
%                      open = sensor is located in a forest clearing (typically size is about 5-8m wide)
%                      tree = sensor is (mostly) covered by a tree canopy
%                        IC = sensor intercomparison (in Aug/Sep 2005 for Tsoil_rtds, also for CS-616s in 2009)
%
%              * Missing or invalid data are NaN
%
%              * Whenever a sensor was moved a new column and description exists.
%
%              * The soil temperature data have an empirical correction applied:
%
```

```
%                  - REBS STP-1 RTD sensors empirical corrections that were determined by Andrew Turnipseed
%                     on Sept 6, 2001 and have a form, Trtd = Gain.*Trtd_raw + Offset
%
%                              Sensor ID   Gain         Offset
%                                RTD01    0.9450       -0.0051
%                                RTD02    0.9670       -0.5600
%                                RTD03    0.9670       -0.6580
%                                RTD04    0.9490       -0.9770
%                                RTD05    0.9863       -0.0205
%
%                  - the 107L empirical correction was determined at the NCAR Calibration Lab (EOL)
%
%              * Note that the REBS STP-1 RTD sensors has a very slow response time (and is an average over
%                 5cm) whereas the 107L has a faster response and is more like a "point" measurement)
%
%              * The "mini-tower" is in an open area about 20 meters to the South West of the CU Tower (where in-canopy sensors are located)
%
%              * For 2005-2008 (Oct), the "soil pit" is about 30 meters to the North West of the CU Tower and is partially covered by a canopy
%                Starting in Oct 2008, there is an "open" soil pit (with no canopy overhead) and a "tree" pit which is near a tree and partially
%                covered by a canopy (see 2008 data file header for more details)
%
%              * The linear and non-linear calculation of soil water potential (SWP) are shown on p.6 in the manual
%
%              * The linear calculation of Soil Water Potential (SWP) is for 0 to 200 kPa
%
%              * The non-linear SWP equation is for 10 to 100 kPa
%
%              * Starting with the January 2006 data, Tsoil_5cm_cs107 (column 8) and h2o_soil_hori_5cm_ucb_cs616 (column 18) are
%                 the soil temperature and moisture data that are in the CU Ameriflux "climate" 30-min data files
%
% Columns are:
%
% 1-6. Year, Month, Day, Hour, Minute, Sec -- in MST, Time Stamp Corresponds to center of Averaging Time Period
% 07. Decimal Day of Year (MST)
% 08. Tsoil_5cm_cs107                          degC            -5cm (horiz at mini-tower)           Soil Temperature                       CSI 107L
% 09. Rs_soil_cs257_kOhms                      kOhms            0 to -15cm                          Sensor Resistance                      CSI-257
% 10. soil_water_pot_lin_cs257_kPa             kPa              0 to -15cm                          Soil Water Potential (Linear Eqn)      CSI-257
% 11. soil_water_pot_cs257_kPa                 kPa              0 to -15cm                          Soil Water Potential (Non-Linear Eqn)  CSI-257
% 12. Tsoil1_rtd_hori_10cm_treepit             degC            -10cm (horiz at "tree" pit)          Soil Temperature              REBS STP-1 PRTD #1
% 13. Tsoil2_rtd_hori_25cm_treepit             degC            -25cm (horiz at "tree" pit)          Soil Temperature              REBS STP-1 PRTD #2
% 14. Tsoil3_rtd_hori_35cm_treepit             degC            -35cm (horiz at "tree" pit)          Soil Temperature              REBS STP-1 PRTD #3
% 15. Tsoil4_rtd_vert_tree                     degC            0 to -10cm                           Soil Temperature              REBS STP-1 PRTD #4
% 16. Tsoil5_rtd_vert_tree                     degC            0 to -10cm                           Soil Temperature              REBS STP-1 PRTD #5
% 17. h2o_soil_hori_5cm_ucb_cs616              m3/m3           -5cm (at mini-tower)                 Volumetric Soil Moisture      CSI-616 (ucb SE ch23)
% 18. h2o_soil_hori_5cm_open_cs616_n1          m3/m3           -5cm (near snowprobe)                Volumetric Soil Moisture    CSI-616 "N1" (soil SE ch23)
% 19. h2o_soil_hori_5cm_tree_cs616_n2          m3/m3           -5cm (tree 20cm from bole)           Volumetric Soil Moisture    CSI-616 "N2" (soil SE ch24)
% 20. h2o_soil1_hori_5cm_open_nr02394_cs615    m3/m3           -5cm (snow sensor 02394)             Volumetric Soil Moisture      CSI-615 #1
% 21. h2o_soil2_hori_5cm_tree_nr02392_cs615    m3/m3           -5cm (snow sensor 02392)             Volumetric Soil Moisture      CSI-615 #2
% 22. h2o_soil3_hori_10cm_open_nr02390_cs615   m3/m3           -10cm (snow sensor 02390)            Volumetric Soil Moisture      CSI-615 #3
% 23. h2o_soil4_hori_5cm_tree_nr02395_cs615    m3/m3           -5cm (snow sensor 02395)             Volumetric Soil Moisture      CSI-615 #4
% 24. h2o_soil5_hori_5cm_open_nr02393_cs615    m3/m3           -5cm (snow sensor 02393)             Volumetric Soil Moisture      CSI-615 #5
% 25. h2o_soil6_hori_3cm_tree_nr02391_cs615    m3/m3           -3cm (snow sensor 02391)             Volumetric Soil Moisture      CSI-615 #6
% 26. h2o_soil7_hori_5cm_open_cs615            m3/m3           -5cm                                 Volumetric Soil Moisture      CSI-615 #7
% 27. h2o_soil8_vert_open_cs615                m3/m3           0 to -15cm                           Volumetric Soil Moisture      CSI-615 #8
% 28. h2o_soil1_hori_11cm_openpit_cs616        m3/m3           -11cm ("open" pit 335cm from bole)   Volumetric Soil Moisture      CSI-616 #1
% 29. h2o_soil2_hori_26cm_openpit_cs616        m3/m3           -26cm ("open" pit 335cm from bole)   Volumetric Soil Moisture      CSI-616 #2
% 30. h2o_soil3_vert_cs616_IC                  m3/m3           0 to -15cm (IC location)             Volumetric Soil Moisture      CSI-616 #3
% 31. h2o_soil4_hori_30cm_openpit_cs616        m3/m3           -30cm ("open" pit 335cm from bole)   Volumetric Soil Moisture      CSI-616 #4
% 32. h2o_soil5_hori_5cm_openpit_cs616         m3/m3           -5cm ("open" pit 335cm from bole)    Volumetric Soil Moisture      CSI-616 #5
% 33. h2o_soil6_hori_5cm_treepit_cs616         m3/m3           -5cm ("tree" pit 85cm from bole)     Volumetric Soil Moisture      CSI-616 #6
% 34. h2o_soil7_vert_cs616_IC                  m3/m3           0 to -15cm (at IC location)          Volumetric Soil Moisture      CSI-616 #7
% 35. h2o_soil8_hori_5cm_open_cs616            m3/m3           -5cm ("open" location 225cm from bole)    Volumetric Soil Moisture   CSI-616 #8
% --------
%
```